*J*OURNAL OF SCIENCE

GAZİ UNIVERSITY

Gazi

1926

| Editorial Board |

| Editorial Board |

| Editorial Board |

| Foreign Editorial Advisory Board |

| English Language Editors |

| Technical Editors |

| INDEXING |

| ACCESSIBILITY |

| CONTENTS |

| CONTENTS |

| CONTENTS |

Advanced CNN-Based Classification and Segmentation for Enhanced Breast Cancer Ultrasound Imaging

Jehad CHEYI[1*]   Yasemin ÇETIN-KAYA[1]

[1] Tokat Gaziosmanpaşa University, Department of Computer Engineering, Tokat, Türkiye

Keywords	Abstract
Deep Learning CNN Breast Cancer Classification Image Processing	Breast cancer (BC) is one of the primary causes of mortality in women globally. Thus, early and exact identification is critical for effective treatment. This work investigates deep learning, more especially convolutional neural networks (CNNs), to classify BC from ultrasound images. We worked with a collection of breast ultrasound images from 600 patients. Our approach included extensive image preprocessing techniques, such as enhancement and overlay methods, before training various deep learning models with particular reference to VGG16, VGG19, ResNet50, DenseNet121, EfficientNetB0, and custom CNNs. Our proposed model achieved a remarkable classification accuracy of 97%, significantly outperforming established models like EfficientNetB0, MobileNet, and Inceptionv3. This research demonstrates the ability of advanced CNNs, when paired with good preprocessing, to significantly enhance BC classification from ultrasound images. We further used Grad-CAM to make the model interpretable so we may see which parts of the images the CNNs focus on when making decisions.

1. INTRODUCTION

The most prevalent cancer among women globally is BC (T. Wu et al., 2019). For women, it ranks second most-often occurring cause of death (Luo et al., 2024). BC affects roughly 2.89 million women globally each year, including 24.2% of all female cancer cases and placing first (Kabir et al., 2021; Pacal, 2022). Early detection of the disease is essential since it aids in lowering the number of premature deaths (G. G. Wu et al., 2019; Pourasad et al., 2021; Jabeen et al., 2022; Cruz-Ramos et al., 2023). Over 30 percent of all cancer fatalities are caused by BC, making it the deadliest cancer for women (Vigil et al., 2022). BC is identified with a variety of imaging methods, including mammography, ultrasound, scanning with magnetic resonance imaging (MRI), and electronic pathology images. Mammography is widely utilized for early detection. However, it has limits in sensitivity and specificity, particularly in thick breasts (Badawy et al., 2021). For breast ultrasound images, state-of-the-art CNN techniques like Single Shot Multibox Detector with YOLO, You Only Look Once have shown significant success in detecting breast lesions (Fujioka et al., 2020). MRI provides detailed images of the breast and is especially helpful in assessing high-risk patients and assessing tumor extent (Peng et al., 2023). Digital pathology pictures are the "golden standard" for recognizing cancer and are critical in cancer detection. Deep learning has demonstrated encouraging outcomes in increasing BC detection and categorization precision and efficiency. Deep learning has also been utilized to identify BC via ultrasound images, where data augmentation and transfer learning find application approaches have been applied to increase performance (G. G. W. et al., 2019). CNNs and deep learning techniques generally, have been used to assess medical images, which are mammography, ultrasound, MRI, and images from pathology

(Mahoro & Akhloufi, 2022). Deep learning has significantly improved diagnosis accuracy and treatment efficiency in a variety of medical areas (Çetin-Kaya & Kaya, 2024; Kaya & Cetin-Kaya, 2024). Deep learning algorithms can extract meaningful characteristics from imagery and make classifications based on them (Luo et al., 2024). For example, in mammogram-based screening and diagnosis, deep learning models have been used to classify mammograms into different categories, such as malignant, benign, or normal (Y. Zhang et al., 2021). Transfer learning involves pre-training a structure on a big dataset and adjusting it for a specific job. It has also been employed to enhance the efficiency of deep learning algorithms in BC imaging (Luo et al., 2024). There are challenges, such as the need for interdisciplinary cooperation, standardized and open databases, and addressing deep learning models' poor generalization ability and interpretability (Han et al., 2017). In this article, we explore the transformative potential of deep learning in BC ultrasound imaging, characterized by a diversity of innovative solutions that extend far beyond classification, with the development of a novel strategy and solutions. Current imaging techniques, such as mammography, often fall short in sensitivity and specificity, especially in women with thick breast tissue. This study seeks to overcome these constraints by investigating sophisticated approaches such as deep learning, notably CNNs, to improve diagnostic precision and help radiologists in ultrasound imaging. Our research seeks to enhance BC diagnosis utilizing ultrasound pictures and powerful deep-learning algorithms. Our contributions are as follows:

- Developed a custom CNN model achieving 97% classification accuracy for BC detection in ultrasound images, outperforming various state-of-the-art algorithms.
- Applied advanced image processing techniques, including U-Net for segmentation and Grad-CAM for model interpretability, to improve diagnostic accuracy and transparency.

The following describes the latter bits of this research. Section 2 addresses related works; Section 3 offers the dataset and approach of the investigation. Section 4 offers the findings of the research. Section 5 presents the findings of the study together with suggestions for next investigations.

2. RELATED WORK

The related work analysis in breast ultrasonography covers a broad spectrum of deep learning and transfer learning applications for classification, diagnosis, detection, and segmentation. Researchers have proposed novel deep neural network architectures and inventive approaches to enhance automated breast ultrasound systems' performance, specificity, and accuracy. Their combined efforts improve the possibility of an early diagnosis and better patient outcomes by advancing the detection and evaluation of BC. Table 1 summarizes previous research on the use of ultrasonography to diagnose BC.

2.1. Classification

In breast ultrasound classification, researchers have used deep-learning models to achieve remarkable accuracy, frequently outperforming traditional methods. These models demonstrate their ability to identify normal, benign, and malignant cases, providing invaluable assistance to radiologists and improving diagnostic accuracy. Classification-focused research contributes significantly to improving automated BC diagnosis and risk assessment.

2.1.1. Deep Learning

Several studies on BC have made significant contributions to diagnosis and classification by implementing deep learning techniques. Jabeen et al. (2022) introduced a probability-based optimum deep learning feature fusion method, achieving an impressive accuracy of 99.1% in BC classification. Their method utilized the Breast Ultrasound Images (BUSI) dataset, including 780 images categorized as normal, malignant, or benign. Zhuang et al. (2021) took a different approach, using image decomposition and fusion, including adaptive multi-model spatial feature fusion. This method yielded a remarkable accuracy of 95.48% and high precision on BUSI dataset. Momot et al. (2022) utilized deep neural networks, the EfficientNet B0, pre-trained using the data set from ImageNet, to automate ultrasound BC image classification. They reached an accuracy of 81.26%, highlighting the promise of deep learning in ultrasound diagnostics. Alrubaie et al. (2023) implemented CNN and transfer learning to achieve a high classification accuracy, with a 96% accuracy rate for one dataset and a

perfect 100% accuracy for another. This study involved datasets divided into Group A, comprising 780 images with three classes (benign, malignant, normal), and Group B, consisting of 9,016 images with benign and malignant BCs. A noise filter network (NF-Net) was used by Cao et al. (2020) to learn from noisy tagged ultrasound images to classify breast tumors. This approach attained classification accuracy of 73%. Furthermore, Kim et al. (2021) provided research regarding deep learning with little supervision for detecting ultrasounds of BC. Moon et al. (2020) focus on the diagnosis of BC. The researchers achieved high accuracy and AUC values using convolutional neural networks for ensemble learning. They used a private dataset containing 1687 tumors, with 953 benign and 734 malignant cases. Along with an open BUSI dataset with 697 tumors, comprising 437 benign, 210 malignant, and 133 normal cases. The study presents a computer-aided diagnostic (CAD) system that utilizes CNN architectures for tumor diagnosis. Liu et al. (2022) performed BC diagnosis using artificial intelligence and deep learning techniques. The suggested grid-based deep characteristic generator model classified breast ultrasonic images with 97.18% accuracy across cancerous, benign, and normal classes. The performance measures include accuracy, recall, precision, F1-score, and geometric mean, exceeded 96 for all classes. The study used a BUSI dataset comprising images from 600 female patients. The method involves grid-based deep feature generation, pre-developed CNN models, incremental feature selection, and a deep classifier to improve BC diagnosis accuracy.

2.1.2. Transfer Learning for Breast Cancer Diagnosis

G. G. Wu et al. (2019) focus on using machine learning, particularly transfer learning, for diagnosing triple-negative BC with ultrasonography. The dataset consists of 140 surgically confirmed BC patients, incorporating both ultrasound and clinical data. Grayscale and color doppler features were utilized for classification. The research demonstrated that machine learning using quantified ultrasonic image characteristics, including color doppler information, effectively differentiates triple-negative BC cases. Moustafa et al. (2020) used color doppler ultrasound introduced to enhance BC detection using machine learning. The dataset contains 159 solid masses, with 95 benign and 64 malignant cases. The study illustrates that incorporating color doppler and grayscale features in the training dataset improves the receiver operating characteristic area, thus enhancing the BC prognosis. Qi et al. (2019) proposed an automated diagnosis method for deep neural networks to process breast ultrasound pictures. Their approach employs a cascade of two neural networks, Mt-Net and Sn-Net, for breast ultrasonography image diagnosis. Mt-Net classifies images for the presence of malignant tumors, while Sn-Net further classifies images for solid nodules. The study used a large-scale ultrasound image collection annotated by experts separated into training, validation, and testing sets. The proposed method demonstrated comparable performance to human sonographers and achieved high accuracy and specificity in BC diagnosis. Several studies have harnessed transfer learning techniques to improve BC diagnosis and classification in the context of ultrasound imaging. Y. Zhang et al. (2021) investigated the use of transfer learning to fine-tune a model for improved BC subtype prediction. The study showed that transfer learning significantly enhanced classification accuracy.

Similarly, Pang et al. (2021) augmented breast ultrasound mass classification data using a semi-supervised Generative Adversarial Network(GAN)-based radiomics model. This approach resulted in an accuracy of 90.41% and high sensitivity, demonstrating the potential of transfer learning in data augmentation. Coronado-Gutiérrez et al. (2019) studied quantification ultrasound evaluation of images to diagnose Metastatic BC invasion. The suggested approach obtained an accuracy of 86.4% and a sensitivity of 84.9% using a dataset of 105 patients submitted 118 lymphatic node ultrasound images selected from two hospitals. Cruz-Ramos et al. (2023) applied transfer learning on a pre-trained architecture to classify benign and malignant BCs in ultrasound and mammography pictures, resulting in 97.6% accuracy. These studies' results show that transfer learning methods improve the efficiency of BC diagnosing and classification techniques using ultrasound imaging.

2.2. Detection using Deep Learning

Several research has investigated the utilization of Deep learning algorithms for detecting BC in radiography and ultrasound imaging. Mahoro and Akhloufi (2022) evaluated therapy response using reference images from

the Evaluating Therapy Response Breast MRI dataset (1,500 DICOM format images) and the BUSI dataset (250 BMP type BC images). Marini et al. (2023) introduced a method called volume sweep imaging for BC detection. Masud et al. (2021) uses CNNs that have been previously trained to identify BC using ultrasound imaging. Their study demonstrated impressive results, with models like DenseNet201, Xception, and ResNet18 achieving 100% accuracy using various optimizers. This study used publically accessible breast ultrasound scans from Rodrigues; there are 250 ultrasound scans, including 100 normal and 150 cancerous instances. The study applied a transfer learning technique to pre-trained models and a K-fold cross-validation procedure for assessment. Li et al. (2022) presented the "BUSnet" Deep learning algorithm for breast tumors lesion detection in ultrasound images. Their dataset included 780 samples, with 133 normal, 487 benign, and 210 malignant cases. The testing dataset was collected from a prior source. The method included unsupervised region proposal, bounding-box regression methods, and a post-processing strategy to improve detection accuracy. Z. Zhang et al. (2021) focused on employing a Deep learning algorithm used in automated breast ultrasonography to detect cancers. They achieved a sensitivity of 0.88 with a false positive rate of 0.19 per second (FP/S). The study employed a unique ABUS imaging dataset from Peking University People's Hospital, which included 170 ABUS tumor volumes obtained from 124 female patients. Their technique comprises employing the Bayesian YOLOv4 network and Monte Carlo dropout and making unique YOLOv4 tweaks for detecting ABUS tumors.

2.3 Segmentation

2.3.1. Deep Learning-Based Segmentation Studies

Gómez-Flores and de Albuquerque Pereira (2020) focus on evaluating the performance of pre-trained CNNs at segmenting BCs in ultrasound pictures. They revealed that SegNet and DeepLabV3+ had the greatest segmentation results, while ResNet18 showed potential for CAD systems. The study included more than 3000 breast ultrasound Images taken from seven separate ultrasound machine models. Ilesanmi et al. (2021) suggested a segmentation strategy producing high dice measures for malignant and normal breast ultrasound image. The study used two datasets: one with 264 photos (100 malignant, 164 benign) and another with 830 images (487 malignant, 210 benign, and 133 normal). Their approach includes a preprocessing stage and a deep learning segmentation stage. Vakanski et al. (2020) incorporating attention blocks into deep-learning models for breast tumor segmentation resulted in models that outperformed the basic U-Net model. The dataset included 510 ultrasound images converted to grayscale 8-bit data and resampled into floating points using normalization. Xu et al. (2019) primarily focused on applying machine learning to segment breast ultrasound pictures, with quantitative measurements achieving more than 80% accuracy. The dataset utilized is not specified. However, their method categorizes BUSI into four tissue types: skin, fibroglandular, mass, and fatty tissue. Zhang et al. (2019) introduced a novel method, Boundary-aware Semi-Supervised Deep Learning (BASDL), for breast ultrasound lesion CAD. BASDL achieved a classification accuracy of around 92.00±2.38% and was evaluated on two breast ultrasound datasets. Chiang et al. (2018) specifically targeted tumor detection in automated ultrasound image with a dataset that includes 230 pathology-proven lesions from 187 individuals, 90 of which are benign and 140 of which are malignant. The proposed method involved preprocessing, segmentation, and feature extraction using a sliding window detector for localized analysis. Lei et al. (2018) obtained the highest segmentation performance by developing a technique for segmenting breast anatomy in full breast ultrasound images. The ConvEDNet is a deep convolutional encoder-decoder network with regularized boundaries. The limited dataset used manual annotation due to the associated cost. Gong et al. (2020) explore a bi-modal approach to BC diagnosis using A support vector machine with several views based on deep neural networks. The classification accuracy achieved was 86.36%, with an AUC of 0.9079. The dataset utilized in this study included a total of 264 pairings of breast ultrasound and ultrasound elastography images of 129 individuals with benign tumors and 135 people with malignant tumors. The suggested model is divided into two parts: Multi-Depth Neural Network and Fusion Deep Neural Networks. The multi-view technique improves diagnosis by combining information from both types of ultrasound images.

2.3.2. Transfer Learning-Based Segmentation Studies

Negi et al. (2020) proposed the WGAN-RDA-UNET technique, which uses Wasserstein GANs. It obtained an

overall accuracy of 0.98 and a PR-AUC of 0.95. The research used the PASCALVOC2012 dataset for training and the Berkeley Segmentation Database (BSDS 300 and BSDS500) for assessment.

Table 1. Overview of deep learning-based ultrasound screening and diagnosis, DL: deep learning, TL: transfer learning, C=Classification, SE=Segmentation, DE=Detection

Author		Methods Used	Dataset	Success rate
Jabeen et al. (2022)	DL, C	Modified DarkNet-53 deep model	BUSI 780 images	99.1% accuracy
Liu et al. (2022)	DL, C	Grid-based deep feature generation-based	BUS 600 images	97.18% accuracy
Zhuang et al. (2021)	DL, C	Fuzzy enhancement	BUS 1328 images	95.48% accuracy
Momot et al. (2022)	DL, C	Efficient Net B1	ImageNet dataset	81.26% accuracy
Alrubaie et al. (2023)	DL, C	CNN Inception-v3	A: BUSI 780 images B: BUS 9016	96% accuracy for data A 100% accuracy for data B
Cao et al. (2020)	DL, C	Noise filter network (NF-Net)	BUS	73% accuracy
Kim et al. (2021)	DL, C	Weakly-supervised Deep learning techniques	BUS 1000 images	AUC values of 0.92-0.96
Moon et al. (2020)	DL, C	Dense Net VGG-16 and VGG-Like ResNet	Private 1687 images BUSI: 697 images	91.10% accuracy 94.62% accuracy
Moustafa, et al. (2020)	DL, C	Color Doppler AdaBoost ensemble classifier	159 solid masses	AUC of 0.986
Qi et al. (2019)	DL, C	Automated BC diagnosis model	BUS 8145	87.79% accuracy
Y. Zhang et al. (2021)	TL, C	(CLSTM)	N/A	91% accuracy
Cruz-Ramos et al. (2023)	TL, C	fusion and handcrafted features	BUSI 780 images	ACC of 97.6% PRE of 98%
Pang et al. (2021)	TL, C	Semi-supervised GAN model – TGAN model	BUS 1447	90.41% accuracy
Coronado-Gutiérrez et al. (2019)	TL, C	QUS image analysis techniques	BUS 217 images	86.4% accuracy
Mahoro and Akhloufi (2022)	DL, DE	different screening methods for BC	(RIDER) 1500 BUS 250 images	Dice coefficient: 0.82 Similarity rate: 0.69
Masud et al. (2021)	DL, DE	DenseNet201 - ResNet50	BUS 250 images	100
Li et al. (2022)	DL, DE	BUSnet	BUSI 780 images	100 accuracies
Z. Zhang et al. (2021)	DL, DE	Bayesian YOLOv4	BUSI 21,624 images	Sens: 0.88 FPs/S: 0.19
Negi et al. (2020)	TL, DE	(WGAN) (RDAU-NET)	PASCALVOC2012	Accuracy 0.98
Gómez-Flores and de Albuquerque Pereira (2020)	DL, SE	Multi models	BUS 3000 images	F1-score > 0.90
Ilesanmi et al. (2021)	DL, SE	End-to-end deep learning segmentation stage	Dataset 1: 264 images Dataset 2: 830 images	89.73% were cancerous and 89.62% were benign.
Vakanski et al. (2020)	DL, SE	U-Net - U-Net-SA	BUS 510 images	(DSC) 90.5%
Xu et al. (2019)	DL, SE	CNNs	Private dataset	80% accuracy
Zhang et al. (2019)	DL, SE	BASDL	UDIAT, UTWS	92.00% accuracy for UDIAT 83.9% accuracy for UTWS
Chiang et al. (2018)	DL, SE	3-D CNN - 2-D CNN	Automated whole breast ultrasound images	95% sensitivity
Lei et al. (2018)	DL, SE	ConvEDNet - Adaptive Domain Transfer (ADT)	Automated Whole Breast Ultrasound images	86.8% intersection over union
Gong et al. (2020)	DL, SE	Multi-view deep neural network	BUS 264 images	86.36% accuracy

3. MATERIAL AND METHOD

3.1. Dataset

BUSI is used as part of the validation procedure in this study. The BUSI Dataset includes 780 breast ultrasound pictures categorized as benign, malignant, or normal. Images were taken from 600 female patients between the ages of 25 and 75. The images are 500 by 500 pixels on average and saved in PNG file format. Images were classified into three categories: there are 133 normal photos, 487 benign images, and 210 malignant images. The normal images reveal healthy breasts, whereas the benign images show benign masses and the malignant images indicate cancerous masses. The original images were preprocessed to reduce noise and improve image quality. This involved cropping the images to remove irrelevant information, scaling the images to a uniform size, and applying contrast enhancement. The data was collected in 2018 using LOGIQ E9 ultrasound systems. The images were captured using standard ultrasound protocols for breast imaging. The images were then manually labeled by expert radiologists (Al-Dhabyani et al., 2020). In addition, ground truth the appropriate B-mode images are supplied with binary mask images. Figure 1 shows the ground truth images.
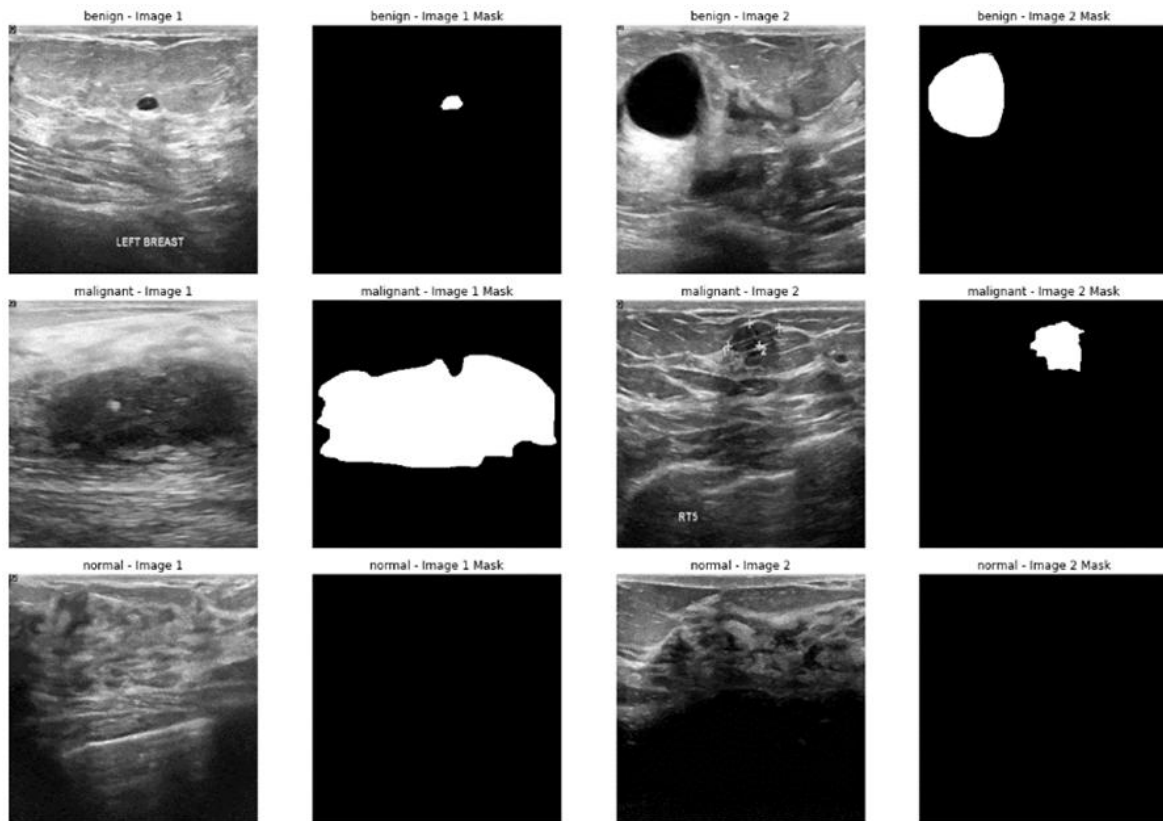
Figure 1. Examples of ultrasound images with ground truth

3.2. Methodology

3.2.1. Image Preprocessing and Segmentation

The segmentation section of our workflow is shown in Figure 2. We use a U-Net architecture to precisely identify areas on breast ultrasonography images that are of interest, distinguishing between benign, malignant, and normal tissues. First, we load and preprocess the dataset. This involves resizing the images and their corresponding masks to a uniform 224x224 pixels and normalizing them to ensure consistency. This preparation step is crucial for feeding the data into our model effectively. For medical image segmentation, the U-Net model is especially well-suited. Its architecture comprises two main parts: decreasing and increasing paths. The contracting path (or encoder) captures detailed contextual information by progressively down sampling the images using convolutional layers and max-pooling operations. This step extracts high-level features while reducing the spatial dimensions of the images. At the deepest point, a bottleneck layer further

refines these features. The expanding path (or decoder) then restores the spatial resolution using up sampling layers. It utilizes skip connections to concatenate high-level features from the contracting path with the corresponding layers in the expanding path, effectively recovering spatial information that might have been lost during down sampling. This combination ensures that the output mask accurately highlights the regions of interest. After constructing the model, we compile it using the Adam optimizer and binary cross-entropy loss, with accuracy as the metric to evaluate performance. We divided the dataset into training and validation sets, with 80% for training and 20% for validation. This ensures the model can adequately generalize to new, previously unknown data. Training the U-Net model involves running multiple iterations (epochs) over the dataset, during which the model learns to segment the images accurately. Once training is complete, we save the model for future use. This allows us to efficiently and precisely segment breast lesions in new ultrasound images, which is critical for early and accurate diagnosis of BC. This automated segmentation process significantly enhances the potential for effective treatment and better patient outcomes.
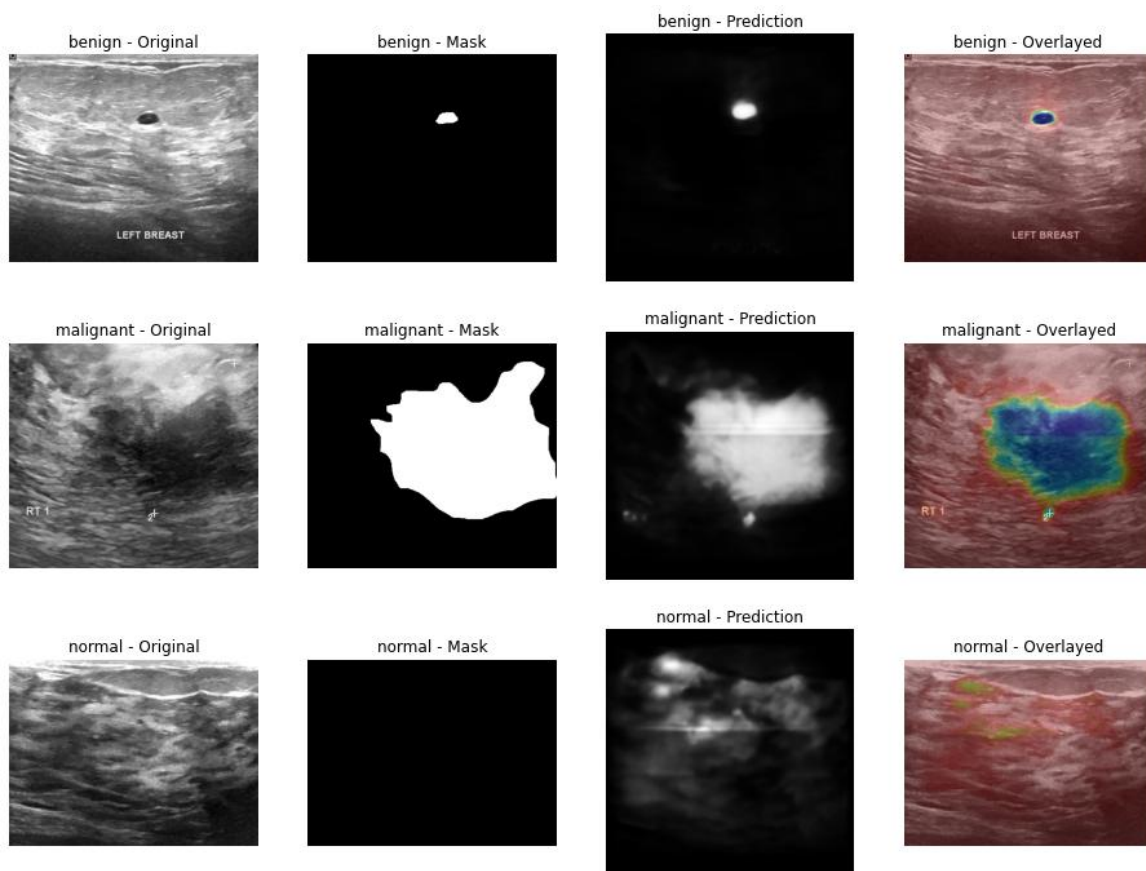
Figure 2. Visual results for classification and segmentation of breast ultrasound images

Image enhancement techniques are crucial for medical image analysis as they help improve the visibility of key structures and features. In this context, the BUSI dataset is enhanced using various techniques to make the images more informative and useful for diagnosis. Fuzzy enhancement focuses on adjusting the contrast of an image. By enhancing contrast, subtle differences in tissue density and composition become more apparent, which is crucial for accurate diagnosis in medical imaging. Sharpness enhancement improves the clarity of edges within the image, which is particularly important in ultrasound images where the edges of lesions or tumors need to be well-defined. Adjusting the brightness of an image can help balance the image intensity, which is useful for highlighting regions of interest that may otherwise be obscured due to uneven lighting or intensity variations in the original image. Rescaling images to a uniform size ensures consistency in visualization and comparison, which is essential for processing large datasets and training machine learning models. As shown in Figure 3, the overlay process involves combining the original ultrasound image with the mask that highlights areas of interest, such as tumors or lesions. As shown in Figure 4, this combined image is then enhanced using the above techniques to provide a clearer and more informative visualization.
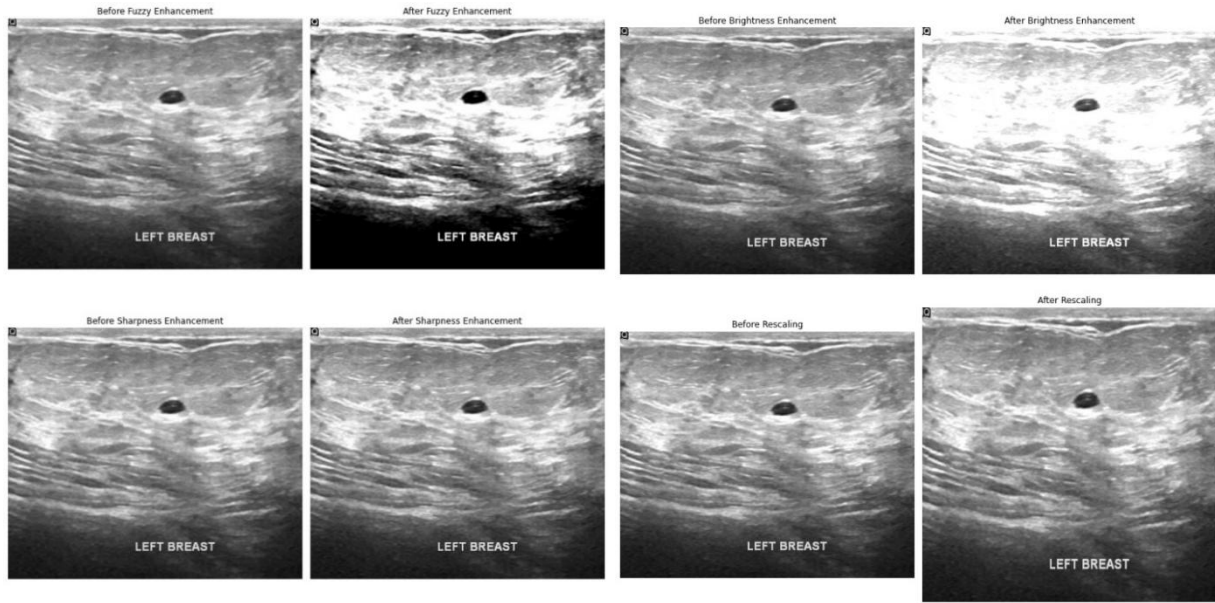
Figure 3. *Ultrasound images of the left breast under different image enhancement techniques*

(a) Before image processing   (b) After image processing.
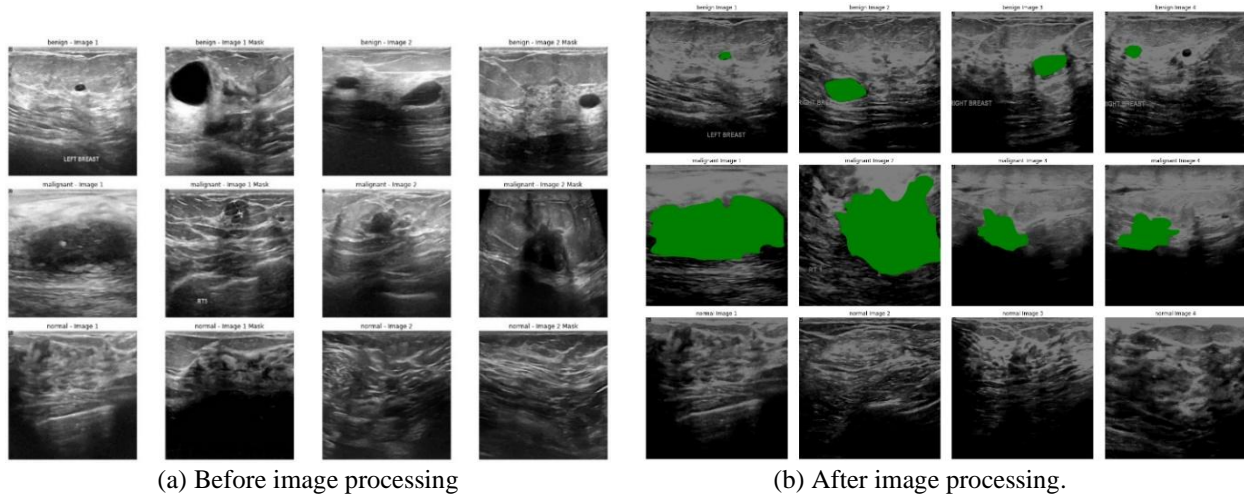
Figure 4. *Enhanced and overlayed image before and after image processing*

3.2.2. Proposed Model

We developed a custom CNN for breast image classification. As shown in Figure 5, our model captures key properties from images using a series of layers of convolution and pooling that preserve the spatial hierarchy. The model starts with a convolutional layer that has 32 filters, each measuring 3x3 pixels. This layer uses a stride of (1, 1) and the same padding to extract key characteristics from the input pictures. It is followed by a max-pooling layer with a kernel size of (2,2) and a stride of (2,2), which reduces spatial dimensions while enhancing translation invariance and model efficiency. Our network has additional convolutional layers with larger filter sizes (64, 128, 256, 256, and 512), followed by max-pooling layers. Except for the last convolutional layer, the output is decreased to 1*1 size to further reduce the sample size of the feature maps while improving abstraction. We use ReLU (Rectified Linear Unit) Functions for activation in these layers to help the network understand complex patterns in the input. The network's depth and structure allow it to captivate both local and global picture functions effectively. Following the convolutional layers, we used GlobalAveragePooling to fully connect the (dense) layer. The model has three dense layers: the first has 512 neurons and employs ReLU activation in conjunction with L2 regularization (at a value of 0.01) to avoid overfitting. We also use a 0.5-rate dropout layer to deactivate neurons during training, randomly increasing generalization. The second layer has 1024 neurons and employs ReLU activation in conjunction with L2

regularization (with a value of 0.01). The last dense layer contains three neurons and employs a softmax activation function to generate probabilistic outputs for the three classes (benign, malignant, and normal). Our Results indicate that the suggested CNN model is highly effective. When we trained it on enriched overlayed datasets, the model had an F1-score of 0.97, with an accuracy of 0.97, precision of 0.98, and recall of 0.96. These metrics were much higher than those obtained while training with all layers without the enhanced overlayed datasets, which yielded an accuracy is 0.83, a precision is 0.80, a recall is 0.83, and an F1-score is 0.81. These findings demonstrate the robustness of our algorithm in detecting subtle patterns in medical images, resulting in extremely accurate categorization. We experimented with various models, architectures, and hyperparameters to achieve an accuracy higher than 97%. However, only this specific model managed to exceed that benchmark on our dataset.
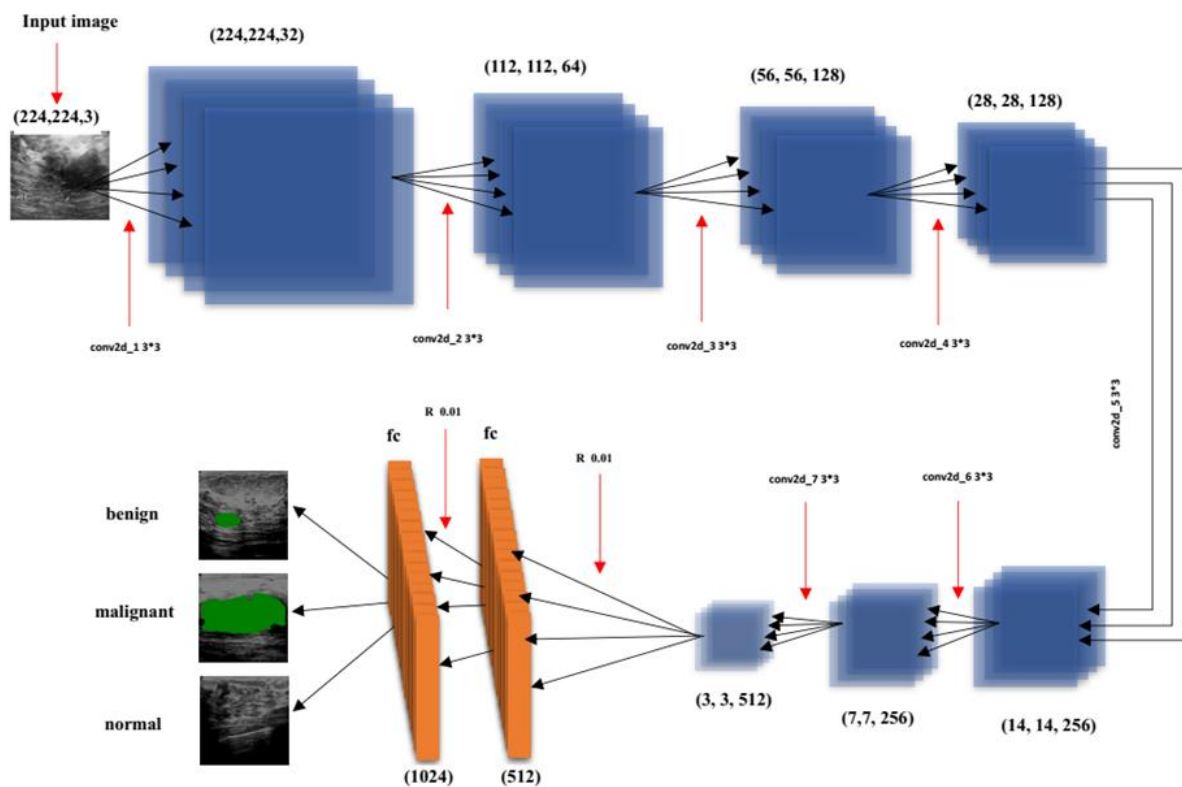
Figure 5. Proposed model

3.2.3. State-of-the-art Models

We selected several state-of-the-art models for their effectiveness in enhancing image classification performance: VGG16, VGG19, DenseNet121, EfficientNetB0, MobileNet, InceptionV3, Xception, and ResNet50. VGG16 and VGG19, created by the University of Oxford's Visual Geometry Group, consist of 16 and 19 layers, respectively, with convolutional and max-pooling layers stacked to capture complex features. DenseNet121 employs densely connected blocks, promoting feature reuse and efficient gradient flow. EfficientNetB0 uses compound scaling to optimize model depth, width, and resolution, achieving superior performance. MobileNet offers lightweight architecture suitable for mobile and embedded devices, utilizing depthwise separable convolutions to reduce complexity. InceptionV3 captures features at multiple scales with inception modules, while Xception replaces standard convolutions with depthwise separable convolutions for increased efficiency. ResNet50 solves the issue of vanishing gradients in deep neural networks by utilizing skip connections. During training and assessment, we fine-tuned the last four layers of each pre-trained model using an enhanced dataset. To improve generalization, we employed an Adam optimizer with a 0.0001 learning rate and a sparse categorical cross-entropy loss. We also employed data augmentation techniques including flipping, rotation, shifting, shear, and zooming. The training lasted 100 epochs with a batch size of 32, and it ended early after five epochs to avoid overfitting. Following training, we examined the models on a separate

test dataset, using measures such as accuracy, F1 score, precision, and recall to assess their classification skills. We implemented a custom top-layer architecture tailored for 3-class classification. This architecture builds on a base model, globalAveragePooling2D, which is used to minimize spatial dimensions, followed by dense layers with regularization for dropouts to avoid overfitting. The final output layer, consisting of three neurons with softmax activation, facilitates accurate multi-class classification.

4. RESULTS AND DISCUSSION

4.1. Proposed Model

We found that, when image preprocessing methods were used, the accuracy reached 0.97. Our proposed model performed amazingly with these preprocessing methods regarding other essential metrics: F1-Score: 0.97, precision: 0.98, recall: 0.96. Figure 6 demonstrates accuracy and loss graphs of the proposed model after data preprocessing. When this model was trained without preprocessing, its performance dropped significantly; it still has respectable metrics. More concretely, the accuracy dropped to 83%, meaning the classification would be less accurate than if preprocessing were applied. The confusion matrix elaborated on the classification capabilities of this model, showing it to be proficient at distinguishing classes. Train validation accuracy and loss graphs represented its learning process during training and provided valuable insights into model convergence and generalization. Such findings strongly emphasize the quests of image preprocessing toward improving custom CNN performance but also point to further ways of optimization and research in this field. Regarding accuracy, recall, and F1-score, the proposed model outperformed all other classes. For class 0, the model achieved 97% accuracy, 98% recall, and an F1 score of 97%. For class 1, this results in a 95% accuracy, 94% recall, and a 93% F1 score. Class 2 had 100% accuracy, 100% recall, and an F1 score of 100%. The confusion matrix also presented the model accuracy, showing minimal misclassification. Figure 7 depicts the confusion matrices obtained prior to and after image preprocessing. Overall, these results underscore the effectiveness of the proposed model in accurately classifying instances across multiple classes. Without data enhancement, there was a slight decline in the classification results. Figure 8 represents the accuracy and loss graphs of the proposed model data preprocessing. For class 0, the model recorded a precision of 85%, a recall of 91%, and an F1-score of 100%. For class 1, this gives a precision of 75%, a recall of 86%, and an F1-score of 80%. Class 2 had an accuracy of 68% and a recall of 56%, with an F1 score of 71%. Despite these variations, the confusion matrix showed the model's accuracy, with minimal misclassifications. These findings highlight the proposed model's effectiveness in accurately classifying instances across multiple classes while demonstrating the significant impact of data preprocessing on model performance.
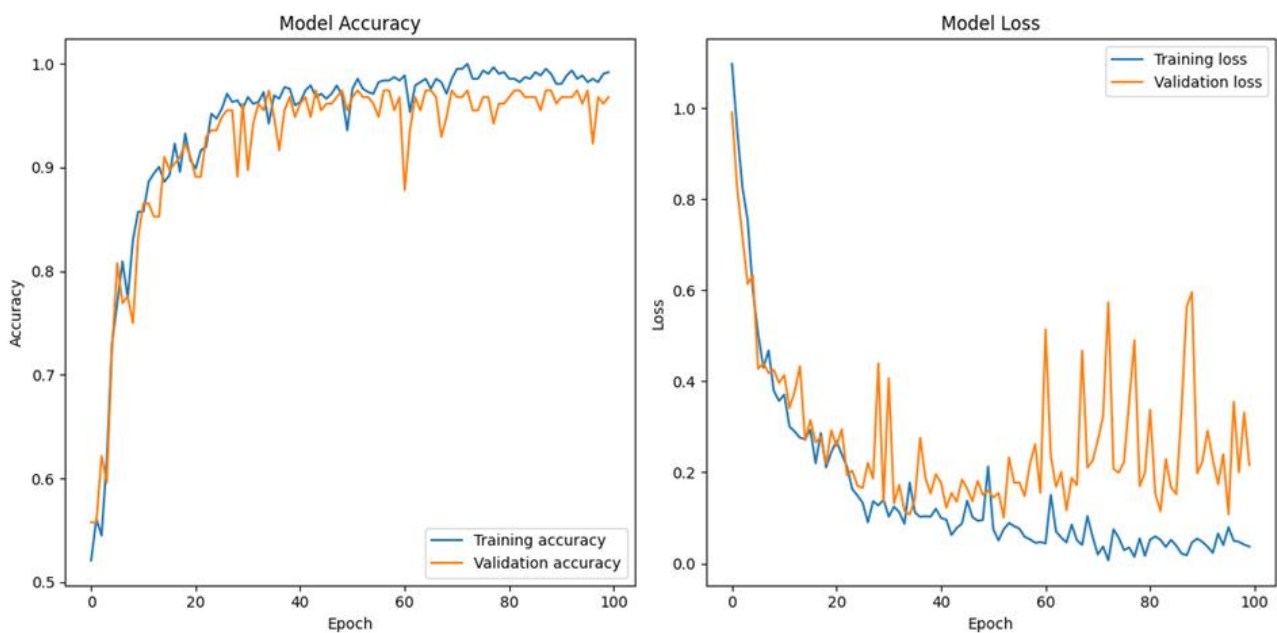
Figure 6. *The accuracy and the loss of the proposed model after data preprocessing*
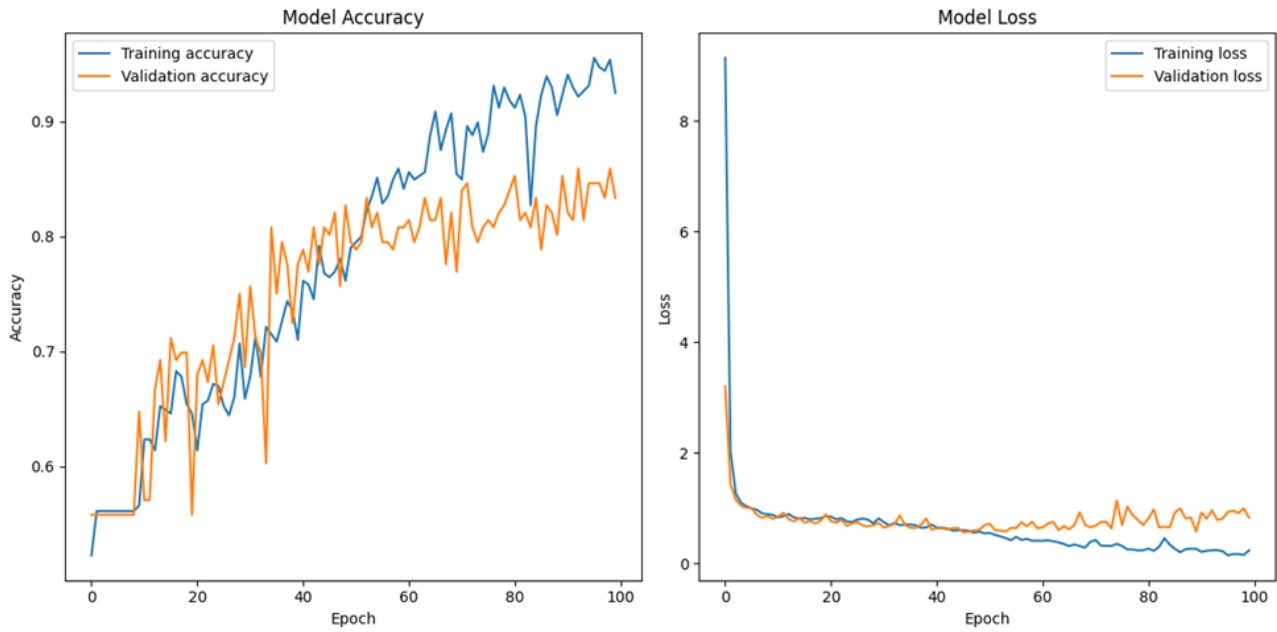
Figure 7. The accuracy and the loss of the proposed model before data preprocessing

(a) Before image processing

(b) After image processing
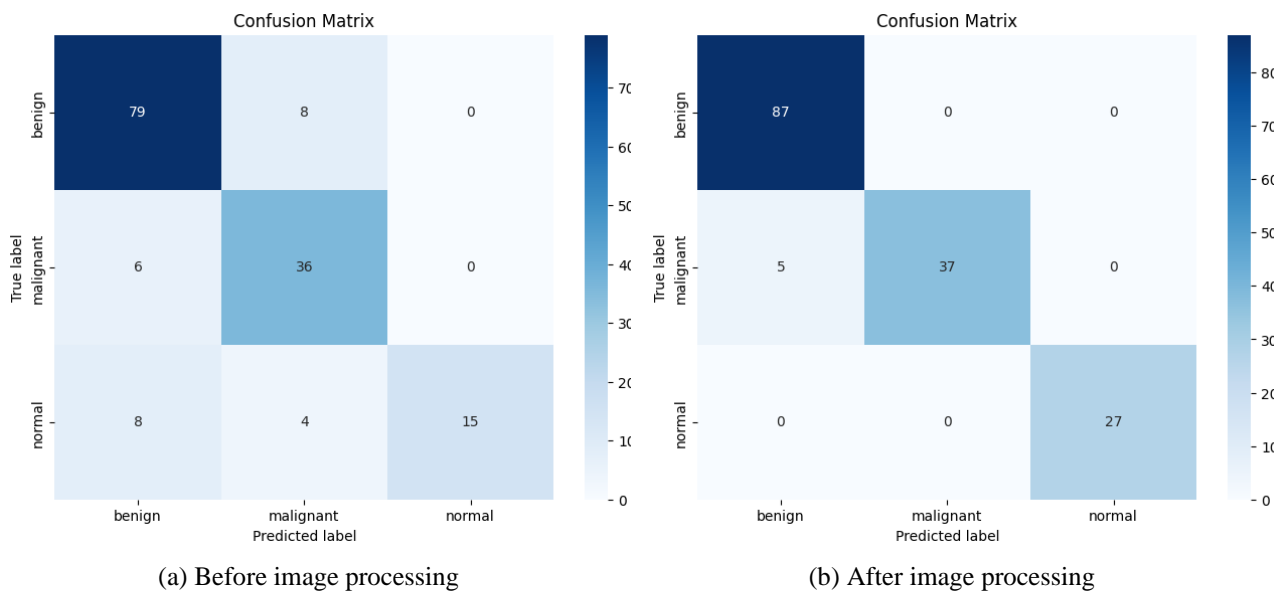
Figure 8. Confusion matrix of the proposed model before and after image preprocessing

4.2. Transfer Learning

In this study, we investigated the performance of fine-tuned models on a dataset augmented with enhanced overlayed images, considering various training scenarios. The performance metrics for each scenario are summarized in Tables 2, 3, 4, and 5. Table 2 presents the performance of models fine-tuned with the last four layers using the enhanced overlayed dataset. VGG19 and EfficientNetB0 demonstrated the highest accuracies of 0.99, with VGG19 achieving a precision of 0.98, a recall of 0.98, and an F1-score of 0.98. VGG16 and ResNet50 also performed exceptionally well, with accuracies of 0.98 and 0.96, respectively. This demonstrates the effectiveness of the enhanced dataset in improving model performance, achieving balanced and high scores across all metrics.

Table 2. *Performance metrics of the models trained with the last four layers with enhancing and overlaying*

Model	Accuracy	Precision	Recall	F1-Score
VGG16	0.98	0.99	0.98	0.98
VGG19	0.99	0.98	0.98	0.98
DenseNet121	0.88	0.91	0.87	0.89
EfficientNetB0	0.97	0.99	0.97	0.98
MobileNet	0.82	0.82	0.81	0.80
Inceptionv3	0.63	0.59	0.55	0.56
Xception	0.69	0.67	0.61	0.63
ResNet50	0.96	0.96	0.96	0.96

Table 3 shows the performance of models fine-tuned with the last four layers without enhancements. There was a noticeable drop in performance across all models. VGG16's accuracy decreased to 0.82, and Inceptionv3's accuracy fell to 0.60. EfficientNetB0 and VGG19, while still relatively higher performing with accuracies of 0.86 and 0.84, respectively, also exhibited declines in their precision, recall, and F1 scores. This indicates the negative impact of the absence of enhancements on model generalization and performance.

Table 3. *Performance metrics of the models trained with the last four layers without enhancing and overlaying*

Model	Accuracy	Precision	Recall	F1-Score
VGG16	0.82	0.79	0.82	0.80
VGG19	0.84	0.81	0.85	0.82
DenseNet121	0.76	0.75	0.71	0.72
EfficientNetB0	0.86	0.85	0.84	0.84
MobileNet	0.74	0.69	0.72	0.70
Inceptionv3	0.60	0.57	0.50	0.51
Xception	0.66	0.61	0.58	0.59
ResNet50	0.81	0.83	0.75	0.78

Table 4 represents the results of models trained with all layers using the enhanced overlayed dataset. These models exhibited outstanding performance, with several achieving near-perfect metrics. EfficientNetB0 reached an accuracy of 0.99, with precision, recall, and an F1-score of around 0.99. VGG19 and DenseNet121 both attained an accuracy of 0.98. The proposed model also showed strong performance with an accuracy of 0.97. These results underscore the benefits of using an enhanced dataset for training models across all layers.

Table 4. *Performance metrics of the models trained with all layers with enhancing and overlaying*

Model	Accuracy	Precision	Recall	F1-Score
VGG16	0.96	0.98	0.95	0.96
VGG19	0.98	0.99	0.98	0.98
DenseNet121	0.98	0.99	0.98	0.98
EfficientNetB0	0.99	0.99	0.98	0.99
MobileNet	0.98	0.98	0.98	0.98
Inceptionv3	0.98	0.99	0.98	0.98
Xception	0.98	0.99	0.98	0.98
ResNet50	0.91	0.91	0.93	0.92
Proposed Model	0.97	0.97	0.97	0.97

Table 5 details the performance of models trained with all layers without enhancements. Although there was a general decrease in performance compared to their enhanced counterparts, models like DenseNet121 and EfficientNetB0 maintained relatively high accuracies of 0.87 and 0.86, respectively. However, models such as VGG16 and MobileNet exhibited more substantial drops, emphasizing the importance of dataset enhancements. The proposed model, without improvements, showed a moderate decrease in performance with an accuracy of 0.83. Our study demonstrates the critical role of dataset quality and preprocessing techniques in enhancing deep learning models' robustness and generalization capabilities. The enhanced overlayed dataset consistently led to significant improvements in model accuracy, precision, recall, and F1 score across various architectures. These findings confirm the value of data enhancement in machine learning tasks, highlighting its importance for achieving superior model performance. Figure 9 and Figure 10 represent the confusion matrices of the transfer learning models after and before data preprocessing.

Table 5. *Performance metrics of the models trained with all layers without enhancing and overlaying*

Model	Accuracy	Precision	Recall	F1-Score
VGG16	0.76	0.75	0.73	0.71
VGG19	0.77	0.74	0.77	0.75
DenseNet121	0.87	0.89	0.83	0.85
EfficientNetB0	0.86	0.85	0.84	0.85
MobileNet	0.86	0.85	0.84	0.83
Inceptionv3	0.82	0.80	0.80	0.80
Xception	0.85	0.84	0.81	0.82
ResNet50	0.85	0.84	0.79	0.81
Proposed Model	0.83	0.87	0.77	0.80

(a) VGG16

(b) VGG19

(c) DensNet121

(d) EfficientNetB0
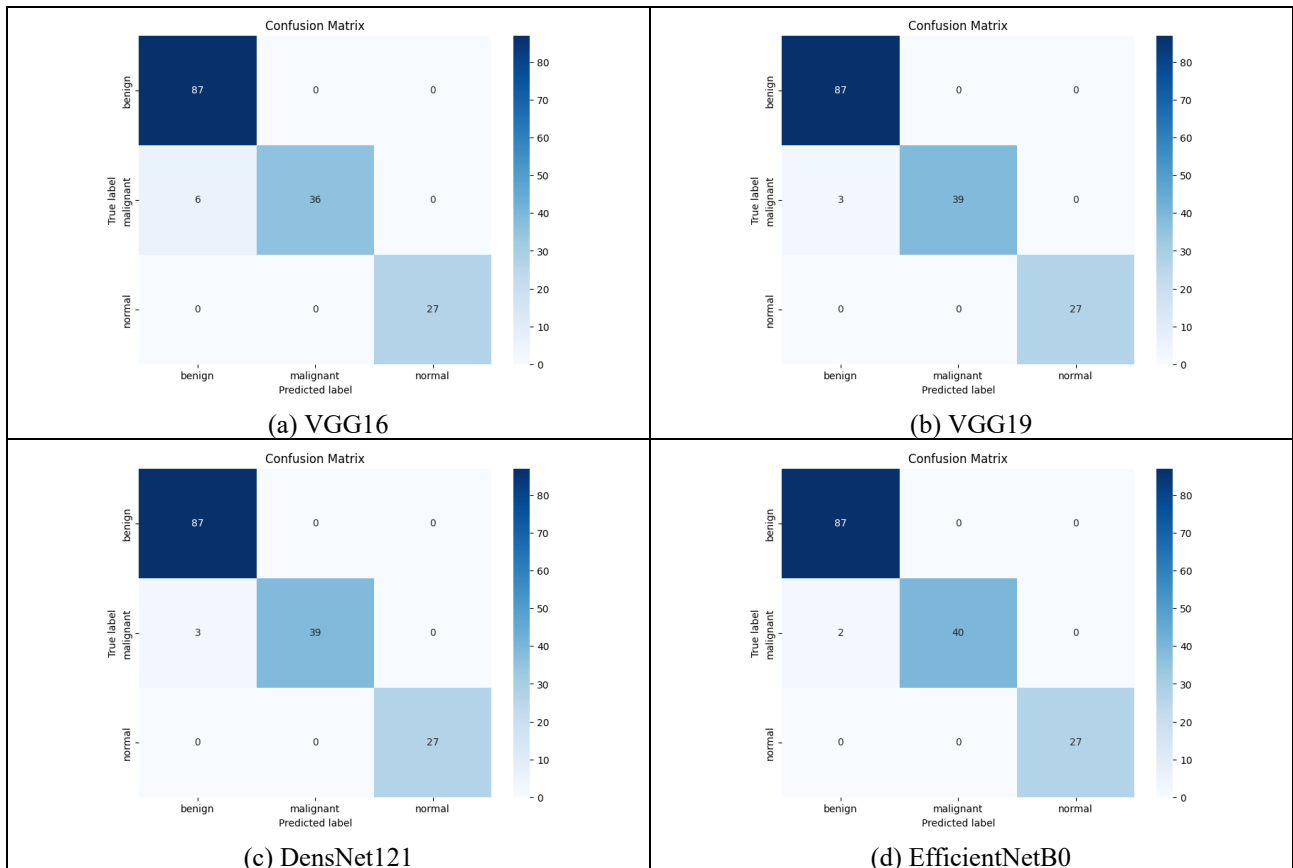
Figure 9. *Confusion matrix of transfer learning models after data preprocessing*

(e) MobileNet   (f) InceptionV3

(g) Xception   (h) ResNet50

Figure 9. *continued*

(a) VGG16   (b) VGG19

(c) DensNet121   (d) EfficientNetB0
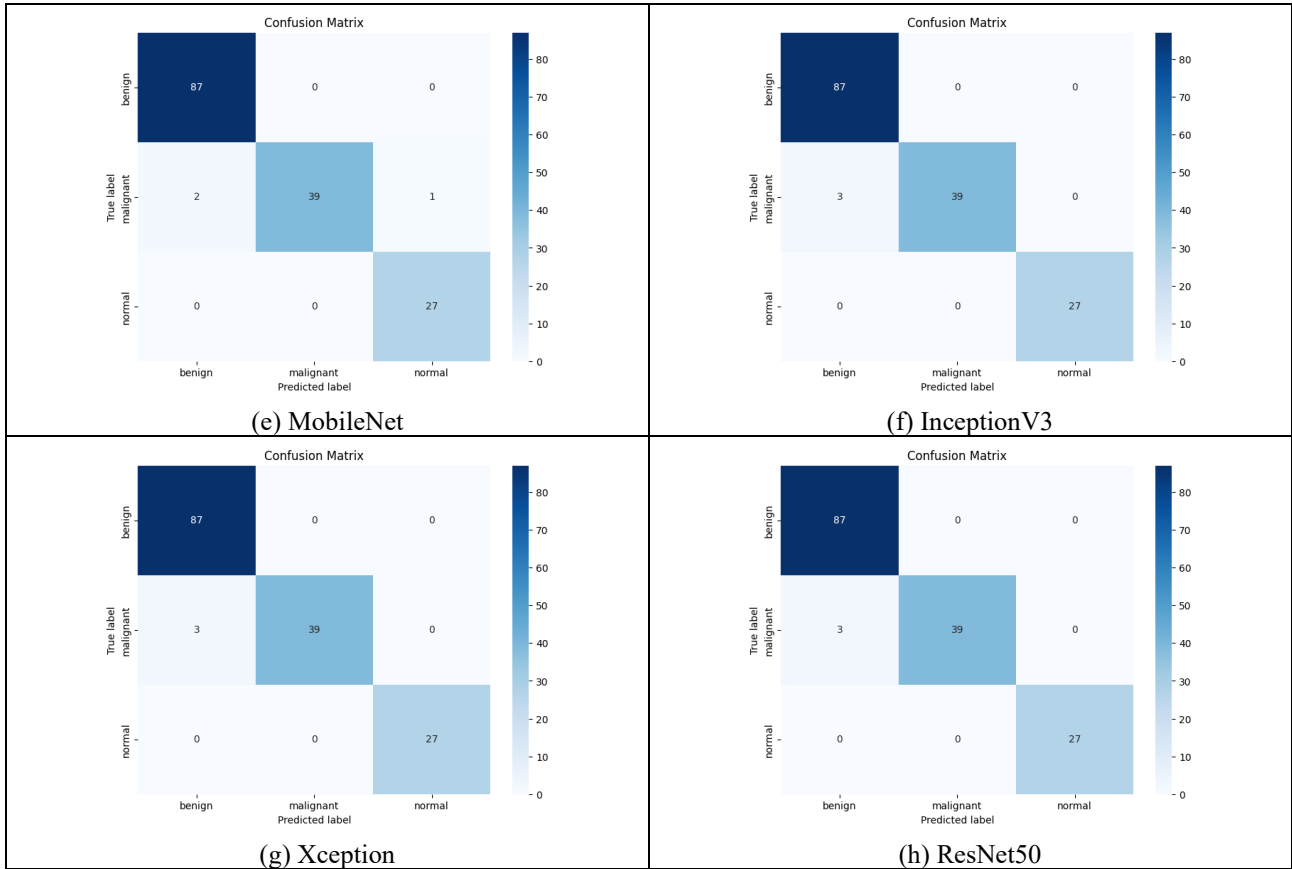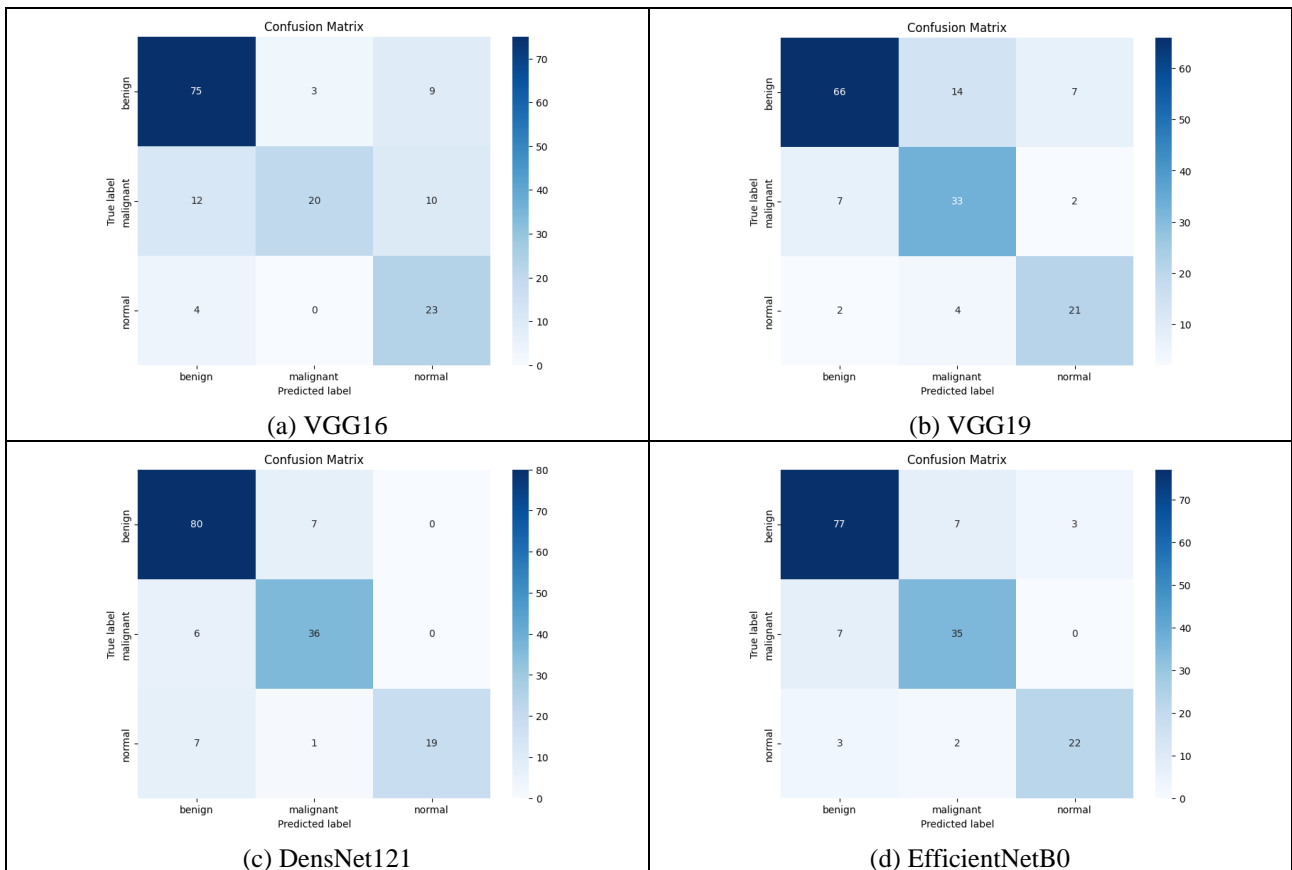
Figure 10. *Confusion matrix of transfer learning models before data preprocessing*
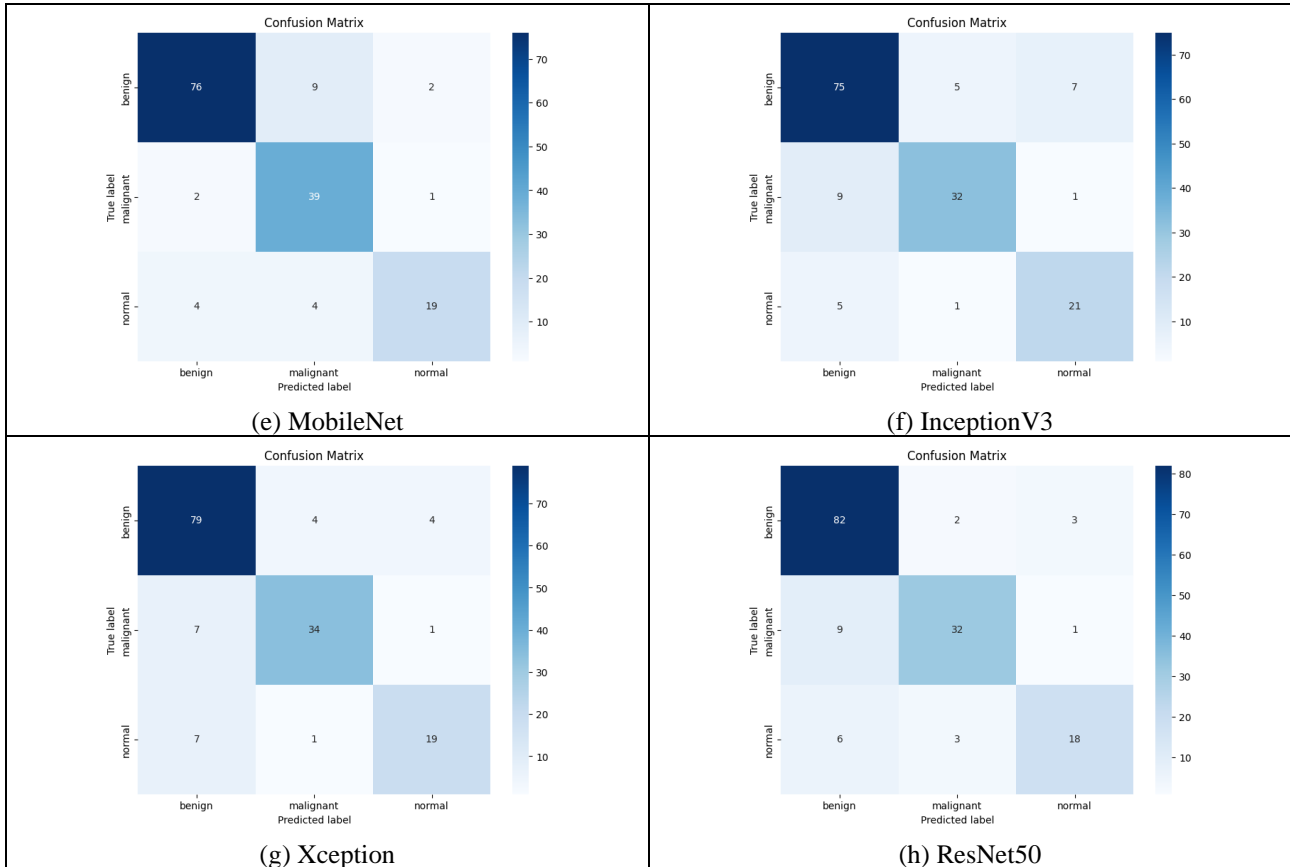
Figure 10. continued

4.3. Comparison of the Models

When comparing our study's findings with other transfer learning models, EfficientNetB0 performed exceptionally well, achieving an accuracy score of 0.99. This indicates its high confidence and precision in categorizing images across various datasets. VGG19, MobileNet, DenseNet121, InceptionV3, and Xception, all performed well with an accuracy of 0.98. VGG16 achieved an accuracy of 0.96. ResNet50, although slightly lower, still maintained strong performance with an accuracy of 0.91. The proposed model also demonstrated excellent performance, achieving an accuracy of 0.97. The proposed model achieved high precision, recall, and F1 scores with significantly fewer parameters than other architectures except EfficientNetB0 and Mobilenet. VGG16 with 14879299, VGG19 with 20188995, Densnet121 with 7333187, EfficientNetB0 with 4410790, Mobilenet with 3524547, InceptionV3 with 22360611, Xception with 21419307, ResNet50 with 24145539. With only 3097283 parameters, our model efficiently extracts relevant features and makes precise classifications without needing an excessive number of parameters. Figure 11 shows the comparison of transfer learning and our proposed model. This emphasizes not only its technical excellence but also its efficiency in using computational resources. Therefore, our proposed model emerges as a standout performer, offering a strong case for its adoption in image classification tasks where both efficiency and accuracy are crucial.

4.4. Comparison with Similar Studies

Several important insights emerge when comparing our study's outcomes with similar studies utilizing deep learning or transfer learning methodologies and comparable datasets for BC analysis. Liu et al. (2022) followed suit with a grid-based deep feature generation approach on the BUS dataset, yielding a commendable accuracy of 97.18%, showcasing the efficacy of this method in achieving high precision. Zhuang et al. (2021) employed fuzzy enhancement techniques on the BUS dataset, resulting in a notable accuracy of 95.48%, demonstrating the potential of such preprocessing methods in improving classification performance. Alrubaie et al. (2023) utilized the Inception-v3 CNN architecture on both BUSI and BUS datasets, achieving remarkable accuracies of 96% and 100%, respectively, underscoring the robustness of their approach across different datasets. Cruz-

Ramos et al. (2023) integrated fusion and handcrafted features on the BUSI dataset, attaining an accuracy of 97.6% and a precision of 98%, showing the effectiveness of feature engineering in enhancing classification outcomes. Pang et al. (2021) leveraged a semi-supervised GAN model on the BUS dataset, achieving a notable accuracy of 90.41%, highlighting the potential of generative models in augmenting classification tasks. Z. Zhang et al. (2021) employed Bayesian YOLOv4 on a large-scale BUSI dataset, achieving a sensitivity of 0.88 and a low rate of false positives, demonstrating the efficacy of their approach in achieving accurate tumor detection. Compared to these studies, our approach, which utilized a custom CNN architecture tailored specifically for breast ultrasound analysis, achieved competitive accuracy. We achieved 97% accuracy, demonstrating the effectiveness of our methodology for accurately classifying breast ultrasound. Through this comparative analysis, we gain valuable insights into the diverse methods and their respective successes in BC analysis tasks. Table 6 shows the comparison of our model with related studies.
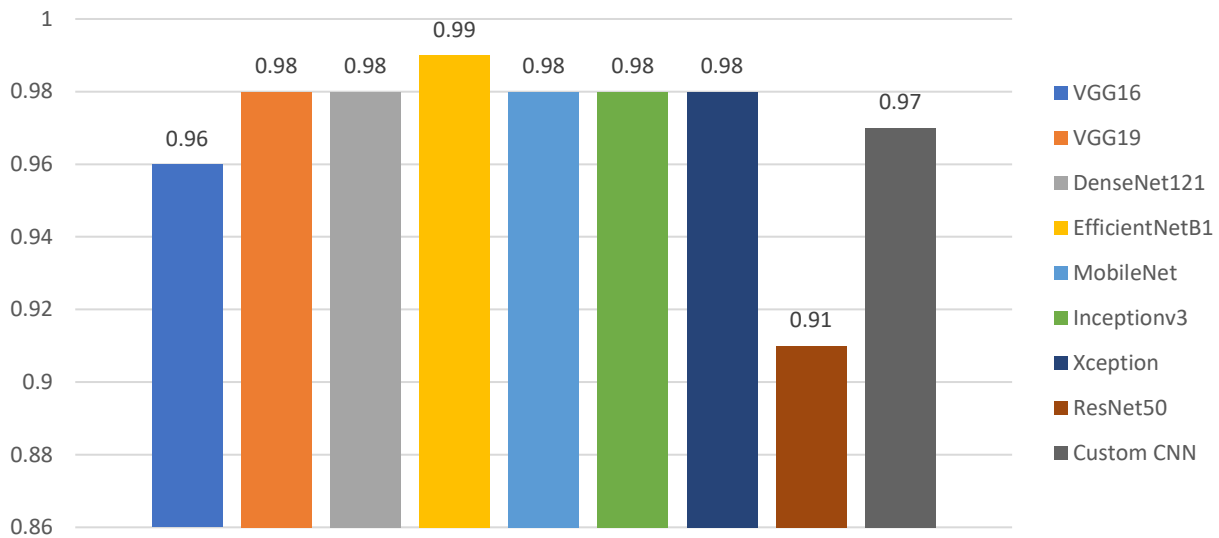
Figure 11. Comparison chart of transfer learning and Custom CNN (proposed model)

Table 6. Comparison table of Proposed Model with related studies

Study	Methods Used	Dataset	Success Rate
Zhuang et al. (2021)	Fuzzy enhancement	BUS (1328 images)	95.48%
Cruz-Ramos et al. (2023)	Fusion and handcrafted features	BUSI (780 images)	97.6%
Pang et al. (2021)	Semi-supervised GAN model	BUS (1447 images)	90.41%
Z. Zhang et al. (2021)	Bayesian YOLOv4	BUSI (21,624 images)	Sens: 0.88 FPs/S: 0.19
Alrubaie et al. (2023)	Inception-v3 CNN	A: BUSI (780 images) B: BUS (9016 images)	96%
Proposed Model	CNN	BUSI (780 images)	97%

4.5. The Grad-CAM Visualizing

The Grad-CAM (Gradient-weighted Class Activation Mapping) technique was utilized to understand the internal processes of a CNN model. At the same time, it made predictions on images from the test dataset. By analyzing the activations of the final convolutional layer of the CNN, Grad-CAM generates heatmaps that highlight the regions of the input image that are most influential in determining the model's output. In this analysis, specific layers of the CNN architecture were chosen to visualize the activation patterns corresponding to different classes. Figure 12 presents the Grad-CAM heatmap for a malignant case, the heatmap for a benign case, and the heatmap for a normal case. Each figure exhibits four distinct visualizations, providing a comprehensive understanding of the model's decision-making process. First, the original input image offers

context. Subsequently, the Grad-CAM heatmap is overlaid onto the input image, offering a visual representation of the areas within the image that strongly influenced the model's prediction. To further enhance interpretability, two additional visualizations were created: one with the Grad-CAM heatmap overlaid with transparency, providing a clearer view of the heatmap's distribution, and the other utilizing a transparent jet colormap, facilitating a more intuitive interpretation of the heatmap. These visualizations not only aid in understanding which image regions contribute most to the model's decision but also offer valuable insights into CNN's feature extraction and classification processes. By clarifying the model's attention mechanism, Grad-CAM enables researchers and practitioners to validate and interpret the model's predictions, enhancing deep learning models' transparency, trustworthiness, and interpretability in image analysis tasks.

5. CONCLUSION

In conclusion, this research demonstrated the enormous potential of deep learning models, especially CNNs, for the efficient classification of ultrasound images in the diagnosis of BC. The subject models were easily interpretable; besides, they showed better diagnostic performance when advanced image processing techniques-segmentation and enhancement-were applied to the images. Our proposed CNN model achieved an accuracy of 97%, compared with other state-of-the-art models such as EfficientNetB0, MobileNet, and InceptionV3. This emphasizes the need for models specially tailored with the ability to handle challenges that come with the uniqueness of medical imaging tasks. More importantly, the interpretability and transparency of our models were taken further with Grad-CAM use, making the decision-making process more comprehensible. This is critical in the clinical field. AI diagnostic tools should be not only precise but also interpretable for healthcare professionals and patients to build confidence in them. These results also suggest the importance of strong techniques for image preprocessing. Techniques such as image enhancement and overlay greatly improved model performance. This work should be extended in further studies to include more data modalities, such as 3D ultrasound or MRI images, and more complex CNN architectures that may result in even better classification outcomes. Moreover, such models' ability to generalize on larger datasets with more diverse data would be reassuring against their clinical use. The current study provided a sufficient backbone regarding the application of CNNs in the diagnosis of BC by using ultrasound images and gave important indications on how to design more efficient and trustworthy diagnostic tools that could potentially improve patient outcomes.

(a) Grad-CAM heatmap for a malignant case   (b) Grad-CAM heatmap for a benign case
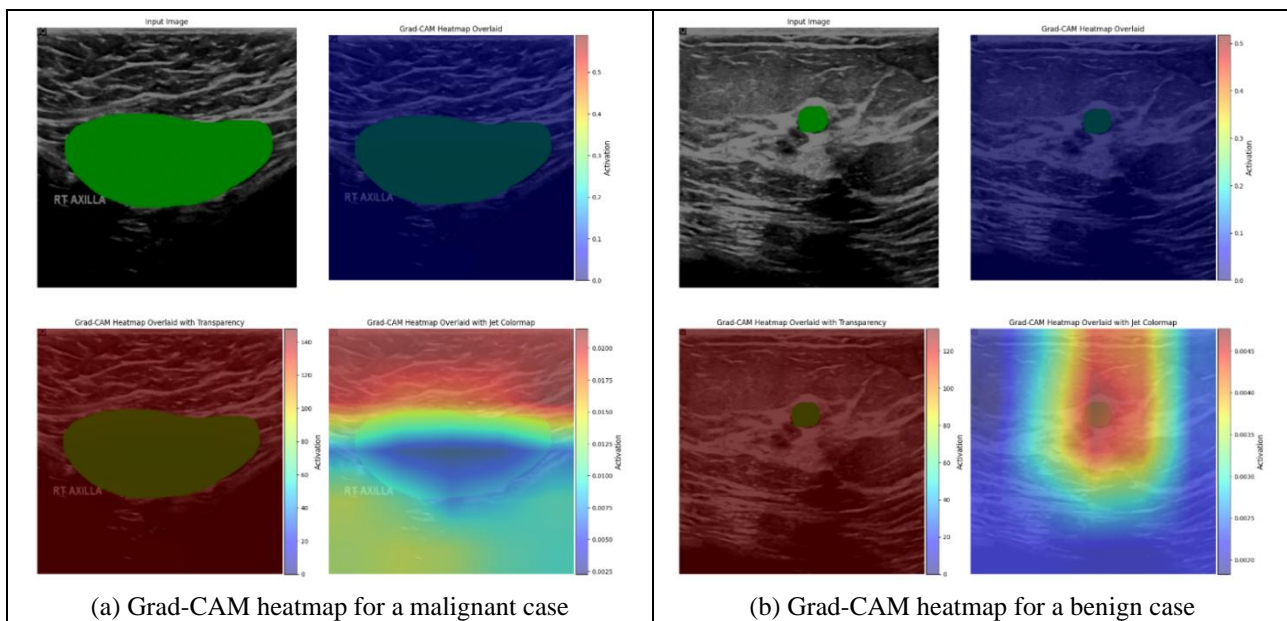
Figure 12. *The Grad-CAM heatmap for a malignant case, the heatmap for a benign case, and the heatmap for a normal case*

(c) Grad-CAM heatmap for a normal case
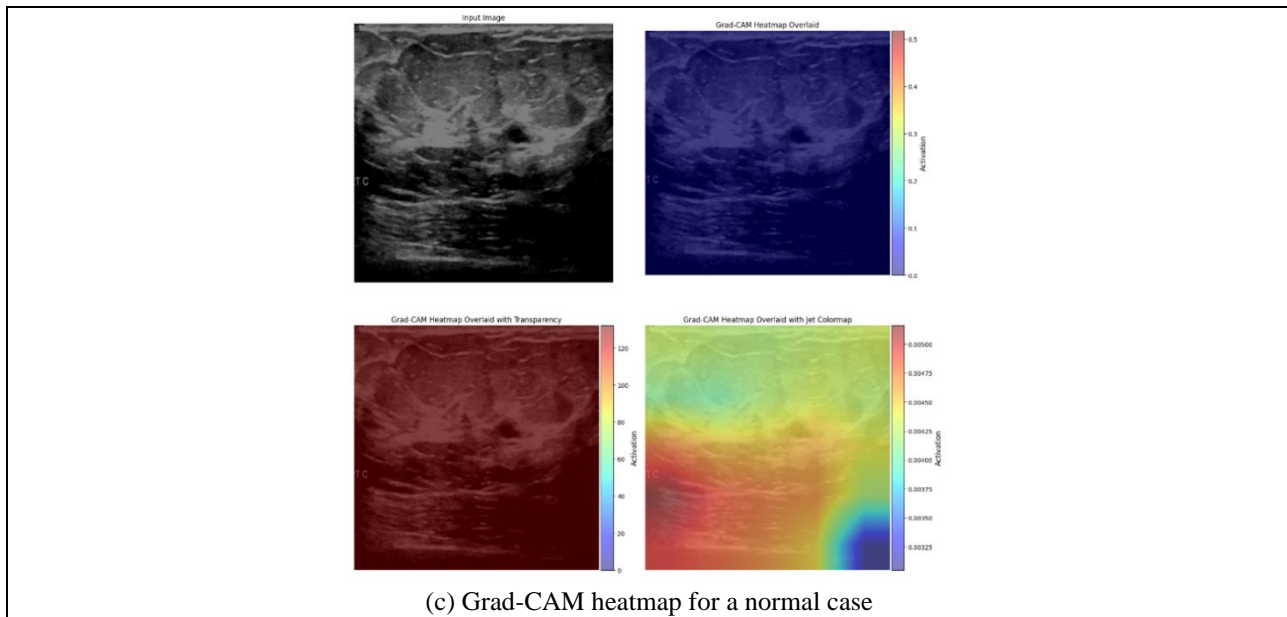
Figure 12. continued

AUTHOR CONTRIBUTIONS

Conceptualization, J.C. and Y.C-K.; methodology, J.C. and Y.C-K.; experiments, J.C.; validation, J. C. and Y.C-K.; manuscript-original draft, J.C. and Y.C-K.; manuscript-review and editing, J.C. and Y.C-K; visualization, J.C.; supervision, Y.C-K.. All authors have read and legally accepted the final version of the article published in the journal.

CONFLICT OF INTEREST

The authors declare no conflict of interest.

REFERENCES

Al-Dhabyani, W., Gomaa, M., Khaled, H., & Fahmy, A. (2020). Dataset of breast ultrasound images. *Data in Brief*, *28*, 104863. https://doi.org/10.1016/j.dib.2019.104863

Alrubaie, H., Aljobouri, H. K., AL-Jobawi, Z. J., & Çankaya, I. (2023). Convolutional neural network deep learning model for improved ultrasound breast tumor classification. *Al-Nahrain Journal for Engineering Sciences*, *26*(2), 57-62. https://doi.org/10.29194/NJES.26020057

Badawy, S. M., Mohamed, A. E.-N. A., Hefnawy, A. A., Zidan, H. E., GadAllah, M. T., & El-Banby, G. M. (2021). Automatic semantic segmentation of breast tumors in ultrasound images based on combining fuzzy logic and deep learning: A feasibility study. *PLOS ONE*, *16*(5), e0251899. https://doi.org/10.1371/journal.pone.0251899

Cao, Z., Yang, G., Chen, Q., Chen, X., & Lv, F. (2020). Breast tumor classification through learning from noisy labeled ultrasound images. *Medical Physics*, *47*(3), 1048-1057. https://doi.org/10.1002/mp.13966

Chiang, T.-C., Huang, Y.-S., Chen, R.-T., Huang, C.-S., & Chang, R.-F. (2018). Tumor detection in automated breast ultrasound using 3-D CNN and prioritized candidate aggregation. *IEEE Transactions on Medical Imaging*, *38*(1), 240-249. https://doi.org/10.1109/TMI.2018.2860257

Coronado-Gutiérrez, D., Santamaría, G., Ganau, S., Bargalló, X., Orlando, S., Oliva-Brañas, M. E., Perez-Moreno, A., & Burgos-Artizzu, X. P. (2019). Quantitative ultrasound image analysis of axillary lymph nodes to diagnose metastatic involvement in breast cancer. *Ultrasound in Medicine & Biology*, *45*(11), 2932-2941. https://doi.org/10.1016/j.ultrasmedbio.2019.07.413

Cruz-Ramos, C., García-Ávila, O., Almaraz-Damián, J.-A., Ponomaryov, V., Reyes-Reyes, R., & Sadovnychiy, S. (2023). Benign and malignant breast tumor classification in ultrasound and mammography

images via fusion of deep learning and handcraft features. *Entropy*, *25*(7), 991. https://doi.org/10.3390/e25070991

Çetin-Kaya, Y., & Kaya, M. (2024). A novel ensemble framework for multi-classification of brain tumors using magnetic resonance imaging. *Diagnostics*, *14*(4), 383. https://doi.org/10.3390/diagnostics14040383

Fujioka, T., Mori, M., Kubota, K., Oyama, J., Yamaga, E., Yashima, Y., Katsuta, L., Nomura, K., Nara, M., Oda, G., Nakagawa, T., Kitazume, Y., & Tateishi, U. (2020). The utility of deep learning in breast ultrasonic imaging: A review. *Diagnostics*, *10*(12), 1055. https://doi.org/10.3390/diagnostics10121055

Gómez-Flores, W., & de Albuquerque Pereira, W. C. (2020). A comparative study of pre-trained convolutional neural networks for semantic segmentation of breast tumors in ultrasound. *Computers in Biology and Medicine*, *126*, 104036. https://doi.org/10.1016/j.compbiomed.2020.104036

Gong, B., Shen, L., Chang, C., Zhou, S., Zhou, W., Li, S., & Shi, J. (2020, April 3-7). *BI-modal ultrasound breast cancer diagnosis via multi-view deep neural network SVM*. In: Proceedings of the 2020 IEEE 17th International Symposium on Biomedical Imaging (ISBI) (pp. 1106-1110), Iowa City, IA, USA. IEEE. https://doi.org/10.1109/ISBI45749.2020.9098438

Han, S., Kang, H.-K., Jeong, J.-Y., Park, M.-H., Kim, W., Bang, W.-C., & Seong, Y.-K. (2017). A deep learning framework for supporting the classification of breast lesions in ultrasound images. *Physics in Medicine & Biology*, *62*(19), 7714. https://doi.org/10.1088/1361-6560/aa82ec

Ilesanmi, A. E., Chaumrattanakul, U., & Makhanov, S. S. (2021). A method for segmentation of tumors in breast ultrasound images using the variant enhanced deep learning. *Biocybernetics and Biomedical Engineering*, *41*(2), 802-818. https://doi.org/10.1016/j.bbe.2021.05.007

Jabeen, K., Khan, M. A., Alhaisoni, M., Tariq, U., Zhang, Y.-D., Hamza, A., Mickus, A., & Damaševičius, R. (2022). Breast cancer classification from ultrasound images using probability-based optimal deep learning feature fusion. *Sensors*, *22*(3), 807. https://doi.org/10.3390/s22030807

Kabir, S. M., Bhuiyan, M. I. H., Tanveer, M. S., & Shihavuddin, ASM. (2021). RiIG modeled WCP image-based CNN architecture and feature-based approach in breast tumor classification from B-mode ultrasound. *Applied Sciences*, *11*(24), 12138. https://doi.org/10.3390/app112412138

Kaya, M., & Çetin-Kaya, Y. (2024). A novel ensemble learning framework based on a genetic algorithm for the classification of pneumonia. *Engineering Applications of Artificial Intelligence*, *133*, 108494. https://doi.org/10.1016/j.engappai.2024.108494

Kim, J., Kim, H. J., Kim, C., Lee, J. H., Kim, K. W., Park, Y. M., Kim, H. W., Ki, S. Y., Kim, Y. M., & Kim, W. H. (2021). Weakly supervised deep learning for ultrasound diagnosis of breast cancer. *Scientific Reports*, *11*(1), 24382. https://doi.org/10.1038/s41598-021-03806-7

Lei, B., Huang, S., Li, R., Bian, C., Li, H., Chou, Y.-H., & Cheng, J.-Z. (2018). Segmentation of breast anatomy for automated whole breast ultrasound images with boundary regularized convolutional encoder-decoder network. *Neurocomputing*, *321*, 178-186. https://doi.org/10.1016/j.neucom.2018.09.043

Li, Y., Gu, H., Wang, H., Qin, P., & Wang, J. (2022). BUSnet: A deep learning model of breast tumor lesion detection for ultrasound images. *Frontiers in Oncology*, *12*, 848271. https://doi.org/10.3389/fonc.2022.848271

Liu, H., Cui, G., Luo, Y., Guo, Y., Zhao, L., Wang, Y., Subasi, A., Dogan, S., & Tuncer, T. (2022). Artificial intelligence-based breast cancer diagnosis using ultrasound images and grid-based deep feature generator. *International Journal of General Medicine*, *15*, 2271-2282. https://doi.org/10.2147/IJGM.S347491

Luo, L., Wang, X., Lin, Y., Ma, X., Tan, A., Chan, R., Vardhanabhuti, V., Chu, W. C., Cheng, K.-T., & Chen, H. (2024). Deep learning in breast cancer imaging: A decade of progress and future directions. *IEEE Reviews in Biomedical Engineering*. https://doi.org/10.1109/RBME.2024.3357877

Mahoro, E., & Akhloufi, M. A. (2022). Applying deep learning for breast cancer detection in radiology. *Current Oncology*, *29*(11), 8767-8793. https://doi.org/10.3390/curroncol29110690

Marini, T. J., Castaneda, B., Iyer, R., Baran, T. M., Nemer, O., Dozier, A. M., Parker, K. J., Zhao, Y., Serratelli, W., Matos, G., Ali, S., Ghobryal, B., Visca, A., & O'Connell, A. (2023). Breast ultrasound volume sweep

imaging: A new horizon in expanding imaging access for breast cancer detection. *Journal of Ultrasound in Medicine*, *42*(4), 817-832. https://doi.org/10.1002/jum.16047

Masud, M., Hossain, M. S., Alhumyani, H., Alshamrani, S. S., Cheikhrouhou, O., Ibrahim, S., Muhammad, G., Rashed, A. E. E., & Gupta, B. B. (2021). Pre-trained convolutional neural networks for breast cancer detection using ultrasound images. *ACM Transactions on Internet Technology*, *21*(4), 1-17. https://doi.org/10.1145/3418355

Momot, A., Galagan, R., & Zaboluieva, M. (2022). Automation of ultrasound breast cancer image classification using deep neural networks. *Sciences of Europe*, (96), 38-41.

Moon, W. K., Lee, Y.-W., Ke, H.-H., Lee, S. H., Huang, C.-S., & Chang, R.-F. (2020). Computer-aided diagnosis of breast ultrasound images using ensemble learning from convolutional neural networks. *Computer Methods and Programs in Biomedicine*, *190*, 105361. https://doi.org/10.1016/j.cmpb.2020.105361

Moustafa, A. F., Cary, T. W., Sultan, L. R., Schultz, S. M., Conant, E. F., Venkatesh, S. S., & Sehgal, C. M. (2020). Color Doppler ultrasound improves machine learning diagnosis of breast cancer. *Diagnostics*, *10*(9), 631. https://doi.org/10.3390/diagnostics10090631

Negi, A., Raj, A. N. J., Nersisson, R., Zhuang, Z., & Murugappan, M. (2020). RDA-UNET-WGAN: An accurate breast ultrasound lesion segmentation using Wasserstein generative adversarial networks. *Arabian Journal for Science and Engineering*, *45*(8), 6399-6410. https://doi.org/10.1007/s13369-020-04480-z

Pacal, İ. (2022). Deep learning approaches for classification of breast cancer in ultrasound (US) images. *Journal of the Institute of Science and Technology*, *12*(4), 1917-1927. https://doi.org/10.21597/jist.1183679

Pang, T., Wong, J. H. D., Ng, W. L., & Chan, C. S. (2021). Semi-supervised GAN-based radiomics model for data augmentation in breast ultrasound mass classification. *Computer Methods and Programs in Biomedicine*, *203*, 106018. https://doi.org/10.1016/j.cmpb.2021.106018

Peng, Y., Tang, W., & Peng, X. (2023). The study of ultrasonography based on deep learning in breast cancer. *Journal of Radiation Research and Applied Sciences*, *16*(4), 100679. https://doi.org/10.1016/j.jrras.2023.100679

Pourasad, Y., Zarouri, E., Salemizadeh Parizi, M., & Salih Mohammed, A. (2021). Presentation of a novel architecture for diagnosis and identifying breast cancer location based on ultrasound images using machine learning. *Diagnostics*, *11*(10), 1870. https://doi.org/10.3390/diagnostics11101870

Qi, X., Zhang, L., Chen, Y., Pi, Y., Chen, Y., Lv, Q., & Yi, Z. (2019). Automated diagnosis of breast ultrasonography images using deep neural networks. *Medical Image Analysis*, *52*, 185-198. https://doi.org/10.1016/j.media.2018.12.006

Vakanski, A., Xian, M., & Freer, P. E. (2020). Attention-enriched deep learning model for breast tumor segmentation in ultrasound images. *Ultrasound in Medicine & Biology*, *46*(10), 2819-2833. https://doi.org/10.1016/j.ultrasmedbio.2020.06.015

Vigil, N., Barry, M., Amini, A., Akhloufi, M., Maldague, X. P. V., Ma, L., Ren, L., & Yousefi, B. (2022). Dual-intended deep learning model for breast cancer diagnosis in ultrasound imaging. *Cancers*, *14*(11), 2663. https://doi.org/10.3390/cancers14112663

Wu, G. G., Zhou, L.-Q., Xu, J.-W., Wang, J.-Y., Wei, Q., Deng, Y.-B., Cui, X.-W., & Dietrich, C. F. (2019). Artificial intelligence in breast ultrasound. *World Journal of Radiology*, *11*(2), 19-26. https://doi.org/10.4329/wjr.v11.i2.19

Wu, T., Sultan, L. R., Tian, J., Cary, T. W., & Sehgal, C. M. (2019). Machine learning for diagnostic ultrasound of triple-negative breast cancer. *Breast Cancer Research and Treatment*, *173*(2), 365-373. https://doi.org/10.1007/s10549-018-4984-7

Xu, Y., Wang, Y., Yuan, J., Cheng, Q., Wang, X., & Carson, P. L. (2019). Medical breast ultrasound image segmentation by machine learning. *Ultrasonics*, *91*, 1-9. https://doi.org/10.1016/j.ultras.2018.07.006

Zhang, E., Seiler, S., Chen, M., Lu, W., & Gu, X. (2019, July 23-27). *Boundary-aware semi-supervised deep learning for breast ultrasound computer-aided diagnosis*. In: Proceedings of the 2019 41st Annual

International Conference of the IEEE Engineering in Medicine and Biology Society (EMBC) (pp. 947-950), Berlin, Germany. IEEE. https://doi.org/10.1109/EMBC.2019.8856539

Zhang, Y., Chen, J.-H., Lin, Y., Chan, S., Zhou, J., Chow, D., Chang, P., Kwong, T., Yeh, D.-C., Wang, X., Parajuli, R., Mehta, R. S., Wang, M., & Su, M.-Y. (2021). Prediction of breast cancer molecular subtypes on DCE-MRI using a convolutional neural network with transfer learning between two centers. *European Radiology*, *31*(4), 2559-2567. https://doi.org/10.1007/s00330-020-07274-x

Zhang, Z., Li, Y., Wu, W., Chen, H., Cheng, L., & Wang, S. (2021). Tumor detection using deep learning method in automated breast ultrasound. *Biomedical Signal Processing and Control*, *68*, 102677. https://doi.org/10.1016/j.bspc.2021.102677

Zhuang, Z., Yang, Z., Raj, A. N. J., Wei, C., Jin, P., & Zhuang, S. (2021). Breast ultrasound tumor image classification using image decomposition and fusion based on adaptive multi-model spatial feature fusion. *Computer Methods and Programs in Biomedicine*, *208*, 106221. https://doi.org/10.1016/j.cmpb.2021.106221

Determination of the Energy Potential of Hazelnut Residues in Ordu, Türkiye

Esra BALCI KURU[1]*   Ömer ERTUĞRUL[2]

[1] Karadeniz Tarımsal Araştırma Enstitüsü Müdürlüğü, Samsun-Türkiye
[2] Kırşehir Ahi Evran University, Faculty of Agriculture, Department of Biosystems Engineering, Kırşehir-Türkiye

Keywords	Abstract
Biomass Energy Bioenergy Waste Management Affordable and Clean Energy Sustainable Energy	Ordu province is the leader in hazelnut production in Türkiye and therefore has an important potential in terms of hazelnut shells and husks. The aim of this study is to determine the biomass potential of the province of Ordu, to investigate the energy potential of hazelnut waste and to provide querryable database using geographic information systems. By collecting data on the geographical distribution of hazelnut production areas and their calculated potential for biomass and energy production in the province of Ordu, a database has been created that allows spatial queries. This database was visualized and analyzed through GeoMedia Professional 6.1. It was determined that the districts with the highest biomass production potential are the central province, Ünye and Fatsa, respectively. In addition, the energy potential was calculated at 2,321 GWh, which is significantly higher than the electricity consumption of the province of Ordu, which is 1,375 GWh. The results showed that hazelnut waste, which has low economic value, has a high potential for biomass and energy production. Using hazelnut waste as biomass in the region both promotes sustainable energy production and prevents dependence on fossil fuels by enabling the city to use clean energy sources.

1. INTRODUCTION

Renewable energy sources are becoming increasingly important around the world. Renewable energy sources are preferred instead of fossil fuels to meet energy needs in a sustainable and environmentally friendly way (Degirmencioglu et. al., 2019). One of the most important reasons for this is the depletion of fossil fuels, another reason is that they play an important role in reducing the environmental impact of fossil fuels and combating global problems such as climate change (Olabi & Abdelkareem, 2022; Ertuğrul, 2023). Organic materials such as plant and animal waste and wood are known as biomass. In this context, biomass is a source of considerable interest among renewable energy sources due to its potential to reduce dependence on fossil fuels and facilitate an environmentally friendly approach to energy production (Olabi & Abdelkareem, 2022).

While hazelnuts are cultivated in numerous countries worldwide, Türkiye stands as a dominant player in global hazelnut production, accounting for approximately 64% of global output (FAO, 2022). As reported by the Turkish Statistical Institute (2017), 16 provinces in Türkiye are engaged in the production of hazelnuts. The Black Sea region is the primary contributor to hazelnut production, which plays an economic and social role for the region. In Türkiye, Ordu province, which is one of the most significant hazelnut production centres of the Black Sea region, leads in hazelnut production, accounting for the largest portion. (Table 1).

Table 1. Distribution of hazelnut production in Türkiye

Provinces	Area (ha)	Production (tons)	%
Artvin	8.665	6.314	1.0
Bartın	6	6.765	1.1
Bolu	1.089	366	0.05
Düzce	62.685	69.344	10.7
Giresun	117.111	105.023	16.25
Gümüşhane	802	723	0.1
Kastamonu	7.471	5.213	0.9
Kocaeli	8.062	7.53	1.2
Ordu	**227.183**	**200.938**	**31.10**
Rize	3.607	1.303	0.2
Sakarya	72.598	82.708	12.8
Samsun	90.623	90.857	14.0
Sinop	1.701	1.175	0.2
Tokat	2.802	3.511	0.5
Trabzon	65.35	39.126	6
Zonguldak	23.593	22.572	3.5
Sum of 16 Provinces	699.341	643.468	99.6
Sum of other Provinces	3.287	2.532	0.4
Total Türkiye	702.628	646.000	100

Moreover, the geographical location and climatic characteristics of the region make Ordu province extremely important for hazelnut production. The hazelnut orchards and production capacity in the region are known to meet a significant portion of the global and local hazelnut demand. The observation that hazelnut is not only used commercially but also has industrial uses makes it a versatile product. Waste from the pruning of hazelnut groves is an important source of biomass production (Monarca et al., 2013). A significant body of research has been conducted recently on the potential contribution of biomass to energy production, with a particular focus on the advantages it offers. These include the reduction in reliance on fossil fuels, the enhancement of rural economies through the utilisation of previously under-utilised waste, and the Carbon-neutral life cycle of biomass sources. Tun and Juchelková (2019) undertook a study to determine the bioenergy potential of Myanmar. Residues provided from agriculture, wood and animal production are taken into account in the study. The residue-to-product ratios (RPR) have been used with production data to determine the waste amounts of plant production. The energy potentials were determined by multiplying the residue amount values with the lower heating values (LHV). It was stated that bioenergy has a significant role to play in the sustainable development of Myanmar by improving self-sufficiency in energy production. Studies on assessing potential of biomass energy revealing utilization possibilities have been published in prestigious journals. In this context, the potential for biomass energy to mitigate climate change and ensure energy sustainability has been determined (Ben-Iwo et al., 2016; Toklu, 2017).

In 2015, Karaca (2015) conducted research to map the potential of biomass energy from field crops and horticultural products by determining the residue amounts by using the residue-to-product ratios (RPR), availability (A) and lower heat values (LHV). Karaca (2015) produced a quarriable database by using ArcGIS

software to map the findings. Ertuğrul et al. (2024) determined the bioenergy potential of South-Central Texas by analysing the outputs of field and horticultural crops including walnut and peach wastes. The research team investigated the potential of pruning and fruit waste for walnuts, which, as a shelled fruit, produces waste that is comparable to that of hazelnuts. In the research, the energy potential of walnut shells and tree pruning waste was calculated and included in the results. Utilizing the wastes as energy sources not only contributes to sustainable energy production but can also be considered as a solution to environmental problems such as waste management. This situation allows the utilization of hazelnut shells in economic, environmental, and social terms. For this purpose, determining the potential of biomass production from hazelnut wastes in Ordu province is of great importance for the development of energy strategies in the region. The objective of this study is to determine the bioenergy potential of hazelnut wastes in Ordu. To achieve this goal, the spatial distribution of hazelnut production, possible utilizable waste amounts and the energy potentials were investigated and mapped in Ordu province.

2. MATERIAL AND METHOD

Material

Hazelnut production, hazelnut varieties and distribution data of the Ordu province (Table 2) were collected from Turkish Statistical Institute (TSI, 2017). GeoMedia Professional 6.1, the geographical information systems (GIS) software was used as a tool for processing data and producing maps. This software has been used reliably in previous studies to create a database where interactions can be queried (Özgünaltay Ertuğrul et al., 2019; Özgünaltay Ertuğrul & Değirmencioğlu, 2021).

Table 2. *Distribution of hazelnut production in Ordu (TSI, 2017)*

District	Production Quantity (tons)
Akkuş	3596
Altınordu	30055
Aybastı	7463
Fatsa	32031
Gölköy	9266
Gülyalı	3906
Gürgentepe	4971
Kabadüz	7404
Kabataş	4456
Korgan	6103
Kumru	7792
Mesudiye	2375
Perşembe	18431
Ulubey	18957
Çamaş	6867
Çatalpınar	4449
Çaybaşı	5292
Ünye	32558
İkizce	7600

Method

This study was carried out within the scope of the master's thesis written by Balci Kuru (2017). In order to determine the biomass potential of hazelnut wastes in Ordu province, areas with hazelnut production and production amounts were organized by Excel. Yield values were calculated together with the potential biomass production amount and the energy yield obtained from this production.

In addition, a literature review was conducted to determine the biomass and energy potential and formulas were examined as a result of this literature review. According to Bilanzdija et al. (2012), the number of fruit-bearing trees (T_f) was taken into account, and it was assumed that there is an available biomass potential of 3.05 kg per tree after pruning. It was also assumed that there is an energy potential (EP_T) of 53.28 MJ per tree (Bilanzdija et al., 2012). Energy potential of hazelnut pruning wastes (EP_P) depending on the number of fruiting trees (Tf) was calculated according to Eq. 1.

$$EP_P \ (MJ) = EP_T \ x \ T_f \tag{1}$$

The ratio of shell/product (RPR) that can be obtained from hazelnut fruit is 1.07 (Mardikis et al., 2004) and the energy potential of hazelnut biomass is 17.47 MJ kg^{-1} according to Bilanzdija et al. (2012). Accordingly, considering the production amount (P) potential shell-based waste amount is calculated by Eq. 2 and the energy potential of shells (EP_S) is calculated by Eq. 3. Total energy potential is determined by summation of the EP_P and the EP_S (Eq. 4).

$$AB_S = P \ x \ RPR \tag{2}$$

$$EP_S \ (MJ) = EP_T \ x \ T_f \tag{3}$$

$$EP \ (MJ) = EP_P + EP_S \tag{4}$$

In order to provide better understanding of the contribution of the thermal potential to the province of Ordu, assuming that electricity can be produced from all available waste, the potential electricity production can be calculated using Eq.5.

$$EP_E \ (kWh) = EP \ x \ 0.277778 \tag{5}$$

3. RESULTS AND DISCUSSION

As a result of both the literature review and the analyses conducted in this study, it has provided important contributions regarding the biomass potential in the province of Ordu. Bilanzdija et al. (2012) underlined that there is a significant amount of pruning waste in fruit production in apple, pear, apricot, peach, nectarine, cherry, sour cherry, walnut, almond, fig, grape and olive. Similarly, when the geographical distribution of hazelnut fruit in Ordu province was examined, it was determined that Ünye, Merkez and Fatsa districts had the highest hazelnut production and yield values among 19 provinces, respectively. Hazelnut trees were found to contribute significantly to the biomass potential in Ordu province, which is in line with the study by Bilanzdija et al. (2012).

Furthermore, it has been found that the amount of biomass did not vary with tree age but was directly proportional to the number of trees, which is consistent with our results (Monarca et al., 2013). Depending on the number of fruits bearing trees, the total biomass potential of Ordu province was determined as 471,465 t. When analysed based on districts, it is observed that the Central district (62,660 t), Ünye (60,587 t) and Fatsa (56,066 t) have the highest biomass potential (Figure 1).
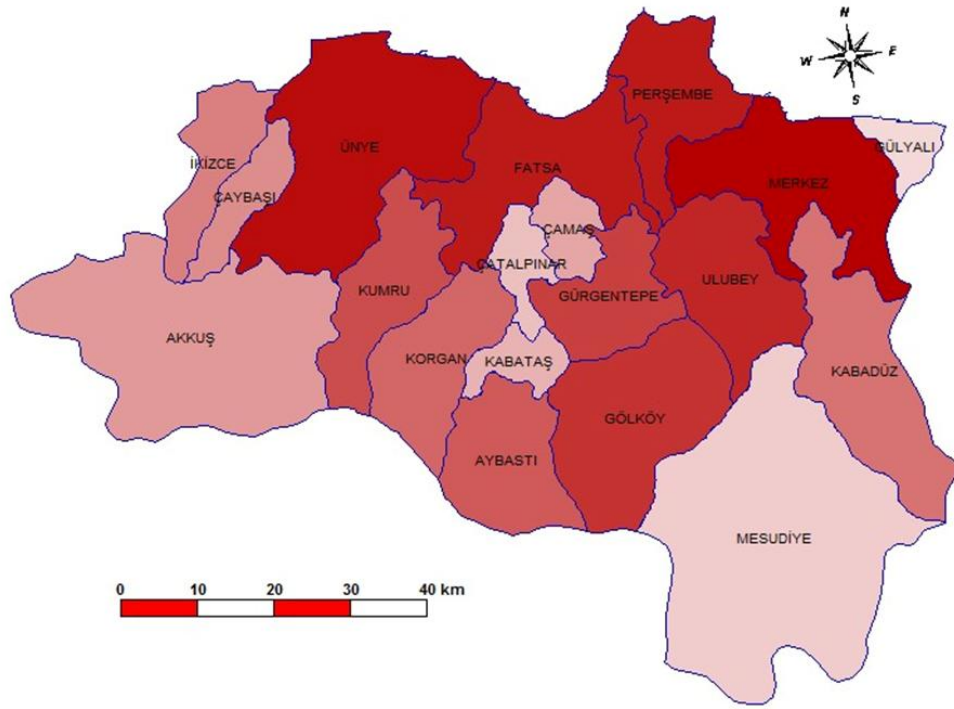
Figure 1. Thematic map of waste potential in Ordu districts

The total energy potential of hazelnut wastes that can be obtained from Ordu is 8,289,371 GJ and much higher than the greenhouse tomato waste in Kırşehir, 4,046 GJ (Boyacı et al., 2021). Based on districts, the energy potential is 1.095GJ for Central District, 1,058 GJ for Ünye and 1.032 GJ for Fatsa (Table 3 and Figure 2). The electricity equivalent of the total energy potential is 2,321 GWh that is much higher than the electricity consumption of the Ordu province which is 1,375 GWh for 2021 (TSI, 2021). This shows that hazelnut residues have a significant potential for energy production.
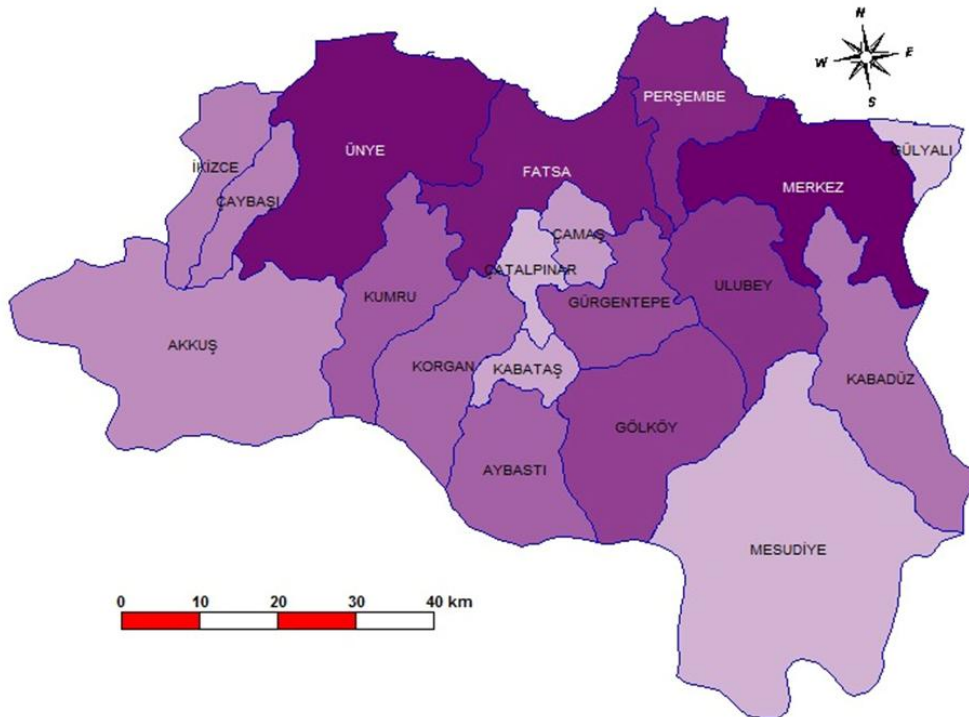
Figure 2. Thematic map of total energy potential of hazelnut wastes

This high energy potential observed in Ordu province can encourage the use of sustainable energy sources while reducing dependence on traditional energy sources. Furthermore, this is likely to support both socio-economic growth at the local level and environmental sustainability by utilization of agricultural wastes.

Table 3. Energy Potential of Hazelnut Wastes by Districts in Ordu in 2015

District Name	Total Production Area (ha)	Production (t)	Number of Bearing Trees	Energy Potential of Pruning Wastes (GJ)	Energy Potential of Shells Pruning Wastes (GJ)	Total Amount of Biomass (t)*	Total Energy Potential (GJ)
Center	27.08	26,961	15,975,000	851,148	243,468	62,660	1,094,616
Ünye	29.67	29,674	14,835,600	790,441	267,968	60,587	1,058,408
Fatsa	26.97	26,747	14,832,950	790,299	241,536	56,066	1,031,835
Perşembe	19.33	17,981	9,664,000	514,898	162,375	38,770	677,273
Ulubey	17.67	15,930	8,837,250	470,849	143,854	35,188	614,703
Gölköy	14.07	9,346	7,520,000	400,666	84,398	27,767	485,064
Gürgentepe	10.13	7,353	6,076,800	323,772	66,400	22,335	390,172
Kumru	11.77	9,051	5,887,000	313,659	81,734	22,634	395,393
Aybastı	9.01	6,318	4,917,000	261,978	57,054	18,263	319,032
Korgan	8.75	7,132	4,822,115	256,922	64,405	18,394	321,327
Kabadüz	8.64	7,702	4,754,365	253,313	69,552	18,482	322,865
İkizce	9.43	8,162	4,718,000	251,375	73,706	18,609	325,081
Çaybaşı	6.33	6,016	3,795,480	202,223	54,327	14,686	256,550
Akkuş	5.50	3,901	3,300,000	175,824	35,228	12,081	211,052
Çamaş	7.01	6,114	3,056,950	162,874	55,212	12,433	218,086
Kabataş	4.67	3,459	2,801,200	149,248	31,236	10,332	180,484
Çatalpınar	4.87	4,014	2,432,500	129,604	36,248	9,494	165,852
Mesudiye	3.04	2,284	1,674,145	89,198	20,625	6,287	109,824
Gülyalı	3.25	2,793	1,624,100	86,532	25,222	6,397	111,754
TOTAL	227.19	200,938	121,524,455	6,474,823	1,814,548	471,465	8,289,371

* This value indicates both potential biomass after pruning and hazelnut shell biomass potential

4. CONCLUSION

As one of the Carbon-neutral and renewable energy sources, biomass not only protects the environment but also reduces the use of fossil fuels and dependence on import of energy. In addition, the utilization of hazelnut shells and pruning wastes in energy production offers an important resource for increasing the renewable energy potential of Ordu province, which is important for both environmental sustainability and economic development of the city. As a result, strategies should be developed to increase the contribution of hazelnuts, one of Türkiye's most important export products, to energy, which is one of our main import expenditures, and to ensure that hazelnut waste is used more effectively in energy production. While research data show that Ordu province has an annual electricity consumption of 1,375 GWh/year, the energy production potential of the province from hazelnut wastes is nearly twice the annual energy consumption. It is estimated that the energy production facilities to be established, particularly in the Central District, Ünye and Fatsa, represent an important opportunity for both Ordu Province and Türkiye.

AUTHOR CONTRIBUTIONS

Conceptualization, E.B. and Ö.E.; methodology, E.B. and Ö.E.; fieldwork, E.B.; software, E.B. and Ö.E.; title, E.B. and Ö.E.; validation, E.B.; formal analysis, E.B.; research, E.B.; sources, E.B.; data curation, E.B.; manuscript-original draft, E.B.; manuscript-review and editing, E.B. and Ö.E.; visualization, E.B.; supervision, Ö.E. All authors have read and legally accepted the final version of the article published in the journal.

ACKNOWLEDGEMENT

CONFLICT OF INTEREST

The authors declare no conflict of interest.

REFERENCES

Balcı Kuru, E. (2017). *Ordu İli örneğinde, fındık artıklarından biyokütle üretim potansiyelinin coğrafi bilgi sistemleri (CBS) kullanılarak belirlenmesi*. MSc Thesis, Kırşehir Ahi Evran University.

Ben-Iwo, J., Manovic, V., & Longhurst, P. (2016). Biomass resources and biofuels potential for the production of transportation fuels in Nigeria. *Renewable and Sustainable Energy Reviews*, *63*, 172-192. https://doi.org/10.1016/j.rser.2016.05.050

Bilanzdija, N., Voca, N., Kricka, T., Matin, A., & Jurisic, V. (2012). Energy potential of fruit tree pruned biomass in Croatia. *Spanish Journal of Agricultural Research*, *10*(2), 292-298. https://doi.org/10.5424/sjar/2012102-126-11

Boyacı, S., Ertuğrul, Ö., & Özgünaltay Ertuğrul, G. (2021) Kırşehir ilinin örtü altı domates yetiştiriciliğinde bitkisel artık kaynaklı enerji potansiyelinin mekânsal olarak değerlendirilmesi. *Mustafa Kemal Üniversitesi Tarım Bilimleri Dergisi*, *26*(3), 600-609. https://doi.org/10.37908/mkutbd.933607

Degirmencioglu, A., Mohtar, R. H., Daher, B. T., Ozgunaltay-Ertugrul, G., & Ertugrul, O. (2019). Assessing the sustainability of crop production in the Gediz Basin, Turkey: a water, energy, and food nexus approach. *Fresenius Environmental Bulletin*, *28*(4), 2511-2522.

FAO, Food and Agriculture Organization. (2022). Crops and livestock products. (Accessed: 14.08.2024) https://www.fao.org/faostat/en/#data/QCL

Ertuğrul, Ö. (2023). A Review on the Mechanization Practices for Regenerative Agriculture and The Related Mechanization Practices. In: A. Kazankaya, & M. A. Ateş. (Eds.), *Advance Concepts on Natural and Agricultural Sciences* (pp. 295-309). Ankara: Iksad Publishing House.

Ertuğrul, Ö., Daher, B., Özgünaltay Ertuğrul, G., & Mohtar, R. (2024). From Agricultural Waste to Energy: Assessing the Bioenergy Potential of South-Central Texas. *Energies*, *17*(4), 802. https://doi.org/10.3390/en17040802

Karaca, C. (2015) Mapping of energy potential through annual crop residues in Turkey. *International Journal of Agricultural and Biological Engineering*, *8*(2), 104-109. https://doi.org/10.3965/j.ijabe.20150802.1587

Mardikis, M., Nikolaou, A., Djouras, N., & Panoutsou, C. (2004). Agricultural biomass in Greece: Current and future trends. In: [Report] *Biomass and Agriculture: Sustainability, markets and policies* (pp. 363-376).

Monarca, D., Cecchini, M., Colantoni, A., Di Giacinto, S., Marucci, A., & Longo, L. (2013). Assessment of the energetic potential by hazelnuts pruning in Viterbo's area. *Journal of Agricultural Engineering*, *44*(2), 117. https://doi.org/10.4081/jae.2013.359

Olabi, A. G., & Abdelkareem, M. A. (2022). Renewable energy and climate change. *Renewable and Sustainable Energy Reviews*, *158*, 112111. https://doi.org/10.1016/j.rser.2022.112111

Özgünaltay Ertuğrul, G., & Değirmencioğlu, A. (2021). A GIS-Based Approach on Annual Tractor Use, Soil Type and Crop Pattern Interactions in Some Provinces of the Aegean Region. *Turkish Journal of Agriculture-Food Science and Technology*, *9*(8), 1384-1389. https://doi.org/10.24925/turjaf.v9i8.1384-1389.4232

Ozgunaltay-Ertugrul, G., Ertugrul, O., & Degirmencioglu, A. (2019). Determination of Agricultural Mechanization Level of Kırsehir Province Using Geographical Information Systems (GIS). *Comptes rendus de l'Académie bulgare des Sciences*, *72*(8), 1144. https://doi.org/10.7546/CRABS.2019.08.18

Toklu, E. (2017). Biomass energy potential and utilization in Turkey. *Renewable Energy*, *107*, 235-244. https://doi.org/10.1016/j.renene.2017.02.008

Tun, M. M., & Juchelková, D. (2019). Biomass Sources and Energy Potential for Energy Sector in Myanmar: An Outlook. *Resources*, *8*(2), 102. https://doi.org/10.3390/resources8020102

TSI, Turkish Statistical Institute (2017). Crop production statistics. (Accessed: 15/05/2017) http://www.tuik.gov.tr/Start.do

TSI, Turkish Statistical Institute (2021). Energy Statistics. (Accessed: 13/08/2024) https://biruni.tuik.gov.tr/

Evaluating the Impact of Edge-Seal on the Performance of Double-Glass Solar Photovoltaic Modules

Melikenur GENC[1]   Abdulkerim GOK[2*]

[1] Department of Chemical Engineering, Gebze Technical University, Gebze/Kocaeli, Türkiye
[2] Department of Materials Science and Engineering, Gebze Technical University, Gebze/Kocaeli, Türkiye

Keywords	Abstract
PV Modules Encapsulants Edge-seal Moisture-ingress Damp Heat Degradation	Solar energy is a vital component of the renewable energy landscape. Nevertheless, photovoltaic (PV) modules face numerous challenges during operation due to environmental stress factors, which can lead to various degradation issues such as delamination, encapsulant discoloration, corrosion of cell metallization, and potential-induced degradation. Ethylene-vinyl acetate (EVA), despite being a prominent encapsulant material, is notably vulnerable to moisture. Upon degradation, EVA releases acetic acid, severely impacting the long-term performance of PV modules. This study investigates the effectiveness of using a polyisobutylene-based edge-seal to minimize moisture ingress in double-glass modules. One-cell mini-modules encapsulated with EVA, with and without edge-seal, are subjected to damp heat testing (85°C / 85% RH) for up to 5000 hours and their performance are evaluated though current-voltage characteristics. Mini-modules without edge-seal exhibit a significant 70% loss in power, primarily due to a 37% decrease in short-circuit current, a 56% decrease in fill factor, and a staggering 650% increase in series resistance. However, mini-modules with edge-seal see only a 33% loss in power, driven mainly by a 21% decrease in fill factor and a 76% increase in series resistance. The use of edge-seal does not completely prevent but effectively reduces moisture ingress and mitigates its detrimental effects on module performance. Additionally, the Network Structural Equation Modeling approach is applied to analyze current-voltage characteristics, enabling the identification of statistically significant relationships, the construction of degradation pathway diagrams, and the determination of key factors contributing to power degradation. This analysis reveals increased series resistance and reduced fill factor as primary causes of power degradation for both mini-module configurations. Although the encapsulant materials exhibit minimal degradation in optical, chemical, and thermo-chemical properties, the presence of moisture within the module construction can still cause corrosion of cell metallization. This results in a decline in power performance even without substantial acetic acid formation. This study highlights the critical importance of preventing moisture ingress to enhance the durability and reliability of PV modules, ensuring their optimal performance throughout their intended service lifetime.

1. INTRODUCTION

Historically, energy production has depended heavily on cost-effective but environmentally harmful fossil fuels. This dependence is increasingly seen as unsustainable due to the environmental damage caused and the finite nature of these resources. In response, renewable energy is promoted through policies and incentives aimed at achieving net-zero emissions. Photovoltaics (PV) have become a leading technology in the shift towards sustainable energy. Utilizing sunlight to generate clean electricity is now widely recognized as a promising solution. Over the past decade, the global installed capacity of PV systems has seen remarkable growth. It reached 1.2 TW in 2022 (IEA PVPS, 2023), expanded to 1.6 TW in 2023 with the addition of approximately 400 GW (IEA PVPS, 2024), and is projected to surpass 2 TW in 2024 (BNEF, 2024). While

*Corresponding Author, e-mail: agok@gtu.edu.tr

the future of PV installations looks promising, challenges related to the durability and reliability of PV modules still need addressing to ensure their long-term performance (Aghaei et al., 2022). These issues must be targeted to maintain sustainable growth in the renewable energy sector.

PV modules are composed of several key components, each playing a crucial role in ensuring efficiency, durability, reliability, and long-term performance. At the core are solar cells, typically made from mono-crystalline silicon, which harness sunlight and convert it into electricity through the photovoltaic effect. These cells are protected by a front glass cover, tempered to enhance durability and minimize reflectivity, allowing maximum light transmission. Surrounding the cells is an encapsulant which provides structural support for mechanical stability, enhances optical coupling, ensures electrical isolation for safety and prevents leakage currents, and provides protection against environmental conditions (Czanderna & Pern, 1996). It also plays a crucial role in managing heat distribution across the module's various layers, making high thermal conductivity essential for reduced cell temperatures and optimal performance. The polymeric backsheet further isolates and protects the module from environmental stressors and provides electrical insulation. An aluminum frame offers structural support and facilitates mounting, while a junction box houses electrical connections along with bypass and blocking diodes. Additionally, an anti-reflective coating is applied to the cells and/or glass cover to increase light absorption.

In recent years, especially after the development of bifacial solar cell technology, the polymeric backsheet film has been replaced with another glass layer. According to International Technology Roadmap for Photovoltaics, double-glass modules captured nearly 40% of the market in 2023 and are projected to dominate with over 70% market share by 2034 (ITRPV, 2024). They offer several advantages over traditional modules with polymeric backsheets (Sinha et al., 2021). The double-glass construction enhances durability, providing better protection against environmental factors, thereby improving the service lifetime of PV modules. This construction also increases mechanical strength, making the modules more resistant to mechanical stresses, and improves fire resistance as glass is fire-resistant compared to polymeric materials. Additionally, double-glass modules maintain a more stable aesthetic and performance over time as glass is less prone to discoloration and degradation. These modules are usually designed as bifacial, capturing light from both sides to boost energy yield, particularly in reflective grounds. Furthermore, they exhibit improved resistance to Potential-Induced Degradation (PID), enhancing reliability and performance. From an environmental perspective, double-glass modules are more sustainable as they are easier to recycle at the end of their life cycle compared to modules with polymeric backsheets, which are made of multi-layer films typically consisting of fluoropolymers (Müller et al., 2021). While they may come with higher initial costs, specifically due to increased weight affecting transportation costs, the long-term benefits make double-glass modules more preferable.

During operation in open-air climates, PV modules face a variety of environmental stress factors that can impact their performance and experience degradation and failure (Köntges et al., 2014; 2017). Prolonged exposure to UV radiation can degrade the polymeric encapsulant and backsheet layers, resulting in discoloration. This degradation, especially the discoloration of the encapsulant, can diminish light transmission, decreasing the amount of light that reaches the cells and consequently lowering energy output. While discoloration may initially appear to be an aesthetic issue, it often indicates deeper problems with the polymeric components. It can signal potential delamination between layers, forming gaps where moisture and contaminants can enter, further compromising the module's integrity. Moisture from rain, snow, and humidity can lead to water ingress, causing corrosion of cell metallization, increased series resistance, and reduced performance. It can react with polymeric materials through hydrolysis, compromising their functionality. High winds can impose mechanical stress on the module's mounting structures, while hail and impact damage can generate physical defects on the surface and cell cracks. Accumulation of dust and debris can block light, reducing energy output, and airborne pollutants can cause material degradation. In coastal areas, saline environments can accelerate corrosion reactions. Additionally, repeated thermal cycling or temperature fluctuations can lead to mechanical stresses, thermal expansion and contraction, material fatigue, and ultimately result in delamination and cell interconnect failures. Addressing these stress factors through robust design and regular maintenance is crucial to ensuring the long-term performance of PV modules.

Ethylene-Vinyl Acetate (EVA) is the most widely used encapsulant material in PV modules, offering numerous benefits (Griffini & Turri, 2016). EVA is a chemically crosslinked, semi-crystalline copolymer made up of

ethylene and vinyl acetate units, usually in a ratio of 70% ethylene to 30% vinyl acetate. Crosslinking agents are added to chemically bond the EVA polymer chains during the lamination process, forming a durable elastomeric network that enhances mechanical strength. EVA's excellent adhesion properties ensure that solar cells remain securely in place, maintaining optimal electrical contact. Its high transparency allows maximum sunlight to reach the cells, which is crucial for achieving high energy conversion efficiency. The material's flexibility and ability to conform to thermal expansion and contraction help minimize the risk of mechanical stress and damage. Additionally, EVA provides electrical insulation, preventing short circuits and ensuring safe operation of the module. EVA is also easy to process during module manufacturing. It can be readily laminated onto solar cells and other layers using standard equipment, streamlining the production process and ensuring consistent quality. Despite these benefits, it does have some significant drawbacks (Oliveira et al., 2018). EVA can degrade over time due to prolonged exposure to environmental conditions, potentially compromising its protective qualities and diminishing module performance. Although EVA is designed to shield cells from moisture, it can still absorb moisture, leading to issues such as corrosion of cell metallization and reduced module performance. EVA's flexibility helps it accommodate thermal expansion and contraction, but it may still experience stress from temperature fluctuations, potentially causing delamination or other damage if not properly managed. While EVA performs adequately across a range of temperatures, it has limitations under extreme conditions. Prolonged high temperatures can diminish its mechanical properties and adhesive strength, while very cold temperatures can make it more brittle, increasing the risk of cracking and affecting durability. Additionally, EVA's production and disposal have environmental implications, as it is not easily recyclable, raising concerns about waste management and sustainability.

When EVA degrades, a key issue is the formation of acetic acid from the breakdown of vinyl acetate (Kempe et al., 2007). This byproduct can accelerate the corrosion of cell metallization, increase series resistance, and ultimately cause power loss. Figure 1 illustrates the degradation reactions that lead to acetic acid formation (Hara & Chiba, 2021). Additionally, acetic acid can affect the adhesion properties of EVA, potentially leading to delamination between the EVA and the front glass or backsheet layers. Degradation by-products that absorb visible light can also cause discoloration, reducing light transmission to the cells. Significant discoloration often signals extensive degradation of the encapsulant. Elevated temperatures can worsen these degradation effects. Residual reactive crosslinking agents, i.e., peroxide species, from the lamination process can further accelerate degradation. Therefore, selecting the right packaging materials, combinations, and lamination processes is crucial for enhancing the durability and reliability of PV modules in various environmental conditions. This approach not only ensures long-term performance but also helps lower the levelized cost of electricity and reduces greenhouse gas emissions, contributing to a more sustainable future (Paç & Gok, 2024).
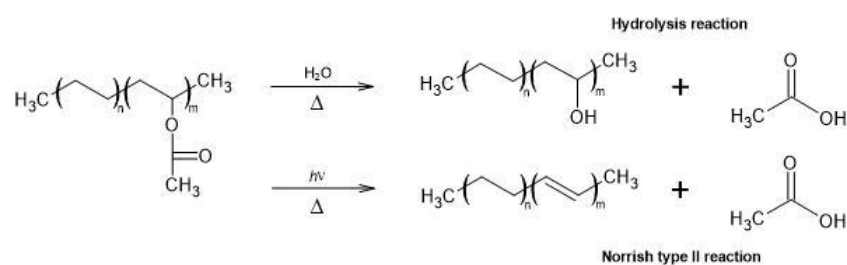
Figure 1. Acetic acid formation during hydro-thermal and photo-thermal degradation of EVA

Reported issues with EVA highlight the importance of ongoing research and development to address material limitations and enhance the overall reliability and sustainability of PV modules. There are several alternatives to EVA, each offering unique advantages (Dintcheva et al., 2023). Recent studies have focused especially on Polyolefin Elastomers (POE), Thermoplastic Olefins (TPO), and ionomers (ION) as promising alternatives to traditional EVA encapsulants (Schnatmann et al., 2022). These materials feature a polyethylene backbone but differ from EVA by incorporating side groups such as acrylates, acrylic acids, or n-alkanes instead of EVA's vinyl acetate. This modification addresses a key drawback of EVA: the formation of acetic acid during degradation. In addition, these alternative encapsulants offer improved volume resistivity and lower water vapor transmission rates, presenting significant advantages over EVA. Moreover, physically crosslinked encapsulants can be more readily recyclable, offering notable benefits in terms of sustainability. Nevertheless,

these alternatives typically come with a higher cost than EVA, and as a result, EVA remains the most cost-effective option, offering a good balance between cost and performance.

In double-glass solar modules, both the front and back surfaces are made of glass, which is impermeable to moisture. However, moisture can still penetrate through the edges. To further reduce the risk of moisture ingress, Polyisobutylene (PIB) is commonly used as an edge-seal material (Kempe et al., 2015). A reliable edge-seal is essential for protecting internal components from environmental factors. PIB is highly effective because of its extremely low water vapor permeability, which helps prevent moisture ingress that could cause corrosion, delamination, and decreased module performance. Its strong adhesion to glass and other module materials, along with its flexibility to accommodate thermal expansion and contraction, ensures a secure seal throughout the module's service lifetime. Additionally, PIB's resistance to UV radiation and other environmental stresses preserves its sealing properties, while its ease of application during manufacturing guarantees consistent sealing. These characteristics make PIB a popular and effective choice for edge-seal application in double-glass modules, significantly enhancing their durability and long-term performance.

This study examines the electrical performance of single-cell mini-modules with a double-glass construction, encapsulated with EVA, both with and without edge-seal. The double-glass design enhances the reliability of modules by effectively minimizing moisture ingress, which is crucial for reducing encapsulant material degradation and solar cell metallization corrosion. The edge-seal further enhances this protection, further mitigating the detrimental impacts of moisture on module performance. Formation and accumulation of acetic acid in double-glass modules can be a serious concern due to unbreathable structure. This trapped acetic acid inside the module can accelerate the degradation processes and lead to service lifetime issues. To ensure long-term performance, the modules underwent rigorous reliability testing beyond the IEC 61215 standards (IEC, 2021). The current-voltage (I-V) characteristics of the modules were extensively analyzed and modeled using the Network Structural Equation Modeling approach to identify key factors contributing to power degradation.

2. MATERIALS AND METHOD

To ensure effective module lamination, commercially available EVA encapsulant material was used. To minimize moisture ingress, a double-glass construction was implemented. Mini-modules, each containing a single, bifacial Passivated Emitter Rear Contact (PERC) cell, were laminated using these encapsulants, both with and without PIB-based edge-seal. Each configuration includes two mini-module samples.

The lamination process plays a vital role in PV module manufacturing, as it ensures proper curing of EVA and strong adhesion between layers, which are essential for the durability and reliability of the final product. In this study, mini-modules with EVA encapsulants were laminated at a temperature of 150 °C, beginning with 5 minutes of evacuation to remove air, followed by 10 minutes under a pressure of approximately 900 mbar.

After lamination, the mini-modules underwent damp heat exposure for up to 5000 hours. This test is part of the IEC 61215 standard, which evaluates the long-term performance of PV modules under high temperature and humidity conditions. The protocol involves exposing modules to 85°C and 85% relative humidity for 1000 hours. This test provides crucial insights into potential manufacturing flaws and hydrothermal degradation mechanisms that could occur in real-world operation. Although the standard mandates 1000 hours of testing, this study extended the testing time to 5000 hours to ensure that the module designs meet long-term performance expectations.

To evaluate the electrical characteristics of the mini-modules during damp heat testing, current-voltage (I-V) curve measurements were conducted approximately every 500 hours. I-V curves are essential for characterizing PV module performance, illustrating the relationship between current and voltage at the module's terminals. Typically, these curves are measured under Standard Testing Conditions (STC), which include an irradiance of 1000 W/m², a cell temperature of 25°C, and an air mass of 1.5. A solar simulator is used to mimic sunlight, while an electronic load adjusts the resistance across the module to capture current and voltage data at various points. Key parameters such as short-circuit current (I_{SC}), open-circuit voltage (V_{OC}), fill factor (FF), series resistance (R_S), shunt resistance (R_{SH}), and maximum power point (P_{MP}) are then extracted from the curve.

The Network Structural Equation Modeling (netSEM) approach was then employed to develop degradation pathways, elucidating the relationships between a primary stressor (S), mechanistic (M) variables, and a performance response (R) variable. netSEM extends traditional SEM by integrating non-linear relationships to analyze complex relationships within data and by incorporating network structures to provide a deeper understanding of interconnected systems (Gok et al., 2019). netSEM not only estimates and tests relationships but also visualizes the network structure, highlighting central nodes and influential paths. netSEM explores the most suitable model between univariate relationships by utilizing various linear and non-linear functional forms, encompassing linear, simple quadratic, quadratic, exponential, logarithmic, and change point models. The change point model is the combination of two linear models with changing slopes. Using the step-wise regression approach, all univariate relationships are rank-ordered based on their adjusted R^2 values sequentially and mapped into a degradation pathway diagram to illustrate the relationships among the stressor, mechanistic, and response variables. In these diagrams, arrows indicate relationships between variables, with statistical metrics displayed along the connecting lines. To rank these connections, three adjusted R^2 cutoff values were used: 0.90, 0.60, and 0.30. Strong relationships (adjusted $R^2 \geq 0.90$) are represented by thick solid lines, moderate relationships ($0.90 >$ adjusted $R^2 \geq 0.60$) by standard solid lines, weak relationships ($0.60 >$ adjusted $R^2 \geq 0.30$) by thin solid lines, and negligible relationships (adjusted $R^2 < 0.30$) by thin dotted lines.

Since this method only evaluates univariate relationships, mechanistic multi-step pathways were derived by substituting one mechanistic variable equation into another. For instance, to determine the multi-step path of "S → M → R," the equations for the "S → M" and "M → R" relationships are first obtained, and then "M" in the first model is substituted into the second model to derive the "M"-dependent multi-step path of "S → R." Plotting these mechanistic relationships over the exposure time illustrates how the mechanistic variables influence overall behavior. A quantitative comparison between the direct "S → R" and the multi-step "S → M → R" pathways is conducted using the root mean square error (RMSE) metric.

In this study, testing time was taken as the main stressor as a proxy to damp heat exposure conditions, P_{MP} was determined as the performance level response, and the remaining I-V curve parameters such as I_{SC}, V_{OC}, FF, and R_S were treated as the mechanistic variables. Since V_{OC} parameter is related to the intrinsic quality of solar cells, recombination mechanisms, and dark saturation current, it did not experience any significant degradation over the exposure time, and thus, it was not included in the analysis in order to focus only on the variables that can explain the observed behavior in power performance with exposure time.

3. RESULTS AND DISCUSSION

Mini-modules encapsulated using EVA, both with and without edge seals, were subjected to damp heat exposure for up to 5000 hours. Their I-V characteristics were periodically evaluated at specific time intervals. Table 1 provides an overview, highlighting the normalized initial and final values to reveal the observed changes. Figure 1 illustrates the temporal progression of I-V curves for a representative mini-module from each configuration. It can be seen that mini-modules demonstrated a significant power loss when edge-seal was not applied; however, this loss was notably less severe with the use of edge-seal.

Table 1. Initial and final I-V characteristics of the mini-modules

Mini-module	Edge-seal	Exposure Time	P_{MP}	I_{SC}	V_{OC}	FF	R_S
EVA		0	1.00	1.00	1.00	1.00	1.00
		5000	0.12	0.44	0.99	0.29	9.64
EVA	×	0	1.00	1.00	1.00	1.00	1.00
		5000	0.48	0.83	0.99	0.59	3.29
EVA		0	1.00	1.00	1.00	1.00	1.00
		5000	0.77	0.99	0.99	0.78	1.79
EVA	✓	0	1.00	1.00	1.00	1.00	1.00
		5000	0.77	0.98	0.98	0.80	1.74

Upon reviewing Table 1 and Figure 2, it becomes evident that the main contributor to power loss is the decrease in fill factor primarily due to the increase in series resistances. The open-circuit voltage remains stable, which is consistent with expectations since it is linked to the intrinsic quality of solar cells, recombination mechanisms, and dark saturation current. The short-circuit current exhibits a moderate impact on power; discoloration of the encapsulants contributes to loss in I_{SC} by affecting the interaction of light with the solar cells. The most pronounced effect is the reduction in fill factor, which can be attributed to the corrosion of cell metallization caused by moisture ingress. The increased resistance is indicated by changes in the slopes of the I-V curves near the open-circuit voltage. While no significant optical, chemical, or thermo-chemical degradation of the encapsulant materials was observed, moisture ingress into the module construction can still induce corrosion in cell metallization, thereby increasing series resistance and reducing fill factor. These variations in electrical parameters provide critical insights into the behavior of these mini-modules during extended damp heat exposure, offering valuable information for analyzing degradation pathways.
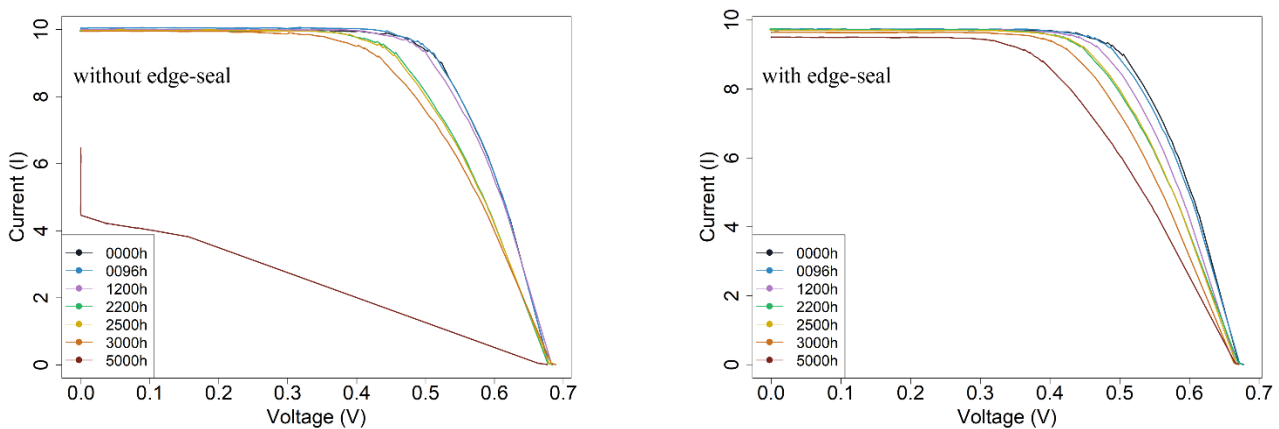
Figure 2. *Temporal evolution of I-V curves of the selected mini-modules under damp heat exposure*

Figure 3 presents the temporal evolution and model predictions of the I-V curve parameters over time (top row), along with the relationship of P_{MP} with these parameters (bottom row) for the mini-modules without edge-seal, using the netSEM approach. Detailed functional forms, goodness-of-fit statistics (adjusted R^2), and model equations are provided in Table 2. The I-V curve parameters exhibit a quadratic trend over time: P_{MP}, I_{SC}, and FF decrease quadratically, while R_S increases. Although the relationship between $P_{MP} \rightarrow I_{SC}$ also follows a quadratic trend, a change point model offers a better fit for the relationships between $P_{MP} \rightarrow FF$ and $P_{MP} \rightarrow R_S$. In these models, the change point is indicated by the value in parentheses followed by the $\pm$ sign. Before the change point, the model is represented by the first part of the equation; after the change point, a combined linear equation applies. For instance, the relationship between $P_{MP} \rightarrow FF$ is described by the equation: $-1.232 + 8.788 \cdot FF - 2.066 \cdot (FF - 0.620)$. The change point for FF is 0.620. Before this point, the relationship is linear, represented by $-1.232 + 8.788 \cdot FF$. After this point, the equation becomes $-1.232 + 8.788 \cdot FF - 2.066 \cdot (FF - 0.620)$, which simplifies to $0.049 + 6.722 \cdot FF$. Both the quadratic and change point models suggest an initial induction (damage accumulation) phase followed by a rapid decline in the parameters.

Figure 4 illustrates the degradation pathway diagram for the mini-modules without edge-seal. It appears that the primary factors influencing power performance are FF, R_S, and I_{SC}. This indicates that moisture ingress into the module construction has led to the corrosion of the cell metallization. Although there is a strong relationship between $I_{SC} \rightarrow P_{MP}$, the moderate correlation between Time $\rightarrow I_{SC}$ indicates that significant degradation of the encapsulant is unlikely. While some discoloration was observed, which correlates with P_{MP}, it is not enough to strongly impact I_{SC}. The relationship between the mechanistic variables, such as between $I_{SC} \rightarrow FF$ (or $FF \rightarrow I_{SC}$), $FF \rightarrow R_S$ (or $R_S \rightarrow FF$), and $I_{SC} \rightarrow R_S$ (or $R_S \rightarrow I_{SC}$) show nearly perfect model fits, highlighting the strong interactions between these parameters. It is important to note that the netSEM analysis explores only statistical correlations; therefore, a strong correlation between two variables does not necessarily imply causation. Expert guidance from domain-specific knowledge is crucial in interpreting the results.
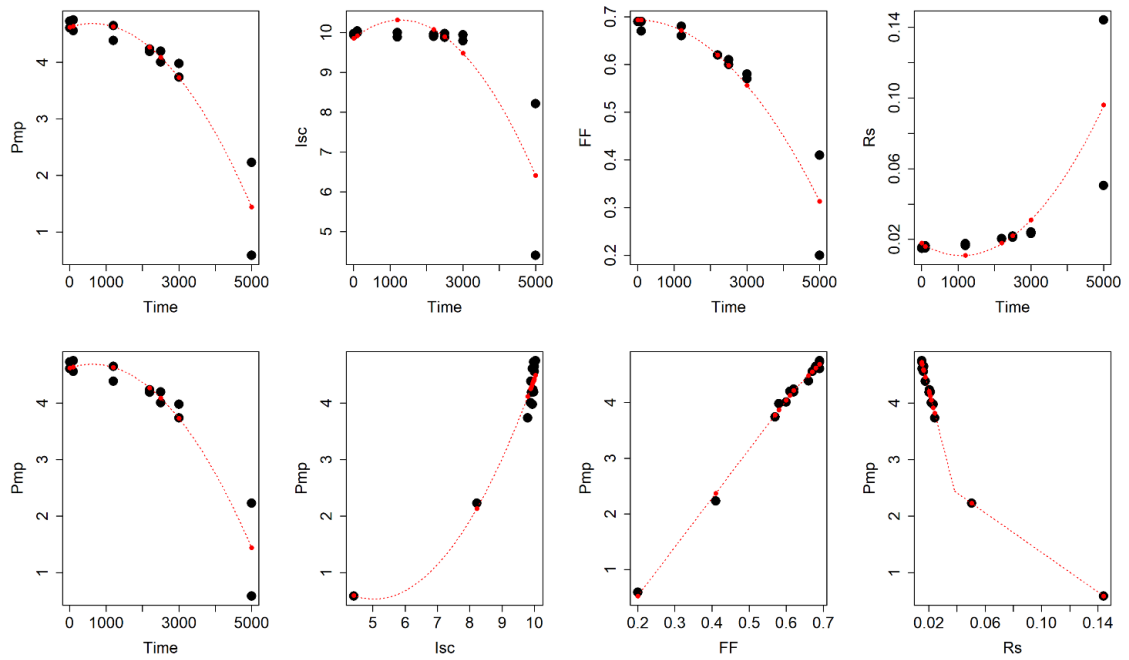
Figure 3. *Model predictions of the I-V curve parameters over time (top row) and model predictions of P_{MP} as a function of I-V curve parameters (bottom row) for the mini-modules without edge-seal*

Table 2. *Model predictions and the corresponding model equations for the selected univariate relationships for the mini-modules without edge-seal*

Path	Model	Adjusted R^2	Model Equation
Time → P_{MP}	Quadratic	0.896	$4.623 + 2.120\text{e-}04 \cdot \text{Time} - 1.696\text{e-}07 \cdot \text{Time}^2$
Time → I_{SC}	Quadratic	0.685	$9.858 + 7.220\text{e-}04 \cdot \text{Time} - 2.823\text{e-}07 \cdot \text{Time}^2$
Time → FF	Simple Quadratic	0.891	$0.693 - 1.519\text{e-}08 \cdot \text{Time}^2$
Time → R_S	Quadratic	0.638	$1.762\text{e-}02 - 1.230\text{e-}05 \cdot \text{Time} + 5.575\text{e-}09 \cdot \text{Time}^2$
Time → P_{MP}	Quadratic	0.896	$4.623 + 2.120\text{e-}04 \cdot \text{Time} - 1.696\text{e-}07 \cdot \text{Time}^2$
I_{SC} → P_{MP}	Quadratic	0.949	$4.541 - 1.591 \cdot I_{SC} + 0.158 \cdot I_{SC}^2$
FF → P_{MP}	Change Point	0.995	$-1.232 + 8.788 \cdot \text{FF} - 2.066 \cdot (\text{FF-}0.620) \pm$
R_S → P_{MP}	Change Point	0.997	$6.180 - 97.494 \cdot R_S + 79.980 \cdot (\text{Rs-}0.038) \pm$
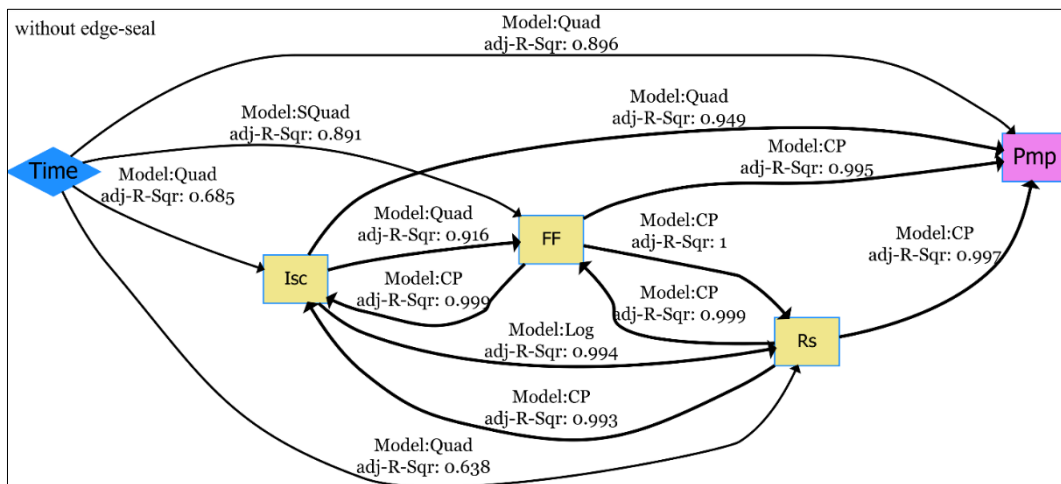
Figure 4. *Degradation pathway diagram for the mini-modules without edge-seal*

Figure 5 compares the direct and mechanistic pathways for the degradation of mini-modules without edge-seal. The direct pathway is represented by the relationship of Time → P_{MP} with an RMSE value of 0.330. Mechanistic pathways include additional variables to this direct pathway. It can be seen that the variation in P_{MP} can be effectively explained by FF with an RMSE value of 0.336, represented by the pathway of Time → FF → P_{MP}. Pathways incorporating R_S and I_{SC} as mechanistic variables also account for the change in P_{MP}, though with slightly higher RMSE values of 0.490 and 0.500, respectively. When considering two mechanistic variables, the combined effect of FF and R_S provides a comprehensive explanation of the observed change in in P_{MP}, resulting in the lowest RMSE value of 0.329, represented by the pathway of Time → FF → R_S → P_{MP}. Although the pathway of Time → R_S → FF → P_{MP} has the highest RMSE value among those with two mechanistic variables, it may better explain the observed change in P_{MP} since exposure increases R_S, which in turn decreases FF. The interplay of three mechanistic variables, namely FF, I_{SC}, and R_S, offers a thorough explanation for the observed variation in P_{MP}. The pathway of Time → FF → I_{SC} → R_S → P_{MP} yields an RMSE value of 0.393, indicating a robust model. Alternatively, the pathway of Time → R_S → I_{SC} → FF → P_{MP}, despite a slightly higher RMSE value, may better reflect the degradation in power due to increased R_S leading to decreased FF. In summary, the decline in FF and power performance can primarily be attributed to moisture-induced reactions, which causes corrosion of cell metallization and discoloration of the EVA encapsulant. For clarity, pathways with more than two mechanistic variables are not shown in Figure 5.
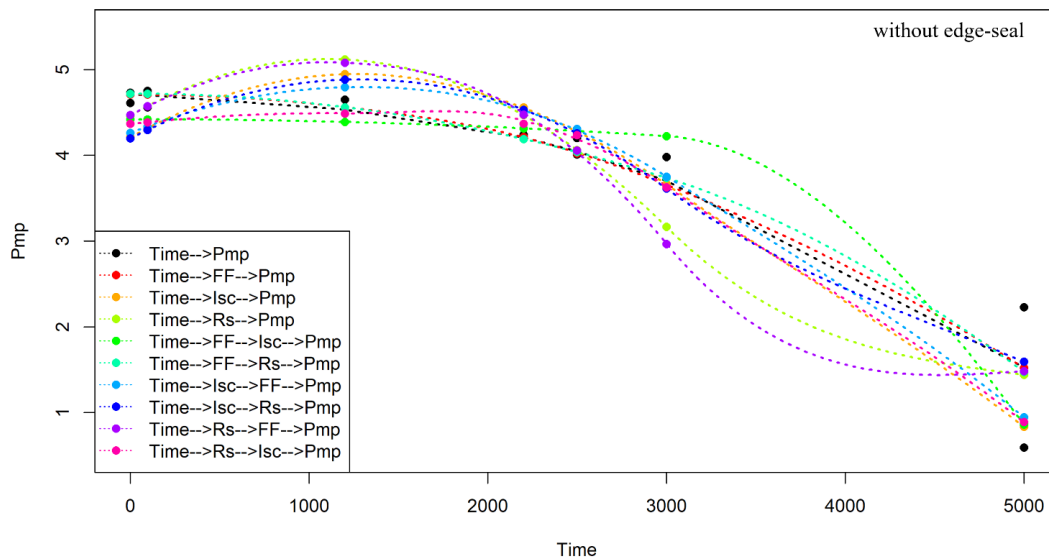
Figure 5. Comparison of direct and mechanistic pathways for the power degradation of mini-modules without edge-seal

Figure 6 presents the temporal evolution and model predictions of the I-V curve parameters over time (top row), along with the relationship of P_{MP} with these parameters (bottom row) for the mini-modules with edge-seal, using the netSEM approach. Detailed functional forms, goodness-of-fit statistics (adjusted R^2), and model equations are provided in Table 3. The I-V curve parameters primarily exhibit linear or change point models over time. Although the relationship between Time → I_{SC} has a quadratic nature, the change in I_{SC} over time is minimal, and the data is scattered, resulting in a weak correlation with an adjusted R^2 value of around 0.35. A change point model offers a better fit for the relationships between Time → FF and Time → R_S, but the changes in slopes at the change points are relatively small, appearing mostly simple linear models. The relationships between FF → P_{MP} and R_S → P_{MP} are represented by simple quadratic and simple linear models, respectively. Despite the logarithmic nature of the I_{SC} → P_{MP} relationship, data quality issues result in a modest goodness of fit with an adjusted R^2 value of 0.56.

These findings suggest that the induction (damage accumulation) phase followed by a rapid decline is not observed when the edge-seal is used within the applied exposure time, indicating that degradation progresses slowly due to minimized moisture ingress. It is important to note that moisture ingress involves the diffusion of water molecules into the module construction (Segbefia et al., 2021). This process begins when these molecules are entered into the module and adsorbed onto the surface of the encapsulant. Driven by a

concentration gradient, the molecules then move through the encapsulant and are desorbed onto other components. The diffusion continues until equilibrium is reached with the surrounding humidity. Since relative conditions are constant during damp heat testing, time becomes the most essential factor for this process. In the case of edge-seal, extending the testing time beyond the applied level of 5000 hours could reveal potential nuances and alterations in the observed results, but this may not be feasible due to cost and time constraints.
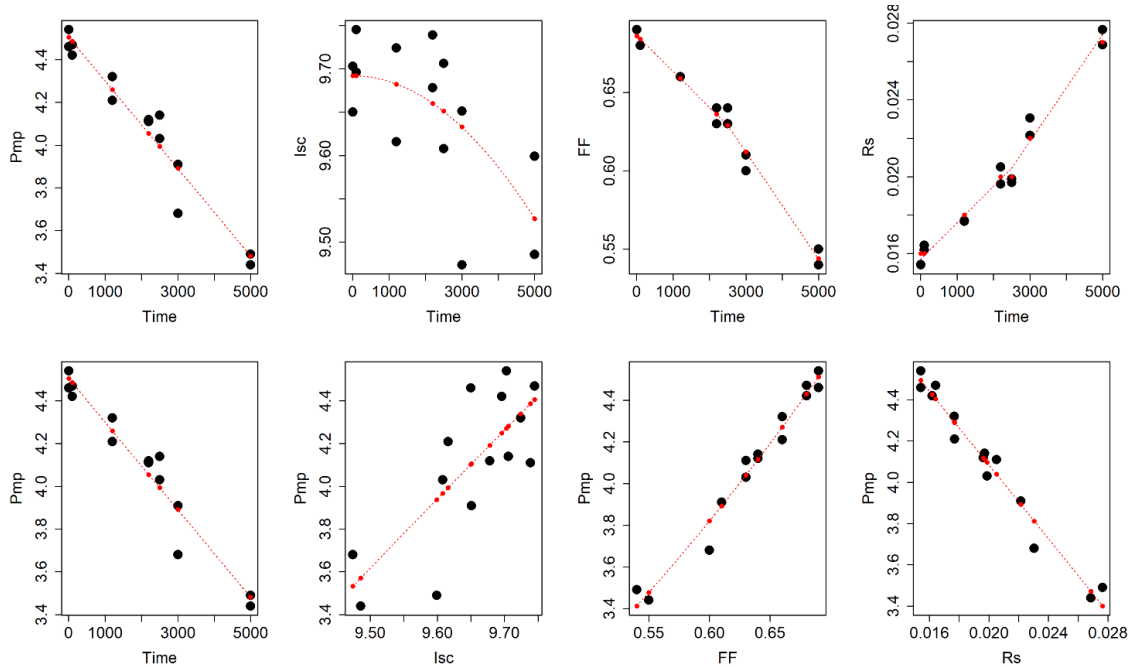
Figure 6. *Model predictions of the I-V curve parameters over time (top row) and model predictions of P_{MP} as a function of I-V curve parameters (bottom row) for the mini-modules with edge-seal*

Figure 7 illustrates the degradation pathway diagram for the mini-modules with edge-seal. The positive impact of using edge-seal is evident here. It appears that the power performance is influenced solely by R_S and FF with no significant effect from I_{SC}. This suggests that encapsulant material degradation is unlikely to be a cause for power loss in this instance. The observed reduction in power performance, though less severe than that in the mini-modules without edge-seal, can still be attributed to moisture ingress and subsequent corrosion of the cell metallization. In this case, the edge-seal did not completely block the entry of moisture, but significantly reduced its extent. Variabilities introduced during the manual lamination and edge-seal application process may also play a role. Given that these mini-modules were assembled manually, these findings highlight the critical importance of maintaining high-quality lamination standards in regular processing conditions. With automated module lamination and edge-seal dispensing, the quality of module construction could be improved, further minimizing moisture ingress.

Table 3. *Model predictions and the corresponding model equations for the selected univariate relationships for the mini-modules with edge-seal*

Path	Model	Adjusted R^2	Model Equation
Time → P_{MP}	Simple Linear	0.940	$4.506 - 2.050e\text{-}04 \cdot Time$
Time → I_{SC}	Simple Quadratic	0.347	$9.692 - 6.583e\text{-}09 \cdot Time^2$
Time → FF	Change Point	0.981	$0.686 - 2.296e\text{-}05 \cdot Time - 1.120e\text{-}05 \cdot (Time\text{-}2500) \pm$
Time → R_S	Change Point	0.974	$1.570e\text{-}02 + 1.899e\text{-}06 \cdot Time + 8.881e\text{-}07 \cdot (Time\text{-}2500) \pm$
Time → P_{MP}	Simple Linear	0.940	$4.506 - 2.050 e\text{-}04 \cdot Time$
I_{SC} → P_{MP}	Logarithmic	0.564	$-66.208 + 31.015 \cdot \log(I_{SC})$
FF → P_{MP}	Simple Quadratic	0.971	$1.674 + 5.960 \cdot FF^2$
R_S → P_{MP}	Simple Linear	0.966	$5.872 - 89.408 \cdot R_S$
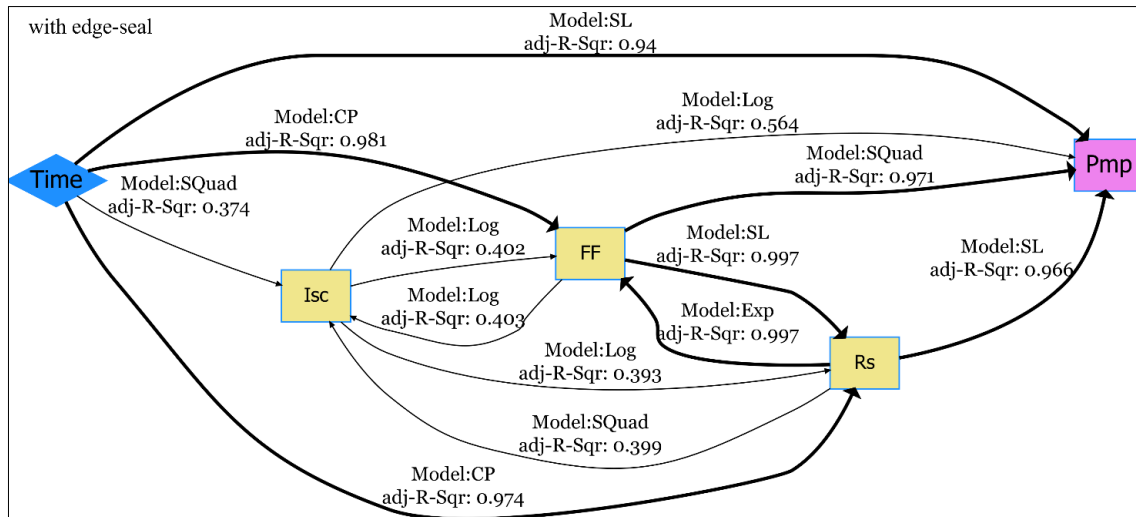
Figure 7. Degradation pathway diagram for the mini-modules with edge-seal

Figure 8 compares the direct and mechanistic pathways for the degradation of mini-modules with edge-seal. The direct pathway, represented by the relationship of Time → P_{MP}, has an RMSE value of 0.081. This analysis exhibits similarities to those observed in mini-modules without edge-seal, where variations in P_{MP} are effectively explained through either FF or R_S with RMSE values of 0.075 and 0.078, respectively. In this context, the effect of I_{SC} is relatively minor compared to the other pathways. When considering pathways involving two mechanistic variables, the interaction between R_S and FF provides a more comprehensive explanation of changes in P_{MP}. The pathway of Time → R_S → FF → P_{MP} offers a more integrated approach to understanding power degradation, resulting in the lowest RMSE value of 0.075. Including I_{SC} in this pathway as the third mechanistic variable does not improve the model due to its weak correlation with both Time and P_{MP}, leading to an RMSE value of 0.178.
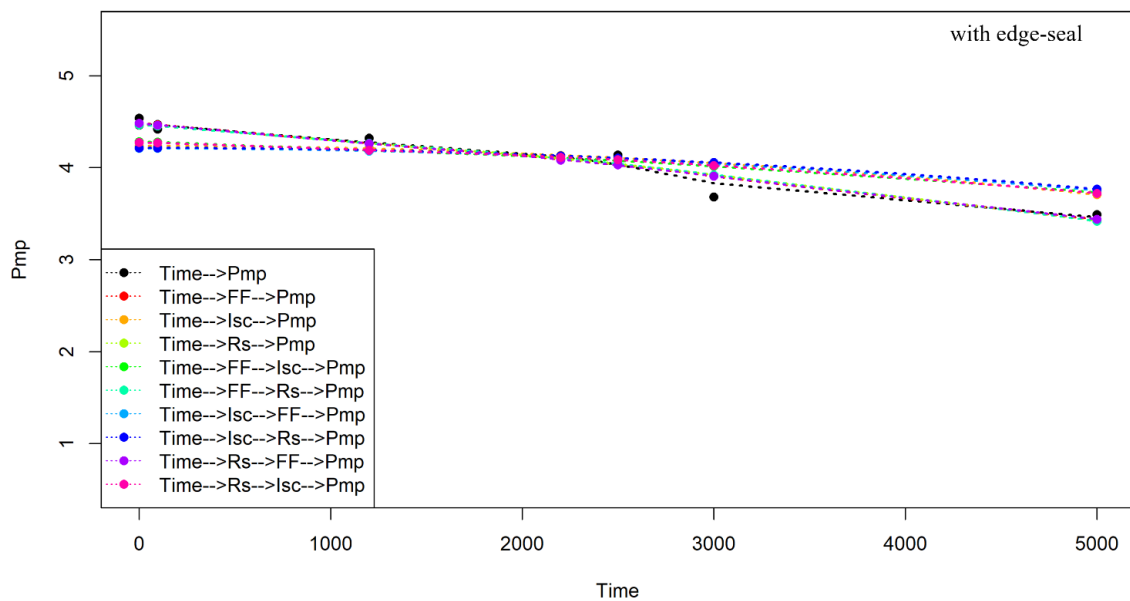
Figure 8. Comparison of direct and mechanistic pathways for the power degradation of mini-modules with edge-seal

Comprehensive results detailing the direct and mechanistic degradation pathways are presented in Table 4. In general, the effects of R_S and FF, whether individually or combined, are critical in explaining the observed variations in P_{MP} for both mini-module configurations. To ensure the modules function effectively throughout their service life, protecting against moisture is crucial. Although the use of double-glass construction, replacing the polymeric backsheet, is a useful strategy to minimize moisture ingress, moisture can still

penetrate from the edges. This study explored the critical role of edge-seal application in minimizing moisture ingress and mitigating its detrimental effects on module performance, particularly for designs with moisture-susceptible encapsulant materials like EVA. Mini-modules without edge-seal experienced a substantial 70% loss in power, primarily caused by a 37% reduction in I_{SC}, a 56% decline in FF, and an astonishing 650% rise in R_S. In contrast, mini-modules with edge-seal showed only a 33% loss in power, mainly attributed to a 21% decrease in FF and a 76% increase in R_S. While the edge-seal did not entirely prevent moisture ingress, it minimized its extent, slowed down the degradation, and thus significantly mitigated its impact. While the encapsulant materials showed minimal degradation in their optical, chemical, and thermo-chemical properties, the presence of moisture within the module construction could still lead to corrosion of the cell metallization. This, in turn, impacts power performance, even without significant acetic acid formation.

Table 4. RMSE values of estimated direct and mechanistic degradation pathways

Length	Pathway	Without edge-seal	With edge-seal
		RMSE	
0	Time $\rightarrow$ P_{MP}	0.330	0.081
1	Time $\rightarrow$ FF $\rightarrow$ P_{MP}	0.336	0.075
1	Time $\rightarrow$ I_{SC} $\rightarrow$ P_{MP}	0.500	0.193
1	Time $\rightarrow$ R_S $\rightarrow$ P_{MP}	0.490	0.078
2	Time $\rightarrow$ FF $\rightarrow$ I_{SC} $\rightarrow$ P_{MP}	0.437	0.178
2	Time $\rightarrow$ FF $\rightarrow$ R_S $\rightarrow$ P_{MP}	0.329	0.078
2	Time $\rightarrow$ I_{SC} $\rightarrow$ FF $\rightarrow$ P_{MP}	0.452	0.211
2	Time $\rightarrow$ I_{SC} $\rightarrow$ R_S $\rightarrow$ P_{MP}	0.452	0.214
2	Time $\rightarrow$ R_S $\rightarrow$ FF $\rightarrow$ P_{MP}	0.529	0.075
2	Time $\rightarrow$ R_S $\rightarrow$ I_{SC} $\rightarrow$ P_{MP}	0.424	0.180
3	Time $\rightarrow$ FF $\rightarrow$ I_{SC} $\rightarrow$ R_S $\rightarrow$ P_{MP}	0.393	0.202
3	Time $\rightarrow$ FF $\rightarrow$ R_S $\rightarrow$ I_{SC} $\rightarrow$ P_{MP}	0.404	0.180
3	Time $\rightarrow$ I_{SC} $\rightarrow$ FF $\rightarrow$ R_S $\rightarrow$ P_{MP}	0.452	0.213
3	Time $\rightarrow$ I_{SC} $\rightarrow$ R_S $\rightarrow$ FF $\rightarrow$ P_{MP}	0.459	0.213
3	Time $\rightarrow$ R_S $\rightarrow$ FF $\rightarrow$ I_{SC} $\rightarrow$ P_{MP}	0.439	0.178
3	Time $\rightarrow$ R_S $\rightarrow$ I_{SC} $\rightarrow$ FF $\rightarrow$ P_{MP}	0.402	0.201

To explore the effects of encapsulant type on degradation, it is essential to understand the interaction between polymers and water (Mitterhofer et al., 2020). Water's polar structure enhances chemical interactions with the polymer, especially if the polymer is also polar, facilitating faster moisture transmission. The hydrophilic nature of vinyl acetate groups makes EVA more susceptible to moisture, leading to easy hydrolysis and acetic acid formation, which accelerates degradation. EVA's polar structure allows moisture to diffuse more rapidly compared to non-polar polymers such as polyolefins. Properties of encapsulant materials, such as chemical and network structure, crystallinity, polarity, free volume, crosslinking degree, and volume resistivity, also play a critical role. Determining all these parameters is challenging and beyond the scope of this study. However, some inferences can be made based on the typical properties of encapsulant materials (Oreski et al., 2021) provided in Table 5. Among these, water vapor transmission rate (WVTR) and volume resistivity are significantly important, as WVTR relates to moisture absorption resistance and volume resistivity relates to ion transport resistance and thus PID. EVA has relatively higher WVTR and lower volume resistivity than relatively newer encapsulant materials such as POE and TPO, making it an unfavorable choice, especially for double-glass modules. Although this study investigated only hydro-thermal degradation, photo-thermal degradation also causes acetic acid formation through Norrish II type reactions, as depicted in Figure 1. When double-glass module construction is equipped with impermeable edge-seal, and acetic acid is formed through photo-thermal degradation, it will be trapped inside and accumulate, leading to faster corrosion of cell metallization and accelerated power degradation (Patel et al., 2020). Therefore, if EVA is used for double-glass module construction, it should be used with caution, and strong stabilization against UV radiation becomes essential.

Table 5. *Typical properties of encapsulant materials*

Encapsulant Material	Polymer Type	Glass Transition Temperature	Elastic Modulus	Refractive Index	Volume Resistivity	Water Vapor Transmission Rate
		T_G [°C]	E [MPa]	n	ρ [$\Omega \cdot$cm]	WVTR [g/m^2/day]
EVA		–40 to –34	≤ 68	1.49	10^{14}	34
POE	Elastomer	–50 to –40	≤ 30	1.49	10^{15} to 10^{16}	3.30
PDMS		≤ -100	≤ 10	1.38 to 1.58	10^{14} to 10^{15}	130 to 200
PVB	Thermoplastic	+12 to +20	≤ 11	1.48	10^{10} to 10^{12}	40.05
Ionomer		+40 to +50	≤ 300	1.49	10^{16}	0.19
TPO	Thermoplastic elastomer	–60 to –40	≤ 32	1.48	10^{14} to 10^{18}	2.85

4. CONCLUSION

Solar energy plays a crucial role in the renewable energy sector, yet PV modules and systems encounter numerous operational challenges due to environmental stresses. These stresses can lead to various forms of degradation, compromising the long-term performance and service lifetime of PV modules. While EVA is a widely used encapsulant in PV modules, it is highly susceptible to moisture. As EVA degrades hydrolytically, it releases acetic acid, leading to corrosion of the cell metallization and performance loss. This study explored the use of a PIB-based edge-seal to reduce moisture ingress in double-glass PV modules. One-cell mini-modules encapsulated with EVA, both with and without edge-seal, were subjected to damp heat testing for up to 5000 hours. Mini-modules without edge-seal suffered a 70% loss in power. In contrast, mini-modules with the edge-seal experienced only a 33% power loss. Although the edge-seal did not fully eliminate moisture ingress, it significantly mitigated its effects. Although the encapsulant materials showed minimal degradation, moisture ingress still led to cell metallization corrosion, resulting in degradation in power even without significant acetic acid formation. Additionally, the netSEM approach was applied to analyze the I-V characteristics, allowing for the identification of statistically significant relationships and the construction of degradation pathway diagrams. This analysis confirmed that increased series resistance and decreased fill factor were the main contributors to loss in power in both module configurations. This study underscores the vital importance of preventing moisture ingress to enhance the durability and reliability of PV modules, thereby ensuring their optimal performance throughout their intended service lifetime.

AUTHOR CONTRIBUTIONS

Conceptualization, A.G.; methodology, A.G.; software, A.G. and M.G.; validation, A.G.; formal analysis, A.G. and M.G.; research, A.G. and M.G.; sources, A.G.; data curation, A.G. and M.G.; manuscript-original draft, A.G. and M.G.; manuscript-review and editing, A.G.; visualization, A.G. and M.G.; supervision, A.G.; project management, A.G.; funding, A.G. All authors have read and legally accepted the final version of the article published in the journal.

ACKNOWLEDGEMENT

CONFLICT OF INTEREST

The authors declare no conflict of interest.

REFERENCES

Aghaei, M., Fairbrother, A., Gok, A., Ahmad, S., Kazim, S., Lobato, K., Oreski, G., Reinders, A., Schmitz, J., Theelen, M., Yilmaz, P., & Kettle, J. (2022). Review of degradation and failure phenomena in photovoltaic modules. *Renewable and Sustainable Energy Reviews*, *159*, 112160. https://doi.org/10.1016/j.rser.2022.112160

BNEF. (2024, March 4). Global PV Market Outlook—1Q 2024. BloombergNEF. https://about.bnef.com/blog/1q-2024-global-pv-market-outlook/

Czanderna, A. W., & Pern, F. J. (1996). Encapsulation of PV modules using ethylene vinyl acetate copolymer as a pottant: A critical review. *Solar Energy Materials and Solar Cells*, *43*(2), 101-181. https://doi.org/10.1016/0927-0248(95)00150-6

Dintcheva, N. T., Morici, E., & Colletti, C. (2023). Encapsulant Materials and Their Adoption in Photovoltaic Modules: A Brief Review. *Sustainability*, *15*(12), 9453. https://doi.org/10.3390/su15129453

Gok, A., Fagerholm, C. L., French, R. H., & Bruckman, L. S. (2019). Temporal evolution and pathway models of poly(ethylene-terephthalate) degradation under multi-factor accelerated weathering exposures. *PLOS ONE*, *14*(2), e0212258. https://doi.org/10.1371/journal.pone.0212258

Griffini, G., & Turri, S. (2016). Polymeric materials for long-term durability of photovoltaic systems. *Journal of Applied Polymer Science*, *133*(11). https://doi.org/10.1002/app.43080

Hara, K., & Chiba, Y. (2021). Spectroscopic investigation of long-term outdoor-exposed crystalline silicon photovoltaic modules. *Journal of Photochemistry and Photobiology A: Chemistry*, *404*, 112891. https://doi.org/10.1016/j.jphotochem.2020.112891

IEA PVPS. (2023). Snapshot of Global PV Markets 2023 (IEA-PVPS T1-44:2023). International Energy Agency (IEA) Photovoltaic Power Systems Programme (PVPS). https://iea-pvps.org/snapshot-reports/snapshot-2023/

IEA PVPS. (2024). Snapshot of Global PV Markets 2024 (IEA-PVPS T1-42: 2024). International Energy Agency (IEA) Photovoltaic Power Systems Programme (PVPS). https://iea-pvps.org/snapshot-reports/snapshot-2024/

IEC. (2021). IEC 61215-1-1:2021: Terrestrial photovoltaic (PV) modules—Design qualification and type approval—Part 1-1: Special requirements for testing of crystalline silicon photovoltaic (PV) modules (Version 2.0) [International Standard]. International Electrotechnical Commission. https://webstore.iec.ch/publication/61346

ITRPV. (2024). International Technology Roadmap for Photovoltaics. VDMA e. V. https://www.vdma.org/international-technology-roadmap-photovoltaic

Kempe, M. D., Jorgensen, G. J., Terwilliger, K. M., McMahon, T. J., Kennedy, C. E., & Borek, T. T. (2007). Acetic acid production and glass transition concerns with ethylene-vinyl acetate used in photovoltaic devices. *Solar Energy Materials and Solar Cells*, *91*(4), 315-329. https://doi.org/10.1016/j.solmat.2006.10.009

Kempe, M. D., Panchagade, D., Reese, M. O., & Dameron, A. A. (2015). Modeling moisture ingress through polyisobutylene-based edge-seals: Polyisobutylene-based edge-seals. *Progress in Photovoltaics: Research and Applications*, *23*(5), 570-581. https://doi.org/10.1002/pip.2465

Köntges, M., Kurtz, S., Packard, C., Jahn, U., Berger, K. A., Kato, K., Friesen, T., Liu, H., & Van Iseghem, M. (2014). Review of failures of photovoltaic modules (IEA-PVPS T13-01:2014). International Energy Agency (IEA) Photovoltaic Power Systems Programme (PVPS). https://iea-pvps.org/key-topics/review-of-failures-of-photovoltaic-modules-final/

Köntges, M., Oreski, G., Jahn, U., Herz, M., Hacke, P., Weiß, K.-A. Razongles, G., Paggi, M., Parlevliet, D., Tanahashi, T., & French, R. H. (2017). Assessment of photovoltaic module failures in the field (IEA-PVPS T13-09:2017). International Energy Agency (IEA) Photovoltaic Power Systems Programme (PVPS). https://iea-pvps.org/key-topics/report-assessment-of-photovoltaic-module-failures-in-the-field-2017/

Mitterhofer, S., Barretta, C., Castillon, L. F., Oreski, G., Topič, M., & Jankovec, M. (2020). A Dual-Transport Model of Moisture Diffusion in PV Encapsulants for Finite-Element Simulations. *IEEE Journal of Photovoltaics*, *10*(1), 94-102. https://doi.org/10.1109/JPHOTOV.2019.2955182

Müller, A., Friedrich, L., Reichel, C., Herceg, S., Mittag, M., & Neuhaus, D. H. (2021). A comparative life cycle assessment of silicon PV modules: Impact of module design, manufacturing location and inventory. *Solar Energy Materials and Solar Cells*, *230*, 111277. https://doi.org/10.1016/j.solmat.2021.111277

Oliveira, M. C. C. de, Diniz Cardoso, A. S. A., Viana, M. M., & Lins, V. de F. C. (2018). The causes and effects of degradation of encapsulant ethylene vinyl acetate copolymer (EVA) in crystalline silicon photovoltaic modules: A review. *Renewable and Sustainable Energy Reviews*, *81*, 2299-2317. https://doi.org/10.1016/j.rser.2017.06.039

Oreski, G., Stein, J., Eder, G., Berger, K., Bruckman, L., Vedde, J., Weiss, K.-A., Tanahashi, T., French, R., & Ranta, S. (2021). Designing New Materials for Photovoltaics: Opportunities for Lowering Cost and Increasing Performance through Advanced Material Innovations (IEA-PVPS T13-13:2021). International Energy Agency (IEA) Photovoltaic Power Systems Programme (PVPS). https://iea-pvps.org/key-topics/designing-new-materials-for-photovoltaics/

Paç, A. B., & Gok, A. (2024). Assessing the Environmental Benefits of Extending the Service Lifetime of Solar Photovoltaic Modules. *Global Challenges*, *8*(8), 2300245. https://doi.org/10.1002/gch2.202300245

Patel, A. P., Sinha, A., & Tamizhmani, G. (2020). Field-Aged Glass/Backsheet and Glass/Glass PV Modules: Encapsulant Degradation Comparison. *IEEE Journal of Photovoltaics*, *10*(2), 607-615. https://doi.org/10.1109/JPHOTOV.2019.2958516

Schnatmann, A. K., Schoden, F., & Schwenzfeier-Hellkamp, E. (2022). Sustainable PV Module Design— Review of State-of-the-Art Encapsulation Methods. *Sustainability*, *14*(16), 9971. https://doi.org/10.3390/su14169971

Segbefia, O. K., Imenes, A. G., & Sætre, T. O. (2021). Moisture ingress in photovoltaic modules: A review. *Solar Energy*, *224*, 889-906. https://doi.org/10.1016/j.solener.2021.06.055

Sinha, A., Sulas-Kern, D. B., Owen-Bellini, M., Spinella, L., Uličná, S., Pelaez, S. A., Johnston, S., & Schelhas, L. T. (2021). Glass/glass photovoltaic module reliability and degradation: A review. *Journal of Physics D: Applied Physics*, *54*(41), 413002. https://doi.org/10.1088/1361-6463/ac1462

Heat Transfer Analysis of a Concentrated-Type Solar Dryer for Ginger

Ige BORI[1*] (iD)   Jonathan Yisa JIYA[1] (iD)   Adamu Mohammed ORAH[2] (iD)   Sunday BAKO[3] (iD)   Muideen Oladele OYEBAMIJI[1] (iD)

[1] Department of Mechanical Engineering, Federal University of Technology, Minna, Niger State, Nigeria
[2] Department of Mechanical Engineering Technology, Federal Polytechnic, Kaura Namoda, Zamfara State, Nigeria
[3] Department of Mechanical Engineering, Nuhu Bamali Polytechnic, Zaria, Kaduna State, Nigeria

Keywords	Abstract
Dryer Drying Chamber Heat Transfer Parabolic Trough Receiver Tube	In recent years, global concern about the preservation of agricultural products for usage and exports through drying has been outstanding. Solar Parabolic Trough Collectors (SPTC) are used to dry various agricultural products for effective moisture removal. A heat transfer fluid (HTF) flows through a receiver tube pipe that absorbs solar radiation reflected from the stainless-steel sheet surfaces of the SPTC. In order to reduce the heat losses, the pipe was linked through a flexible, thermally insulated cross-linked polyethene pipe to the copper tubes inside the drying chamber. The heat transfer analysis of the SPTC is essential to understand the thermal behavior and its performance during the drying process. This paper examined the heat exchanges developed in the designed concentrated-type solar dryer, and the heat transfer rates in the receiver tube and the drying chamber, as well as the heat transfer coefficients for the solar drying of ginger, were determined. The thermal analysis of the convective heat exchanges within the receiver tube and the drying chamber is presented. The heat transfer coefficients h_{Rec} and h_{DC} for the convective heat transfer process in the receiver tube and the drying chamber were 1372.48W/m.K and 17.60W/m.K, respectively. The dryer's thermal efficiency was 30%, showing considerable moisture removal from the ginger samples. The mean temperature difference between the drying chamber and the ambient showed a considerable increase of about +11oC. This resulted in considerable moisture removal, and the final moisture content achieved by the concentrated solar dryer for the ginger samples was 11.1%, compared to the 23.74% achieved by the open-air solar (OAS) drying method.

Author ID (ORCID Number)		Article Process	
0000-0001-7001-094X	Ige BORI	**Submission Date**	26.08.2024
0009-0008-7166-7044	Jonathan Yisa JIYA	**Revision Date**	23.09.2024
0000-0001-6778-8443	Adamu Mohammed ORAH	**Accepted Date**	14.10.2024
0000-0003-2348-1217	Sunday BAKO	**Published Date**	30.12.2024
0009-0002-8060-5239	Muideen Oladele OYEBAMIJI		

1. INTRODUCTION

In order to minimise post-harvest losses and ensure crop availability for future use, crops are typically preserved through drying. In order to keep crops from spoiling, moisture must be removed. Inadequate techniques for preserving agricultural products, which are generated in greater numbers during harvest, are a common issue faced by Nigerian farmers. Ekechukwu (2010), related that the standard open-air solar drying method is minimal, causing crop spoilage due to inadequate drying, rodent, bird and insect encroachment, and mildews attack. Ebewele and Jimoh (1981) also asserted that crop exposure to harsh weather conditions like rain, dust, and wind is one of the drawbacks of insufficient drying techniques. Fumen et al. (2003) related that crop spoilage occurs annually and is valued at millions of dollars. However, these restrictions made it necessary to use dependable solar technologies for drying procedures. The majority of agricultural fields now use solar technology. Because solar thermal technology is abundant, renewable, and non-polluting, it is quickly gaining attraction in the energy-saving market. Various sun dryer types have been developed in various parts of the world.

*Corresponding Author, e-mail: ige.bori@futminna.edu.ng

The two categories of solar dryers are forced-convection and naturally convection. Airflow generated by a fan or blower powered by fossil fuel, electricity, or solar panels powers the former, whilst buoyancy-induced airflow powers the latter. Because of its high rate of ginger production, Okafor (2002) claimed that Nigeria continues to be the country's top exporter of ginger. Significant ginger production occurs in Nigeria's Benue, Niger, Gombe, Nasarawa, and Kaduna states. Still, Kaduna state provides roughly 95% of Nigeria's total ginger production. Nigerian ginger production, estimated at 110,000 metric tonnes in 2005, climbed to roughly 60% after five years, with 90% of the crop being exported in dried form and 10% being consumed fresh locally (Gucheman, 2010). Njoku et al. (1995), declared that Nigerian ginger is known for its strong scent, pungency, and oil and oleoresin content. For worldwide, ginger is one of the main ingredients for the production of wine, meat, soft beverages, bakery goods, perfumes, and toiletries. It is possible to use dried ginger both medicinally and as a solitary spice. In certain nations, ginger is also used to treat particular illnesses like cholera, dyspepsia, rheumatism, cancer, nausea, growths in the throat, cataracts, pulmonary and neuralgia, and fabric disease.

Processing ginger involves first selecting the best pieces, then giving them a thorough washing and soak. Next, it is split and peeled, and dried until the moisture level reaches 7–12% (Ebewele & Jimoh, 1981). Because of insufficient and subpar drying procedures, the majority of ginger produced in Nigeria and beyond is of low quality and falls short of the requirements and expectations of most importers.Traditionally, ginger is sun-dried in an open yard in only one layer to produce a brown, unevenly wrinkled surface that reveals a dark brown colour when cracked. There are various kinds of dried ginger available, including slices, splits, and entire dried ginger. Direct solar drying and indirect solar drying are the two primary forms of solar drying. Compared to the open-air drying method, the solar dryer has five major advantages: it is more economical, hygienic, faster, more efficient, and healthier (Tiris et al., 1995). Augustus Leon et al. (2002) categorised the drying system based on the type and layout of solar energy use, as seen in Figure 1.

According to Njoku et al. (1995), the ginger produced in Nigeria has high oil and oleoresin content, pungency and aroma. Ginger processing after harvest entails first sorting out the good ones, after which they are thoroughly washed and soaked. It is then split and peeled before drying to a moisture content of 7-12% as stated by Ebewele and Jimoh (1981). Most ginger processed in Nigeria is of low quality and falls below most importers' expectations and specifications due to inadequate and sub-standard drying processes. There are two main types of solar drying namely: (i) Direct solar drying and (ii) Indirect solar drying.

The natural convection drier, sometimes referred to as an active sun dryer, works by moving hot air across the surfaces of the crop that has to be dried. When solar radiation strikes the dryer's glass cover, some of it is absorbed by the cabin dryer and some is reflected back into space. The temperature of the crop rises significantly as a result of the absorbed solar energy being reflected back from the crop surface and the remaining portion being absorbed into the crop. In contrast to an open sun drying system, a glass cover prevented the long wavelength radiation from escaping to the atmosphere, which decreased convective losses within the dryer and raised the drying chamber and crop temperatures considerably (Tiris et al., 1995). Despite being less portable than direct dryers, indirect solar dryers frequently show higher efficiency and may dry more agricultural products, according to Sharma et al. (2009). The main drawback of utilizing a direct solar dryer is eliminated with this type of dryer since the agricultural product is not exposed to sunlight directly. To get the most solar energy, the solar collectors need to be positioned correctly. When the solar collector surface was orientated perpendicular to the sun, more solar energy was typically captured. The natural convection concept also aids in air movement when the solar collector is tilted at an appropriate inclination. The solar dryer is made out of a drying chamber that holds the trays or shelves that hold the farm produce and a collector that heats the air (Sharma et al., 2009). A thorough analysis of different solar energy drying system designs, construction specifics, and operating principles was carried out by Ekechukwu and Norton (1999). According to their research, well-designed forced convection (active) solar dryers operate more efficiently and are easier to regulate than natural-circulation (passive) models. In this study, the ginger was dried using the indirect (active) solar dryer concept.

Augustus Leon et al. (2002) classified the drying system according to the mode and design of solar energy utilization, as seen in Figure 1. Drying, an intricate procedure of concurrent heat and mass transfer, is of significant importance in various industries. Initial and final moisture content, drying air temperature, relative humidity, and velocity are some of the variables that affect how much energy is needed to dry a particular

product (Shukla & Sahu, 2019). Several investigations have been carried out regarding the heat transfer analysis of solar dryers to ascertain the heat transfer coefficient and augment efficiency (Alimohammadi et al., 2020). Sansaniwal and Kumar (2015) reported that in open-air drying settings with natural convection, ginger's convective heat transfer coefficient was 26.25 W/m^2, and the hybrid drier has a higher drying rate than open sun drying, with an overall drying efficiency of 13% and 18% in the summer and winter, respectively.
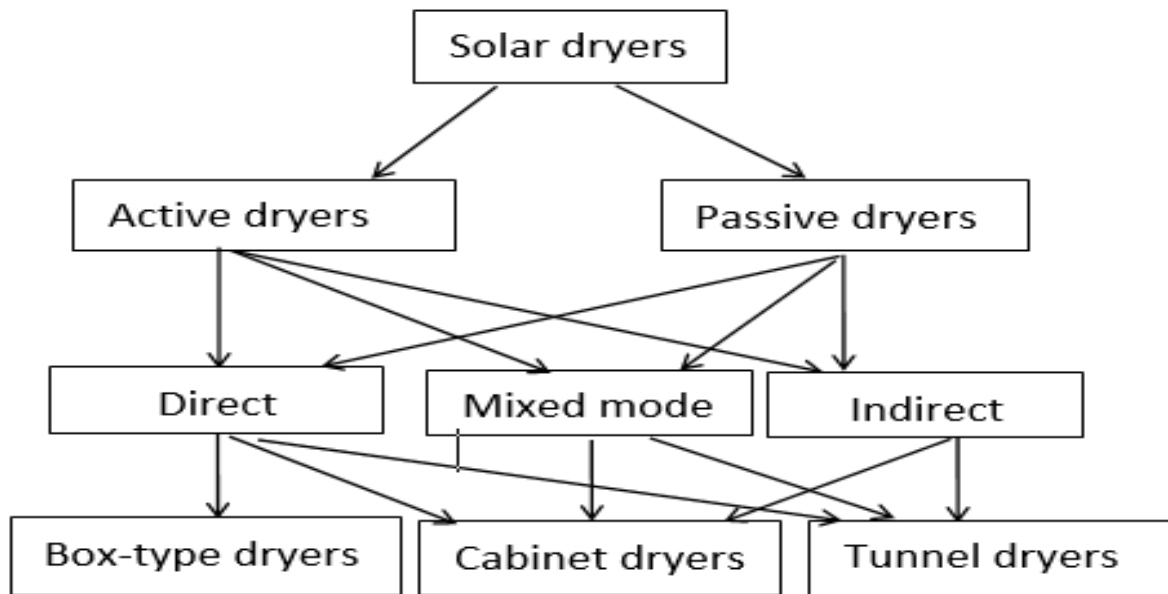
Figure 1. *Classification of solar heating modes and dryers (Augustus Leon et al., 2002)*

A straightforward and useful program that allowed the concentrator's parameters to be changed for assessing the thermal performance was created by de Oliveira Siqueira et al. (2014) after they developed and implemented a mathematical model to compute heat transfer and flow parameters harnessed to parabolic trough solar collectors. The software proved effective as a design tool since it is possible to determine the thermal efficiency and optical and thermal losses, among other things. The mathematical model that was constructed was logical. Padilla et al. (2011) created a thorough heat transfer model for the thermal analysis of solar receivers with parabolic troughs. More precise correlations and a thorough investigation of radiative heat transfer were features of the suggested model. Their findings strongly correlate with both alternative heat transport models and experimental data. After the thermal characteristics of the air inside the parabolic solar collector dryer was examined, it was found that the air at the collector's inlet warmed up by 9°C and then somewhat dropped before entering the drying chamber (Ouedraogo et al., 2021). A thermal analysis of the SPTC dryer is essential to understand the thermal behaviour and performance during the drying process. Therefore, this paper aims to examine the heat transfer developed in the fabricated concentrated-type solar dryer and determine the heat transfer coefficient for solar drying of the ginger.

2. MATERIAL AND METHOD

A drying chamber and a parabolic trough solar collector make up the concentrated solar drier. The stainless-steel parabolic trough (1190 x 450 x 300 mm) directs solar radiation onto an 18 mm-diameter water-carrying receiver tube pipe. The pipe was positioned throughout the whole parabolic trough, at its centre. The flexile, heat-resistant cross-linked polyethene pipe (PEX) was used to join the pipe to the drying chamber's copper radiator tubes, which were 1300 x 410 x 400 mm. The water flow was provided by a straightforward syphon tank that was big enough to give enough of time for testing. A picture of the concentrated solar dryer is shown in Figure 2.

Figure 2. Pictorial view of the Experimental setup

To minimize heat loss from convection from the heat tube and provide the desired glazing appearance, an 8mm thick glass cover was placed over the parabolic trough solar collector. To absorb the heat required for the drying of the ginger, the interior of the drying chamber was painted black. In order to reduce heat loss, fiberglass lagged the drying chamber. Copper tubes in the drying chamber allowed the heated water in the tube air in the collector to return to the tank. To force convection and circulate heat from these copper tubes to the ginger, a fan is coupled to a ten-watt solar panel. Five kilograms of precisely weighed ginger samples were equally divided on the dryer's rectangular wire mesh trays (1150 x 335 x 10 mm), and an additional five kilograms of ginger samples were put on the open-air tray. The samples were weighed using a weighing scale balance at one-hour intervals, and the weight reduction figures were noted. A digital hygrometer was used to measure the relative humidity in the drying chamber and its surroundings. Thermocouples at the water entry and exit of the heat receiving tube and the drying chamber were used to measure the air temperature.

2.1. Heat Transfer Analysis

Heat transfer is essential for analyzing the thermal behavior of heat transfer in fluids (water and air) in the concentrated-type solar dryer. The thermal analysis considered the transmission of heat delivered by the concentrating solar collector, the convective heat transfer with the HTF, and the heat transfer within the drying chamber. The following formula provides the radiative heat exchange rate to a concentrating solar collector's focus point:

$$\dot{Q}_{col} = \eta_{col} A_{col} G_i \qquad (1)$$

Where η_{col} signifies the collector's efficiency, A_{col} signifies the collector's area, and G_i is the collector's solar incident radiation.

The parabolic trough collectors consist of reflectors that are curved around an axis in a linear parabolic shape. Around a single focus line that is placed where a lengthy receiver pipe is supposed to heat the heat exchange fluid, they collect parallel rays. One method of heat transport is convection. It includes the heat transfer fluid (HTF) and the annulus between the absorber and receiver (de Oliveira Siqueira et al., 2014; Alimohammadi et al., 2020).

$$\dot{Q}'_{Receiver} = hD\pi(T_{hot} - T_{cold}) \tag{2}$$

But,

$$h = Nuk/D \tag{3}$$

Under laminar conditions, the HTF convection is determined by the Nusselt number; in the case of laminar flow inside the tube (where the Reynolds number is less than 2300), the mean Nusselt number is provided by equation (4) (Plappally & Lienhard, 2012):

$$Nu_{mean} = 3.66 + \frac{0.0668 \times Re \times Pr \times D_{ri}/L}{1 + 0.04(Re \times Pr \times \frac{D_{ri}}{L})^{2/3}} \tag{4}$$

Where Pr denotes the Prandtl number, D_{ri} denotes inner receiver diameter, Re denotes the Reynolds number, and L denotes the tube length. Equation (4) assumes an isothermal tube, a close estimate used in this study.

A forced convection drying scheme was related as an excellent method for quicker drying as the convective heat transfer coefficient associated with it is greater than natural convection drying (Sansaniwal & Kumar, 2015). Therefore, forced convection influenced the heat exchange in the drying chamber. The drying chamber's (DC) heat transfer is given in equation (5) (Lienhard & Lienhard, 2002).

$$\dot{Q}_{DC} = hA_{DC}(T_{hot} - T_{cold}) \tag{5}$$

But,

$$h_{DC} = Nu_L k/L \tag{6}$$

The convective heat transfer in the DC is of forced convection, which depends on the Nusselt number in turbulent conditions; the mean Nusselt number for this condition is as shown in Equation (7), from the work of Sansaniwal and Kumar (2015):

$$\overline{Nu_L} = 0.0370Re_L^{0.8}Pr^{0.43} \tag{7}$$

Equation (8) was used to determine the amount of heat required to evaporate the moisture (Gyawali et al., 2022).

$$Q_{evap} = M_w \times h_{fg} \tag{8}$$

Where Q_{evap} signifies the required heat energy for the drying process (kJ), h_{fg} signifies the Latent heat of vaporization (kJ/kg H_2O).

The latent heat of vaporization used for this study is given by Equation (9) (Youcef-Ali et al., 2001)

$$h_{fg} = c_{pw} \times (597 - 0.56T_{DC}) \tag{9}$$

Where, c_{pw} connotes the water's specific heat capacity and T_{DC} connotes the temperature in the DC.

Equation (10) gives the mass of moisture (Mw) to be removed (Rulazi et al., 2023).

$$M_W = \frac{M_p(M_i - M_f)}{100 - M_f} \tag{10}$$

Where M_p connotes the ginger samples' mass before drying (kg), M_i connotes the initial moisture content of the ginger sample (w.b %), M_f connotes the final moisture content of the ginger sample (w.b %).

The parameters considered for the heat transfer analysis of the concentrating solar dryer in this study is displayed in Table 1.

Table 1: Parameters for the dryer's heat transfer investigation

Parameters	Symbol	Value	Unit
Reciever Tube			
Incident Solar Radiation	I	396	W/m^2
Extraterrestrial Radiation	G_{ext}	1661	W/m^2
Area of Parabolic trough	A_p	0.09	m^2
Collector thermal Efficiency	η	30	%
Receiver Diameter	D_{ri}	0.018	m^2
Nusselt number (flow in tube)	Nu	38.79	
Prandtl number	Pr	3.3	
Reynold's number	Re	6621	
Thermal conductivity (water)	k	0.63688	W/m.K
heat transfer coefficient (Reciever)	h	1372.48	W/m^{2}K
Drying Chamber			
Area of Dryer	A_D	0.533	m^2
Quantity of moisture to be evaporated	M_w	4.22	kg
Water's Specific heat	c_p	4.18 $\times 10^3$	J/kg.ºC
Prandtl Number	Pr	0.708	
Air mass flow rate	m	1.085	kg/m^3
Average Velocity of air	U_{av}	1.73	m/s
Reynolds number	Re	123857.3	
Mean Nusselt number	Nu_{mean}	378.5	
Thermal conductivity (air)	k	0.027964	W/m.K
heat transfer coefficient (air)	h	17596.15	

3. RESULTS AND DISCUSSION

The model matches the trends of the experimental values, and the results obtained for the dryer's heat transmission are reported. From sunny February to March, temperatures were measured after 7 hours of drying with the concentrated solar dryer, and experimental data were acquired every 1 hour. The concentrated solar collector's focal point received 10.692W of heat transfer rate, which was then transported to the receiving tube. Table 2 shows the convective heat transmission to the HTF in the receiver tube. 1372.48 W/m.K was found to be the heat transfer coefficient (h_{Rec}) for the convective heat transfer process in the receiver tube.

Table 2: Convective heat transfer rate for the receiver tube

Drying Time	T_{amb} (ºC)	$T_{HTFentry}$ (ºC)	T_{hot} (ºC)	$T_{HTFexit}$ (ºC)	$Q_{Reciever}$ (W)
10:00	40	35	75	35	2715.0
11:00	42	37	79	73	5662.8
12:00	45	38	83	80	6205.8
13:00	46	43	89	82	6361.0
14:00	48	58	106	99	7679.7
15:00	48	65	113	113	8765.7
16:00	47	89	136	100	7757.3
17:00	45	72	117	92	7136.7

The forced air flow convection from the fan over the ginger samples influences the convective heat exchange in the drying chamber (DC). The results of the heat transmitted across the drying chamber are presented in Table 3. The coefficient of heat transfer h_{DC} for the convective heat transfer process in the drying chamber was got as 17.60 W/m.K.

Table 3: Convective heat transfer rate for the drying chamber.

Drying Time	T_{amb} (ºC)	T_{hot} (ºC)	T_{DC} (ºC)	T_{DCexit} (ºC)	Q_{DC} (W)
10:00	40	35	39	35	365771.2
11:00	42	73	49	52	459558.6
12:00	45	80	52	57	487694.9
13:00	46	82	55	60	515831.1
14:00	48	99	58	63	543967.4
15:00	48	113	59	78	553346.1
16:00	47	100	58	75	543967.4
17:00	45	92	57	66	534588.6

Figure 3 shows a thermal analysis of the high temperatures influencing heat transmission by the fluid in the dryer's drying chamber and receiver tube. The temperature in the receiver tube was always higher relative to the temperature in the drying chamber per hour due to the parabolic-cylindrical concentration at the receiver tube and the heat exchange between the receiver tube and the drying chamber. This conforms with the findings of Ouedraogo et al. (2021). However, an equilibrium temperature was established after 5 hours of drying, as observed in Figure 3.
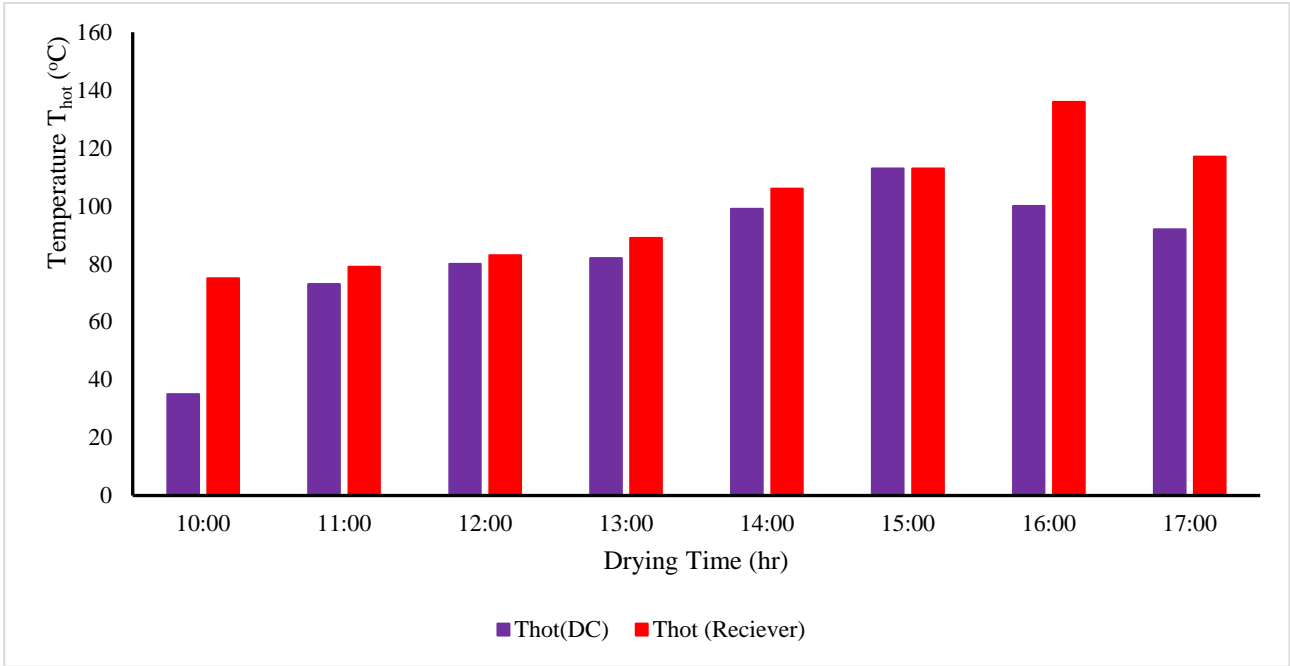
Figure 3. Comparison of receiver temperature and drying chamber temperature per hour

The convective heat transfer rate between the drying chamber and the receiver tube was also taken into account in the thermal study. As seen in Figure 4, there was a greater heat transfer rate per hour in the drying chamber as compared to the receiver tube. This may be explained by the dryer's increased thermal efficiency due to the drying chamber's airflow rate being higher than the receiver tube's HTF flow rate. This is in line with what Tagle-Salazar et al. (2018) reported.
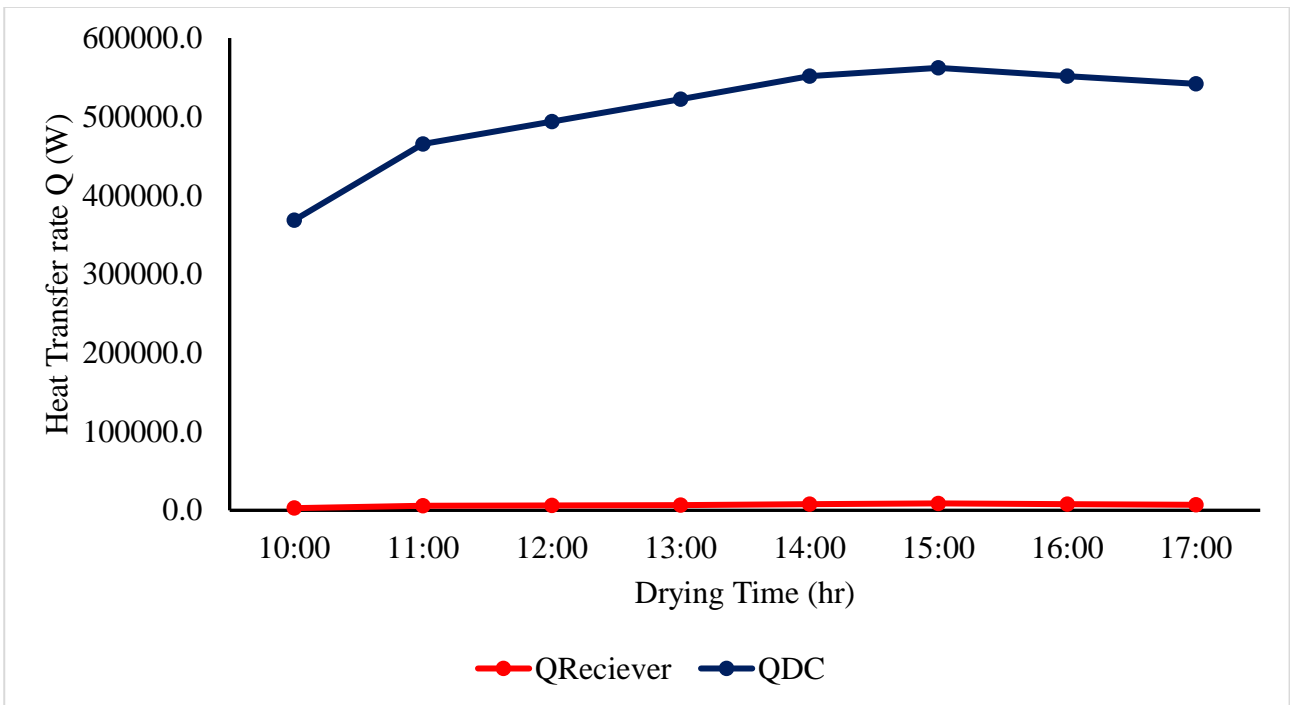
Figure 4. Heat transfer rate in the receiver tube and drying chamber per hour

As the drying temperature increased, the dryer's evaporative heat transfer rate dropped, as shown in Figure 5. This could be due to the reduction in the ginger sample's moisture content placed in the drying chamber. The lower the sample moisture content, the lower the dryer's evaporative heat transfer rate.
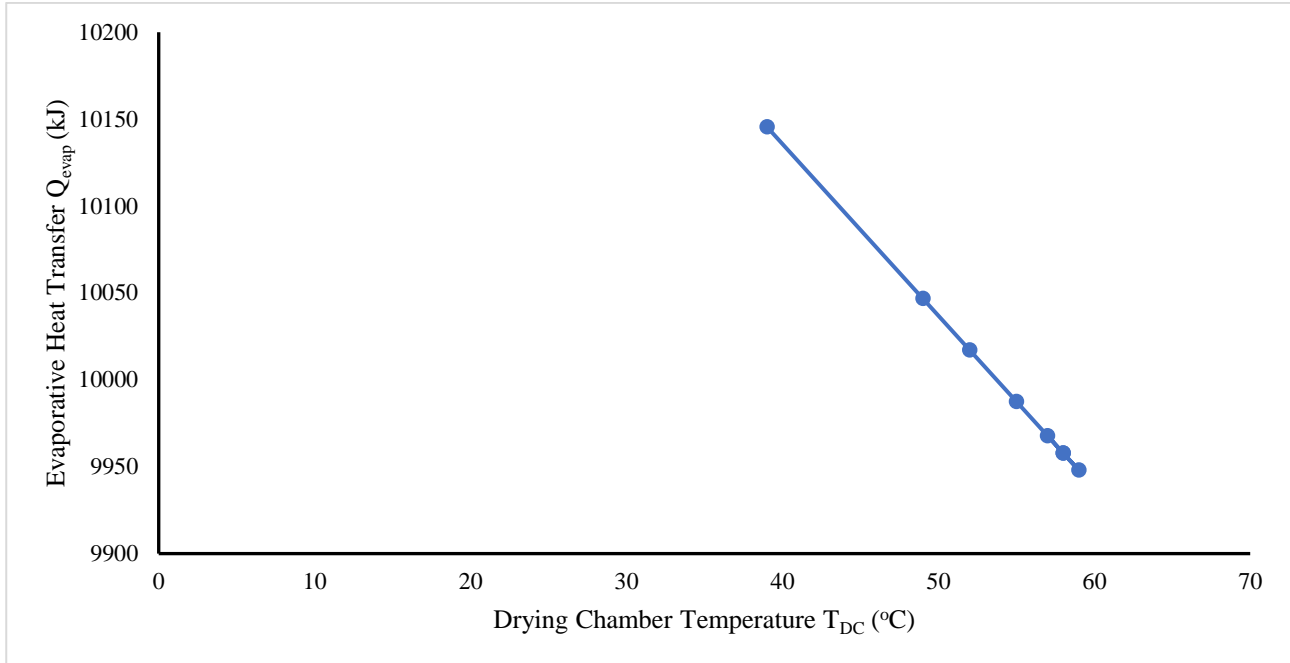
Figure 5. Evaporative heat transfer rate in the drying chamber

4. CONCLUSION

The solar parabolic trough collector (SPTC) dryer was used to dry 5kg of ginger samples, and the rates of heat transmitted in the receiver tube and the drying chamber (DC) and the heat transfer coefficients were examined in this study. The drying experiments were conducted within 7 hours on sunny days throughout February to March. The heat transfer rate delivered to the focus of the concentrating solar collector was 10.692W. Thermal analysis of the hot temperatures of the fluids in the dryer's receiver tube and drying chamber showed that the temperature in the receiver tube was always higher relative to the temperature in the drying chamber per hour. Thermal analysis of the convective heat transfer rate between the receiver tube and the drying chamber also showed a higher heat transfer rate per hour in the drying chamber relative to the receiver tube, thus enhancing the thermal efficiency of the dryer. The coefficients of heat transfer hRec and hDC for the convective heat transmission process in the receiver tube and the drying chamber were determined to be 1372.48W/m.K and 17.60W/m.K respectively. The thermal efficiency of the dryer was found to be 30%, a significant result that underscores the effectiveness of the SPTC dryer. The drying chamber's measured average temperature was 58.5oC, while the ambient temperature was 47.5oC between 15:00hrs and 16:00hrs. The ginger samples had a significant amount of moisture removed due to this notable +11oC temperature differential between the drying chamber and the surrounding air. In contrast to the 23.74% achieved by the open-air solar drying method, the ginger samples' final moisture content of 11.1% can be credited to the effective operation of the SPTC dryer. The design considered is simple and performed better in terms of lower final moisture contents, when compared with the work of Bhavsar and Patel (2023), that used both double air pass collector and phase change materials as thermal storage material, with a final moisture content record of 12.5%.

AUTHOR CONTRIBUTIONS

For the Conceptualization: Ige Bori, Methodology: Jonathan Yisa Jiya, Sunday Bako, Ige Bori, Supervision of fabrication process: Adamu Mohammed Orah, Jonathan Jiya, Muideen Oladele Oyebamiji, Performance evaluation: Ige Bori, Sunday Bako, Manuscript first draft: Adamu Mohammed Orah, Ige Bori, Manuscript review, editing and submission: Ige Bori.

ACKNOWLEDGEMENT

CONFLICT OF INTEREST

The authors declare no conflict of interest.

REFERENCES

Alimohammadi, Z., Samimi Akhijahani, H., & Salami, P. (2020). Thermal analysis of a solar dryer equipped with PTSC and PCM using experimental and numerical methods. *Solar Energy*, *201*, 157-177. https://doi.org/10.1016/j.solener.2020.02.079

Augustus Leon, M., Kumar, S., & Bhattacharya, S. C. (2002). A comprehensive procedure for performance evaluation of solar food dryers. *Renewable and Sustainable. Energy Reviews*, *6*(4), 367-393. https://doi.org/10.1016/S1364-0321(02)00005-9

Bhavsar, H., & Patel, C. M. (2023). Performance analysis of cabinet type solar dryer for ginger drying with & without thermal energy storage material. *Materials Today: Proceedings*, *73*, 595-603. https://doi.org/10.1016/j.matpr.2022.11.280

de Oliveira Siqueira, A. M., Gomes, P. E. N., Torrezani, L., Lucas, E. O., & Pereira, G. M. da C. (2014). Heat Transfer Analysis and Modeling of a Parabolic Trough Solar Collector: An Analysis. *Energy Procedia* ,*57*, 401-410. https://doi.org/10.1016/j.egypro.2014.10.193

Ebewele, R. O., & Jimoh, A. A. (1981). Feasibility Study of Kaduna State Ginger Processing Industry. Nigeria: Ahmadu Bello University Chemical Engineering Consultant.

Ekechukwu, O. V. (2010, May 16-19). *Solar Drying Technology: An Overview*. In: Proceedings of the FUTO Alternative Energy Conference, Federal University of Technology, Owerri, Nigeria.

Ekechukwu, O. V., & Norton, B. (1999). Review of solar-energy drying systems II: an overview of solar drying technology. *Energy Conversion and Management*, *40*(6), 615-655. https://doi.org/10.1016/S0196-8904(98)00093-4

Fumen, G. A., Yiljep, Y. D., & Ajisegiri, E. S. A. (2003, September 8-12). *Survey of ginger processing and drying methods in Nigeria: A case of Southern Kaduna of Kaduna State*. In: Proceedings of the Fourth International Conference and 25th AGM of the Nigeria Institution of Agricultural Engineers, Damaturu, Nigeria.

Gucheman (2010). Focusing on Export of Ginger (Zingiber Officinale) Produce from Nigeria. (Accessed: 27/11/2015) http://www.gucheman.com/mitsue-stanley

Gyawali, M., Acharya, A., Adhikari, T., Dahal, K., Kafle, B., Kim, D. H., & Kafle, S. (2022). A mixed-mode ginger and turmeric solar dryer: design, simulation, biochemical and performance analysis. *BIBECHANA*, *19*(1-2), 40-60. https://doi.org/10.3126/bibechana.v19i1-2.46386

Lienhard IV, J. H., & Lienhard V, J. H. (2002). *A heat transfer Textbook* (3rd Ed.). Massachusetts: Phlogiston Press.

Njoku, B. O. Mbanaso, E. N. A., & Asumugha, G. N. (1995). Ginger Production by Conventional and Tissue Culture Techniques. Dolf publishers, Owerri, Imo State, pp. 9-12.

Okafor, G. I. (2002). Processing and Utilization of Ginger: Effect of Processing Methods on Product Quality, and its Application in Fruit and Bakery Products. TWAS-CSRI postdoctoral fellowship research report, CFTRI, India (2002), p. 32

Ouedraogo, G. W. P., Kaboré, B., Magloire Pakouzou, B., Sawadogo, K., Zoma, V., Kam, S., & Joseph Bathiébo, D. (2021). Thermal Analysis of a Solar Dryer with Parabolic Collector. *Science Research*, *9*(6), 127-131. https://doi.org/10.11648/j.sr.20210906.15

Padilla, R. V., Demirkaya, G., Goswami, D. Y., Stefanakos, E., & Rahman, M. M. (2011). Heat transfer analysis of parabolic trough solar receiver. *Applied Energy*, *88*(12), 5097-5110. https://doi.org/10.1016/j.apenergy.2011.07.012

Plappally, A. K., & Lienhard V, J. H. (2012). Energy requirements for water production, treatment, end use, reclamation, and disposal. *Renewable and Sustainable Energy Reviews*, *16*(7), 4818-4848. https://doi.org/10.1016/j.rser.2012.05.022

Rulazi, E. L., Marwa, J., Kichonge, B., & Kivevele, T. (2023). Development and Performance Evaluation of a Novel Solar Dryer Integrated with Thermal Energy Storage System for Drying of Agricultural Products. *ACS Omega*, *8*(45), 43304-43317. https://doi.org/10.1021/acsomega.3c07314

Sansaniwal, S. K., & Kumar, M. (2015). Analysis of ginger drying inside a natural convection indirect solar dryer: An experimental study. *Journal of Mechanical Engineering and Sciences*, *9*, 1671-1685. http://doi.org/10.15282/jmes.9.2015.13.0161

Sharma, A., Chen, C. R., & Vu Lan, N. (2009). Solar-energy drying systems: A review. *Renewable and Sustainable Energy Reviews*, *13*(6-7), 1185-1210. https://doi.org/10.1016/j.rser.2008.08.015

Shukla, S., & Sahu, Prof. H. S. (2019). Analysis of Heat Transfer for Solar Air Heater – A Perspective View. *International Journal of Trend in Scientific Research and Development*, *3*(2), 1054-1058. https://doi.org/10.31142/ijtsrd21612

Tagle-Salazar, P. D., Nigam, K. D. P., & Rivera-Solorio, C. I. (2018). Heat transfer model for thermal performance analysis of parabolic trough solar collectors using nanofluids. *Renewable Energy*, *125*, 334-343. https://doi.org/10.1016/j.renene.2018.02.069

Tiris, C., Tiris, M., & Dincer, I. (1995). Investigation of the thermal efficiencies of a solar dryer. *Energy Conversion and Management*, *36*(3), 205-212. https://doi.org/10.1016/0196-8904(94)00051-Z

Youcef-Ali, S., Messaoudi, H., Desmons, J. Y., Abene, A., & Le Ray, M. (2001). Determination of the average coefficient of internal moisture transfer during the drying of a thin bed of potato slices. *Journal of Food Engineering*, *48*(2), 95-101. https://doi.org/10.1016/S0260-8774(00)00123-0

Machine Learning Approaches for Differentiating Thermophilic and Mesophilic Lipases

Nurcan VARDAR-YEL[1*]

[1] Altınbaş University, Vocational School of Health Services, Medical Laboratory Techniques Program, İstanbul, Türkiye

Keywords	Abstract
Mesophilic Thermophilic Lipase Machine Learning	Differentiating thermophilic proteins from their mesophilic counterparts presents a significant challenge, yet achieving this distinction is crucial for the rational design of more stable proteins. In this study, a systematic analysis was performed on 3,715 unreviewed bacterial lipase enzymes obtained from the UniProt web server and screened according to their Tm values. Furthermore, a tree was constructed using the MEGA 11 program and lipase sequences from different families were selected. The final dataset consists of 88 mesophilic proteins and 123 thermophilic proteins were used. We found that Ile, Leu, aliphatic index, hydropathy, aliphatic amino acids, hydrophobic amino acids, tiny amino acids, and small amino acids are the key variables distinguishing thermophilic from mesophilic lipase proteins. These findings suggest that amino acid composition is crucial in differentiating these two groups.

1. INTRODUCTION

One of the features that make protein thermostability an important issue in both biochemical and biotechnological research is its ability to increase reaction rate and efficiency at high temperatures. (Rigoldi et al., 2018). Unfortunately, few proteins are stable at high temperatures, resulting in the need for accurate methods to predict whether a protein is globally thermodynamically stable from its primary sequence. The key elements that are correlated with high protein thermostability are salt bridges, dipeptide patterns, ion pairs, and amino acid content (Kumar et al., 2000; Gromiha et al., 2002; Lin & Chen, 2011; Ahmed et al., 2022). For example, thermophilic proteins often have higher levels of residues like Ile, Arg, Glu, Lys, and Pro, while Ser, Asn, Gln, Thr, and Met are lower compared to mesophilic proteins (Gromiha & Suresh, 2008; Feng et al., 2020). As a result, the identification of protein thermostability-driving forces in sequence features have been utilized to develop methods which predict thermophilic properties from amino acid coupling patterns and dipeptide compositions (Das & Gerstein, 2000; Liang et al., 2005; Zhang & Fang, 2006a; 2006b; 2007; Lin & Chen, 2011). Additionally, single point mutations also modulate thermostability, which emphasizes the need for careful sequence analysis (Capriotti et al., 2004; 2005; Gromiha, 2007; Montanucci et al., 2008; Tian et al., 2010; Li et al., 2012; Marabotti et al., 2021). Numerous structural characteristics, including disulfide bonds, hydrophobic interactions, pi-pi and cation-pi interactions and salt bridges are fundamental in defining thermostability and should be evaluated when designing proteins and enzymes (Loladze et al., 1999; Razvi & Scholtz 2006; Strickler et al., 2006; Vardar-Yel et al., 2024). Thermophilic organisms are useful for industrial applications because they produce high-functioning enzymes and can withstand temperatures between 41°C and 122°C (Das & Gerstein, 2000). Proteins that are particularly thermophilic were searched for to identify the contributions of sequence and structural features associated with thermostability (Mrozek & Małysiak-

Mrozek, 2011; Dao et al., 2017; Charoenkwan et al., 2021). Increased levels of non-polar amino acids in thermostable enzyme structures are believed to enhance the hydrophobicity of proteins, which attracts them to the catalytic pocket and increases their rigidity. Furthermore, thermostable enzymes exhibit a greater number of hydrophobic and disulfide linkages. These characteristics facilitate conformational folding and provide enzymes with a more rigid structure (Li et al., 2005; Hussian et al., 2023). Additionally, stronger electrostatic contacts in a protein's outer regions lead to more ion pair interactions when amino acids have a greater charge. In thermophilic proteins as opposed to their mesophilic counterparts, these electrostatic forces play a larger role in maintaining the stability of the folded form. This shows that in order to keep proteins stable at high temperatures, electrostatic interactions are essential (Dominy et al., 2004; Hussian et al., 2023). In their study, Zhou et al. (2008) examined the differences in amino acid composition between mesophilic and thermophilic proteins, highlighting key features in thermophilic proteins such as increased hydrophobicity, decreased uncharged polar residues, elevated charged and aromatic residues, specific amino acid coupling patterns, and distinct amino acid preferences (Zhou et al., 2008). Other studies have isolated specific patterns of cavity dipeptide specific to thermophilic protein sequences (Wijma et al., 2013). This level of comparison is highly helpful since it provides detailed information about the major impacts of packing, hydrophobic interactions, disulfide bridges, and aromatic interactions on protein thermostability (Christensen & Kepp, 2013). The ability to distinguish between mesophilic and thermophilic proteins with accuracy has been demonstrated by machine learning methods such as support vector machines, decision trees, neural networks, and logistic functions (Ding et al., 2004; 2010; Zhang & Fang, 2006a; 2006b; 2007; Gromiha & Suresh, 2008; Lin & Chen, 2011; Ai et al., 2012; Albayrak & Sezerman, 2012; Chakravorty et al., 2017; Feng et al., 2020). In this study, two distinct algorithms, Support Vector Machines (SVM) and Decision Trees, have been used to analyze the differences between thermophilic and mesophilic lipase enzymes from bacteria that are unreviewed from the Uniprot database.

2. MATERIAL AND METHOD

2.1. The Dataset

3715 unreviewed bacterial lipase enzymes from the Uniprot web server were screened for Tm values. Redundancies were removed using the CD-HIT (Cluster Database at High Identity with Tolerance) algorithm and erroneous sequences were eliminated. Furthermore, a tree was constructed using the MEGA 11 program and lipase sequences from different families were selected (Tamura et al., 2021). The final dataset consists of 88 mesophilic proteins and 123 thermophilic proteins were used. Lipase enzymes screened from different thermophilic and mesophilic bacterial sources are listed in Table 1. Enzymes from various thermophilic and mesophilic bacterial organisms, identified under names such as triacylglycerol lipase, monoacylglycerol lipase, carboxylesterase, esterase, alpha/beta hydrolase, lipase, and Lipase EstA, were screened (Table 1). A comprehensive analysis was conducted on 38 distinct variables, including amino acid composition, sequence length, aliphatic index, instability index, net charge, hydropathy, molecular weight (Da), and the number of various amino acid groups. These groups consisted of charged (DEKHR), aliphatic (ILV), aromatic (FHWY), polar (DERKQN), neutral (AGHPSTY), hydrophobic (CFILMVW), positively charged (KRH), negatively charged (DE), as well as tiny (ACDGST), small (EHILKMNPQV), and large (FRWY) amino acids. Data was collected from the COPid-Calculate Composition of Whole Protein and Tm Predictor website (Kumar et al., 2008; Ku et al., 2009).

2.2. Cross Validation

The correctness of results determines the success of systems developed for any objective. The most common approach is k-fold cross-validation (Alataş et al., 2023). Here, an original dataset is divided into k subsets of roughly equal size. The system trains itself in k-1 subsets and tests itself in the remaining one. The hypothesis' validity is indicated by the average of the error value throughout the course of these k experiments.

For this experiment, a value of k equated to 5 was used as the size of the dataset was of medium scale, and more than that would have required additional computational power. This method has been used to compensate for the inadequacies of the test-train split method. Finally, the dataset was split into a training and testing set in a 7:3 ratio. The accuracy derived from this split was measured and the results were compared with those developed by the cross-validation method.

Table 1. *Lipase enzymes screened from different thermophilic and mesophilic bacterial sources*

Thermophilic protein	Source	Mesophilic protein	Source
Triacylglycerol lipase	*Geobacillus sp.* GHH01	Triacylglycerol lipase	*Streptococcus downei*
Triacylglycerol lipase	*Geobacillus stearothermophilus*	Triacylglycerol lipase	*Cupriavidus necator*
Triacylglycerol lipase	*Geobacillus thermoleovorans*	Lipase	*Rhodococcus* sp.
Monoacylglycerol lipase	*Thermus thermophilus*	Lipase1	*Streptomyces ambofaciens*
Monoacylglycerol lipase	*Geobacillus thermopakistaniensis*	Triacylglycerol lipase	*Mycolicibacterium fortuitum*
Monoacylglycerol lipase	*Chloroflexi bacterium*	Lipase EstA	*Limnohabitans* sp.
Monoacylglycerol lipase	*Thermoflexales bacterium*	Triacylglycerol lipase	*Pseudomonas fluorescens*
Carboxylesterase	*Geobacillus stearothermophilus*	Esterase/lipase lipF	*Mycobacterium tuberculosis*
Carboxylesterase	*Geobacillus thermodenitrificans*	Monoacylglycerol lipase	*Bacillus* sp.
Carboxylic ester hydrolase	*Geobacillus thermodenitrificans*	Lipase2	*Staphylococcus aureus*
GDSL-family esterase	*Geobacillus thermodenitrificans*	Lipase	*Pseudomonas* sp.
Triacylglycerol lipase	*Geobacillus thermoleovorans (Bacillus thermoleovorans)*	Triacylglycerol lipase	*Escherichia coli*
Triacylglycerol lipase	*Geobacillus zalihae*	Triacylglycerol lipase	*Staphylococcus epidermidis*
Esterase-lipase	*Thermochaetoides thermophila*	Triacylglycerol lipase	*Staphylococcus* sp.
Monoacylglycerol lipase	*Thermoflexales bacterium*	Triacylglycerol lipase	*Bacillus anthracis*
Monoacylglycerol lipase	*Thermosipho africanus*		
Alpha/beta hydrolase	*Aquifex aeolicus*		

2.3. Machine Learning Algorithms

The algorithms used for the study were chosen in relation to the dataset used, looking for algorithms that work well with the limited amount of data available, can deal effectively with imbalanced class problems, are robust to outliers, and can be applied to a large number of data structures. Furthermore, the machine learning applications used in this study were implemented using scikit-learn, a free software library for the Python programming language. The anaconda suite (https://www.anaconda.com/download), which includes a chosen collection of Python packages, is the simplest method to obtain Python, the core packages, and Jupyter Notebook.

2.3.1. Random Forest (RF)

Numerous tree classifiers are used in combined machine learning methods like Random Forest. Each tree votes once for the popular class, and the final classification result is calculated by adding up all of the tree classifier ratings. The characteristics of RF are high classification accuracy, robust tolerance to noise and outliers, and resistance to overfitting (Liu et al., 2012).

2.3.2. Decision Tree (DT)

Due to their structured, reliable and user-friendly nature, Decision Trees have been widely applied to both classification and regression problems. Other reasons supporting its popularity are its interoperability with other systems and the existence of understandable concepts. DTs are constructed in a top-down manner: they start with the most general data and are progressively specialized. The methodology applied for their construction and the starting point for tree building are the main factors taken into account in the application of DTs (Kotsiantis, 2013)

2.3.3. Performance Evaluation Metrics

Table 2 displays the confusion matrix of the multiple categorization results.

Table 2. *The confusion matrix of the outcomes. Cell1=TN: True Negative; Cell2=FP: False Positive; Cell3=FN: False Negative; Cell4=TP: True Positive*

Predicted Values	0: Mesophilic	TN Cell 1	FP Cell 2
	1: Thermophilic	FN Cell 3	TP Cell 4
		0: Mesophilic	1: Thermophilic
	Real Values		

As a result, Equations 1-4 were used to calculate a range of metrics that were utilized to assess the performance of the algorithm. These metrics include accuracy, precision (P), recall (R), the F-score, and the area under the ROC curve (AUC).

$$Accuracy = \frac{TN + TP}{TP + TN + FP + FN} \tag{1}$$

$$P = \frac{TP}{TP + FP} \tag{2}$$

$$R = \frac{TP}{TP + FN} \tag{3}$$

$$F\ score = \frac{2(R * P)}{R + P} \tag{4}$$

In this context, the terms TP, FP, TN, and FN represent specific classifications within the data analysis process. TP means true positives, where thermophiles are positively identified as thermophiles. FP or false positives are where mesophiles are classified as thermophiles. TN stands for true negatives, which are the number of mesophiles correctly identified as mesophiles, while FN stands for false negatives, which are cases where thermophiles are classified as mesophiles. The AUC was calculated from a plot of the relationship between the false positive rate on the x-axis and the true positive rate on the y-axis. This allows a visual and quantitative assessment of how well the algorithm discriminates between thermophiles and mesophiles according to the thresholds used for classification.

3. RESULTS AND DISCUSSION

This study compared the effectiveness of different machine learning techniques in discriminating between mesophilic and thermophilic proteins with amino acid composition as the main feature for classification. Several criteria were used to compare the performance of machine learning algorithms in this study: precision (%), accuracy (%), F1 score (%), recall (%), AUC values (%) and corresponding ROC curves (%). In this study, multiclass classification was used to predict the dependent variables of mesophilic and thermophilic bacterial lipase groups. These two dependent variables were treated as two different outputs. The confusion matrices obtained from both machine learning methods are shown in Figure 1. The first and fourth cells show the correctly predicted values, while the remaining cells show the incorrectly predicted values.
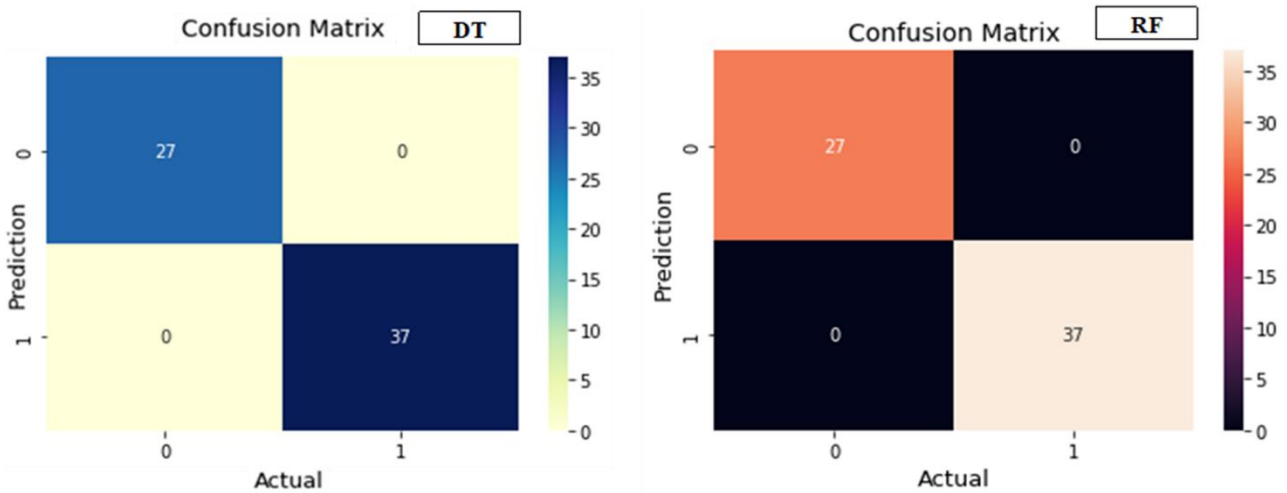
Figure 1. *Confusion matrix for RF and DT used in the prediction of mesophilic and thermophilic bacterial lipase enzyme.*

The results demonstrated that the majority of machine learning techniques exhibited an accuracy of approximately 99.5% in differentiating between thermophilic and mesophilic proteins. The results demonstrated that the random forest and decision tree approaches exhibited a high degree of similarity in this regard. Therefore, based on this finding, there is no significant difference in the performance of any of these machine learning algorithms.

ROC curves offer a very insightful approach for excellent visualization of the balance of sensitivity and specificity in a model with respect to the total predictive power of the classes presented in the model. For multi-class classification problems, an ROC curve can be constructed as a one-to-one approximation where each class is compared with all other classes. Thus, the number of ROC curves is equal to the number of classes used. In this case, the structure of the ROC curve was the same for both classes, indicating equal prediction performance. Figure 2 shows the ROC curve of DT.
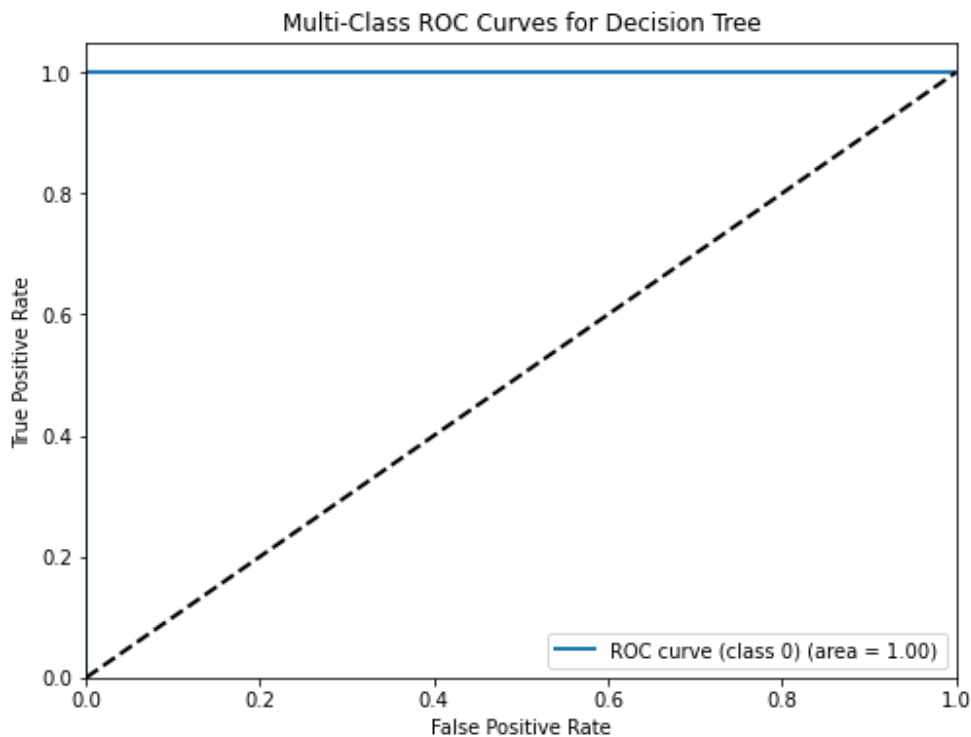
Figure 2. *ROC curve for classes 0, 1 and 2 with Decision Tree algorithms.*

A widely adopted approach for assessing model performance in classification tasks is the evaluation of accuracy, largely due to its simplicity and intuitive interpretation. Accuracy is calculated by taking the ratio of the total number of correct predictions to the overall number of predictions made by the model. Following the training-test split (7:3) and 10-fold cross-validation for the RF and DT algorithms, the accuracy values were calculated as 1. Following the evaluation of the ROC curve, AUC, and accuracy metrics, it was concluded that the Random Forest (RF) and Decision Tree (DT) algorithms demonstrated the highest effectiveness for machine learning classification of class 0 and class 1, corresponding to mesophilic and thermophilic categories within the dataset. As a result, the link between the features in the dataset and the living temperature classes were analyzed using the RF approach since both algorithms gave similar results. The feature importance values of the final model are shown in Figure 3.
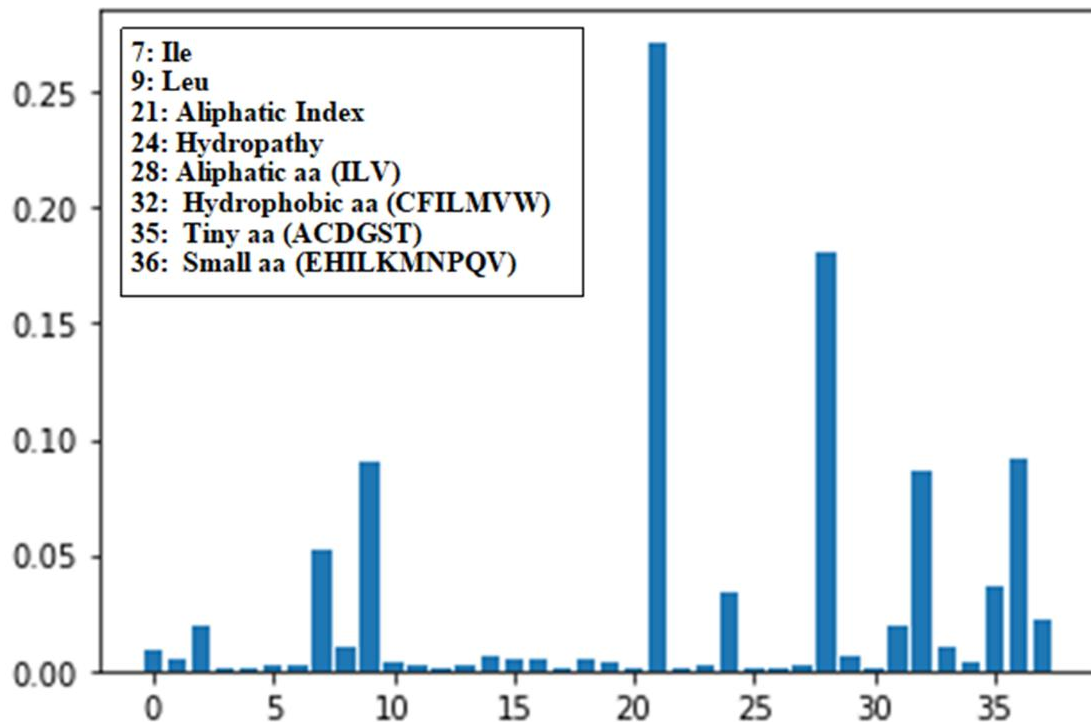
Figure 3. *Feature importance results for Random Forest*

The prediction involving thermophilic bacterial lipase enzymes resulted in the aliphatic index having the most dominant percentage contribution. This is probably to be expected because most of the analyzed protein data is normally filtered according to this parameter and thus proves that machine learning serves as a self-correcting function that produces excellent results. The aliphatic amino acids (I, L, V) also emerge as crucial, ranking second with a value of 18%. The association between the aliphatic index and aliphatic amino acid composition with thermostability is well-documented in numerous studies (Ikai, 1980; Ponnuswamy et al., 1982; Pack & Yoo, 2004; Wu et al., 2009; Sahoo et al., 2019).

Furthermore, the importance of hydrophobic amino acids (CFILMVW), Leu amino acid, and small amino acids (EHILKMNPQV) were found to be 8.7%, 9%, and 9%, respectively. Factors with lesser effects included Ile amino acid at 5.1%, hydropathy at 3.7%, and tiny amino acids (ACDGST) at 3.8%. These findings are consistent with those of previous studies. For example, Lin and Chen (2011) observed that individual amino acids such as glutamic acid, lysine and isoleucine play a crucial role in contributing to the thermostability of proteins. Indeed, related to this view, their research has shown that such amino acids significantly influence the structure of thermophilic proteins, allowing them to maintain their functionality at relatively high temperatures. In another study, Gromiha and Suresh (2008) compared the amino acid compositions between mesophilic and thermophilic proteins. They showed that compared to mesophilic proteins, thermophilic proteins had more charged residues such as Lys, Arg, Glu and Asp. They also found that among the hydrophobic residues, especially Val and Ile were more abundant in thermophilic proteins than in mesophilic proteins.

Numerous studies have emphasized that amino acid composition, dipeptide composition are distinguishing factor between thermophilic, mesophilic and psychrophilic proteins (Ding et al., 2004; 2010; Dominy et al., 2004; Zhang & Fang, 2006a; 2006b; 2007; Gromiha & Suresh, 2008; Lin & Chen, 2011; Ai et al., 2012; Albayrak & Sezerman, 2012; Chakravorty et al., 2017; Feng et al., 2020; Wang et al., 2020; Charoenkwan et al., 2021). However, a major difference in our study lies in the fact that we concentrated specifically on mesophylic and thermophilic bacterial-originated lipase proteins and non-protein types in general. In this way, our focused approach enabled an exploration that is going to be much more in-depth with regard to certain property and characteristic changes experienced by lipase proteins within these different thermal environments.

The results obtained in the lipase proteins and in the machine-learning studies need to strongly correlate with each other, which generally goes on to show that the mesophilic, thermophilic, and psychrophilic proteins present a high correlation among them. It can thus be stated that the data in question provides compelling evidence of the precision and reliability of the results obtained. The fact that our findings are consistent with some of the most advanced computational studies validates our methodology of research and further testifies to how amino acid compositions feature prominently in dictating thermal stability and functionality in lipase enzymes.

4. CONCLUSION

This study identifies the effective factors distinguishing mesophilic and thermophilic bacterial lipase enzymes. The results revealed that both machine learning algorithms demonstrated nearly identical accuracy, achieving a ten-fold cross-validation accuracy of 99% on a dataset consisting of 3,715 unreviewed bacterial lipase entries. According to feature importance results, Ile, Leu, aliphatic index, hydropathy, aliphatic amino acids, hydrophobic amino acids, tiny amino acids, and small amino acids are variables able to differentiate the thermophilic from the mesophilic lipase proteins. Therefore, this observation may indicate the role of amino acid composition in the differentiation of these two groups. The results obtained align with the results of previous studies comparing mesophilic and thermophilic proteins by machine learning.

ACKNOWLEDGEMENT

CONFLICT OF INTEREST

The author declares no conflict of interest.

REFERENCES

Ahmed, Z., Zulfiqar, H., Tang, L., & Lin, H. (2022). A statistical analysis of the sequence and structure of thermophilic and non-thermophilic proteins. *International Journal of Molecular Sciences*, *23*(17), 10116. https://doi.org/10.3390/ijms231710116

Alataş, E., Tanyıldızı Kökkülünk, H., Tanyıldızı, H., & Alcın, G. (2023). Treatment prediction with machine learning in prostate cancer patients. *Computer Methods in Biomechanics and Biomedical Engineering*, 1–9. https://doi.org/10.1080/10255842.2023.2298364

Albayrak, A., & Sezerman, U. O. (2012). Discrimination of thermophilic and mesophilic proteins using reduced amino acid alphabets with n-grams. *Current Bioinformatics*, *7*(2), 152-158. https://doi.org/10.2174/157489312800604435

Ai, H., Zhang, L., Zhang, J., Cui, T., Chang, A. K., & Liu, H. (2018). Discrimination of thermophilic and mesophilic proteins using support vector machine and decision tree. *Current Proteomics*, *15*(5), 374-383. https://doi.org/10.2174/1570164615666180718143606

Capriotti, E., Fariselli, P., & Casadio, R. (2004). A neural-network-based method for predicting protein stability changes upon single point mutations. *Bioinformatics*, *20*, 63-68. https://doi.org/10.1093/bioinformatics/bth928

Capriotti, E., Fariselli, P., & Casadio, R. (2005). I-Mutant2.0: predicting stability changes upon mutation from the protein sequence or structure. *Nucleic Acids Research*, *33*(2), 306-310. https://doi.org/10.1093/nar/gki375

Chakravorty, D., Faheem Khan, M., & Patra, S. (2017). Thermostability of proteins revisited through machine learning methodologies: From nucleotide sequence to structure. *Current Biotechnology*, *6*(1), 39-49. https://doi.org/10.2174/2211550105666151222183232

Charoenkwan, P., Chotpatiwetchkul, W., Lee, V. S., Nantasenamat, C., & Shoombuatong, W. (2021). A novel sequence-based predictor for identifying and characterizing thermophilic proteins using estimated propensity scores of dipeptides. *Scientific Reports*, *11*(1), 23782. https://doi.org/10.1038/s41598-021-03293-w

Christensen, N. J., & Kepp, K. P. (2013). Stability mechanisms of a thermophilic laccase probed by molecular dynamics. *PloS One*, *8*(4), e61985. https://doi.org/10.1371/journal.pone.0061985

Dao, F.-Y., Yang, H., Su, Z.-D., Yang, W., Wu, Y., Hui, D., Chen, W., Tang, H., & Lin, H. (2017). Recent advances in conotoxin classification by using machine learning methods. *Molecules*, *22*(7), 1057. https://doi.org/10.3390/molecules22071057

Das, R., & Gerstein, M. (2000). The stability of thermophilic proteins: a study based on comprehensive genome comparison. *Functional & Integrative Genomics*, *1*(1), 76-88. https://doi.org/10.1007/s101420000003

Ding, Y., Cai, Y., Zhang, G., & Xu, W. (2004). The influence of dipeptide composition on protein thermostability. *FEBS Letters*, *569*(1-3), 284-288. https://doi.org/10.1016/j.febslet.2004.06.009

Ding, Y. R., Cai, Y. J., Sun, J., & Xu, B. W. (2010). Identifying the mesophilic and thermophilic proteins from their amino acid composition with ν-support vector machines. *Journal of Algorithms & Computational Technology*, *4*(3), 335-348. https://doi.org/10.1260/1748-3018.4.3.335

Dominy, B. N., Minoux, H., & Brooks III, C. L. (2004). An electrostatic basis for the stability of thermophilic proteins. *Proteins: Structure, Function, and Bioinformatics*, *57*(1), 128-141. https://doi.org/10.1002/prot.20190

Feng, C., Ma, Z., Yang, D., Li, X., Zhang, J., & Li, Y. (2020). A method for prediction of thermophilic protein based on reduced amino acids and mixed features. *Frontiers in Bioengineering and Biotechnology*, *8*, 285. https://doi.org/10.3389/fbioe.2020.00285

Gromiha, M. M. (2007). Prediction of protein stability upon point mutations. *Biochemical Society Transactions*, *35*(6), 1569-1573. https://doi.org/10.1042/BST0351569

Gromiha, M. M., & Suresh, M. X. (2008). Discrimination of mesophilic and thermophilic proteins using machine learning algorithms. *Proteins: Structure, Function, and Bioinformatics*, *70*(4), 1274-1279. https://doi.org/10.1002/prot.21616

Gromiha, M. M., Thomas, S., & Santhosh, C. (2002). Role of cation-π interactions in the stability of thermophilic proteins. *Preparative Biochemistry and Biotechnology*, *32*(4), 355-362. https://doi.org/10.1081/PB-120015459

Hussian, C. H. A. C., & Leong, W. Y. (2023). Thermostable enzyme research advances: a bibliometric analysis. *Journal of Genetic Engineering and Biotechnology*, *21*(1), 37. https://doi.org/10.1186/s43141-023-00494-w

Ikai, A. (1980). Thermostability and aliphatic index of globular proteins. *The Journal of Biochemistry*, *88*(6), 1895-1898. https://doi.org/10.1093/oxfordjournals.jbchem.a133168

Kotsiantis, S. B. (2013). Decision trees: a recent overview. *Artificial Intelligence Review*, *39*(4), 261-283. https://doi.org/10.1007/s10462-011-9272-4

Ku, T., Lu, P., Chan, C., Wang, T., Lai, S., Lyu, P., & Hsiao, N. (2009). Predicting melting temperature directly from protein sequences. *Computational Biology and Chemistry*, *33*(6), 445-450. https://doi.org/10.1016/j.compbiolchem.2009.10.002 (The Tm Index program is available at http://tm.life.nthu.edu.tw/)

Kumar, S., Tsai, C.-J., & Nussinov, R. (2000). Factors enhancing protein thermostability. *Protein Engineering, Design and Selection*, *13*(3), 179-191. https://doi.org/10.1093/protein/13.3.179

Kumar, M., Thakur, V., & Raghava, G. P. S. (2008). COPid: composition based protein identification. *In Silico Biology*, *8*(2), 121-128. (Calculate Composition of Whole Protein is available at https://webs.iiitd.edu.in/raghava/COPid/whole_comp.html)

Liang, H.-K., Huang, C.-M., Ko, M.-T., & Hwang, J.-K. (2005). Amino acid coupling patterns in thermophilic proteins. *Proteins: Structure, Function, and Bioinformatics*, *59*(1), 58-63. https://doi.org/10.1002/prot.20386

Li, W. F., Zhou, X. X., & Lu, P. (2005). Structural features of thermozymes. *Biotechnology advances*, *23*(4), 271-281. https://doi.org/10.1016/j.biotechadv.2005.01.002

Li, Y., Zhang, J., Tai, D., Russell Middaugh, C., Zhang, Y., & Fang, J. (2012). PROTS: A fragment-based protein thermo-stability potential. *Proteins: Structure, Function, and Bioinformatics*, *80*(1), 81-92. https://doi.org/10.1002/prot.23163

Lin, H., & Chen, W. (2011). Prediction of thermophilic proteins using feature selection technique. *Journal of Microbiological Methods*, *84*(1), 67-70. https://doi.org/10.1016/j.mimet.2010.10.013

Liu, Y., Wang, Y., & Zhang, J. (2012, September 14-16). *New machine learning algorithm: Random Forest*. In: B. Liu, M. Ma, & J. Chang (Eds.), Proceedings of the Information Computing and Applications (pp. 246-252), Chengde, China. https://doi.org/10.1007/978-3-642-34062-8_32

Loladze, V. V., Ibarra-Molero, B., Sanchez-Ruiz, J. M., & Makhatadze, G. I. (1999). Engineering a thermostable protein via optimization of charge−charge interactions on the protein surface. *Biochemistry*, *38*(50), 16419-16423. https://doi.org/10.1021/bi992271w

Marabotti, A., Scafuri, B., & Facchiano, A. (2021). Predicting the stability of mutant proteins by computational approaches: An overview. *Briefings in Bioinformatics*, *22*(3), bbaa074. https://doi.org/10.1093/bib/bbaa074

Montanucci, L., Fariselli, P., Martelli, P. L., & Casadio, R. (2008). Predicting protein thermostability changes from sequence upon multiple mutations. *Bioinformatics*, *24*(13), i190-i195. https://doi.org/10.1093/bioinformatics/btn166

Mrozek, D., & Małysiak-Mrozek, B. (2011). An improved method for protein similarity searching by alignment of fuzzy energy signatures. *International Journal of Computational Intelligence Systems*, *4*(1), 75-88. https://doi.org/10.2991/ijcis.2011.4.1.7

Pack, S. P., & Yoo, Y. J. (2004). Protein thermostability: structure-based difference of amino acid between thermophilic and mesophilic proteins. *Journal of Biotechnology*, *111*(3), 269-277. https://doi.org/10.1016/j.jbiotec.2004.01.018

Ponnuswamy, P. K., Muthusamy, R., & Manavalan, P. (1982). Amino acid composition and thermal stability of proteins. *International Journal of Biological Macromolecules*, *4*(3), 186-190. https://doi.org/10.1016/0141-8130(82)90049-6

Razvi, A., & Scholtz, J. M. (2006). Lessons in stability from thermophilic proteins. *Protein Science*, *15*(7), 1569-1578. https://doi.org/10.1110/ps.062130306

Rigoldi, F., Donini, S., Redaelli, A., Parisini, E., & Gautieri, A. (2018). Engineering of thermostable enzymes for industrial applications. *APL Bioengineering*, *2*(1), 011501. https://doi.org/10.1063/1.4997367

Sahoo, R. K., Sanket, A. S., Gaur, M., Das, A., & Subudhi, E. (2019). Insight into the structural configuration of metagenomically derived lipase from diverse extreme environment. *Biocatalysis and Agricultural Biotechnology*, *22*, 101404. https://doi.org/10.1016/j.bcab.2019.101404

Strickler, S. S., Gribenko, A. V., Gribenko, A. V., Keiffer, T. R., Tomlinson, J., Reihle, T., Loladze, V. V., & Makhatadze, G. I. (2006). Protein stability and surface electrostatics: a charged relationship. *Biochemistry*, *45*(9), 2761-2766. https://doi.org/10.1021/bi0600143

Tamura, K., Stecher, G., & Kumar, S. (2021). MEGA11: molecular evolutionary genetics analysis version 11. *Molecular Biology and Evolution*, *38*(7), 3022-3027. https://doi.org/10.1093/molbev/msab120

Tian, J., Wu, N., Chu, X., & Fan, Y. (2010). Predicting changes in protein thermostability brought about by single- or multi-site mutations. *BMC Bioinformatics*, *11*, 1. https://doi.org/10.1186/1471-2105-11-370

Vardar-Yel, N., Tütüncü, H. E., & Sürmeli, Y. (2024). Lipases for targeted industrial applications, focusing on the development of biotechnologically significant aspects: A comprehensive review of recent trends in protein engineering. *International Journal of Biological Macromolecules*, *273*, 132853. https://doi.org/10.1016/j.ijbiomac.2024.132853

Wang, X.-F., Gao, P., Liu, Y.-F., Li, H.-F., & Lu, F. (2020). Predicting thermophilic proteins by machine learning. *Current Bioinformatics*, *15*(5), 493-502. https://doi.org/10.2174/1574893615666200207094357

Wijma, H. J., Floor, R. J., & Janssen, D. B. (2013). Structure-and sequence-analysis inspired engineering of proteins for enhanced thermostability. *Current Opinion in Structural Biology*, *23*(4), 588-594. https://doi.org/10.1016/j.sbi.2013.04.008

Wu, L.-C., Lee, J.-X., Huang, H.-D., Liu, B.-J., & Horng, J.-T. (2009). An expert system to predict protein thermostability using decision tree. *Expert Systems with Applications*, *36*(5), 9007-9014. https://doi.org/10.1016/j.eswa.2008.12.020

Zhang, G., & Fang, B. (2006a). Application of amino acid distribution along the sequence for discriminating mesophilic and thermophilic proteins. *Process biochemistry*, *41*(8), 1792-1798. https://doi.org/10.1016/j.procbio.2006.03.026

Zhang, G., & Fang, B. (2006b). Discrimination of thermophilic and mesophilic proteins via pattern recognition methods. *Process Biochemistry*, *41*(3), 552-556. https://doi.org/10.1016/j.procbio.2005.09.003

Zhang, G., & Fang, B. (2007). LogitBoost classifier for discriminating thermophilic and mesophilic proteins. *Journal of Biotechnology*, *127*(3), 417-424. https://doi.org/10.1016/j.jbiotec.2006.07.020

Zhou, X.-X., Wang, Y.-B., Pan, Y.-J., & Li, W.-F. (2008). Differences in amino acids composition and coupling patterns between mesophilic and thermophilic proteins. *Amino Acids*, *34*(1), 25-33. https://doi.org/10.1007/s00726-007-0589-x

An Analysis of Fatal Construction Machinery Accidents in Türkiye between 2013 and 2018

Ali Kaan ÇOKTU[1,2*]   Fatih EREL[1,2]   Hasan Basri ULAŞ[3]

[1] *Gazi University, Ankara, Türkiye*
[2] *Ministry of Labour and Social Security, Directorate General of Occupational Health and Safety, Türkiye*
[3] *Gazi University, Faculty of Technology, Manufacturing Engineering, Ankara, Türkiye*

Keywords	Abstract
Construction Machinery Work Accident Occupational Safety and Health	Accidents involving construction machinery often result in injury and fatality. In this study, fatal work accidents involving construction machinery, which play an important role in the execution of work, in Türkiye between 2013 and 2018 are examined. The research utilized notifications made by workplaces to the Social Security Institution (SSI). The parameters used to statistically analyze the data were classified into three categories: accident time, the victim, and the cause of the accident. Based on the available data, the highest number of accidents occurred in 2017 with 23.03%, while September recorded the highest number of monthly accidents at 10%. Trucks were the most frequent construction machinery involved, accounting for 51.18% of all cases, and traffic accidents ranked first as the leading cause at 28.06%. This highlights the necessity of considering traffic accidents in workplace safety statistics and emphasizes the importance of traffic safety in ensuring occupational safety and health. Notably, truck accidents comprise more than half of all fatal incidents involving the 16 types of construction machinery analyzed.

1. INTRODUCTION

The use of machinery in workplaces today provides significant time and labor savings. If the tasks performed by machinery were to be carried out by human labor, work losses and accidents would be much more frequent. According to Law No. 6331 on Occupational Safety and Health, published in the Official Gazette No. 28339 on 30.06.2012, a "work accident" is defined as an incident that occurs in the workplace or due to the execution of work, causing death or physical and mental disability. The use of inappropriate equipment, failure to maintain, repair, and inspect equipment on time, failure to take necessary precautions in the work environment, and workers' negligent behavior cause accidents in workplaces. In Türkiye, the Social Security Institution (SSI) collects data on work accidents. According to Article 14 of Law No. 6331 on Occupational Safety and Health, work accidents must be reported to the SSI by the employer within three working days following the accident (Occupational Safety and Health Law, 2012).

According to construction accident statistics published by the Construction Department of the Sectoral Risk Management and Statistics Directorate of the Directorate General of Occupational Health and Safety (DGOHS), based on SSI (2024) accident data, 64,184 insured workers in the construction sector in Türkiye experienced work accidents in 2022. Of these accidents, 422 people—27.8% of workers who died in work accidents in Türkiye in 2017—lost their lives. An examination of 2,578 fatal work accidents that occurred between 2013 and 2017 revealed that 44.4% of the accidents were due to falls from heights, 17.8% were due

to traffic and machinery accidents, 6% were electrical accidents, and 5% were caused by equipment (DGOHS, 2019).

Gürcanlı et al. (2008) found that 42.9% of the 5,289 fatal and injury-causing accidents that occurred in construction areas in Türkiye between 1969 and 1999 were due to falls, 12.2% were due to contact with electricity, 10.5% were due to injuries from falling objects, 8.6% were due to machinery accidents, and 7.0% were caused by traffic accidents on-site.

In the United States, 5,250 fatal accidents were recorded in 2018, with transportation ranking first in all work-related fatalities with 2,080 accidents. Following transportation, the construction sector drew attention as the industry with the highest number of accidents. Drivers and truck drivers were the occupational group with the highest number of fatalities, with 966 fatal accidents. The highest data within this group was for heavy truck and trailer drivers, with 831 fatal accidents (BLS, 2023).

The Occupational Safety and Health Administration (OSHA) in the United States (OSHA, 2020) has categorized construction accidents into four main groups; falls, electrocution, being struck by or caught in/between objects and being struck by a vehicle.

Construction machinery is defined in the Highways Traffic Law No. 2918, published in the Official Gazette No. 18195 on 18.10.1983, as motor vehicles equipped with various equipment according to their work purpose and used in the work and services of institutions such as agriculture, industry, public works, and national defense. These vehicles are not used for transporting people, animals, or loads on highways. Some examples of construction machinery include asphalt plant machines, backhoe loaders, concrete pumps, concrete spraying machines, concrete batching machines, concrete mixers, bulldozers, pavers, graders, and personnel and load elevators. The required G-type license codes for construction machinery used on highways, including trucks, are expressed under code 105.15.

Sadeghpour and Teizer (2009) noted that many activities conducted on construction sites inherently carry risks, and due to the limited space in which construction machinery operates and the fast-paced nature of work, further complexities arise, as machinery may be constrained by materials, equipment, and temporary structures or buildings.

Ruff (2004) stated that blind spots in construction machinery pose significant risks and that in highway construction in the United States, 22 deaths occur annually due to risks associated with such construction machinery. Poor visibility, low light, and sudden movements are among the sources of risk. These risks increase particularly when vehicles are reversing or maneuvering in confined spaces. To reduce and eliminate these risks, sensor and camera systems, warning systems, signalers wearing appropriate personal protective equipment, and proper signage are used. Proper planning and operator training are also effective in reducing risks.

Hinze et al. (2005) noted that injuries resulting from being caught in or between objects are mostly caused by vehicle overturning or moving equipment parts.

Three main legal regulations exist for operator training in machinery. According to Article 11 of the Regulation on Safety and Health Requirements for the Use of Work Equipment (2013), published in the Official Gazette No. 28628 on April 25, 2013, the employer is required to ensure that workers responsible for using work equipment receive training on the risks that may arise from the use of this equipment and how to avoid them. If the equipment is to be used on the road, it will be subject to the Highways Traffic Law. According to Article 42 of this Law, "the training of machine operators and the certification of those who succeed in the exam will be provided by the Ministry of National Education or institutions authorized by the Ministry of National Education. The procedures and principles related to the operation of these institutions, as well as the training programs to be implemented, will be determined by the Ministry of National Education" (Highways Traffic Law, 1983). Finally, according to Article 5 of the Regulation on Vocational Training for Workers to Be Employed in Hazardous and Highly Hazardous Works (2013), published in the Official Gazette No. 28706 on July 13, 2013, it is mandatory for workers employed in jobs listed in the Annex-1 schedule to receive vocational

training before being hired. The use of construction machinery is particularly mentioned in the construction section of the Annex-1 schedule. Article 6(c) of the same regulation mandates the obtaining of an operator's certificate and driver's license issued by the Ministry of National Education or institutions authorized by the Ministry for the certification of the requirement specified in Article 5. It is important to regularly update the knowledge of machine operators and instill in them the habit of complying with precautions to reduce accidents. Operators should know the capacities, limits, and operational capabilities of the machines they use.

When examining the studies in the literature, it is observed that data related to the number of accidents in sectoral statistics are utilized. No direct study on accidents caused by construction machinery has been identified in Türkiye, but it has been mentioned in studies focusing on work accidents in the construction sector. This study examines accidents caused by machinery between 2013 and 2018 in Türkiye in detail, focusing on the time of the accident, the victim affected by the accident, and the cause of the accident.

2. MATERIAL AND METHOD

2.1. Data Collection and Evaluation

A system for reporting accidents that occur in the course of work is used by employers, and the accident reporting form of the SSI has been standardized according to the European Statistics on Accidents at Work (ESAW) methodology and published under code SSI-032 on the SSI website (Work Accident Occupational Disease E-Notification, 2023). Accordingly, when an accident occurs, the employer must report information about the workplace as well as the insured person's date of birth, nationality, gender, employment date, employment status, whether they have received vocational and occupational safety and health training, the activity they were performing at the time of the accident, the equipment/tool they were using, the event causing the injury, the type of injury, the cause of the accident, and the equipment/tool causing the accident. The accident data collected is published annually on the website of the SSI (Social Security Institution). These accidents are classified according to the codes of the classification of economic activities (NACE), the number of days of incapacity for work, gender, provinces, type of insurance, and the event causing the injury. Furthermore, accident frequency and severity rates are also presented. Within the scope of this study, data reported to the SSI between 2013 and 2018 was obtained from the Occupational Safety and Health Information Management System, and document analysis, one of the qualitative research methods, was used. In this context, the data related to accidents involving construction machinery was separated and classified according to the type of construction machinery. The classified data was evaluated using the SPSS 26 statistical package program. After obtaining the classification, descriptive statistical techniques were used to analyze the dataset in detail. Descriptive statistics were determined according to the parameters specified in the ESAW methodology. The ESAW methodology adopts an approach that facilitates categorization when analyzing accidents and aims to provide comparable data across European Union countries (Eurostat, 2012). Descriptive statistics are important as they provide summary information about the sample and observations made. In this study, univariate frequency analysis was used to better understand and interpret the dataset. Ethical standards for research and publication were adhered to in this study.

2.2. Variables

The data categories included in the ESAW methodology were considered as the main variables in this study. These are: the day, month, year, and time of the accident; the age, gender, marital status, and educational background of the insured affected by the accident; whether they had received occupational safety and health and vocational training; the construction machinery that caused the accident; the event that caused the accident; the event that caused the injury; and a description of the accident site. The parameters related to the timing of the accident are presented in Table 1.

To describe the demographic characteristics of workers who lost their lives in construction machinery-related work accidents, six parameters were used to obtain descriptive statistics regarding the victims. These parameters include educational background, occupational safety and health training, vocational training, gender, marital status, and age. The educational background was categorized into eight subcategories: illiterate, literate, primary school, middle school, high school, vocational school (associate degree), university

(bachelor's degree), and postgraduate. Age ranges were classified into five subcategories. The details of these parameters are presented in Table 2.

Table 1. Parameters and Subcategories Related to the Timing of Accidents

Variable	Subcategory
Accident Year	2018, 2017, 2016, 2015, 2014, 2013
Accident Month	January, February, March, April, May, June, July, August, September, October, November, December
Accident Day	Monday, Tuesday, Wednesday, Thursday, Friday, Saturday, Sunday
Accident Time	00:01-07:59, 08:00-11:59, 12:00-15:59, 16:00-19:59, 20:00-00:00

Table 2. Parameters Related to the Victims and Subcategories

Variable	Subcategory
Educational Background	Illiterate, Literate, Primary School, Middle School, High School, Vocational School (Associate Degree), University (Bachelor's Degree), Postgraduate
OSH Training	Yes, No
Vocational Training	Yes, No
Gender	Female, Male
Marital Status	Single, Married, Divorced, Unknown
Age	15-24, 25-32, 33-40, 41-50, 51+

The parameters regarding the work equipment involved in the accident, the event causing the accident, the event leading to injury, and the location of the accident are shown in Table 3. The event causing injury and the accident location were used in alignment with ESAW (European Statistics on Accidents at Work) definitions. The categorization of equipment and the events causing accidents was carried out by two Occupational Safety and Health Experts with over 10 years of experience.

Table 3. Accident-Related Parameters

Variable	Subcategory
Equipment	Water tanker, Asphalt equipment, Concrete mixer, Concrete pump, Pipe layer, Tractor-trailer, Garbage truck, Bulldozer, Excavator, Grader, Jumbo, Truck, Snow blower, Loader, Vacuum truck, Road marking machine
Event Causing Accident	Trapped-Crushed Under, Traffic accidents, Overturning, Impact from equipment parts, Falling into a ravine/ditch, Falling materials, Heart attack, Squeezed between equipment and a structure, Crushed while reversing, Electric shock
Mode of Injury	Contact with electrical voltage, temperature, hazardous substances, Contact with sharp, hard, or rough material, Crushing/squeezing, Hit by a moving object, Suffocation, burial, entrapment, Horizontal or vertical impact with a stationary object, Health issue (heart attack), Unknown, Other
Accident Location	Inside the workplace, Outside the workplace

3. RESULTS AND DISCUSSION

Between 2013 and 2018, 1358 fatal work accidents involving equipment classified as machinery occurred. Figure 1, 2, and 3 provide information regarding the year, month, and day the accidents took place. In Figure 1, the accident percentage represents the ratio of the number of machinery-related accidents in the given year to the total number of construction machinery accidents between 2013 and 2018. Accordingly, the highest number of accidents occurred in 2017, accounting for 23.03% of the total.
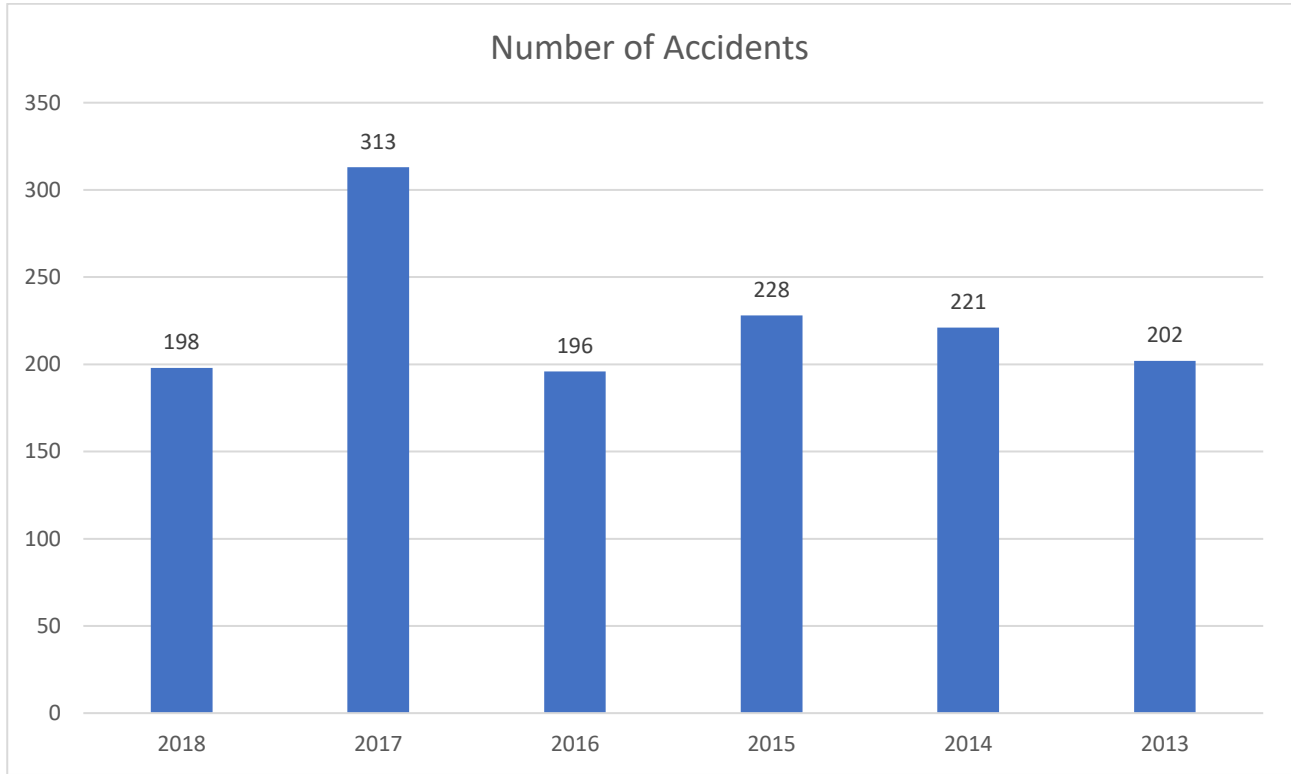
Figure 1. Number of accidents by Year
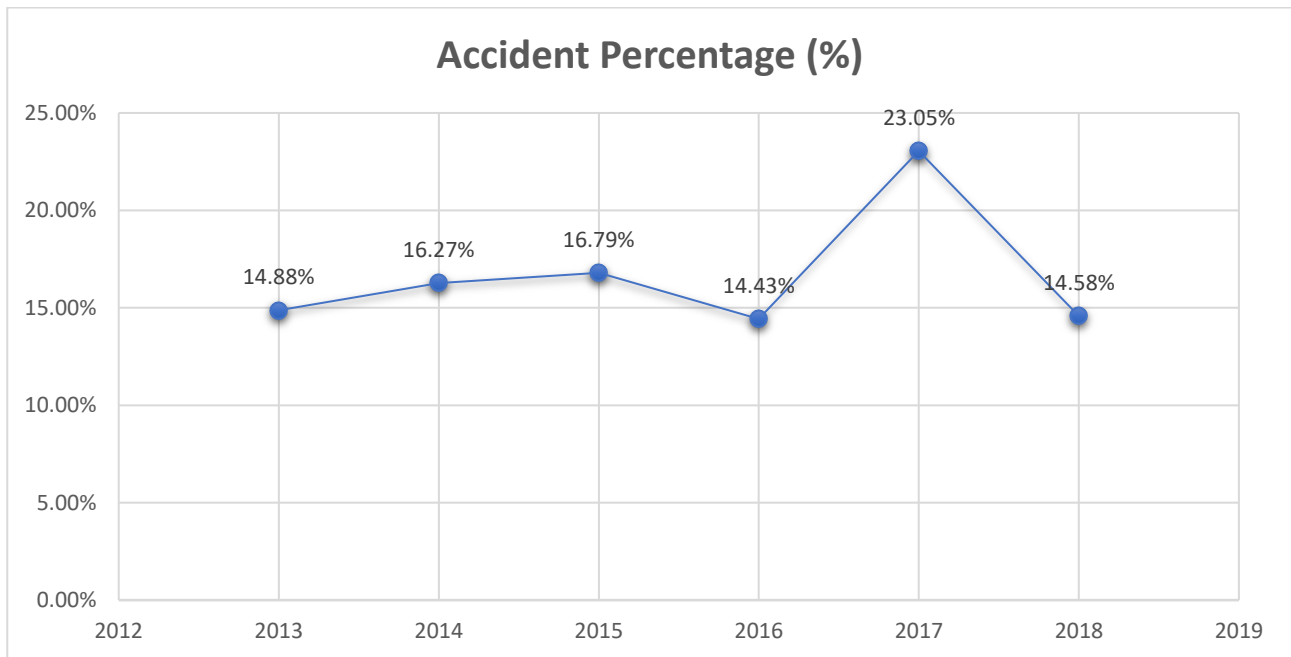
Figure 2. Accident Percantages by Year

Between 2013 and 2018, fatal accidents involving machinery most frequently occurred in September, July, and June. In Figure 3, the accident percentage represents the ratio of accidents in a particular month to the total number of accidents within the relevant time frame.
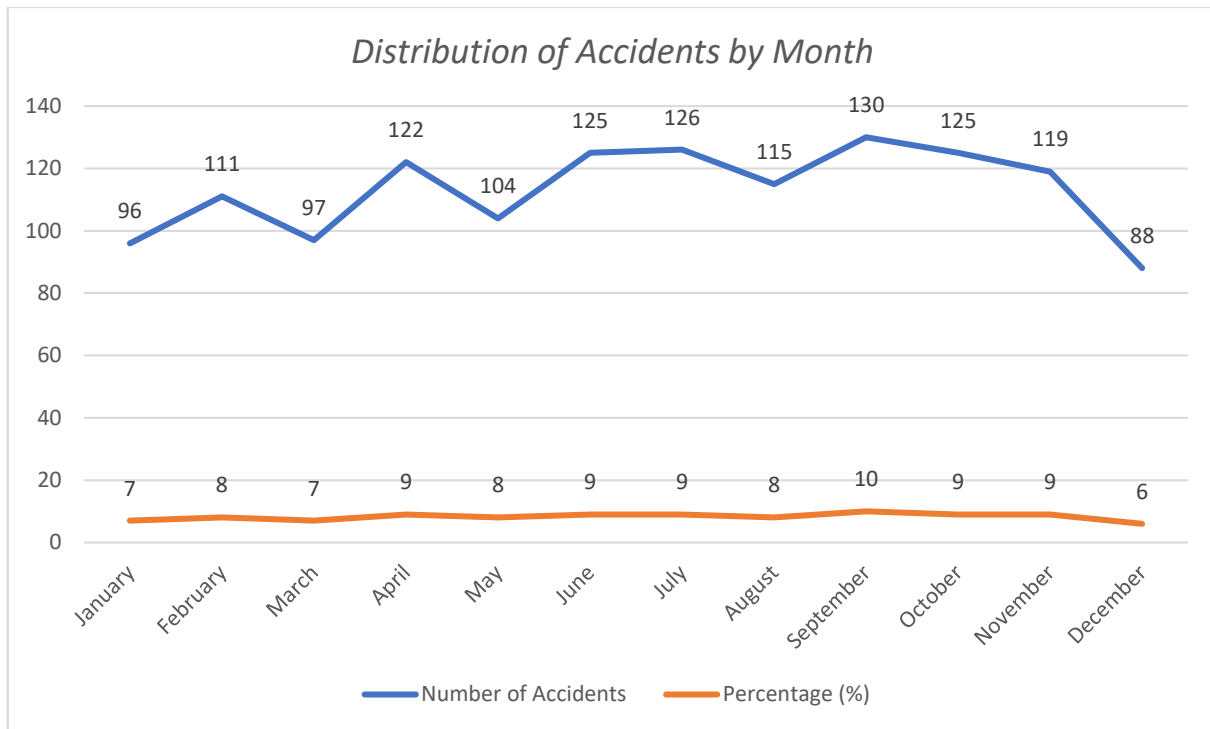
Figure 3. Distribution of Accidents by Month

Figure 4 shows the percentage of accidents by day, indicating the proportion of accidents on a given day relative to the total number of accidents during the specified period. Fatal construction machinery accidents were most frequent on Monday (17.3%), followed by Wednesday (16.1%) and Tuesday (15.5%).
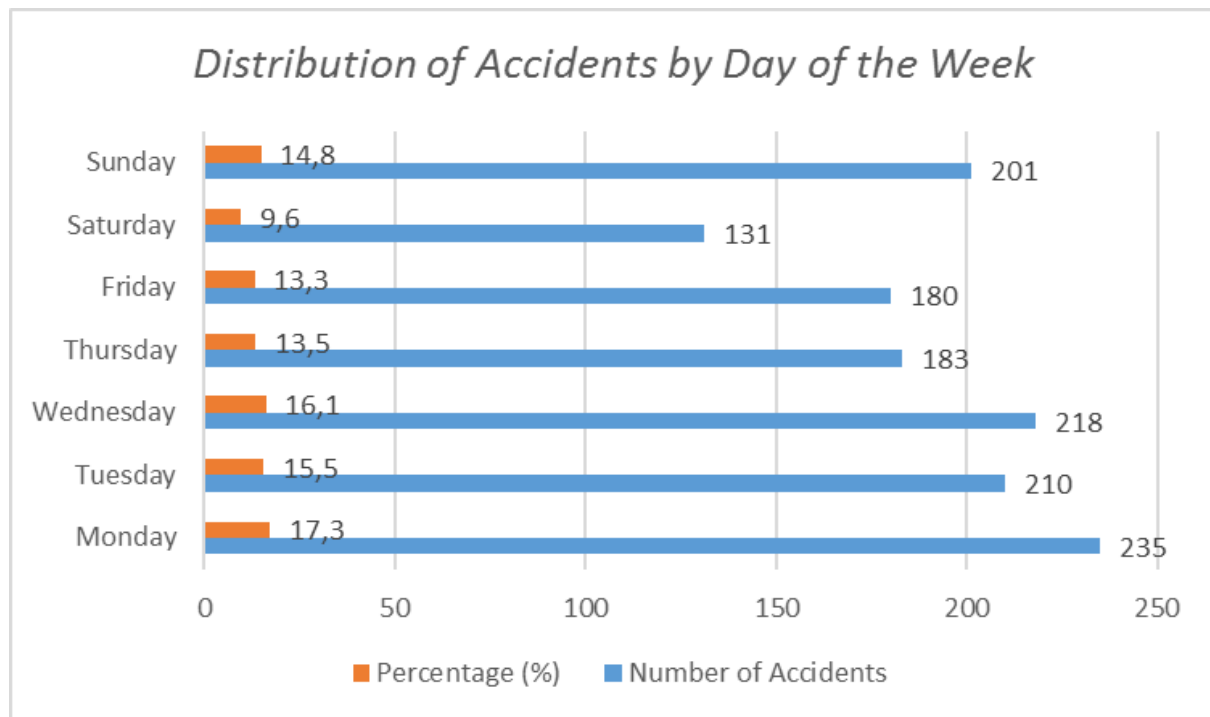
Figure 4. Distribution of Accidents by Day of the Week

Between 2013 and 2018, fatal accidents involving construction machinery most commonly occurred between 08:00-11:59 (27.6%) and 12:00-15:59 (23.2%). The fewest accidents (10.3%) occurred between 20:00-00:00.

Workers aged 15-24, including young employees, constituted 6.1% of the victims, while this figure was 12.7% for the 25-32 age group, 18.3% for the 33-40 age group, 30% for the 41-50 age group, and 32.9% for workers over the age of 51.

Among the deceased workers, 13.9% were literate without formal education, 36.9% had completed primary school, 11.3% were graduates of elementary school, 18.4% had completed high school, and 1.1% held a university degree. Details are provided in Figure 5.
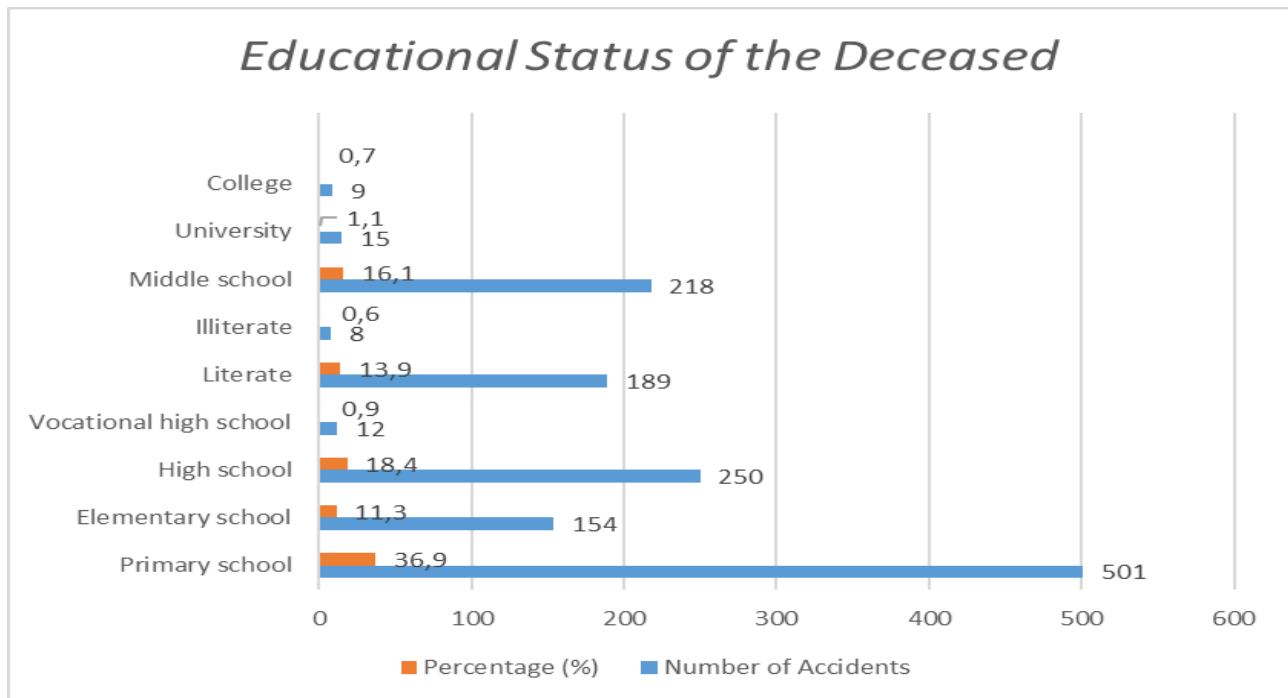
Figure 5.*Educational Status of the Deceased*

Among the deceased workers, 79.2% had received OSH training, while 81% had received vocational training. Of the accidents, 47.86% occurred outside the workplace, and 52.14% occurred within the workplace.

The equipment most frequently involved in fatal accidents included trucks (51.18%), tractors (22.46%), loaders (8.91%), and concrete mixers (3.76%). When fatal accidents involving construction machinery are analyzed by occupation, trucks and tractor + trailer/semi-trailer machines caused the most deaths among operators. Among those who died in tractor + trailer/semi-trailer accidents, 90.49% were operators, while 82.5% of those who died in truck accidents were operators. None of the workers who died in accidents involving jumbo machines, vacuum trucks, or road marking machines were operators. Details are provided in Table 4.

When examining the causes of accidents, it was found that traffic accidents accounted for 28.06% of all cases, making it the leading cause. As shown in Figure 6, other major causes of fatalities include overturning (15.83%), heart attack (13.62%), falling into a cliff/ditch (8.39%), and being crushed under machinery (7.36%).

Construction machinery, widely used in the construction industry, often differs in accident types due to their inherent nature compared to the more common accidents observed in the sector. While falls from heights, electrical hazards, moving machinery parts, and material falls are prominent causes of accidents in the industry, this study identifies traffic accidents, overturning, and heart attacks as the leading causes of fatal accidents (Winge & Albrechtsen, 2018).

Table 4. Distribution of Accidents by Construction Machinery

Equipment	Number of Accidents	Number of Operator Fatalities	Accident Percentage (%)
Water truck	3	2	0,22
Asphalt equipment (finisher, distributor, roller)	16	4	1,18
Concrete mixer	51	38	3,76
Concrete pump	43	9	3,17
Pipe layer	1	1	0,07
Tractor + trailer/semi-trailer	305	276	22,46
Garbage collection truck	45	11	3,31
Bulldozer	10	5	0,74
Excavator	44	23	3,24
Grader	17	9	1,25
Jumbo machine	3	0	0,22
Truck	695	574	51,18
Snow blower	1	1	0,07
Loader	121	46	8,91
Vacuum truck	2	0	0,15
Road marking machine	1	0	0,07
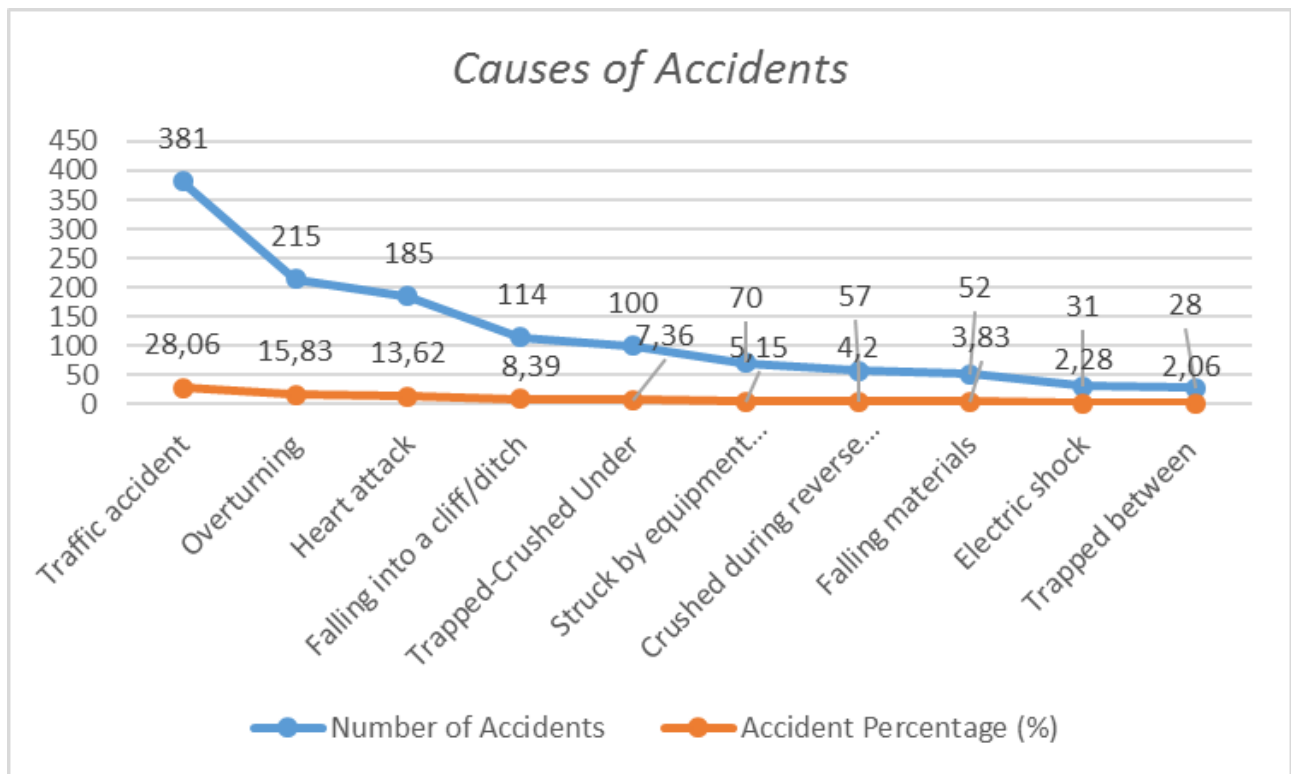
Figure 6. Causes of Accidents

The day with the highest frequency of fatal construction machinery accidents is Monday. This finding can be explained by the "Monday Effect" discussed by Card and McCall (1996), which suggests that employees tend to be less focused and engaged on the first day back at work.

In this study, the percentage of injured employees without occupational safety and health (O) training and vocational training was found to be 20.8% and 19%, respectively. Similar findings were reported by Hoła and Szóstak (2017) for construction accidents in Poland, where 20% of deceased employees lacked general OHS training and 25% had not received job-specific training. These figures underscore the importance of OHS training, vocational education, and on-the-job training in preventing work-related accidents.

Unlike the study by Gürcanlı et al. (2008), which focused specifically on the construction sector, this study includes all traffic accidents involving construction machinery. Gürcanlı's study was sector-specific, while this study aims to highlight the role of equipment in accidents and offer recommendations. The significant number of accidents involving trucks justifies this broader approach. However, it also brings to light the importance of traffic safety alongside occupational safety.

Yakar and Taçgın's study (2012-2016) identified the loader as the most frequently involved equipment in construction accidents, with a 36% share. This study finds that, similarly, trucks and tractors (which include traffic elements) rank highest in accident frequency, followed by loaders and concrete mixers (Yakar & Taçgın, 2019).

Hinze et al. (2005) observed that construction accidents were most frequent in March, April, summer months, and October. This study found that the highest number of fatal accidents occurred in September, with lower numbers in December and March. This pattern is likely related to the slower pace of construction activities during rainy or snowy weather.

Crushing accidents during reverse maneuvers are one of the most common causes of death in construction machinery accidents, apart from traffic accidents. The amendment added on February 18, 2022, to the Regulation on Health and Safety Conditions in the Use of Work Equipment (2013), mandates the use of object detection and warning systems in blind spots where workers can access, the use of markers in areas where such systems are not feasible, and ensuring that no one enters the equipment's operational area.

Teizer et al. (2010) integrated real-time fully automated warning devices for blind spots and pedestrian detection into construction equipment, and the application has been successfully used. Similarly, in the U.S., OSHA regulations (29 CFR 1926.601 and 602) require all trucks and mobile machinery to be equipped with reverse alarms (Kazan, 2013).

Yi et al. (2012) found that using correct color codes enhances visibility, helping older workers better distinguish objects and equipment. In cases where technical measures are inadequate, individuals in the working environment should wear high-visibility clothing (such as vests), and the area should be marked with appropriate colors. According to TS EN ISO 20471, the colors used for high-visibility clothing include fluorescent yellow, fluorescent orange-red, and fluorescent red (TSE, 2013).

4. CONCLUSION

This study examined 1,358 fatal accidents involving construction machinery across Türkiye from 2013 to 2018. The fact that truck accidents account for 51.18% and traffic accidents account for 28.06% of the total highlights the need for further scrutiny of traffic safety and the inclusion of traffic accidents in work accident assessments. The high frequency of accidents involving equipment such as loaders and concrete mixers also indicates the need for both technical and awareness-raising interventions.

Despite the publication of the Occupational safety and health Law in 2012 and the issuance of over thirty regulations, the sector has not yet achieved the desired reduction in work-related accidents. Thus, legislation alone or solutions based solely on field needs are not sufficient; these measures must be supported by safety culture and awareness-raising initiatives. The effectiveness of preventive measures is directly reflected in the reduction of accident numbers. For example, safety training and awareness programs can help workers identify

risks and implement preventive measures. Additionally, regular inspections based on industry or risk, and identifying potential hazards, will contribute to reducing accidents. In the study, the share of fatalities resulting from truck accidents is greater than that of all other equipment combined among the 16 types of construction machinery examined. Developing occupational health and safety policies for trucks has the potential to prevent many deaths, as they account for 51.18% of fatal construction machinery accidents. In this context, it is recommended to implement regulations specifically targeting the transportation, construction, mining, and agriculture sectors.

When examining the root causes of accidents involving trucks, they can be categorized as excessive speed and loss of control, fatigue, vehicle maintenance deficiencies, overloading, infrastructure issues and road conditions, and lack of driver training and experience. Focusing on all these causes and determining, implementing, and monitoring environmental, administrative, and technical measures will be a solution to prevent many fatalities.

AUTHOR CONTRIBUTIONS

In this article, the contributions of the authors are equal.

ACKNOWLEDGEMENT

CONFLICT OF INTEREST

The authors declare no conflict of interest.

REFERENCES

BLS, Bureau of Labor Statistics. (2023, December 19). *National Census of Fatal Occupational Injuries in 2022*. (Accessed: 20/02/2024) https://www.bls.gov/news.release/pdf/cfoi.pdf

Card, D., & McCall, B. P. (1996). Is workers' compensation covering uninsured medical costs? Evidence from the Monday effect. *ILR Review*, *49*(4), 690-706. https://doi.org/10.2307/2524517

DGOHS, Directorate General of Occupational Health and Safety. (2019). *Causes of Fatal Work Accidents*. (Accessed: 10/02/2024) http://www.guvenliinsaat.gov.tr/

Eurostat. (2012, September 5). *European Statistics on Accidents at Work*. (Accessed: 18/07/2024) https://ec.europa.eu/eurostat/documents/3888793/5850901/KS-RA-12-002-EN.PDF.pdf/96c2040e-6dc6-4cfc-9991-7465d160ff97?t=1414780238000

Gürcanlı, E., Müngen, U., & Akad, M. (2008). Construction equipment and motor vehicle-related injuries on construction sites in Turkey. *Journal of Industrial Health*, *46*(4), 375-388. https://doi.org/10.2486/indhealth.46.375

Highways Traffic Law of the Council of Ministers. (1983, October 13). TR Official Gazette, No. 2918. (Accessed: 05/02/2024) https://www.mevzuat.gov.tr/MevzuatMetin/1.5.2918.pdf

Hinze, J., Huang, X., & Terry, L. (2005). The nature of struck-by accidents. *Journal of Construction Engineering and Management*, *131*(2), 262–268. https://doi.org/10.1061/(ASCE)0733-9364(2005)131:2(262)

Hoła, B., & Szóstak, M. (2017). An occupational profile of people injured in accidents at work in the Polish construction industry. *Procedia Engineering*, *208*, 43-51. https://doi.org/10.1016/j.proeng.2017.11.019

Kazan, E. E. (2013). *Analysis of Fatal and Nonfatal Accidents Involving Earthmoving Equipment Operators and On-Foot Workers*. PhD Thesis, Wayne State University Dissertations.

OSHA, Occupational Safety and Health Administration. (2020, August 6). *Top Four Construction Hazards*. (Accessed: 10/02/2024) https://www.osha.gov/Publications/3216-6N-06-english-06-27-2007.html

Occupational Safety and Health Law (2012, June 20). T.R. Official Gazette, 28339. (Accessed: 10/02/2024) https://www.mevzuat.gov.tr/mevzuatmetin/1.5.6331.pdf

Regulation on Health and Safety Conditions in the Use of Work Equipment (2013, April 25). Official Gazette of Turkish Republic, 28628. (Accessed:19/12/2023) https://www.mevzuat.gov.tr/mevzuat?MevzuatNo=18318&MevzuatTur=7&MevzuatTertip=5

Regulation on Vocational Education for Workers in Hazarouds and Very Hazardous Jobs (2013, July). Official Gazette of Turkish Republic, 28706. (Accessed:10/02/2024) https://www.mevzuat.gov.tr/File/GeneratePdf?mevzuatNo=18581&mevzuatTur=KurumVeKurulusYonetmeligi&mevzuatTertip=5

Ruff, T. (2004). Evaluation of Devices to Prevent Construction Equipment Backing Incidents. *SAE Technical Paper* 2004-01-2725. https://doi.org/10.4271/2004-01-2725

Sadeghpour, F., & Teizer, J. (2009, May 20-22). *Modeling three-dimensional space requirements for safe operation of heavy construction equipment*. In: Proceedings of the Fifth International Conference on Construction in the 21st Century: Collaboration and Integration in Engineering, Management and Technology (pp. 740-747), İstanbul, Türkiye.

SSI, Social Security Institution. (2024). *SSI Statistical Years*. (Accessed: 10/02/2024) https://www.SSI.gov.tr/Istatistik/Yillik/fcd5e59b-6af9-4d90-a451-ee7500eb1cb4/

Teizer, J., Allread, B. S., & Mantripragada, U. (2010). Automating the blind spot measurement of construction equipment. *Automation in Construction*, *19*(4), 491-501. https://doi.org/10.1016/j.autcon.2009.12.012

TSE, Turkish Standards Institute. (2013). TS EN ISO 20471 High Visibility Warning Clothing – Test Methods and Specifications. Accepted June 12, 2013.

Winge, S., & Albrechtsen, E. (2018). Accident types and barrier failures in the construction industry. *Safety Science*, *105*, 158-166. https://doi.org/10.1016/j.ssci.2018.02.006

Work Accident and Occupational Disease E-Notification (Employer Notification). (2013). (Accessed:19/12/2023) https://uyg.SSI.gov.tr/IsvBildirimFormu/welcome.do

Yakar, H., & Taçgın, H. (2019). Assessments and recommendations for reducing work accidents in the use of construction machinery. *Mühendis ve Makina*, *60*(697), 303-326. https://doi.org/10.46399/muhendismakina.678023

Yi, J-s., Kim, Y-w., Kim, K-a., & Koo, B. (2012). A suggested color scheme for reducing perception-related accidents on construction work sites. *Accident Analysis and Prevention*, *45*, 185-192. https://doi.org/10.1016/j.aap.2011.04.022

Shielding Behaviour of TiO₂ Reinforced Composite Materials Against 4 MeV Energy Photons and Neutrons

Zübeyde ÖZKAN[1*]   Uğur GÖKMEN[2]

[1] Department of Advanced Technologies, Graduate School of Natural and Applied Sciences, Gazi University, Ankara, Türkiye
[2] Department of Metallurgical and Materials Engineering, Faculty of Technology, Gazi University, Ankara, Türkiye

Keywords	Abstract
Al 6068 TiO₂ Gamma Shielding Fast Neutron Shielding	In order to eliminate or minimize the possible negative effects that may arise due to the use of increased artificial radiation, the radiation permeability properties of Al 6082 alloy material, Al 6082+5% TiO₂, Al+15% TiO₂, and Al 6082+25% TiO₂ metal matrix composite materials against 4 MeV fast neutron and gamma radiation were analyzed in the NGCal program. Mass attenuation coefficient (MAC), mean free path (MFP), linear attenuation coefficient (LAC), tenth value layer (TVL), and half value layer (HVL) and parameters were analyzed for both fast neutron and gamma radiation. As a result of the analysis of 4 MeV energy fast neutron and gamma radiation, the linear attenuation values of the material against both fast neutron and photon increased depending on the increasing reinforcement ratio, while the half value layer, tenth value layer and mean free path values decreased. While the LAC values of Al 6082, Al 6082+5% TiO₂, Al+15% TiO₂, Al 6082+25% TiO₂ materials against fast neutrons vary between approximately 0.00074 cm^{-1} and 0.0173 cm^{-1}, their LAC values against photons vary between 0.084 cm^{-1} and 0.96 cm^{-1}.

Cite

1. INTRODUCTION

With the spread of radiation such as X-ray, electron, beta, proton, gamma, neutron, and alpha, the field of radiation technologies has become increasingly widespread in recent years. Nuclear radiation is used in science, neutron capture therapy, agriculture, medicine, nuclear power plants, industry, and material inspection. Gamma rays are high-energy and intense ionizing radiation because they have short wavelengths and the highest frequencies in the electromagnetic spectrum. Neutrons are uncharged particles that are often used in nuclear reactors to produce nuclear, plant mutation breeding, cancer therapy, neutron imaging, neutron activation analysis, and neutron microscopy. Because they are uncharged, they easily pass through the material and react with the nucleus of the target atom. Although the basic theory of neutron shielding is known, the radiation shielding process is more complex than gamma rays due to its wide energy range. The most frequently used materials for neutron shielding in theoretical and experimental studies conducted by many researchers are; concrete, boron-containing compounds such as polyethylene, gadolinium, cadmium heavy metals, boron, boron nitrides, boron oxide, boron carbide, etc. (Reda & Saled, 2021; Chang et al., 2023). Radiation protective materials are barriers designed to protect against various negative effects caused by radiation. They reduce the amount of dose that individuals are exposed to by attenuating or absorbing radiation.

*Corresponding Author, e-mail: zubeydeozkan@gazi.edu.tr

Among the Mo–TiO$_2$, TiO$_2$, and Co–TiO$_2$ nanocomposite materials produced by Mahmoud et al. (2024) and his colleagues, the Co–TiO$_2$ composite obtained a LAC value of 0.845 cm^{-1} at 0.1 MeV energy and the best shielding material at 0.1 MeV energy was the Co–TiO$_2$ composite. Jandaghian et al. (2024) designed a radiation shield for the ARGUS reactor. They found that the 180 cm thick shielding material they designed from barite concrete was better than the 230 cm thick polyethylene shielding material. In their studies examining the shielding properties of tellurium glasses against 100 kGy and 50 kGy, Juhim et al. (2023) determined that the Al$_2$O$_3$ ceramic added to tellurium increased the MAC value of tellurium glasses. Huo et al. (2024) in their studies investigating the gamma and neutron shielding properties of Sm$_2$O$_3$ filled polymer composite materials, found that Sm$_2$O$_3$ filling improved the radiation shielding properties of the composite material. Aldawood et al. (2024) in study to determine the radiation properties of Ti6Al4V alloy reinforced polymer composite materials with Ti6Al4V alloy reinforcement ratios ranging from 20-50% by weight, found that the LAC value of the material increased with increasing reinforcement ratio. Almuqrin et al. (2023) found that MoO$_3$ reinforced C$_2$H$_4$ composites, which they investigated as an alternative material to concrete, showed better shielding properties than concrete at energies of 32.5 keV, 40.3 keV and 36.5 keV. Akman et al. (2021) as a result of experimental and theoretical gamma analysis of polymer composite materials reinforced with 5-10-15% FeCr, found that the shielding properties of the materials improved with increasing FeCr ratio. Huwayz et al. (2024) in their studies investigating the effect of BaO on the radiation shielding properties of SiO$_2$-B$_2$O$_3$-SrO-ZrO$_2$, found that the materials they produced were better than many conventional concrete materials and recently advanced glasses. Eke (2024), found that as the amount of WO$_3$ in the glass material incremented, the radiation shielding properties improved in his study of the effect of WO$_3$ on ZnO-Na$_2$O-B$_2$O$_3$ glasses. Nafee et al. (2024) investigated the X-ray shielding properties of polymer composite materials with different ZnO and CdO concentrations and found that the TVL value of the composite materials they manufactured was lower than that of gypsum and concrete materials.

In the literature, many different materials are being investigated by many researchers, combining different types of materials (composite, Mg alloys, ceramics, glass, super alloys etc.), to be used as alternative materials to traditional materials. In this study, a composite material was designed to be an alternative material to traditional materials in shielding both fast neutron and gamma radiation. The Al 6082 matrix material in the Al 6xxx series, whose strength value can be increased by adding reinforcement materials, will be reinforced with TiO$_2$ ceramic material at 5%, 15% and 25% and the radiation permeability of the Al 60682 alloy, the tenth value layer (TVL), mass attenuation coefficient (MAC), mean free path (MFP), half value layer (HVL), and linear attenuation coefficient (LAC) parameters in neutron and gamma sources will be examined and analyzed in the NGCal program.

2. MATERIAL AND METHOD

NGCal, an online software (Gökçe et al., 2021), enables the theoretical calculation of MAC, LAC, HVL, TVL, MFP parameters that describe the shielding properties of compounds, elements and composite materials exposed to fast neutrons (4 MeV), thermal neutrons (25.4 meV) and photons (gamma and X-rays). It performs analysis in the range of 0.002 MeV photon energy to 20 MeV photon energy. Thanks to the program, information can be entered without restricting the content of oxides, carbides, etc. found in alloys and composite materials with mixed chemical composition.

The units and formulas of the parameters used are given in Table 1. Information including matrix/reinforcement ratios and codes of the analyzed materials is given in Table 2.

Table 1. Information on shielding parameters

Parameters	Formulas	Units	References
Linear attenuation coefficient (LAC)	$I = I_o \, e^{-\mu x}$	cm^{-1}	(Alım et al., 2022)
Mass attenuation coefficient (MAC)	$\mu_m = \dfrac{\mu}{\rho}$	cm^2/g	(Kılıçoglu & Tekin, 2020)
Half value layer (HVL)	$HVL = \dfrac{ln(2)}{\mu}$	cm	(Kavun et al., 2022)
Tenth value layer (TVL)	$TVL = \dfrac{ln(10)}{\mu}$	cm	(Kılıçoglu & Tekin, 2020)
Mean free path (MFP)	$MFP = \dfrac{1}{\mu}$	cm	(Kavun et al., 2022)

I: Intensity after passing through material
I_o: Initial intensity before entering material
μ: Linear attenuation coefficient
x: Thick of the material
ρ: Density

Table 2. Materials chemical composition

Name of the sample	Composition
T0	Al 6082
T5	Al 6082+5% TiO$_2$
T15	Al 6082+15% TiO$_2$
T25	Al 6082+25% TiO$_2$

3. RESULTS

LAC

Linear attenuation coefficients against photons and fast neutrons with 4 MeV energy The LAC values of the samples coded T0-T5-T15-T25 are given in Figure 1. In the face of a photon with 4 MeV energy; The LAC value of the material has raised because of increasing TiO$_2$. The reason for this is that the higher the density and atomic number of the shielding material, the higher the probability of attenuating the incoming photon. This is because the atomic numbers of the Ti (22) and O (8) atoms that make up the TiO$_2$ ceramic material are higher than the atomic numbers of Al (13), which is the main material of the Al 6082 alloy, and that TiO$_2$ ceramics is higher than Al 6082. A neutron with an energy above 1 MeV is called a fast neutron. Absorption of fast neutrons is practically impossible, therefore, to stop a fast neutron, its energy must first be reduced to the level of thermal neutrons fewer than 0.025 eV (first step - attenuation), and then such thermalized neutrons are captured (second step - absorption) (Piotrowski, 2021). The LAC values of the samples coded T0-T5-T15-T25 in the face of a fast neutron with 4 MeV energy; the LAC value of the material has raised due to increasing TiO$_2$.

This is because fast neutrons interact more with the shielding material as they pass through dense materials, causing them to lose their energy. When the graph is examined, the LAC values of the T0-T5-T15-T25 coded materials against gamma are higher than the LAC value of the fast neutron. The reason for this is; gamma rays are a type of electromagnetic radiation. They lose their energy with the gamma shielding material by photoelectric effect (PE), pair production (PP) and Compton scattering (CS). Neutrons are electrically neutral particles. Neutrons can interact with the shielding material through various processes, these processes include scattering, thermalization, absorption and nuclear reactions. For these reasons, they have different LAC values despite having the same energies.
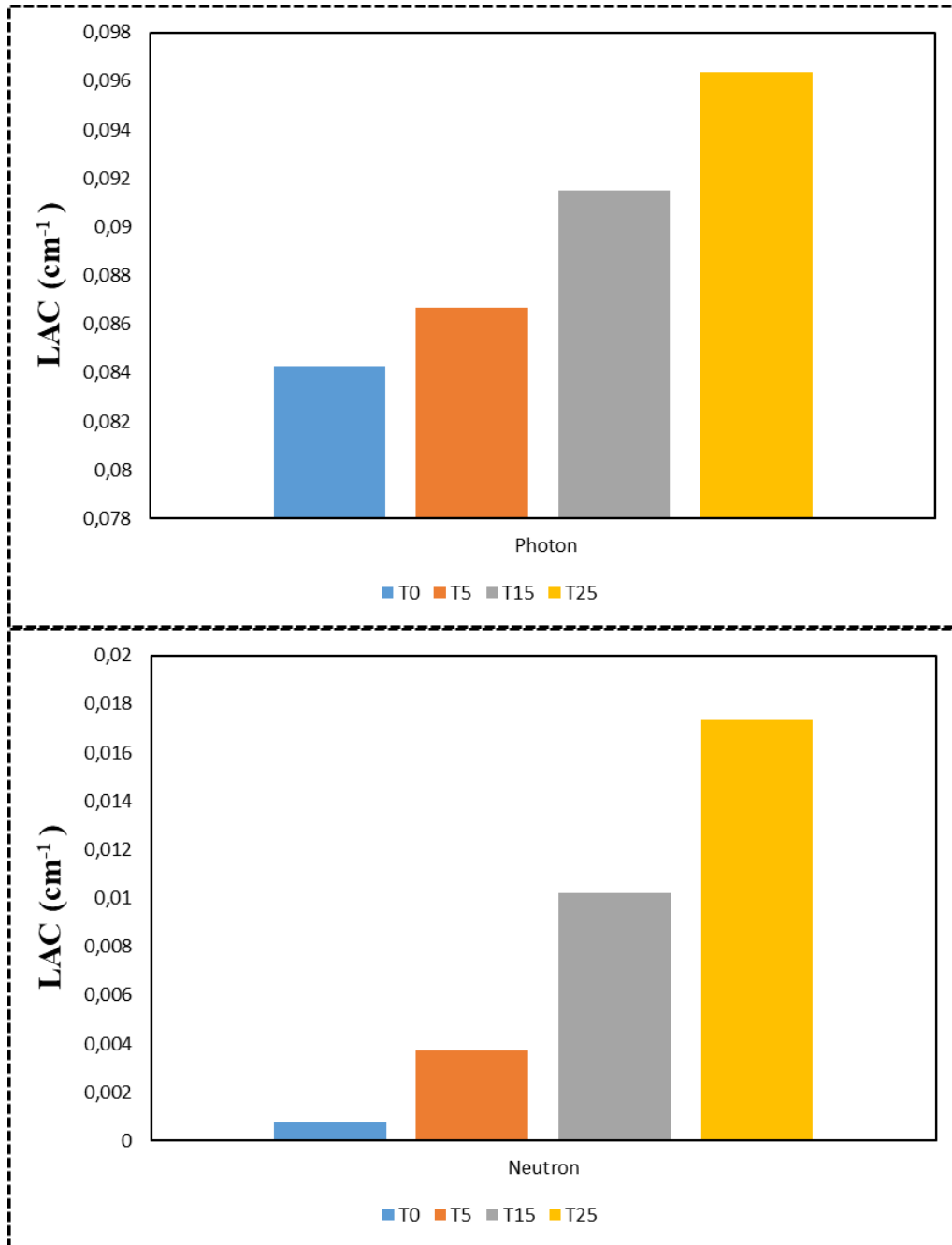
Figure 1. LAC graphs of samples coded T0-T5-T15-T25

MAC

The MAC values of the T0-T5-T15-T25 coded samples against photons and fast neutrons with 4 MeV energy are given in Figure 2. Depending on the decreasing TiO_2 ratio, the MAC values of the materials against both photons and fast neutrons do not decrease. The MAC values of the T0-T5-T15-T25 coded samples against fast neutrons are approximately 0.000274 cm^2/g; 0.00134 cm^2/g; 0.00348 cm^2/g; 0.0056 cm^2/g, respectively. Against photons, they have taken the values of approximately 0.031 cm^2/g; 0.03111 cm^2/g; 0.03114 cm^2/g; 0.03118 cm^2/g, respectively. Because the LAC values of the materials against photons are higher than the LAC values against neutrons, the MAC values of photons are higher. The addition of TiO_2 to Al 6082 caused increases in the density values of composite materials. The higher the number of atoms per unit volume in materials with high density, the higher the possibility of fast neutrons interacting.
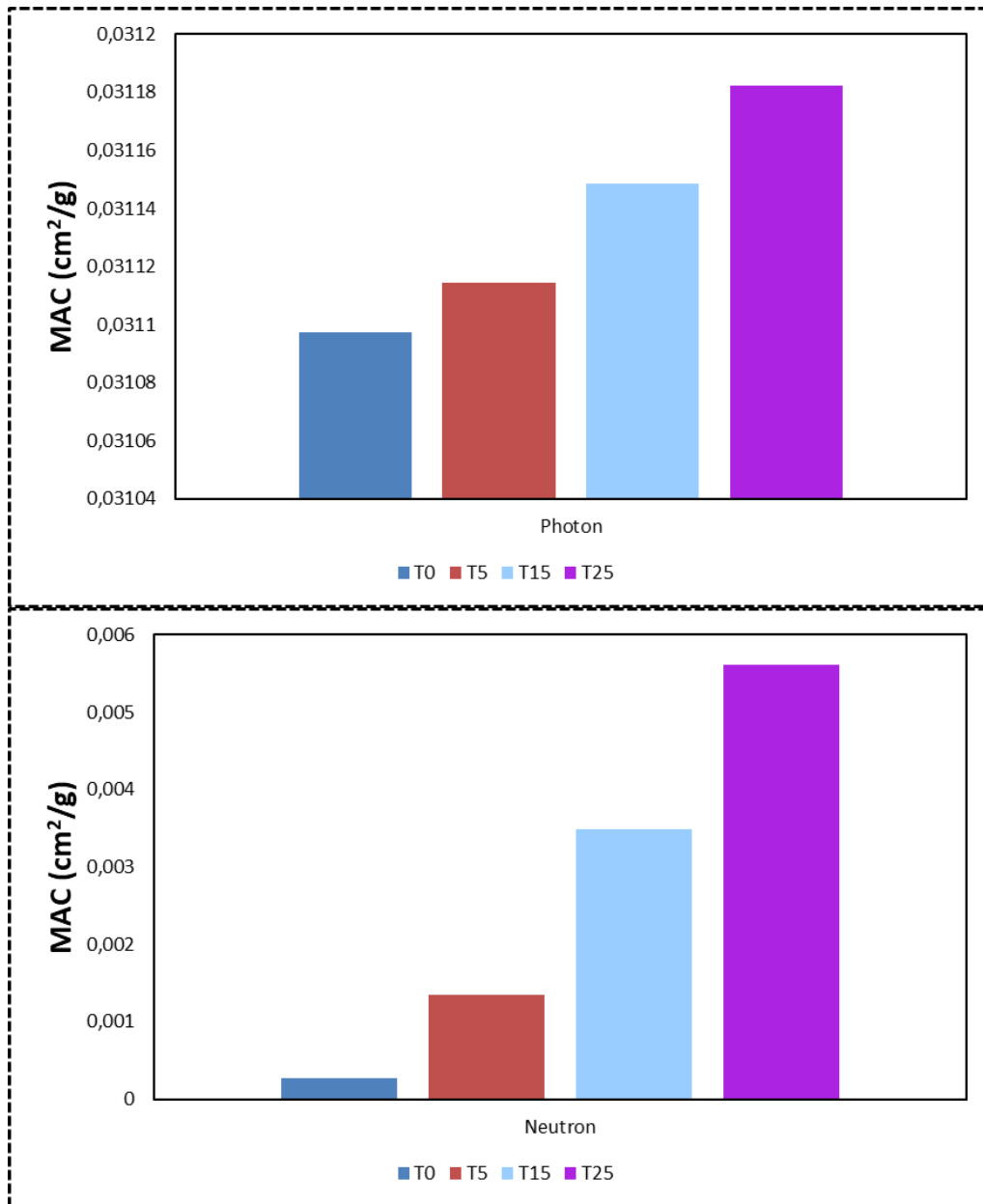
Figure 2. MAC graphs of samples coded T0-T5-T15-T25

TVL

The HVL values of the T0-T5-T15-T25 coded samples against 4 MeV energy photons and fast neutrons are given in Figure 3. In the face of 4 MeV energy photons; the HVL value of the material decreased due to increasing TiO_2. As a result of adding 25% TiO_2 into Al 6082, the HVL value against 4 MeV neutron energy decreased by approximately 95.7%. This provided a significant decrease in the material thickness required for the Al 6082 material to be a neutron shielding material with the addition of TiO_2. The thickness values of the materials to be used as neutron and gamma shielding materials are very important parameters in terms of usability, manufacturability and cost. For this reason, the addition of TiO_2 increased the possibility of the material being usable as a neutron shielding material. Decreases occurred in the TVL values of the T0-T5-T15-T25 coded samples due to the increasing TiO_2 ratio against 4 MeV energy photons. However, the decrease in TVL values due to the increase in TiO_2 is not as clear and sharp as the neutron TVL values. The addition of 25% TiO_2 to Al 6082 caused a decrease of approximately 12.5% in TVL values. When photons interact with material, they could lose an important amount of energy in an interaction, causing their intensity to decrease more rapidly.
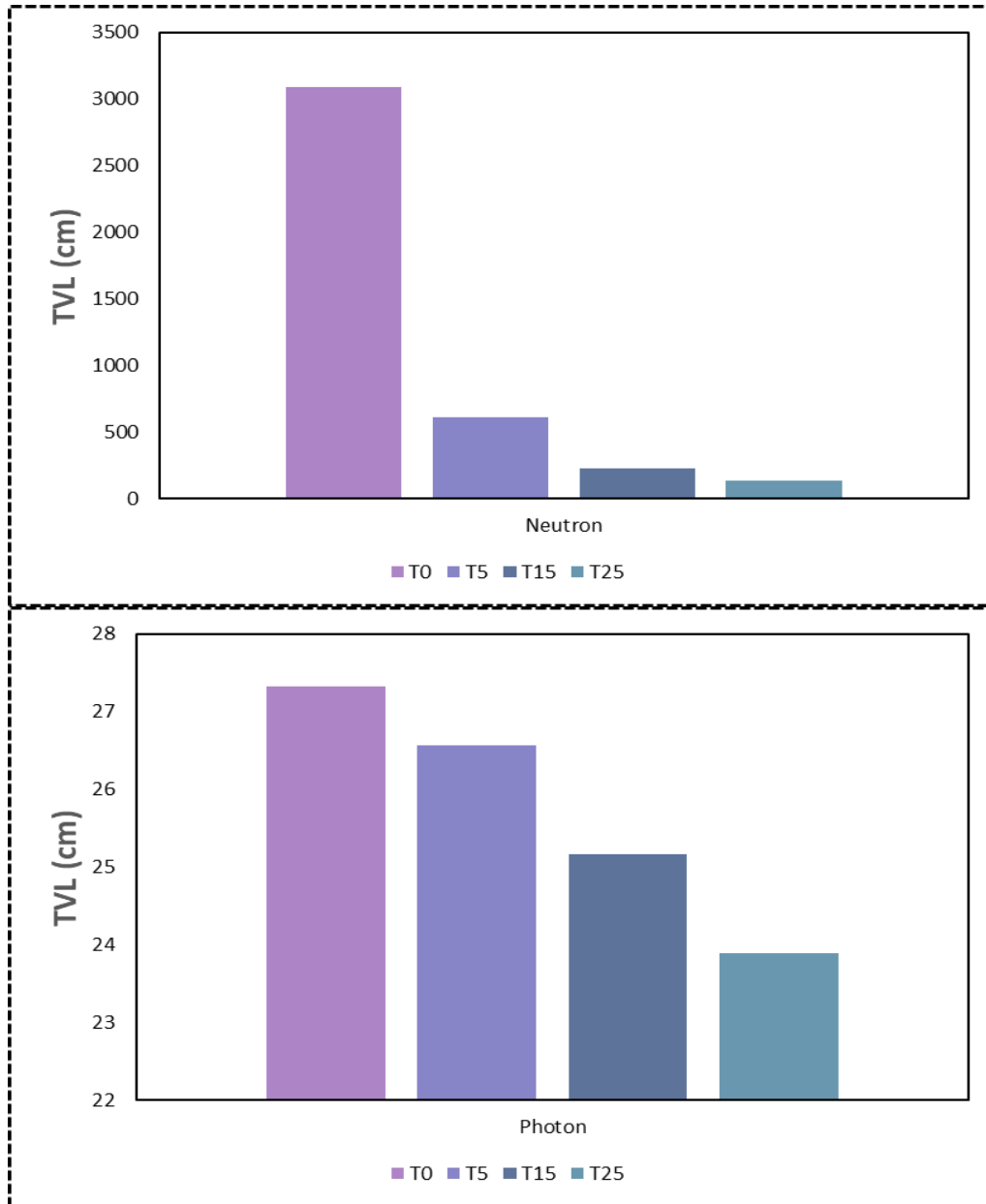
Figure 3. TVL graphs of samples coded T0-T5-T15-T25

Neutrons, on the other hand, can pass through many nuclei without losing significant energy before they interact, causing them to travel a longer distance before they are effectively stopped. This has resulted in the difference between the distances required to decrease the density of the incident photon by 90% and the distances required to reduce the intensity of the neutrons by 90%, as shown in Figure 3.

HVL

The HVL values of the T0-T5-T15-T25 coded samples against photons and fast neutrons with 4 MeV energy are given in Figure 4. Depending on the increasing TiO_2 ratio, the HVL values of the materials against both photons and fast neutrons decrease. The HVL values of the T0-T5-T15-T25 coded samples against fast neutrons are approximately 930.8 cm; 185.6 cm; 67.7 cm; 39.9 cm, respectively. In the photon case, they are approximately 8.2 cm; 7.99 cm; 7.57 cm; 7.19 cm, respectively. The HVL values of the photons are lower because the LAC values of the materials against photons are higher than the LAC values against neutrons. Neutrons have a high ability to penetrate matter, but since they do not experience electromagnetic interactions like gammas, they lose energy at a low rate. For this reason, the distance required to stop neutrons is generally much greater than that of gamma radiation.
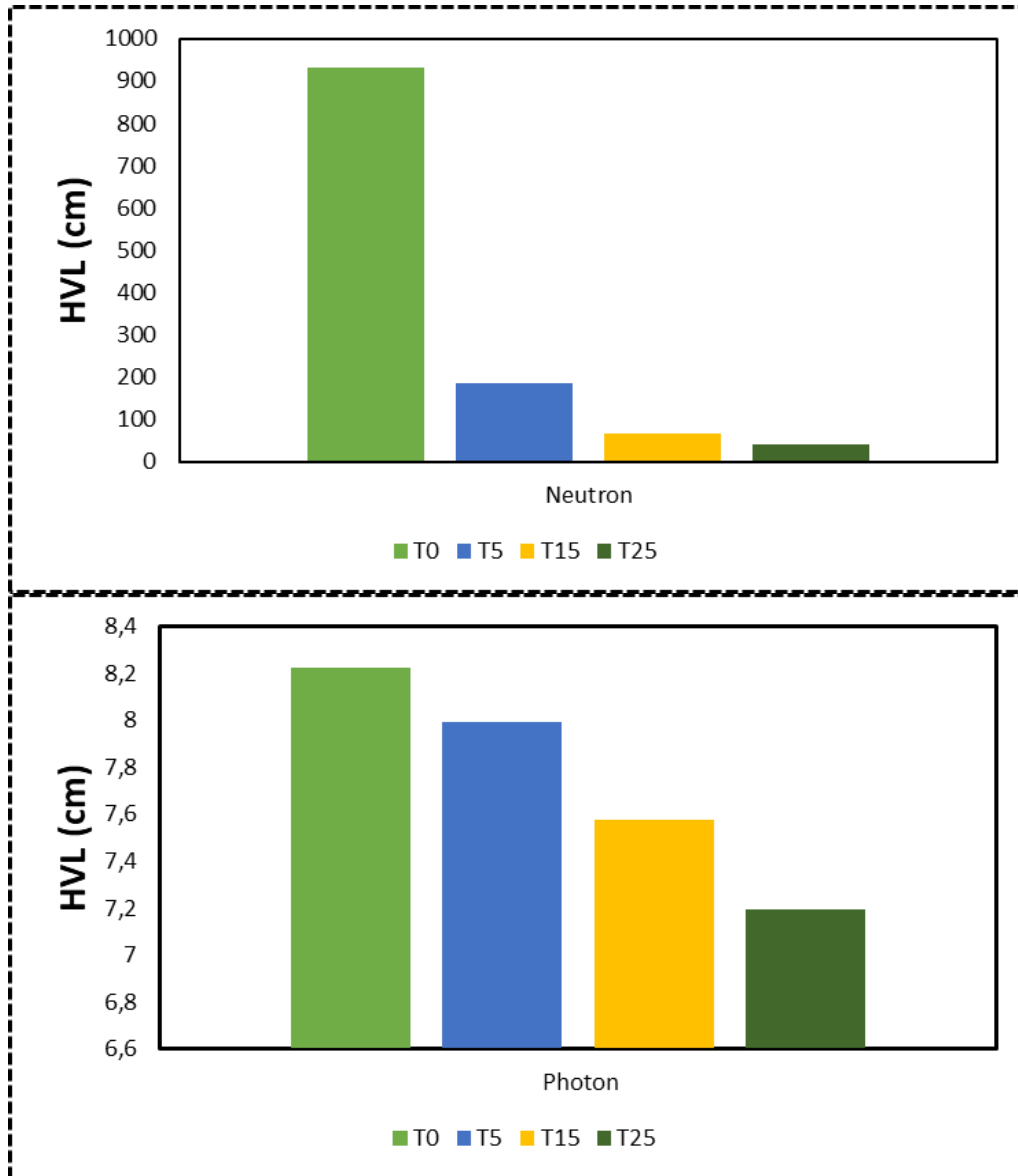
Figure 4. *HVL graphs of samples coded T0-T5-T15-T25*

MPF

The MFP values of the T0-T5-T15-T25 coded samples against photons and fast neutrons with 4 MeV energy are given in Figure 5. Depending on the increasing doping ratio, there was a rapid decrease in the distance required for the material to make two successive successful collisions with fast neutron particles. There was a reduce in the MFP values against photons with 4 MeV energy. However, it was not as much as the decrease in the distance against fast neutrons. The MFP values of the T0-T5-T15-T25 coded samples against fast neutrons with 4 MeV energy varied between approximately 1343 cm and 58 cm. In the case of photons with 4 MeV energy, it varied between approximately 12 cm and 10 cm. Fast neutrons with energies of 4 MeV can interact by inelastic scattering and elastic scattering. Depending on the type of scattering, this can affect the mean free path. Fast neutrons generally have higher mean free paths in lighter materials because they are less likely to interact with heavier nuclei.
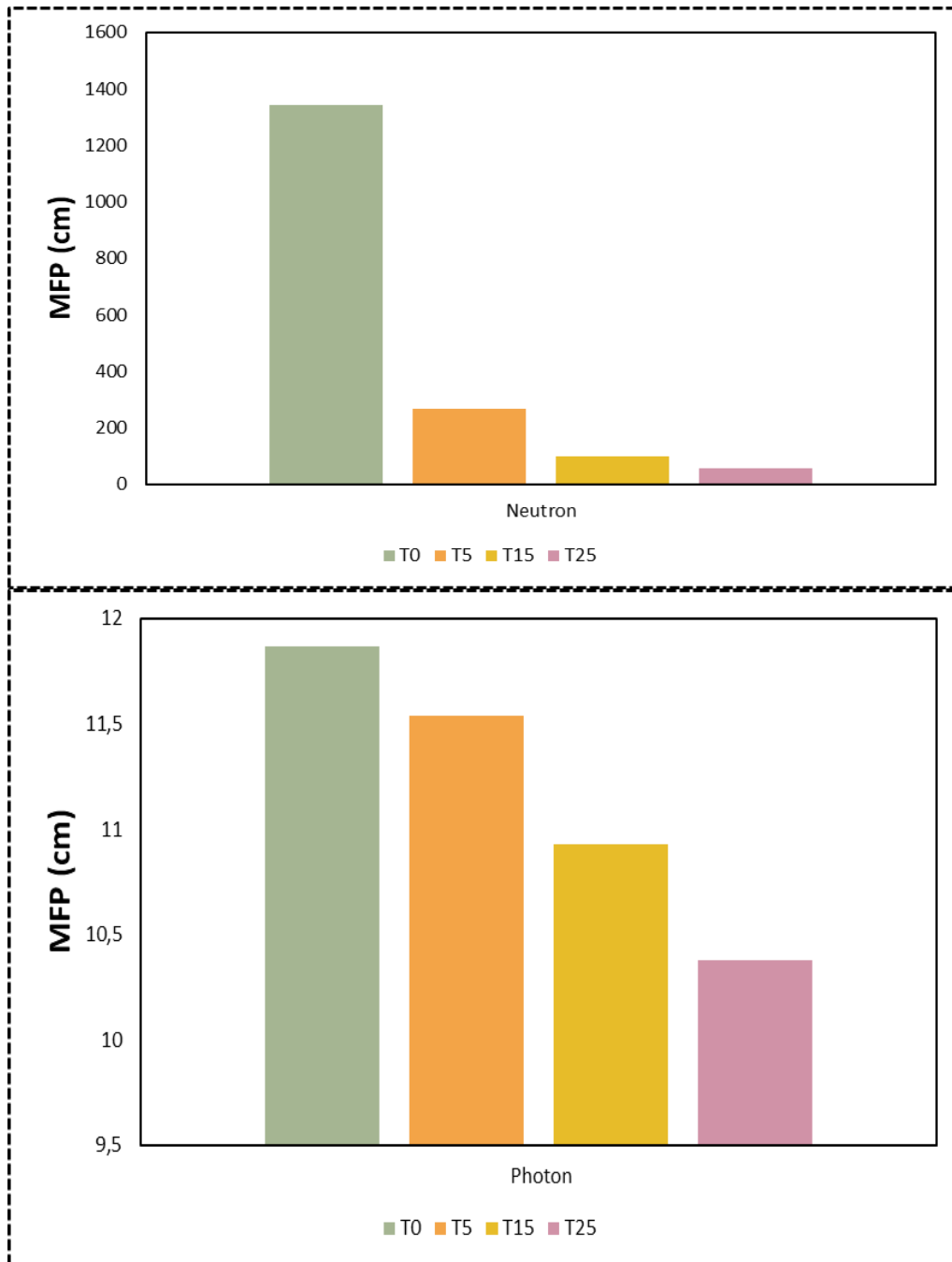
Figure 5. MFP graphs of samples coded T0-T5-T15-T25

4. CONCLUSION

The increasing use of artificial radiation (nuclear power plants, hospitals, industry) leads to an increase in the annual dose intake determined by ALARA. This causes many irreversible damages on humans, animals and nature. For this reason, radiation shielding has attracted the attention of many researchers. For this reason, in this study, a study was carried out for a shielding material that can be used for neutron and gamma rays, which are ionising radiations. In this study, MAC, LAC, HVL, MFP and TVL analyses of metal matrix composite materials to which 5-15-25 wt.% TiO_2 ceramic material was added to Al 6082 metal alloy were performed in NGCal program, which provides important information about photon and fast neutron radiations at 4 MeV energy. Among Al 6082, Al 6082+5% TiO_2, Al 6082+15% TiO_2 and Al 6082+25% TiO_2 samples, Al 6082+25% TiO_2 had the highest high LAC values against fast neutrons and photons, while Al 6082 alloy had the lowest LAC values. While Al 6082 alloy material had the highest HVL values against 4 MeV energy fast neutrons and photons, Al 6082+25% TiO_2 composite material had the lowest HVL

values. The MFP values of the T0-T5-T15-T25 coded samples against fast neutrons with 4 MeV energy varied between approximately 1343 cm and 58 cm. In the case of photons with 4 MeV energy, it varied between approximately 12 cm and 10 cm. By increasing the doping ratio of TiO_2 ceramic material, the photon and fast neutron radiation shielding properties of 4 MeV energy Al 6082 material were improved. The shielding properties of TiO_2 doped metal composites against photons were better than their shielding properties against neutrons.

ACKNOWLEDGEMENT

AUTHOR CONTRIBUTIONS

Conceptualization, Z.Ö and U.G.; methodology, U.G.; fieldwork, Z.Ö.; software, Z.Ö.; title, Z.Ö and U.G.; validation, Z.Ö., and U.G.; laboratory work, Z.Ö.; formal analysis, Z.Ö.; research, Z.Ö.; sources, Z.Ö.; data curation, Z.Ö.; manuscript-original draft, Z.Ö. and U.G.; manuscript-review and editing, Z.Ö and U.G.; visualization, Z.Ö and U.G.; supervision, U.G.; project management, U.G.; funding, Z.Ö. All authors have read and legally accepted the final version of the article published in the journal.

CONFLICT OF INTEREST

The authors declare no conflict of interest.

REFERENCES

Akman, F. Ozkan, I. Kaçal, M. R. Polat, H. Issa, S. A. M. Tekin, H. O. & Agar, O. (2021). Shielding features, to non-ionizing and ionizing photons, of FeCr-based composites. *Applied Radiation and Isotopes*, *167*, 109470. https://doi.org/10.1016/j.apradiso.2020.109470

Aldawood, S., Asemi, N. N., Kassim, H., Aziz, A. A., Saeed, W. S., & Al-Odayni, A.-B. (2024). Gamma radiation shielding by titanium alloy reinforced by polymeric composite materials. *Journal of Radiation Research and Applied Sciences*, *17*(1), 100793. https://doi.org/10.1016/j.jrras.2023.100793

Alım, B., Ozpolat, O. F., Sakar, E., Han, I., Arslan, I., Singh, V. P., & Demir, L. (2022). Precipitation hardening stainless steels: potential use radiation shielding materials. *Radiation Physics and Chemistry*, *194*, 110009. https://doi.org/10.1016/j.radphyschem.2022.110009

Almuqrin, A., Tijani, S. A., Al-Ghamdi, A., Alhuzaymi, T., & Alotiby, F. (2023). Radiation shielding properties of high-density polyethylene (C_2H_4)/ molybdenum III oxide (MoO3) polymer composites for dental diagnostic applications. *Journal of Radiation Research and Applied Sciences*, *16*(4), 100681. https://doi.org/10.1016/j.jrras.2023.100681

Chang, Q., Guo, S., & Zhang, X. (2023). Radiation shielding polymer composites: Ray-interaction mechanism, structural design, manufacture and biomedical applications. *Materials & Design*, *233*, 112253. https://doi.org/10.1016/j.matdes.2023.112253

Eke, C. (2024). The role of WO_3 on the optical and radiation attenuation characteristics of $ZnO–Na_2O–B_2O_3$ glasses. *Radiation Physics and Chemistry*, *224*, *112036*. https://doi.org/10.1016/j.radphyschem.2024.112036

Gökçe, H. S., Güngör, O., & Yılmaz, H. (2021). An online software to simulate the shielding properties of materials for neutrons and photons: NGCal. *Radiation Physics and Chemistry*, *185*, 109519. https://doi.org/10.1016/j.radphyschem.2021.109519

Huo, H., Lu, Y., Zhang, H., & Zhong, G. (2024). Sm_2O_3 micron plates/B4C/HDPE composites containing high specific surface area fillers for neutron and gamma-ray complex radiation shielding. *Composites Science and Technology*, *251*, 110567. https://doi.org/10.1016/j.compscitech.2024.110567

Huwayz, M. A., Basha, B., Alalawi, A., Alrowaili, Z. A. Sriwunkum, C., Alsaiari, N. S., & Al-Buriahi, M. S. (2024). Influence of BaO addition on gamma attenuation and radiation shielding performance of $SiO_2-B_2O_3$-

SrO-ZrO$_2$ glasses. *Journal of Radiation Research and Applied Sciences*, *17*(4), 101119. https://doi.org/10.1016/j.jrras.2024.101119

Kavun, Y., Kerli, S., Eskalen, H., & Kavgacı, M. (2022). Characterization and nuclear shielding performance of Sm doped In$_2$O$_3$ thin films. *Radiation Physics and Chemistry*, *194*, 110014. https://doi.org/10.1016/j.radphyschem.2022.110014

Kılıçoglu, O., & Tekin, H. O. (2020). Bioactive glasses with TiO$_2$ additive: behavior characterization against nuclear radiation and determination of buildup factors. *Ceramics International*, *46*(8), 10779-10787. https://doi.org/10.1016/j.ceramint.2020.01.088

Jandaghian, B., Dastjerdi, M. H. C., & Mokhtari, J. (2024). Characterization of neutronic parameters and radiation shielding design for an aqueous homogeneous reactor. *Nuclear Engineering and* Design, *417*, 112832. https://doi.org/10.1016/j.nucengdes.2023.112832

Juhim, F., Chee, F. P., Awang, A., Moh, P. Y., Salleh, K. A. M., Ibrahim, S., Dayou, J., Alalawi, A., & Al-Buriahi, M. S. (2023). Study of gamma radiation shielding on tellurite glass containing TiO$_2$ and Al2O$_3$ nanoparticles. *Heliyon*, *9*(11), e22529. https://doi.org/10.1016/j.heliyon.2023.e22529

Mahmoud, K. A., Binmujlli, M., Marashdeh, M., Sayyed, M. I., Aljaafreh, M. J., Akhdar, H., Alhindawy, I. G. (2024). Comprehensive analysis of the effects of Mo and Co on the synthesis, structural, and radiation-shielding properties of TiO2 based composites. *Progress in Nuclear Energy*, *169*, 105105. https://doi.org/10.1016/j.pnucene.2024.105105

Nafee, S., Tijani, S. A., Al-Hadeethi, Y., & Hussein, M. A. (2024). Radiation shielding potential of cellulose acetate-CdO-ZnO polymer composites in comparison with concrete and gypsum. *Radiation Physics and Chemistry*, *225*, 112145. https://doi.org/10.1016/j.radphyschem.2024.112145

Piotrowski, T. (2021). Neutron shielding evaluation of concretes and mortars: A review. *Construction and Building Materials*, *277*, 122238. https://doi.org/10.1016/j.conbuildmat.2020.122238

Reda, S. M., & Saleh, H. M. (2021). Calculation of the gamma radiation shielding efficiency of cement-bitumen portable container using MCNPX code. *Progress in Nuclear Energy*, *142*, 104012. https://doi.org/10.1016/j.pnucene.2021.104012

Chaotic Dynamics and Analysis with Artificial Neural Networks of Aftershocks of 2019 Silivri Earthquake

Fatma AYDOĞMUŞ[1*] 🆔   Yeşim ÖNİZ[2] 🆔   Eljan SIMURATLI[1] 🆔   Eren TOSYALI[2] 🆔   İsmail KAPLANVURAL[3] 🆔

Ahu KÖMEÇ MUTLU[4] 🆔   Deniz ÇAKA[3] 🆔   Halil TÜRKER[5] 🆔   Zeynep ÖNEM[1] 🆔

[1] Istanbul University, Faculty of Science, Physics Department, İstanbul, Türkiye
[2] Istanbul Bilgi University, Faculty of Engineering and Natural Science, Department of Mechatronics Engineering, İstanbul, Türkiye
[3] Kocaeli University, Faculty of Engineering, Department of Geophysics Engineering, Kocaeli, Türkiye
[4] Gebze Teknik University, Faculty of Engineering, Department of Civil Engineering, Kocaeli, Türkiye
[5] İstanbul University, Faculty of Communication, , Department of Radio, TV and Cinema, İstanbul, Türkiye

Keywords	Abstract
Aftershock Chaos Theory Time Series Artificial Neural Network	Earthquakes, whose physical, economic, psychological, and social damages can last for many years, are of vital importance for Türkiye, which is located in the most active earthquake zone that causes many earthquakes in the world. The North Anatolian Fault (NAF) is one of Türkiye's most important tectonic elements as it is the world's fastest-moving right-lateral and strike-slip active fault zone consisting of many segments. The recent 5.8 magnitude 2019 Silivri earthquake, which occurred in the part of the NAF zone crossing the Marmara Sea, is an indicator that earthquake activity continues in the region. Aftershocks play a crucial role in seismicity research and seismic hazard assessments in terms of providing data and usable information in the examination of seismic dynamics with the changes observed in their time-dependent behavior and regional distribution. In this study, the aftershocks of the Silivri earthquake were examined as a natural laboratory using nonlinear analysis methods. Within the scope of the study, aftershocks of the Silivri earthquake were analyzed with a hybrid artificial neural network as well as different neural network structures, and for this purpose, data from 361 aftershocks with a magnitude greater than 1.5 in the year following the earthquake were used.

Author ID (ORCID Number)		Article Process	
0000-0003-1434-2143	Fatma AYDOĞMUŞ	**Submission Date**	18.10.2024
0000-0002-8337-7852	Yeşim ÖNİZ	**Revision Date**	04.11.2024
0009-0006-2290-2701	Eljan SIMURATLI	**Accepted Date**	15.11.2024
0000-0001-9118-851X	Eren TOSYALI	**Published Date**	30.12.2024
0000-0003-2898-4657	İsmail KAPLANVURAL		
0000-0003-2243-7302	Ahu KÖMEÇ MUTLU		
0000-0003-2125-6489	Deniz ÇAKA		
0000-0001-5776-3250	Halil TÜRKER		
0000-0003-0662-0641	Zeynep ÖNEM		

1. INTRODUCTION

Earthquakes, the effects of which can last for many years due to the physical, economic, psychological, and social damages they cause, are of vital importance for Türkiye, which is located on the most active earthquake zone called Mediterranean-Alpine-Himalayan and where many earthquakes occur at frequent intervals resulting in serious loss of life and economic loss (Chang et al., 2024). The North Anatolian Fault (NAF) is one of the most important tectonic elements of Türkiye and is the fastest-moving right-lateral and strike-slip active fault zone consisting of many segments (Bolt, 1993). The NAF, which is known in the world earthquake literature for its westward migration and earthquakes of very high magnitudes, is divided into two main branches: the southern branch, which passes south of Lake Iznik and connects to the Gemlik Bay, and the

northern branch, which extends to the Gulf of Izmit and passes through the Marmara Sea and connects to the Ganos Fault (Türker, 2021).

Linearity refers to the direct proportionality of the output of a system to its input. In linear systems, small changes lead to small changes and the behavior of the systems can be predicted. Nonlinearity is when the output of a system is not directly proportional to the input. In nonlinear systems, small changes can lead to large changes and the behavior of the systems can be unpredictable (Hilborn, 2003). Earthquakes are nonlinear systems caused by the movements of the earth's crust. For example, small-scale fault movements can lead to earthquakes and small changes can lead to large earthquakes. In other words, the dynamics of seismicity involve nonlinear elements and processes (Takanashi et al., 1975).

Earthquake predictions are of great importance in minimizing the possible risks of earthquakes. These prediction studies are very important in terms of being able to predict seismic hazards and manage the emergency system. As mentioned above, earthquakes have dynamics that contain nonlinear elements (Kamgar et al., 2022). Therefore, in the analysis of such dynamic systems, it is possible to refer to the analysis methods carried out within the framework of chaos theory (Çalım et al., 2023). Chaos theory focuses on examining nonlinear irregular systems (Davies, 1999). These systems can produce large results even with small changes and exhibit unpredictable behaviors. This theory is widely studied in mathematics, physics, biology, economics, social sciences, and other branches of science. One of the important characteristics of chaos is that chaotic systems are extremely sensitive to initial conditions (Abarbanel et al., 1993).

All interdisciplinary studies carried out to minimize the possible risks of earthquakes are of great importance. In addition, regarding both preparations and precautions before earthquakes and the accuracy and applicability of decisions taken during and after earthquakes, it is also very important to gain appropriate attitudes and behaviors by using the symbols and icons related to earthquakes effectively. In this phenomenon, which can be referred to as earthquake literacy (Gurel, 2024), studies and research that bring together different disciplines, such as communication, engineering, science, and earth sciences, are of vital importance. In the digital age we live in, it is possible to raise public awareness about natural disasters such as earthquakes through the widespread use of traditional media tools as well as rapidly developing new media (internet, social media, etc.) and to provide society with the ability to be minimally affected by the possible risks of earthquakes through earthquake literacy.

Among machine learning techniques, artificial neural networks (ANNs) are particularly preferred because they do not require any prior assumptions or knowledge about the system and can learn by adapting parameters on their own using the data obtained (Mignan & Broccarda, 2020), unlike model-based techniques where success is directly related to the accuracy and completeness of the model. Alves has undertaken one of the first studies in which ANNs were used in the field of earthquake prediction (Alves, 2006). Based on the fact that both systems have a chaotic structure, the author applied a method similar to financial forecasting applications for earthquake prediction. In Lakshmi and Tiwari (2007), a similar approach was used to predict earthquakes in three regions of the Himalayas (central, western and northeastern). The authors created a time series using the number of earthquakes that occurred in each month in the relevant regions between 1960 and 2003 and tried to predict the number of earthquakes that will occur in the next month using 5-month windows in this time series. The earthquake prediction studies conducted by Moustra et al. (2011) for the Greek region consist of two main parts. In the first part of the study, the focus was on estimating the next day's largest seismic event using only time series and earthquake magnitude data, while in the second part, seismic electrical signals (SES) were used to estimate the magnitude of the next seismic event. ANN was preferred in both studies, and a time series containing the maximum seismic activity magnitudes recorded for each day between 1980 and 2001 was used to determine the input signals of the ANN used in the first part of the study. In the above-mentioned studies, time and/or magnitude information of previous earthquakes was used as the basis for earthquake estimation in a specific region. Although the results obtained are promising, many researchers have argued that these data alone are not sufficient for earthquake modeling and that additional indicators are required. Eight seismic indicators were proposed to estimate the magnitude of the largest seismic event that could occur in a predefined time interval and in a given area (Panakkat & Adeli, 2007). These suggested indicators were widely accepted by researchers in the field of seismology and used in many studies. In the study (Panakkkat et al., 2007), the magnitudes of the earthquakes were divided into various classes according to the Richter scale

and these classes were used as the outputs of the ANN, and the inputs of the network were these 8 indicators suggested by the authors. As a result of their studies, the authors determined that probabilistic neural networks provide better predictions for small and medium-sized earthquakes with magnitudes ranging from 4.5 to 6.0, while cyclic neural networks provide better predictions for larger earthquakes.

Aftershocks are very important in seismic hazard studies in terms of providing usable information. The 5.8 magnitude (M=5.8) Silivri earthquake, which occurred in the part of the NAF zone passing through the Marmara Sea and recently occurred on this fault line (Utkucu et al., 2023), is an indicator that earthquake activities continue in the region. In this study, the aftershocks of the 2019 Silivri earthquake are examined as a natural laboratory using nonlinear analysis methods. In addition, hybrid structures using ANNs together with other machine learning techniques and computational intelligence methods have become a widely used method by many researchers recently (Konstantaras et al., 2008; Joelianto et al., 2009; Zamani et al., 2013; Asim et al., 2017). In this study, aftershocks of the 2019 Silivri earthquake were analyzed with a hybrid artificial neural network as well as different neural network structures. For this purpose, data from 361 aftershocks with magnitudes greater than 1.5 in the year following the earthquake were used. The data in the study were obtained from the earthquake catalogs of the Disaster and Emergency Management (AFAD) and the Kandilli Observatory Earthquake Research Institute (KOERI). Since the distribution of earthquake stations of the institutions whose data will be used is not homogeneous, the number of earthquakes in the catalogs of the institutions for different regions or the quality of their solutions vary. In the studies conducted within the scope of the article, data recorded and cataloged by active earthquake stations were included. Thus, the aftershocks of an earthquake occurring in our Türkiye can be analyzed in detail with the methods presented in this study, which have a unique value for modeling seismic time series and making seismic hazard predictions.

2. MATERIAL AND METHOD

Many of the processes in nature are complex and mutually related. In this respect, dynamic systems can describe events that occur in nature, such as earthquakes. Very few dynamic systems are inherently isolated from the environment and form a whole within themselves. Due to a nonlinear variable in a model that defines a dynamic system, unpredictable dynamics may occur in the system. Chaos theory and nonlinear analysis techniques are used to analyze such unpredictable dynamics.

The first step in the nonlinear analysis techniques, which constitute the analysis methods applied in this study, is the collection of data based on experiments and observations and the extraction of reliable data to be used. AFAD and KOERI earthquake catalogs were combined to obtain the final catalog. In the first stage, the AFAD and KOERI catalog data were filtered according to the study area corner coordinates. In the merging of the catalogs of the two institutions, if there was a difference of more than 5 s between earthquakes that were close in time, both events were processed in the catalog as separate earthquakes. A locational query was also performed for two events that were smaller than 5 s in time. At this stage, earthquakes with a difference of more than 0.2 degrees in latitude and longitude were also considered as separate events and both events were processed in the catalog. In the events that did not meet the criteria, AFAD data was processed in the events after 2012 and KOERI data was processed in the events before. Time series, phase space, power spectrum and recurrence graphs were obtained using these seismic data.

2.1. Time Series

Time series is a concept that refers to the frequency of data that can be measured at periodic time intervals. Time series are sequences of data recorded at a given time taken at equidistant time points. Time series analysis is a method for examining how data changes over time. It allows the extraction of meaningful statistics that can be attributed to dependency relationships between observations and is used to model, predict, and understand recurring events over time. This process includes the mathematical construction of the phase space with the obtained time series data using sampling and sorting methods (Cambel, 1993; Scott, 1999; Rızaoğlu & Sünel, 2011; Devaney, 2021; Simuratli, 2023).

2.2. Phase Space Structures

The first step for nonlinear analysis is to reconstruct the signal in the form of data in phase space. Thus, it is possible to obtain information about the entire phase space of the system thanks to the time series recorded from the system while analyzing the system. It is shown as a scalar measurement. The scalar measurement is denoted as $x(t_0 + n\tau_s) = x(n)$, where t_0 is the start time and τ_s is the sampling time used in the experiment. Phase space is a mathematical space consisting of all possible states of the dynamic system and is a concept frequently used in the analysis of dynamic systems. Each state corresponds to a point in the phase space and shows all possible states of this system on a single graph. Time of analysis describes the motion or evolution of the system as the movement of a point in phase space, and this movement can be expressed by a mathematical model of the system. Phase space analysis can be used to understand various properties of a dynamic system (Cambel, 1993; Scott, 1999; Rızaoğlu & Sünel, 2011; Devaney, 2021; Simuratli, 2023).

2.3. Power Spectrum

It is possible to distinguish a chaotic signal from a non-chaotic signal by looking at its power spectra. Periodic signals give spikes (peaks) at certain frequencies, while if the signal is chaotic, it gives broadband components in the power spectrum. The power spectrum is also known as the energy spectral density. The power spectrum of the phase space of a system is a powerful tool for understanding the fundamental physical processes that drive the behavior of the system. It can be used to study a wide range of phenomena in many scientific fields, from the behavior of simple oscillators to the dynamics of complex systems such as the earth's climate (Cambel, 1993; Scott, 1999; Rızaoğlu & Sünel, 2011; Devaney, 2021; Simuratli, 2023).

2.4. Recurrence Plots

One way to visualize the recurring nature of states by their trajectory through a phase space is the recurrence plot proposed by Eckmann et al. In chaos theory, a recurrence plot is a plot that shows, for each moment i in time, the times at which the state of a dynamical system returns to the previous state in i, i.e., when the phase space trajectory rotates. In an iteration, the trajectory returns to a previously visited position (state) in phase space, up to a small error of ε (Cambel, 1993; Scott, 1999; Rızaoğlu & Sünel, 2011; Devaney, 2021; Simuratli, 2023).

2.5. Forecasting Studies with Artificial Neural Networks

A total of 361 aftershocks with magnitudes greater than Mw=1.5 were recorded in the year following the earthquake that occurred off the coast of Silivri on September 26, 2019. Nonlinear time series generated using the data from these earthquakes have been used to create predictive models in the field of earthquake seismology. In this study, artificial neural networks (ANN), long short-term memory (LSTM) networks, convolutional neural networks (CNN), echo state networks (ESN) and adaptive network-based fuzzy inference system (ANFIS) were used for prediction studies on aftershocks of the earthquake. 361 aftershock data for the aftershocks after the Silivri earthquake were obtained from catalogs. 300 of the obtained data were used to create the training time series of the networks, and the remaining 61 were used to create the test time series. In the studies, the magnitude of the aftershocks, the distance between two consecutive shocks, and the duration of raw seismic data were used as input signals for networks with different architectures.

The most typical form of feed-forward artificial neural network structures can be established by sequentially combining layers formed from neurons. The layer to which the inputs are applied is called the input layer, and the layer from which the outputs are received is called the output layer. In this structure, there may be one or more hidden layers between the input layer and the output layers.

In this study, various earthquake characteristics, such as magnitude, duration, and distance between consecutive aftershocks, were employed to estimate the characteristics of the next aftershock. For this purpose, (n, n-1, n-2, 0)-step delayed time series of consecutive aftershocks are applied to the input connections of artificial neural networks to predict the characteristics of the next aftershock. The error value calculated by comparing the obtained output value with the relevant characteristics of the next aftershock was used in the training of the network with gradient descent-based learning algorithms. After the error value was calculated

for the first input data, the time window was shifted one step, and the same processes were repeated until the entire data set was covered.

For the ANNs, the number of layers and number of neurons in each layer can be called among the parameters that have the most effect on the performance of the ANNs. Although increasing the number of layers might enable the network to capture more complex data, it can also lead to the overfitting problem. Similarly, increasing the number of neurons in a layer can help the network capture more features and thus increase the accuracy; it can also lead to the overfitting problem. In the current study, as the number of available data points is limited, the number of hidden layers has been restricted to one, and the best performance has been attained for 50 neurons. The time window size is the same as the number of neurons in the input layer. After normalization, the time series data were applied to the network as the input signal. In training the network, the learning coefficient was selected as 0.25 and the momentum coefficient as 0.1. In another study, the long short-term memory (LSTM) neural network architecture, which has the ability to learn long-term connections with its memory transition mechanism, was used. The most important feature that distinguishes the LSTM network, which is frequently preferred in time series prediction, from the traditional ANN structure is the presence of forget gates and memory cells that provide "remembering" for the neurons in the hidden layer. To better understand the effects of the forget gates and memory units on the performance, the same number of LSTM cells, 50, as the number of hidden neurons in ANN has been utilized. The output cell consists of a single neuron. The learning coefficient was determined as 0.1 using empirical methods.

In addition to these two methods, which are frequently used in time series forecasting, the echo state network (ESN) architecture was also applied to the nonlinear time series of aftershocks since aftershocks are found to exhibit chaotic characteristics. The most important features that distinguish this network from other architectures, which have a recurrent neural network structure, are that the weights between the input-hidden layer ('reservoir') are randomly assigned and not trained, the hidden layer is very sparsely connected, and learning is provided only by adapting the weights between the output layer and the reservoir. In addition to these structural features, since learning in echo state networks is performed at once for the entire data set with the linear regression method, it is possible to solve the prediction problem very quickly compared to networks with the traditional backpropagation networks. In the literature, it was observed that the applications where ESNs were previously used in the field of earthquake prediction were very limited. In general, increasing the reservoir size helps to capture more intrinsic patterns; however, if the training data is limited, this might increase the risk of overfitting. In the present study, the best performance has been attained for a reservoir size of 750 neurons while keeping only five percent of the connections active (non-zero).

Due to the limited size of the available data, two convolutional layers, each followed by a max pooling layer, have been employed for the CNN architecture. To avoid overfitting, the maximum kernel size and the number of filters have been set to 10 and 3, respectively, as larger values of these parameters result in better performance for training but lower accuracy in the testing part.

The prediction performance of ANFIS highly depends on the number of membership functions. More membership functions enable a finer input space division but also make the training process more difficult and time-consuming as the number of adaptable parameters increases with the number of membership functions. In the present study, three membership functions were used to "fuzzify" each input signal (Simuratli, 2023) as the simulations for higher values of membership functions take considerably longer time while better performance couldn't be attained.

3. RESULTS AND DISCUSSION

Aftershocks play a crucial role in seismicity research and seismic hazard assessments in terms of providing data and usable information in the examination of seismic dynamics with the changes observed in their time-dependent behavior and their regional distribution. The 5.8 magnitude Silivri earthquake, which occurred on September 26, 2019 at 13:59 öff the coast of Silivri and in the part of the NAF zone passing through the Sea of Marmara, is a medium-high magnitude earthquake that occurred on this fault line recently and has been observed that earthquake activities continue in the same region. Considering the earthquakes that may occur in the future in this region, the examination of the aftershocks of the Silivri earthquake by means of the

techniques proposed within the scope of this study and the nonlinear time series modeling will be the first time in the literature that the aftershocks of an earthquake have been examined with methodologically original techniques. The time series, phase space structure, power spectrum, and recurrence graphs obtained for the Silivri earthquake aftershocks are given in Figure 1, 2, 3 and 4:
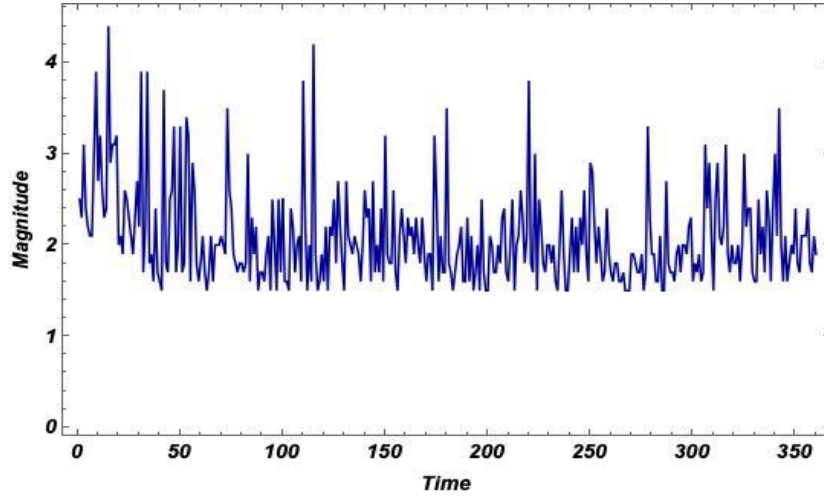
Figure 1. *Time Series Graph for Silivri Earthquake Aftershocks*
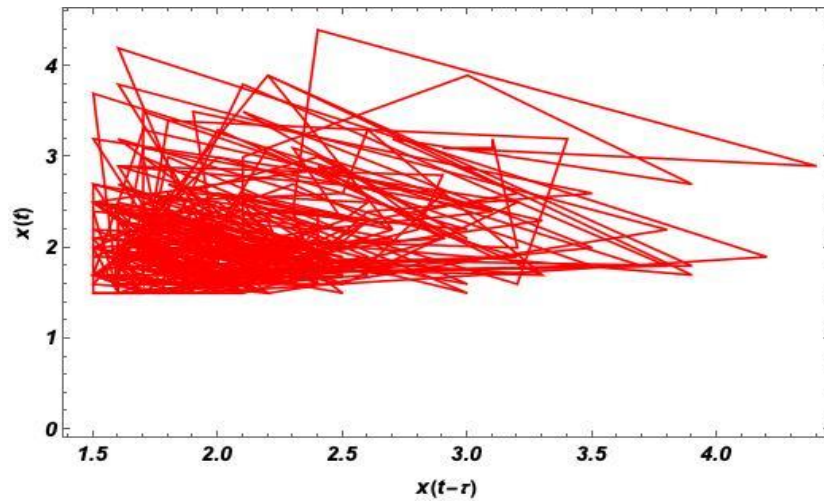
Figure 2. *Phase Space for Silivri Earthquake Aftershocks*
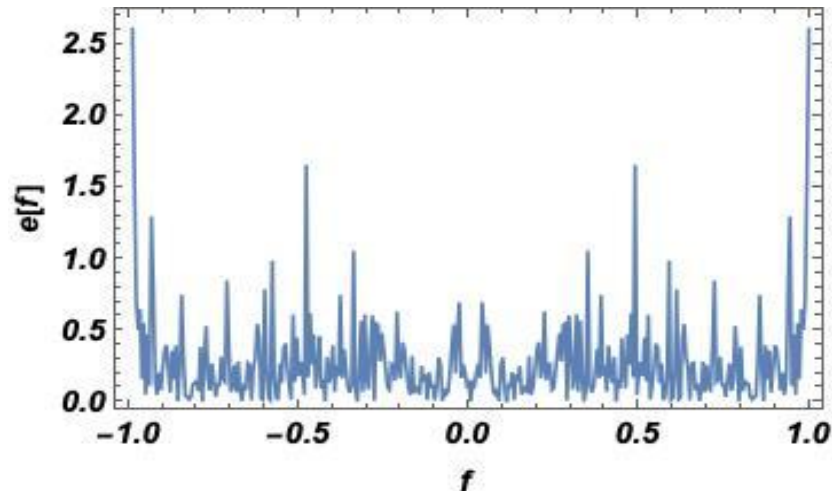
Figure 3. *Power Spectrum Graph for Silivri Earthquake Aftershocks*
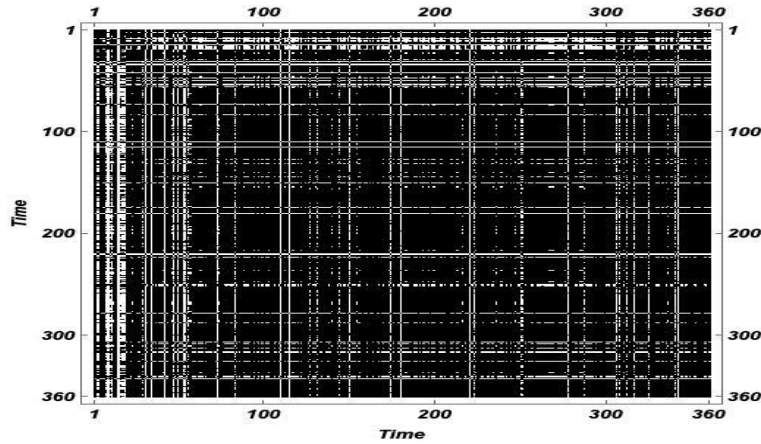
Figure 4. Recurrence Graph for Silivri Earthquake Aftershocks

The time series graph for the Silivri earthquake data is given in Figure 1. The data obtained by experiment, measurement or observation and characterizing the behavior of any dynamic system constitute the time series of the system. These are the values that the variables describing the system can take. We can see the change of the time series by drawing the graph of this data according to time or iteration step. If the change in question does not occur according to any order, but is completely random and irregular, the behavior of the system determined by these numbers may indicate chaos. Since there can be a very large number of numerical values in the time series, it is not easy to understand whether the time series contains any order by just looking at the graph we mentioned above. In order to understand the existence of order in the time series, it is necessary to perform other analyses such as phase space structure, power spectrum, and recurrence graphs. The phase space, where each state of the dynamic system is represented by a point in the phase space of the system, is presented in Figure 2, the power spectrum in Figure 3 and the recurrence graph in Figure 4. The results given in Figures 1, 2, 3 and 4 show that the dynamics of the aftershocks of the 2019 Silivri earthquake contain chaotic elements. In addition, the maximum Lyapunov exponent was determined as 0.00872464 using the code written in Python programming language. In addition to the results given above, the fact that the maximum Lyapunov exponent calculated for the data set was positive is another important indicator that the seismic process is chaotic.

In the prediction studies carried out with different neural network architectures, 300 of the 361 aftershocks recorded were used for training, and the remaining 61 were used to test the performance of the network used. In the studies carried out using different time window sizes for five different network architectures, raw seismic data of the magnitude of the earthquakes, the distance between two consecutive shocks and the duration were used. Root mean squared error (RMSE) values were calculated to evaluate the performance of different models. The simulations have been carried out five times, and average RMSE values have been reported Table 1. When this table is examined, it is seen that increasing the time window size does not always provide better results due to the overfitting problem resulting from the limited number of data.

Table 1. RMSE values obtained for different architectures

				Magnitude		
	RMSE	**h=1**	**h=3**	**h=5**	**h=8**	**h=10**
ESN	Training	0.391	0.303	0.286	0.287	0.264
	Test	0.575	0.592	0.618	0.618	0.624
LSTM	Training	0.432	0.412	0.423	0.421	0.418
	Test	0.511	0.492	0.487	0.493	0.490
ANN	Training	0.469	0.429	0.427	0.424	0.412
	Test	0.535	0.553	0.556	0.540	0.534
CNN	Training	0.384	0.392	0.420	0.431	0.455
	Test	0.594	0.528	0.545	0.530	0.486
ANFIS	Training	0.462	0.424	0.444	0.436	0.432
	Test	0.514	0.523	0.506	0.512	0.498

Table 1. *continued*

Distance between two consecutive aftershocks						
	RMSE	h=1	h=3	h=5	h=8	h=10
ESN	Training	3.416	3.379	3.364	3.389	3.393
	Test	3.706	3.769	3.548	3.999	3.816
LSTM	Training	3.523	3.137	3.266	3.357	3.416
	Test	4.081	4.318	4.264	4.258	4.175
ANN	Training	3.755	3.742	2.738	3.742	3.732
	Test	3.571	3.697	3.862	4.014	4.088
CNN	Training	3.726	3.628	3.625	3.612	3.611
	Test	4.732	4.541	4.651	4.696	4.783
ANFIS	Training	3.487	3.224	3.554	3.678	3.592
	Test	4.143	4.458	4.511	4.486	4.481
Time between two consecutive aftershocks						
	RMSE	h=1	h=3	h=5	h=8	h=10
ESN	Training	0.123	0.113	0.101	0.092	0.091
	Test	0.938	0.991	1.132	1.095	1.030
LSTM	Training	0.115	0.089	0.078	0.065	0.082
	Test	0.921	0.835	0.844	0.868	1.027
ANN	Training	0.233	0.234	0.235	0.236	0.237
	Test	1.276	1.303	1.320	1.366	1.400
CNN	Training	0.131	0.132	0.182	0.119	0.117
	Test	1.073	1.340	1.156	1.231	1.257
ANFIS	Training Training m	0.164	0.298	0.265	0.242	0.241
	Test	0.942	0.975	0.969	0.961	0.956

4. CONCLUSION

Within the scope of this study, our main objective in time series analysis is to identify the dynamics underlying the seismicity and to make prediction studies in accordance with the dynamics. Before nonlinear time series modeling is performed, the identification and analysis of the nonlinear system is performed, which constitutes the most important part of the work. In this study, the aftershocks of the 2019 Silivri earthquake (Mw = 5.8) that occurred in the Marmara Region of the NAF zone and recently off the coast of Silivri were examined and dynamic analysis of tectonic movements in the epicenter region after an earthquake was performed. The magnitudes of these aftershocks within certain periods were reconstructed in the signal phase space in the form of scalar data, and it was determined whether the data was random, periodic, or chaotic. Phase space structures were constructed by obtaining the time series of the data. In addition, the aftershocks of the 2019 Silivri earthquake were analyzed using a hybrid artificial neural network. Other analyses and numerical results obtained are given in detail under the subheadings above, and as a result of the analyses, the time delay from the time-dependent data of the Silivri earthquake's aftershocks was found to be 1 month and the embedding size for this delay time was calculated as 4. In addition, the maximum Lyapunov exponent for this time series was found to be 0.00872464. These results show us that there is a chaotic structure in the dynamics of the 2019 Silivri earthquake's aftershocks. These results provide us with the opportunity to use the techniques, algorithms, and models we use in many nonlinear dynamic systems in earthquake analysis, modeling, and prediction studies.

The results we obtained for the 2019 Silivri earthquake, which is the subject of this article, show the suitability of using these techniques in earthquake prediction studies. By looking at the Lyapunov exponents obtained with fault-based data, comparative evaluations can be made for each earthquake magnitude data. For example, by using the data produced by only one fault, the change in the Lyapunov exponents in the system in the temporal evolution can be examined. The earthquake generating activity of the fault over time and its positive-

negative effects on triggering a new earthquake can be discussed. A new perspective can be gained for earthquake predictions by extracting the long-term temporal evolution of a fault that has produced a large earthquake and by nonlinear analysis of the time series to be created. More reliable prediction studies can be carried out by observing the dynamics of the time series created with data taken at certain time intervals and the changes in the Lyapunov exponents in dynamic systems such as earthquakes.

AUTHOR CONTRIBUTIONS

Conceptualization, F.A. and Y.Ö.; methodology, F.A., Y.Ö and E.T.; software, F.A., Y.Ö, E.S. and E.T; title, F.A.; validation, F.A., Y.Ö., A.K.M. and İ.K.; formal analysis, F.A., Y.Ö., E.S. and İ.K.; research, F.A. Y.Ö., E.S., E.T., A.K.M., D.Ç., İ.K., H.T. and Z.Ç.; sources, E.S., E.T., A.K.M. and Z.Ç.; data curation, F.A., Y.Ö., E.S.; manuscript-original draft, F.A.; manuscript-review and editing, Y.Ö., İ.K., A.K.M. and H.T.; visualization, F.A., E.T., Y.Ö., D.Ç. and E.S.; supervision, F.A.; project management, F.A. All authors have read and legally accepted the final version of the article published in the journal.

ACKNOWLEDGEMENT

CONFLICT OF INTEREST

The authors declare no conflict of interest.

REFERENCES

Abarbanel, H. D. I., Brown, R., Sidorowich, J. J., & Tsimring, L. Sh. (1993). The Analysis of Observed Chaotic Data in Physical Systems. *Reviews of Modern Physics*, *65*(4), 1331-1392. https://doi.org/10.1103/RevModPhys.65.1331

Alves, E. I. (2006). Earthquake forecasting using neural networks: results and future work. *Nonlinear Dynamics*, *44*(1-4), 341-349, https://doi.org/10.1007/s11071-006-2018-1

Asim, K. M., Martínez-Álvarez, F., Basit, A., & Iqbal, T. (2017). Earthquake magnitude prediction in Hindukush region using machine learning techniques. *Natural Hazards*, *85*(1), 471-486. https://doi.org/10.1007/s11069-016-2579-3

Bolt, B. A. (1993). *Earthquakes and Geological Discovery*. Scientific American Library.

Cambel, A. B. (1993). *Applied Chaos Theory a Paradigm for Complexity*. Academic Press, Boston.

Chang, Y., Zhang, Y., & Zhang, H. (2024). Tectonic geomorphology of Türkiye and its insights into the neotectonic deformation of the Anatolian Plate. *Earthquake Research Advances*, *4*(1), 100267. https://doi.org/10.1016/j.eqrea.2023.100267

Çalım, Z., Çam Taşkıran, Z. G., & Yıldırım, T. (2023). Risk zone analysis using chaos theory from earthquake data. *Recent Advances in Science and Engineering*, *3*(2), 15-32. https://doi.org/10.14744/rase.2023.0003

Davies, B. (1999). *Exploring Chaos: Theory And Experiment*. Westview Press. https://doi.org/10.1201/9780429502866

Devaney, R. L. (2021). *An Introduction to Chaotic Dynamical Systems* (3rd Ed.). Boston University Press. https://doi.org/10.1201/9780429280801

Gurel, E., Nazli, A., & Yoltay, S. (2024, February, 16-18). *Deprem Okuryazarlığı: İletişimsel Bir Yaklaşım*. In: D. Solisworo (Eds.), Anadolu 14th International Conference on Social Sciences, Gaziantep, Türkiye.

Hilborn, R. C. (2003). *Chaos and Nonlinear Dynamics*. Oxford University Press, New York.

Joelianto, E., Widiyantoro, S., & Ichsan, M. (2009). Time series estimation on earthquake events using ANFIS with mapping function. *International Journal of Artificial Intelligence*, *3*(A09), 37-63.

Kamgar, R., Dadkhah, M., & Naderpour, H. (2022). Earthquake-induced nonlinear dynamic response assessment of structures in terms of discrete wavelet transform. *Structures*, *39*, 821-847. https://doi.org/10.1016/j.istruc.2022.03.060

Konstantaras, A., Vallianatos, F., Varley, M. R., & Makris, J. P. (2008). Soft-computing modelling of seismicity in the southern Hellenic arc. *IEEE Geoscience and Remote Sensing Letters*, *5*(3), 323-327. https://doi.org/10.1109/LGRS.2008.916069

Lakshmi, S. S., & Tiwari, R. K. (2007). Are northeast and western Himalayas earthquake dynamics better "organized" than Central Himalayas: An artificial neural network approach. *Geofísica Internacional*, *46*(1), 65-75. https://doi.org/10.22201/igeof.00167169p.2007.46.1.2152

Mignan, A., & Broccarda, M. (2020). Neural Network Applications in Earthquake Prediction (1994–2019): Meta-Analytic and Statistical Insights on Their Limitations. *Seismological Research Letters*, *91*(4), 2330-2342. https://doi.org/10.1785/0220200021

Moustra, M., Avraamides, M., & Christoduolou, C. (2011). Artificial neural networks for earthquake prediction using time series magnitude data or Seismic Electric Signals. *Expert Systems with Applications*, *38*(12), 15032-15039. https://doi.org/10.1016/j.eswa.2011.05.043

Panakkat, A., & Adeli, H. (2007). Neural network models for earthquake magnitude prediction using multiple seismicity indicators. *International Journal of Neural Systems*, *17*(1), 13–33. https://doi.org/10.1142/S0129065707000890

Rızaoğlu, E., & Sünel N. (2011). *Klasik Mekanik*. Seçkin Yayıncılık.

Scott, A. (1999). *Nonlinear Science*. Oxford University Press.

Simuratli, E. (2023). *Kuzey Anadolu Fay Zonu Depremsellik Dinamiğinin Makine Öğrenmesi Algoritmaları Kullanılarak İncelenmesi*. MSc Thesis, İstanbul University.

Takanashi, K., Udagawa, K., Seki, M., Okada, T., & Tanaka, H. (1975). Non-linear earthquake response analysis of structures by a computer-actuator on-line system: Part 1 Detail of the System. *Transactions of the Architectural Institute of Japan*, *229*, 77-83. https://doi.org/10.3130/aijsaxx.229.0_77

Türker, T. (2021). *Kuzey Anadolu Fay Zonu (KAFZ) ve Doğu Anadolu Fay Zonu (DAFZ) İçin Bayes Yöntemi İle Farklı Dağılım Yöntemleri Birleştirilerek Deprem Tahmin ve Tehlike Analizleri*. PhD Thesis, Karadeniz Teknik University.

Utkucu, M., Uzunca, F., Utkucu, Y., Durmuş, H., & Kırım, S. (2023). The September 26, 2019 Silivri Earthquake (Mw=5.6), NW Türkiye. *Academic Platform Journal of Natural Hazards and Disaster Management*, *4*(2), 65-75. https://doi.org/10.52114/apjhad.1219257

Zamani, A., Sorbi, M. R., & Safavi, A. A. (2013). Application of neural network and ANFIS model for earthquake occurrence in Iran. *Earth Science Informatics*, *6*(2), 71-85. https://doi.org/10.1007/s12145-013-0112-8

UKnow-Net: Knowledge-Enhanced U-Net for Improved Retinal Vessel Segmentation

Zeki KUŞ[1]* iD

[1] Fatih Sultan Mehmet Vakif University, Department of Computer Engineering, Istanbul, Türkiye

Keywords	Abstract
Retinal Vessel Segmentation Knowledge Distillation and Enhancement Semi-supervised Learning	Retinal vessel segmentation plays a critical role in diagnosing and managing ophthalmic and systemic diseases, as abnormalities in retinal vasculature can indicate disease progression. Traditional manual segmentation by expert ophthalmologists is time-consuming, labor-intensive, and prone to variability, underscoring the need for automated methods. While deep learning approaches like U-Net have advanced retinal vessel segmentation, they often struggle to generalize across diverse datasets due to differences in image acquisition techniques, resolutions, and patient demographics. To address these challenges, I propose UKnow-Net, a knowledge-enhanced U-Net architecture designed to improve retinal vessel segmentation across multiple datasets. UKnow-Net employs a multi-step process involving knowledge distillation and enhancement techniques. First, I train four specialized teacher networks separately on four publicly available retinal vessel segmentation datasets—DRIVE, CHASE_DB1, DCA1, and CHUAC—allowing each to specialize in the unique features of its respective dataset. These teacher networks generate pseudo-labels representing their domain-specific knowledge. We then train a student network using the ensemble of pseudo-labels from all teacher networks, effectively distilling the collective expertise into a unified model capable of generalizing across different datasets. Experiments demonstrate that UKnow-Net outperforms traditional handcrafted networks (such as U-Net, UNet++, and Attention U-Net) and several state-of-the-art models in key performance metrics, including sensitivity, specificity, F1 score, and Intersection over Union (IoU). Specifically, our two variants, UKnowNet-A and UKnowNet-B, show well performance; UKnowNet-A, trained solely on pseudo-labels, achieved higher sensitivity across all datasets, indicating a superior ability to detect true positives, while UKnowNet-B, which combines pseudo-labels with ground truth annotations, achieved balanced precision and recall, leading to higher F1 scores and IoU metrics. The integration of pseudo-labels effectively transfers the collective expertise of the teacher networks to the student network, enhancing generalization and robustness. I aim to ensure fair comparison and reproducibility in future research by publicly sharing our source code and model weights.

Author ID (ORCID Number)		Article Process	
0000-0001-8762-7233	Zeki KUŞ	Submission Date	30.10.2024
		Revision Date	11.11.2024
		Accepted Date	14.11.2024
		Published Date	30.12.2024

1. INTRODUCTION

Retinal vessel segmentation is a crucial task in medical image analysis, vital for diagnosing and managing eye-related and systemic conditions like diabetic retinopathy, glaucoma, hypertension, and cardiovascular diseases (Abràmoff et al., 2010). The retinal vasculature reflects the body's microcirculation state, and vessel morphology abnormalities can indicate disease progression (Patton et al., 2006; Fraz et al., 2012). Accurate segmentation of retinal vessels enables clinicians to quantify vascular changes, assess disease severity, and monitor treatment efficacy.

Traditionally, expert ophthalmologists have performed retinal vessel segmentation manually, which is a process that is time-consuming, work-intensive, and prone to variability between different observers. (Niemeijer et al., 2004). Manual feature extraction, while precise, is not feasible for large-scale screenings or real-time applications due to the high costs and resource requirements. Consequently, there is a pressing need for automated segmentation methods that can provide rapid, reliable, and reproducible analysis of retinal images. Early computational approaches employed handcrafted features and classical image processing techniques, such as matched filters (Chaudhuri et al., 1989), morphological operations (Zana & Klein, 2001), and multiscale analysis (Mendonca & Campilho, 2006). These methods aimed to enhance vessel-like structures and suppress background noise. However, they frequently encountered difficulties due to differences in image quality, lighting, and patient anatomy, which restricted their ability to generalize across various datasets and imaging modalities.

The emergence of deep learning has transformed medical image segmentation by allowing models to learn hierarchical feature representations directly from samples (Litjens et al., 2017). Convolutional neural networks (CNNs), particularly fully convolutional networks and encoder-decoder architectures, have demonstrated remarkable success in biomedical segmentation tasks. U-Net (Ronneberger et al., 2015) introduced a symmetric encoder-decoder structure with skip connections, effectively fusing semantic and spatial information. U-Net has been successfully applied to brain tumor segmentation in MRI scans, demonstrating its capability to handle complex structures and improve diagnostic accuracy (Isensee et al., 2018). The model has also been used in dermatology for skin lesion segmentation, aiding in the early detection of melanoma by accurately segmenting lesions from surrounding skin (Anand et al., 2022). U-Net variants have been adapted for object detection tasks, providing precise localization and classification in images (Jaeger et al., 2019). The architecture has been instrumental in analyzing satellite imagery for land cover classification, urban planning, and environmental monitoring (Amritesh et al., 2023). In agriculture, U-Net has been applied to segment leaves for plant phenotyping and disease detection, contributing to advancements in crop management (Mu et al., 2024).

Variants of U-Net and other deep learning architectures have since been applied to retinal vessel segmentation with notable improvements in accuracy (Fu et al., 2016; Liskowski & Krawiec, 2016; Zhou et al., 2021; Liu et al., 2022; Qu et al., 2023). Mou et al. (2019) present CS-Net, a novel network architecture designed to segment curvilinear structures within various medical imaging modalities. CS-Net incorporates channel and spatial attention mechanisms to enhance feature extraction and improve segmentation accuracy, outperforming existing state-of-the-art methods across multiple datasets. Attention Guided Network (AG-Net) (Zhang et al., 2019) enhances retinal image segmentation by preserving structural information through a novel attention-guided filter. This filter integrates an attention mechanism to reduce background noise and improve the accuracy of segmenting retinal structures such as blood vessels and optic discs/cups. Wang et al. (2020) introduce RVSeg-Net, a new and efficient network for segmenting retinal vessels. It tackles challenges like different sizes, small blood vessels, and complex image structures. The network employs a feature pyramid cascade (FPC) module to capture multi-scale features and a multi-frequency convolution (MFC) module to reduce redundancy and improve efficiency, thereby overcoming overfitting issues. SCS-Net (Wu et al., 2021) is a novel scale and context-sensitive network designed for retinal vessel segmentation, addressing challenges such as large-scale variations and complex anatomical contexts. Zhou et al. (2021) present a Study Group Learning (SGL) framework designed to enhance the robustness of retinal vessel segmentation models trained with noisy labels. It introduces a novel method for synthesizing noisy labels and demonstrates improved performance on the DRIVE and CHASE DB1 datasets using a K-fold cross-validation-inspired training scheme. FR-UNet (Liu et al., 2022), combined with a dual-threshold iterative algorithm (DTI) for improved vessel segmentation images. It enhances vessel connectivity and sensitivity by maintaining full image resolution and integrating multiscale feature maps, outperforming state-of-the-art methods on several datasets. Qu et al. (2023) introduce TP-Net, a novel two-path network designed for refined retinal vessel segmentation, addressing challenges in segmenting thin and low-contrast vessels. TP-Net comprises a main-path for detecting vessel trunks, a sub-path for capturing edge information, and a multi-scale feature aggregation module (MFAM) to combine predictions, enhancing segmentation accuracy. Despite these advancements, developing models that generalize well across diverse retinal datasets remains challenging. Differences in image acquisition techniques, resolutions, and patient demographics can hinder a model's performance when applied

to unseen data sources. Addressing this issue requires strategies that enhance a model's ability to learn robust and transferable features.

Knowledge distillation is an effective method for transferring knowledge from a larger, complex teacher model to a smaller, more efficient student model (Hinton et al., 2015). By learning to mimic the teacher's outputs, the student model can achieve competitive performance with reduced complexity. Knowledge enhancement extends this concept by leveraging the expertise of multiple teacher models, allowing the student model to capture a broader range of features and improve generalization (Wang & Yoon, 2021). Several studies have explored knowledge distillation and enhancement in medical imaging. These techniques have been explored to improve model efficiency and performance. For instance, Qin et al. (2021) employed knowledge distillation to enhance the segmentation of medical scans, achieving state-of-the-art results with reduced computational complexity. Shen et al. (2019) utilized knowledge distillation to improve lesion detection in mammography by transferring knowledge from a teacher model trained on a large dataset to a student model with fewer parameters. Zhang and Lu (2024) proposed a knowledge distillation framework for skin lesion segmentation, transferring knowledge from teacher network to enhance performance.

In this study, we propose UKnow-Net, a knowledge-enhanced U-Net architecture designed to improve retinal vessel segmentation across multiple datasets. UKnow-Net addresses the challenges of variability and complexity in retinal images by employing a multi-step process that utilizes the strengths of multiple teacher networks. Each teacher network is trained separately on different datasets—DRIVE, CHASE_DB1, DCA1, and CHUAC—allowing them to specialize in the unique features and patterns specific to their respective datasets. This specialization ensures that each teacher network becomes an expert in its domain, which is crucial for accurately capturing the diverse characteristics of retinal images. A key aspect of UKnow-Net is using pseudo-labels generated by the teacher networks. These pseudo-labels represent the distilled knowledge and expertise of the teacher networks, serving as a rich source of information for training the student network. Using these pseudo-labels effectively distills the domain-specific knowledge from the teacher networks into the student network. This process allows the student network to learn from the teacher networks' collective expertise, enhancing its ability to generalize across different datasets. The experimental studies conducted demonstrate that UKnow-Net outperforms traditional handcrafted networks and state-of-the-art models in several key metrics, including sensitivity, specificity, F1 score, and intersection over union (IoU). UKnowNet-A and UKnowNet-B, the two variants of the proposed model, show superior performance in detecting true positives and achieving balanced precision and recall across different datasets. For instance, UKnowNet-A achieved a sensitivity of 85.37% on the DRIVE dataset, surpassing the handcrafted networks. On the CHASE_DB1 dataset, UKnowNet-A excelled in sensitivity with 89.84%, significantly outperforming the handcrafted networks. The integration of pseudo-labels and ground truths in UKnowNet-B provides a more robust learning framework, allowing it to generalize better across different datasets. Our contributions are as follows:

1. **Unified Model for Multi-Dataset Segmentation:** I develop a single student model capable of segmenting retinal vessels in four publicly available datasets (DRIVE, CHASE_DB1, DCA1, and CHUAC), addressing the challenge of variability across data sources.
2. **Knowledge Enhancement via Teacher Networks:** I train separate teacher networks on each dataset to specialize in their respective domains. By generating pseudo-labels from these specialized networks, we capture diverse feature representations.
3. **Integration of Pseudo-Labels for Student Training:** The student network is trained using the ensemble of pseudo-labels from all teacher networks, effectively distilling knowledge from multiple experts and enhancing generalization.
4. **Comprehensive Evaluation:** We evaluate UKnow-Net on test sets from all four datasets, demonstrating improved segmentation performance and robustness compared to baseline models and existing methods.
5. **Fair Comparison and Reproducibility:** I have publicly shared the source code on [GitHub](#) and the best model weight on the same platform.

The rest of this paper is structured as follows: Section 2 outlines the architecture of UKnow-Net and details the experimental setup. Section 3 presents the results and provides a comparative analysis with current state-of-the-art methods. Lastly, Section 4 concludes the study and proposes possible directions for future research.

2. MATERIAL AND METHOD

2.1. UKnow-Net: Knowledge-Enhanced U-Net

U-Net is a convolutional neural network architecture proposed for biomedical image segmentation (Ronneberger et al., 2015). It has a U-shaped structure and consists of encoder and decoder blocks. Encoder networks extract helpful information and features from a given image, followed by maximum pooling layers that decrease the image size by half. After performing encoder blocks, a latent representation of the image is obtained. Then, the image is reconstructed in decoder blocks using deconvolution operations, doubling the image size. It also has skip connections, which allow features from earlier layers to be reused in later layers. This design allows U-Net to effectively utilize both high-level and low-level features, making it particularly well-suited for applications in medical imaging, such as tumor detection and organ segmentation. Its ability to work with relatively small datasets and produce high-quality segmentation maps has led to its widespread adoption in various fields beyond medical imaging, including satellite image analysis and autonomous driving.

Knowledge distillation is a machine learning method where a smaller, more efficient model, called the student, learns from a larger, more complex model, known as the teacher. The aim is to improve the student model's performance by leveraging the insights, patterns, and features learned by the teacher model. This allows the student model to reach a similar level of accuracy and effectiveness as the teacher while being more efficient and suitable for deployment in resource-limited environments. The process involves training the student model to mimic the teacher model's outputs by reducing the discrepancy between their predictions. Knowledge enhancement is the objective of distillation. Knowledge enhancement aims to train student networks to develop more generalized feature representations by leveraging the expertise of specialized teacher networks. This approach enables the student networks to consistently deliver strong performance across various tasks.

In this study, I have proposed UKnow-Net to improve the segmentation performance of the U-Net model for different retinal vessel segmentation problems. Figure 1 illustrates the general structure of the proposed method. The proposed method includes three steps: (1) Four teacher networks are trained separately on different datasets: DRIVE, CHASEDB1, DCA1, and CHUAC. Each teacher network specializes in learning the features and patterns specific to its respective dataset, ensuring that it becomes an expert in that particular domain. I have selected the original U-Net structure (Ronneberger et al., 2015) as the teacher network for each dataset. (2) Step 2 involves using these pre-trained teacher networks to generate pseudo-labels. Each pre-trained teacher network (trained at Step 1) produces pseudo-labels for its corresponding dataset, which are essentially the predictions made by the teacher networks. These pseudo-labels serve as a form of distilled knowledge that will be used to train the student network. (3) In Step 3, the student network is trained using the combination of pseudo-labels generated by all the teacher networks. This approach allows the student network to learn from the collective expertise of all the teacher networks, potentially enhancing its ability to generalize across different datasets. Finally, the student network is evaluated on test sets from all four datasets (DRIVE, CHASEDB1, DCA1, CHUAC) to evaluate its performance and generalization capabilities. This method leverages the strengths of multiple teacher networks to create a robust student model, aiming for improved performance on unseen data.

UKnow-Net addresses the challenges of variability and complexity in retinal images by employing a multi-step process that utilizes the strengths of multiple teacher networks. Each of these teacher networks is trained separately on different datasets—DRIVE, CHASEDB1, DCA1, and CHUAC—allowing them to specialize in the unique features and patterns specific to their respective datasets. This specialization ensures that each teacher network becomes an expert in its domain, which is crucial for accurately capturing the diverse characteristics of retinal images. A key aspect of UKnow-Net is using pseudo-labels generated by the teacher networks. These pseudo-labels represent the distilled knowledge and expertise of the teacher networks, serving as a rich source of information for training the student network. Using these pseudo-labels effectively distills the domain-specific knowledge from the teacher networks into the student network. This process allows the student network to learn from the teacher networks' collective expertise, enhancing its ability to generalize

across different datasets. The robustness and versatility of UKnow-Net are further highlighted by its ability to create a robust student model that performs well across various conditions and datasets. By training the student network on the combination of pseudo-labels from all teacher networks, the method ensures that the student network can generalize effectively to unseen data. This collective learning approach improves the model's performance on test sets from all four datasets and makes it a versatile tool for retinal vessel segmentation. Overall, UKnow-Net represents a significant step forward in developing models that can handle the complexities of retinal images, ultimately aiming for improved performance and generalization capabilities.
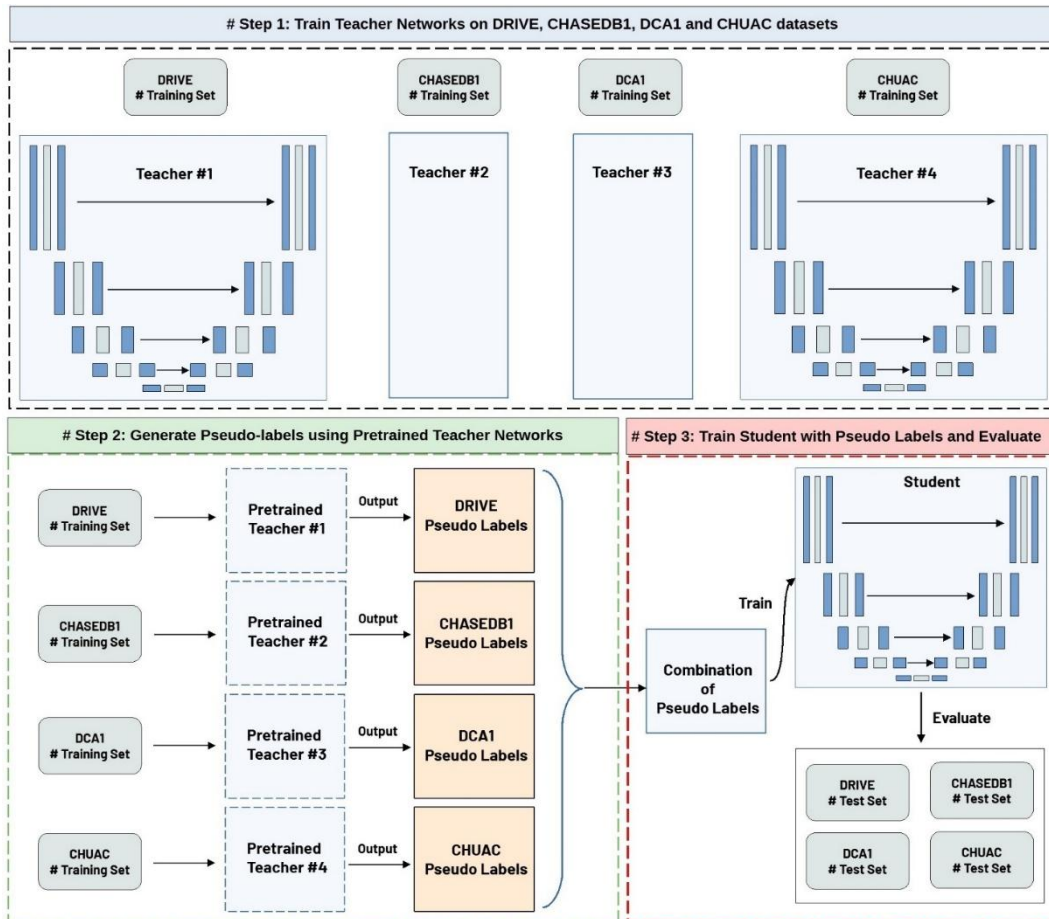
Figure 1. *Overview of the UKnow-Net*

2.2. Experimental Design

2.2.1. Datasets

I have selected the most commonly used retinal vessel segmentation datasets, DRIVE, CHASE_DB1, DCA1, and CHUAC, to evaluate the proposed method. These datasets are widely recognized and frequently used in the field of retinal vessel segmentation (Liu et al., 2022; Kuş & Kiraz, 2023; Qu et al., 2023). They offer a diverse range of imaging modalities (CHUAC-DCA1 vs DRIVE-CHASE_DB1), resolutions, and patient demographics, which are crucial for evaluating the generalization capabilities of our proposed model.

Figure 2 presents the exemplary two images and corresponding ground truths for each dataset.

Digital Retinal Images for Vessel Extraction (DRIVE) (Staal et al., 2004**)**: It is a valuable resource for medical image analysis, specifically for retinal vessel segmentation. It consists of high-resolution retinal images from 40 subjects collected as part of a diabetic retinopathy screening program in the Netherlands. Each image is manually annotated by experts to identify the blood vessels. Researchers and practitioners use this dataset to develop and benchmark automated methods for detecting and analyzing retinal vasculature, crucial in diagnosing and monitoring conditions like diabetic retinopathy, hypertension, and cardiovascular diseases.

I have selected annotations created by the first expert. The dataset contains 40 images, each sized 565×584, and the first 20 images are used for training, while the rest are used for testing, as in other studies (Liu et al., 2022).

CHUAC (Carballal et al., 2018): The dataset originates from the University Hospital Complex of a Coruña in Spain. It is a collection of coronary angiography retinal images gathered for research focused on ophthalmic diseases. It is a valuable resource for developing and testing algorithms for the early detection and assessment of conditions such as diabetic retinopathy and age-related macular degeneration. The dataset contains 30 samples with 512×512 sized images. The first 20 images are used to train the model, and others are used for evaluation (Samuel & Veeramalai, 2021).

The Child Heart and Health Study in England Database 1 (CHASE_DB1) (Carballal et al., 2018): It is a specialized dataset consisting of retinal images collected from a pediatric population. Specifically, the images are obtained from children aged between 7 and 8 years old as part of a study investigating cardiovascular risk factors in early life. CHASE_DB1 includes high-quality retinal photographs along with expert annotations of the blood vessel network. This dataset is essential for researchers focusing on the development of image processing algorithms for vessel segmentation and analysis in children's retinal images. It consists of 28 colored images sized at 999×960 sized. The images are annotated by two different experts, and I have used the annotations made by the first expert. I have used the first 20 images out of 28 for training and the remaining for testing (Liu et al., 2022; Li et al., 2023)

DCA1 (Cervantes-Sanchez et al., 2019): The DCA1 dataset, which stands for Digital Retinal Images for Vessel Extraction, is a widely used collection of retinal images in the medical imaging community for developing and evaluating algorithms. The dataset contains color fundus images showing various retinal conditions, which are crucial for researchers working on automated detection and analysis of retinal diseases. Each image in DCA1 is often accompanied by expert annotations, including segmentation maps of retinal vessels and identification of pathological features. Utilizing the DCA1 dataset enables the advancement of computer-aided diagnostic systems, contributing to improved screening processes and patient care in ophthalmology. It includes 134 samples sized at 300x300. I have chosen 100 images for model training and the remaining 34 for model evaluation (Kuş & Kiraz, 2023).
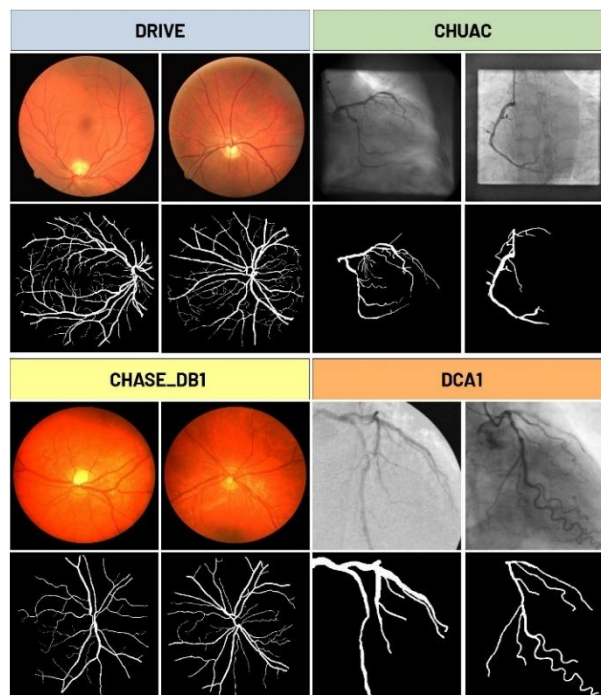
Figure 2. Exemplary images from DRIVE, CHUAC, CHASE_DB1, and DCA1 datasets. In the figure, the first row represents the input image, and the second row represents the corresponding ground truth image.

2.2.2. Pre-processing

In the training phases, I employ several preprocessing steps. First, I transform colored images into grayscale and normalize them to standardize the input data. To increase the volume of training data, we extract image patches using a sliding window of size 48×48 pixels with a stride of 48 pixels; overlapping patches are excluded to maintain data independence. I further enhance the diversity of the training dataset by applying data augmentation techniques, including random horizontal and vertical flips and rotations at angles of 90°, 180°, and 270° (Kuş & Kiraz, 2023). Notably, I have not performed any augmentation steps or patch generation to samples in the test set. I have used raw test images to evaluate the actual performance of the model.

2.2.3. Implementation Details

Pytorch library is used for all implementations. During both the training and test phases, each network is trained for 200 epochs. For all experiments, the Adam optimizer and Binary Cross Entropy (BCE) loss are used. I have set the learning rate to 1×10^{-3} and used the batch size of 128. The experiments are executed on a system equipped with a Ryzen 5600X processor, RTX 3060 GPU with 12 GB of memory, and 16 GB of RAM. The source codes are shared on [Github](#).

2.2.4. Performance Measures

I have used several performance measures, including accuracy, sensitivity, specificity, intersection over union (IoU), and F1-score, to evaluate the proposed methods. Sensitivity and specificity measure the model's ability to correctly identify true positives and true negatives, respectively, which are critical for medical applications. The F1 score balances precision and recall, offering insight into the model's overall accuracy. IoU evaluates the spatial accuracy of the segmentation, which is essential for assessing the overlap between predicted and actual vessel structures. Each measure offers a unique perspective on the methods' effectiveness, ensuring a comprehensive assessment across different evaluation criteria. I have also selected these measures to make a fair comparison with reported results in recent literature. Accuracy indicates the overall correctness of the methods. It is the proportion of all predictions that were correct. While useful, accuracy alone might not be sufficient, especially if the data is imbalanced, with some classes being much more common than others. Sensitivity, also known as recall or true positive rate, measures how effectively the methods identify positive cases. It quantifies the percentage of true positives that are accurately identified. This metric shows the ability of the methods to detect the presence of a condition or feature. Specificity, or true negative rate, measures how effectively the methods identify negative cases. It calculates how many actual negatives are accurately classified. Intersection over Union (IoU) evaluates the overlap between the predicted results and the ground truth. Calculated as the area of overlap divided by the area of union between the prediction and the actual result, IoU provides insight into the spatial accuracy of the methods. The F1-score, which calculates their harmonic mean, offers a balance between recall and precision. This metric is especially useful when the data has an imbalanced class distribution, as it accounts for both false positives and false negatives.

3. RESULTS AND DISCUSSION

In this section, I have compared UKnowNet with handcrafted networks, other U-shaped networks, and neural architecture search studies in terms of Sensitivity, Specificity, F1 Score, and Intersection over Union measures. Tables 1 and 2 present the results DRIVE-CHASE_DB1 and DCA1-CHUAC datasets separately. In these tables, red and blue colors highlight the two best performance results obtained for each metric.

3.1. Comparison with Handcrafted Networks

The handcrafted networks, namely U-Net, UNet++, and Attention U-Net, have been foundational in medical image segmentation, particularly for tasks like retinal vessel segmentation. These models are characterized by their U-shaped architectures, which facilitate the capture of both local and global features through a series of downsampling and upsampling layers. Despite their simplicity and effectiveness, these models often rely heavily on the availability of labeled data for training.

In contrast, UKnowNet-A and UKnowNet-B represent more recent advancements that leverage both pseudo-labels and ground truths from multiple datasets, including DRIVE, CHASE_DB1, CHUAC, and DCA.

UKnowNet-A, trained solely on pseudo-labels, demonstrates the potential of semi-supervised learning to achieve competitive performance without extensive labeled data. This approach is particularly advantageous in scenarios where obtaining ground truth annotations is challenging or resource-intensive. UKnowNet-B, on the other hand, combines pseudo-labels with ground truths, likely enhancing its performance by utilizing the strengths of both semi-supervised and supervised learning paradigms.

Table 1. *Performance evaluation of retinal vessel segmentation methods on DRIVE and CHASE_DB1 datasets. The comparison includes traditional handcrafted networks (U-Net, UNet++, Attention U-Net), state-of-the-art models, neural architecture search studies (MedUNAS GA, ODE) and our proposed UKnowNet variants. Metrics include Sensitivity (SEN), Specificity (SPE), F1 Score (F1), and Intersection over Union (IOU). The checkmark (✓) indicates U-shaped architecture. Red indicates the best performance for each metric across the evaluated methods, and blue signifies the second-best performance for each metric.*

Methods	U shape	DRIVE				CHASE_DB1			
		SEN	SPE	F1	IOU	SEN	SPE	F1	IOU
U-Net[(Ronneberger et al., 2015)]	✓	80.57	98.33	81.41	68.64	76.50	**98.84**	78.98	65.26
UNet++[(Zhou et al., 2018)]	✓	78.91	98.50	81.14	68.27	83.57	98.32	80.15	66.88
Attention U-Net[(Oktay et al., 2018)]	✓	79.06	98.31	80.39	67.21	83.84	98.20	79.64	66.17
HRNet[(Sun et al., 2019)]	✗	80.40	**98.64**	82.65	**70.43**	84.43	98.47	81.48	**68.75**
CS-Net[(Mou et al., 2019)]	✓	81.70	98.54	80.39	70.17	84.00	98.32	80.42	67.25
AG-Net[(Zhang et al., 2019)]	✓	81.00	98.48	-	69.65	81.86	98.48	-	66.69
RVSeg-Net[(Wang et al., 2020)]	✓	81.07	98.45	-	-	80.69	98.36	-	-
SCS-Net[(Wu et al., 2021)]	✓	82.89	98.38	-	-	83.65	98.39	-	-
SGL[(Zhou et al., 2021)]	✓	83.80	98.34	83.16	-	86.90	98.43	82.71	-
VSSCNet[(Samuel& Veeramalai, 2021)]	✗	78.27	98.21	-	-	72.33	**98.65**	-	-
RV-GAN[(Kamran et al., 2021)]	✗	79.27	**99.69**	**86.90**	-	81.99	98.06	**89.57**	-
FR-UNet[(Liu et al., 2022)]	✓	83.56	98.37	83.16	**71.20**	**87.98**	98.14	81.51	**68.82**
TP-Net[(Qu et al., 2023)]	✗	**87.49**	97.58	**85.69**	-	86.00	98.41	**85.18**	-
MedUNAS GA[(Kuş & Kiraz, 2023)]	✓	84.54	**98.64**	82.06	69.59	86.52	98.44	79.50	66.03
MedUNAS ODE[(Kuş & Kiraz, 2023)]	✓	83.41	98.36	82.18	69.77	84.50	98.60	80.22	67.01
UKnowNet-A	✓	**85.37**	97.87	82.10	69.66	**89.84**	97.40	78.57	64.76
UKnowNet-B	✓	85.12	98.04	82.65	70.44	87.38	97.94	80.14	66.90

When comparing the performance metrics, UKnowNet-A and UKnowNet-B generally outperform the handcrafted networks across several key metrics. For instance, UKnowNet-A achieves a sensitivity of 85.37% on the DRIVE dataset, surpassing the handcrafted networks, which range from 78.91% to 80.57%. Similarly, UKnowNet-B shows improved specificity and F1 scores, indicating better overall accuracy and balance between precision and recall. This suggests that the integration of pseudo-labels and ground truths in UKnowNet-B provides a more robust learning framework, allowing it to generalize better across different

datasets. On the DRIVE dataset, UKnowNet-A and UKnowNet-B both demonstrate superior sensitivity compared to the handcrafted networks, with UKnowNet-A achieving 85.37% and UKnowNet-B 85.12%, significantly higher than the 80.57% of U-Net, the best among the handcrafted models. This indicates that the UKnowNet models are more effective at correctly identifying true positives. In terms of specificity, the handcrafted networks maintain a slight edge, particularly UNet++ with 98.50%, while UKnowNet-B closely follows at 98.04%, suggesting a minor trade-off in specificity for the increased sensitivity seen in the UKnowNet models. For the F1 score, which balances precision and recall, UKnowNet-B leads with 82.65%, surpassing the handcrafted networks, with U-Net at 81.41% being the highest among them. This suggests that UKnowNet-B offers a more balanced performance. The Intersection over Union (IOU) metric further highlights UKnowNet-B's superior segmentation accuracy, achieving 70.44%, compared to U-Net's 68.64%, the best among the handcrafted models.

On the CHASE_DB1 dataset, UKnowNet-A excels in sensitivity with 89.84%, significantly outperforming the handcrafted networks, where Attention U-Net achieves the highest at 83.84%. This highlights UKnowNet-A's strong ability to detect true positives, likely due to its training with pseudo-labels. However, in terms of specificity, the handcrafted networks, particularly U-Net with 98.84%, outperform the UKnowNet models, which show a slight decrease, with UKnowNet-B at 97.94%. This suggests a trade-off where the UKnowNet models prioritize sensitivity over specificity. The F1 score for UKnowNet-B on CHASE_DB1 is 80.14%, matching UNet++ and indicating a balanced performance between precision and recall. In terms of IOU, UKnowNet-B slightly surpasses UNet++ with 66.90%, reflecting its improved segmentation accuracy. Overall, the UKnowNet models, particularly UKnowNet-B, demonstrate the benefits of integrating pseudo-labels and ground truths, achieving higher sensitivity and balanced F1 scores, while the handcrafted networks maintain high specificity, especially on the CHASE_DB1 dataset. This comparison underscores the effectiveness of modern training strategies in enhancing model performance across different datasets.

Table 2. *Performance evaluation of retinal vessel segmentation methods on DCA1 and CHUAC datasets. The comparison includes traditional handcrafted networks (U-Net, UNet++, Attention U-Net), state-of-the-art models, neural architecture search studies (MedUNAS GA, ODE) and our proposed UKnowNet variants. Metrics include Sensitivity (SEN), Specificity (SPE), F1 Score (F1), and Intersection over Union (IOU). The checkmark (✓) indicates U-shaped architecture. Red indicates the best performance for each metric across the evaluated methods, and blue signifies the second-best performance for each metric.*

Methods	U shape	DCA1				CHUAC			
		SEN	SPE	F1	IOU	SEN	SPE	F1	IOU
U-Net[(Ronneberger et al., 2015)]	✓	78.16	98.66	77.35	63.07	58.81	**99.40**	67.68	51.15
UNet++[(Zhou et al., 2018)]	✓	79.54	98.62	77.86	63.75	66.87	**99.37**	73.23	57.77
Attention U-Net[(Oktay et al., 2018)]	✓	79.86	98.53	77.48	63.24	65.26	99.13	71.54	55.69
HRNet[(Sun et al., 2019)]	✗	80.07	98.76	**79.19**	**65.54**	74.56	99.06	75.26	60.33
CS-Net[(Mou et al., 2019)]	✓	78.95	98.67	77.90	63.80	67.35	99.18	71.71	55.89
FR-UNet[(Liu et al., 2022)]	✓	82.48	98.75	**80.22**	**67.08**	**81.71**	98.68	**76.01**	**61.51**
VSSCNet[(Samuel& Veeramalai, 2021)]	✗	77.28	98.09	-	-	78.92	97.97	-	-
MedUNAS GA[(Kuş & Kiraz, 2023)]	✓	80.89	**99.05**	78.20	64.33	78.65	99.16	71.96	56.31
MedUNAS ODE[(Kuş & Kiraz, 2023)]	✓	**84.12**	**98.89**	78.22	64.37	78.29	99.12	74.56	59.54
UKnowNet-A	✓	81.49	98.58	78.30	64.47	**79.22**	98.72	**75.39**	**60.63**
UKnowNet-B	✓	83.18	98.38	78.01	64.11	73.42	99.04	74.01	58.94

On the DCA1 dataset, UKnowNet-A and UKnowNet-B demonstrate superior performance compared to the handcrafted networks (U-Net, UNet++, and Attention U-Net) across all evaluated metrics. In terms of sensitivity, UKnowNet-B achieves 83.18%, and UKnowNet-A follows with 81.49%, both surpassing the handcrafted networks, where the highest sensitivity is 79.86% by Attention U-Net. This indicates that the UKnowNet models are more effective at detecting true positives. Although the handcrafted networks maintain slightly higher specificity, with U-Net leading at 98.66%, the UKnowNet models show a trade-off, achieving slightly lower specificity but significantly higher sensitivity. For the F1 score, which balances precision and recall, UKnowNet-A and UKnowNet-B achieve 78.30% and 78.01%, respectively, outperforming the handcrafted networks, with UNet++ having the highest F1 score among them at 77.86%. In terms of IOU, both UKnowNet models also lead, with UKnowNet-A achieving 64.47% and UKnowNet-B 64.11%, compared to UNet++'s 63.75%, the best among the handcrafted models.

On the CHUAC dataset, UKnowNet-A particularly excels, achieving a sensitivity of 79.22%, which is significantly higher than the handcrafted networks, where UNet++ reaches 66.87% as the highest. This highlights UKnowNet-A's superior ability to detect true positives. In terms of specificity, the handcrafted networks perform slightly better, with U-Net achieving 99.40%, while UKnowNet-B maintains a competitive specificity of 99.04%. For the F1 score, UKnowNet-A achieves 75.39%, surpassing all handcrafted networks, with UNet++ having the highest F1 score among them at 73.23%. This suggests that UKnowNet-A offers a more balanced performance between precision and recall. In terms of IOU, UKnowNet-A again leads with 60.63%, compared to UNet++'s 57.77%, indicating superior segmentation accuracy.

Overall, the comparison highlights the evolution from traditional handcrafted networks to more sophisticated models like UKnowNet-A and UKnowNet-B, which effectively utilize both labeled and unlabeled data to enhance performance. This shift underscores the growing importance of leveraging diverse data sources and advanced training strategies in developing state-of-the-art models for medical image analysis.

3.2. Comparison with State-of-the-art Networks

When comparing UKnowNet-A and UKnowNet-B with other state-of-the-art models, it's insightful to separate the analysis based on whether the network architecture is U-shaped, as the UKnowNet models are proposed as U-shaped networks.

For the DRIVE dataset, UKnowNet-A and UKnowNet-B demonstrate strong performance among U-shaped networks. UKnowNet-A achieves a sensitivity of 85.37%, and UKnowNet-B follows closely with 85.12%, both outperforming other U-shaped models like SGL and SCS-Net, which have sensitivities of 82.89% and 83.80%, respectively. This indicates that the UKnowNet models are particularly effective at identifying true positives. In terms of specificity, UKnowNet-B achieves 98.04%, which is competitive with other U-shaped models such as CS-Net (98.54%) and AG-Net (98.48%). The F1 score for UKnowNet-B is 82.65%, surpassing CS-Net (80.39%) and closely matching FR-UNet (83.16%), suggesting a balanced performance between precision and recall. For the IOU metric, UKnowNet-B achieves 70.44%, slightly lower than FR-UNet's 71.20% but higher than CS-Net's 70.17%, reflecting strong segmentation accuracy.

On the CHASE_DB1 dataset, UKnowNet-A excels with a sensitivity of 89.84%, leading all U-shaped models and highlighting its capability in detecting true positives effectively. However, in terms of specificity, UKnowNet-B's 97.94% is slightly lower than other U-shaped models like AG-Net, which achieves 98.48%. The F1 score for UKnowNet-B is 80.14%, competitive but slightly lower than FR-UNet's 81.51%. For IOU, UKnowNet-B achieves 66.90%, close to FR-UNet's 68.82%, indicating robust segmentation performance.

In contrast, non-U-shaped models like HRNet and RV-GAN show different strengths. On the DRIVE dataset, HRNet achieves high specificity (98.64%) and IOU (70.43%), comparable to UKnowNet-B. RV-GAN excels in specificity (99.69%) and F1 score (86.90%), outperforming the UKnowNet models in these metrics. On the CHASE_DB1 dataset, VSSC Net achieves the highest specificity (98.65%) but has lower sensitivity (72.33%). RV-GAN leads in F1 score (89.57%), significantly higher than the UKnowNet models.

On the DCA1 dataset, UKnowNet-A and UKnowNet-B demonstrate superior performance among U-shaped networks. UKnowNet-B achieves a sensitivity of 83.18%, and UKnowNet-A follows closely with 81.49%,

both showing robust performance in detecting true positives. In terms of specificity, UKnowNet models have slightly lower values, with UKnowNet-A at 98.58% and UKnowNet-B at 98.38%, compared to FR-UNet's 98.75%. This suggests a trade-off where UKnowNet models prioritize sensitivity over specificity. For the F1 score, UKnowNet-A achieves 78.30%, and UKnowNet-B achieves 78.01%, both competitive but slightly lower than FR-UNet's leading score of 80.22%. In terms of IOU, UKnowNet-A achieves 64.47%, and UKnowNet-B achieves 64.11%, both slightly lower than FR-UNet's 67.08%.

On the CHUAC dataset, UKnowNet-A achieves a better sensitivity value with 79.22% than other U-shaped models (except FR-UNet). UKnowNet-B, with a sensitivity of 73.42%, also performs well, though slightly lower than some other models. In terms of specificity, UKnowNet-B achieves 99.04%, which is competitive with other U-shaped models like CS-Net, which achieves 99.18%. For the F1 score, UKnowNet-A achieves 75.39%, the second highest among U-shaped models, indicating a balanced performance between precision and recall. This surpasses FR-UNet's 76.01%, which is the highest among other models. In terms of IOU, UKnowNet-A achieves 60.63%, the second highest among U-shaped models, reflecting its strong segmentation accuracy. UKnowNet-B achieves an IOU of 58.94%, which is competitive but slightly lower than FR-UNet's 61.51%.

In contrast to U-shaped models, non-U-shaped models like HRNet and VSSC Net demonstrate distinct advantages. On the DCA1 dataset, HRNet achieves a high specificity of 98.76% and an F1 score of 79.19%, making its performance comparable to that of UKnowNet models. However, VSSC Net exhibits lower sensitivity at 77.28% compared to UKnowNet models. On the CHUAC dataset, HRNet again shows strong performance with a sensitivity of 74.56% and an F1 score of 75.26%, remaining competitive with UKnowNet models. In contrast, VSSC Net achieves a higher sensitivity of 78.92%, but its specificity is lower at 97.97%.

3.3. Comparison with Neural Architecture Search Studies

A detailed comparison of UKnowNet-A and UKnowNet-B with neural architecture search studies (MedUNAS GA and MedUNAS ODE) reveals distinct performance characteristics across different metrics and datasets. On the DRIVE dataset, UKnowNet models demonstrate superior sensitivity, with UKnowNet-A achieving 85.37% and UKnowNet-B reaching 85.12%, both surpassing MedUNAS GA (84.54%) and MedUNAS ODE (83.41%). This indicates that UKnowNet models are more effective at detecting true positives in vessel segmentation. However, in terms of specificity, MedUNAS GA leads with 98.64%, followed by MedUNAS ODE at 98.36%, while UKnowNet-B achieves 98.04% and UKnowNet-A reaches 97.87%. The F1 score comparison on the DRIVE dataset shows UKnowNet-B achieving the highest value at 82.65%, slightly outperforming both MedUNAS ODE (82.18%) and MedUNAS GA (82.06%), with UKnowNet-A following closely at 82.10%. This indicates that UKnowNet-B offers the most balanced performance between precision and recall. In terms of IOU, UKnowNet-B leads with 70.44%, demonstrating superior segmentation accuracy compared to MedUNAS ODE (69.77%) and MedUNAS GA (69.59%), while UKnowNet-A achieves 69.66%.

On the CHASE_DB1 dataset, the performance differences become more pronounced. UKnowNet-A achieves remarkable sensitivity at 89.84%, significantly outperforming MedUNAS GA (86.52%) and MedUNAS ODE (84.50%), with UKnowNet-B also showing strong performance at 87.38%. However, the specificity results show MedUNAS ODE leading at 98.60%, followed by MedUNAS GA at 98.44%, while UKnowNet-B achieves 97.94% and UKnowNet-A reaches 97.40%. This further emphasizes the sensitivity-specificity trade-off in the UKnowNet models' design. The F1 score comparison on CHASE_DB1 shows MedUNAS ODE achieving 80.22%, closely followed by UKnowNet-B at 80.14% and MedUNAS GA at 79.50%, while UKnowNet-A reaches 78.57%. For IOU, MedUNAS ODE leads with 67.01%, followed by UKnowNet-B at 66.90% and MedUNAS GA at 66.03%, with UKnowNet-A achieving 64.76%. These results suggest that while UKnowNet models excel in sensitivity, MedUNAS models maintain more balanced performance across all metrics.

On the DCA1 dataset, MedUNAS ODE demonstrates the highest sensitivity at 84.12%, followed closely by UKnowNet-B at 83.18%, while UKnowNet-A achieves 81.49% and MedUNAS GA reaches 80.89%. This indicates that MedUNAS ODE is particularly effective at detecting true positives, though UKnowNet-B maintains very competitive performance. In terms of specificity, MedUNAS models show superior

performance, with MedUNAS GA achieving the highest value at 99.05% and MedUNAS ODE following at 98.89%, while UKnowNet-A and UKnowNet-B achieve 98.58% and 98.38% respectively. This suggests that MedUNAS models are more effective at reducing false positives. The F1 score comparison reveals a close competition, with UKnowNet-A slightly leading at 78.30%, followed by MedUNAS ODE at 78.22%, MedUNAS GA at 78.20%, and UKnowNet-B at 78.01%. These nearly identical F1 scores indicate that all models maintain a similar balance between precision and recall. For the IOU metric, UKnowNet-A achieves the highest value among these models at 64.47%, slightly surpassing MedUNAS ODE (64.37%), MedUNAS GA (64.33%), and UKnowNet-B (64.11%), suggesting slightly better segmentation accuracy.

On the CHUAC dataset, UKnowNet-A leads in sensitivity with 79.22%, slightly outperforming MedUNAS GA (78.65%) and MedUNAS ODE (78.29%), while UKnowNet-B achieves 73.42%. This demonstrates UKnowNet-A's superior ability to detect true positives in this dataset. However, in terms of specificity, MedUNAS models again show stronger performance, with MedUNAS GA achieving 99.16% and MedUNAS ODE reaching 99.12%, compared to UKnowNet-B's 99.04% and UKnowNet-A's 98.72%. The F1 score comparison on CHUAC shows UKnowNet-A achieving 75.39%, followed by MedUNAS ODE at 74.56%, UKnowNet-B at 74.01%, and MedUNAS GA at 71.96%. This indicates that UKnowNet-A provides the most balanced performance between precision and recall. In terms of IOU, UKnowNet-A leads with 60.63%, followed by MedUNAS ODE at 59.54%, UKnowNet-B at 58.94%, and MedUNAS GA at 56.31%, demonstrating UKnowNet-A's superior segmentation accuracy on this dataset.

Overall, this comparison highlights the distinct strengths of each approach: UKnowNet models, particularly UKnowNet-A, outperform in sensitivity, true positive detection, and balanced performance, while MedUNAS models offer higher specificity. UKnowNet-B emerges as a strong compromise, achieving competitive results across all metrics while maintaining the sensitivity advantages of the UKnowNet architecture. These differences reflect the underlying design and training strategies of each approach, with UKnowNet models potentially being more suitable for applications where high sensitivity and balanced performance are crucial, while MedUNAS models might be preferred in scenarios requiring more specificity.

3.4. Evaluation of Pre-trained Networks with Fine-tuning

In this study, I have conducted an ablation analysis to evaluate whether conventional pre-trained convolutional neural networks—DenseNet-121, EfficientNet, ResNet-18, ResNet-34, and ResNet-50—initialized with ImageNet weights and fine-tuned over 50 epochs (200 epochs for UKnowNet-A) using identical training protocols as proposed UKnowNet-A model (see Section 2.1), could achieve performance comparable to UKnowNet-A. I have selected these pre-trained convolutional neural networks for the following reason: DenseNet-121 offers a good balance between model complexity and performance, making it suitable for medical image analysis tasks where feature reuse is beneficial. EfficientNet models are designed to achieve high performance with fewer parameters by scaling depth, width, and resolution. ResNet architectures are renowned for their residual learning framework, which helps in training deeper networks by diminishing the vanishing gradient problem. The evaluation focused on key performance metrics: Sensitivity, Specificity, F1 Score, and Intersection over Union across the four datasets. The results are shown in Figure 3. In Figure 3, Best represents the obtained results from UKnowNet-A for each metric and dataset.

For DRIVE, EfficientNet stands out with the highest Sensitivity (83.15%) and IOU (67.18%), indicating its superior ability to identify positive instances correctly and accurately overlap predictions with ground truth. ResNet-50 also performs commendably, with a SEN of 76.83% and an IOU of 66.71%. However, the "Best" results surpass all models, achieving a SEN of 85.37%, SPE of 97.87%, F1 of 82.1%, and IOU of 69.66%, demonstrating the potential of UKnowNet with pseudo-labels.

On CHASE_DB1, EfficientNet again leads with a high SEN of 87.32%, significantly outperforming other models. ResNet-34 follows with a respectable SEN of 80.04%. The IOU metrics reveal ResNet-34 as the best-performing network among the models with 62.57%, closely following the "Best" result of 64.76%. Notably, despite EfficientNet's high SEN, its F1 score (72.76%) is lower than the "Best," highlighting a trade-off between sensitivity and overall balance captured by the F1 metric.

Performance across models is more uniform in DCA1 dataset. ResNet-34 achieves the highest SEN (82.2%) and competitive IOU (61.49%), while DenseNet-121 and ResNet-18 maintain solid performances with SENs around 81%. The "Best" results continue to lead with an SEN of 81.49% and IOU of 64.47%, indicating that even marginal improvements can be crucial in specific applications. The F1 scores are relatively close among models, with the "Best" achieving the highest at 78.3%.

CHUAC dataset presents the most significant performance gaps among the models. EfficientNet achieves the highest SEN (72.95%) among the networks, yet it falls short of the "Best" result by over 6 percentage points. ResNet variants exhibit lower SENs, with ResNet-18 at 62.12%. Specificity remains high across all models, hovering around 98%, which underscores their effectiveness in correctly identifying negative instances. The "Best" results dramatically outperform individual models across all metrics, particularly in SEN (79.22%) and F1 Score (75.39%), highlighting substantial gains possible through UKnowNet and pseudo-label techniques.
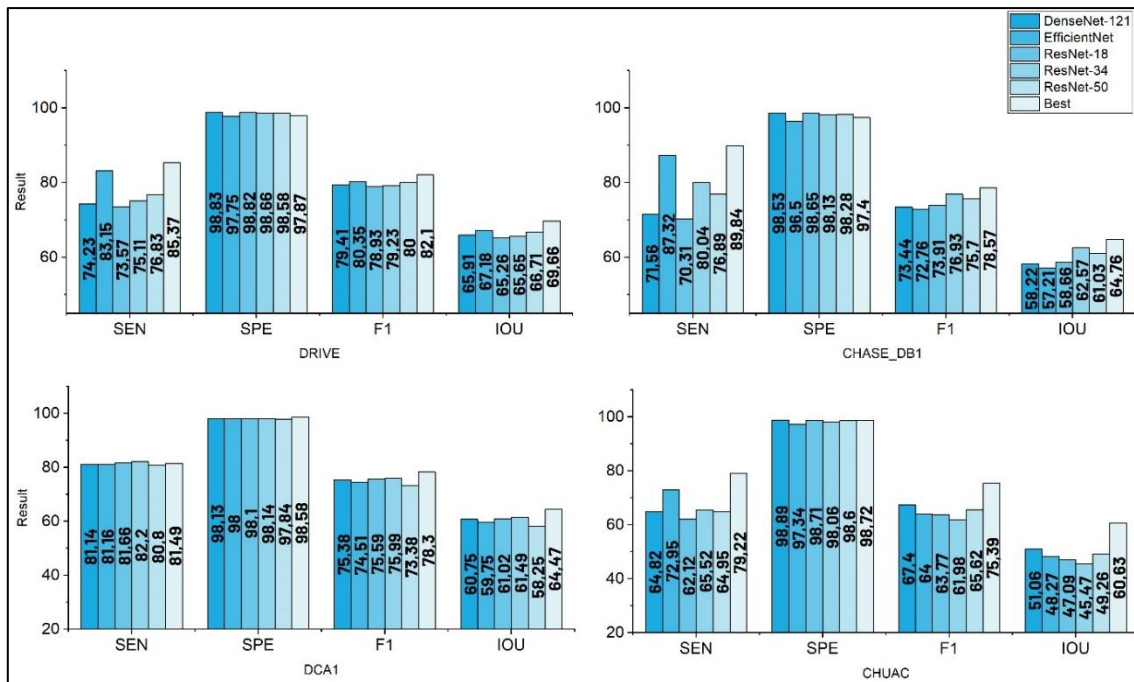
Figure 3. *Performance comparison of different neural network architectures (DenseNet-121, EfficientNet, ResNet-18, ResNet-34, ResNet-50, and Best) across four datasets (DRIVE, CHASE_DB1, DCA1, and CHUAC) using four evaluation metrics (SEN: Sensitivity, SPE: Specificity, F1: F1-Score, and IOU: Intersection over Union). Best represents the obtained results from UKnowNet-A for each metric and dataset.*

Across all evaluated datasets, EfficientNet consistently demonstrated strong sensitivity, while ResNet architectures, particularly ResNet-34 and ResNet-50, maintained high specificity and balanced performances across other metrics. DenseNet-121 also showed competitive specificity and F1 scores. However, UKnowNet-A consistently outperformed all individual pre-trained models across all metrics and datasets. This superior performance can be attributed to the use of pseudo-labels from multiple datasets, which likely enhances the model's ability to generalize and accurately segment diverse retinal images The ablation study confirms that while standard pre-trained networks provide robust baseline performances with limited fine-tuning, the comprehensive training approach employed by UKnowNet-A—utilizing multi-dataset pseudo labeling and advanced fine-tuning strategies—yields significant improvements. This confirms its efficacy in achieving state-of-the-art results in retinal image segmentation.

These findings underscore the critical importance of customized training methods in medical image segmentation tasks. While pre-trained models offer a strong baseline performance, integrating pseudo-labels from diverse sources and using specialized training techniques significantly improve segmentation accuracy and robustness. Future research could investigate the combined effects of ensemble learning and the further augmentation of training data to enhance the precision of segmentation models.

4. CONCLUSION

In this study, I have introduced UKnow-Net, a knowledge-enhanced U-Net architecture designed to improve retinal vessel segmentation across multiple datasets. By leveraging the strengths of multiple teacher networks, each trained on distinct retinal image datasets (DRIVE, CHASE_DB1, DCA1, and CHUAC), UKnow-Net addresses the challenges posed by variability and complexity in retinal images. UKnow-Net involves a multi-step process where specialized teacher networks use pseudo-labels to train a unified student network. This approach allows the student network to distill domain-specific knowledge from the teacher networks, enhancing its ability to generalize across diverse datasets. The integration of pseudo-labels effectively transfers the collective expertise of the teacher networks to the student network, resulting in improved segmentation performance.

The experimental results demonstrate that UKnow-Net outperforms traditional handcrafted networks (U-Net, UNet++, and Attention U-Net) and several state-of-the-art models in key performance metrics, including sensitivity, specificity, F1 score, and intersection over union (IoU). Specifically, UKnowNet-A, trained solely on pseudo-labels, achieved higher sensitivity across all datasets, indicating its superior ability to detect true positives. UKnowNet-B, which combines pseudo-labels with ground truth annotations, achieved a balanced performance in precision and recall, leading to higher F1 scores and IoU metrics. Our ablation study further confirms the effectiveness of the proposed knowledge enhancement approach. The comparison with pre-trained convolutional neural networks fine-tuned on the same datasets revealed that UKnow-Net consistently delivers superior performance. This underscores the importance of leveraging pseudo-labels from multiple specialized networks to improve generalization and robustness in medical image segmentation tasks. I aim to ensure fairness in comparison and reproducibility in future research by publicly sharing the source code and the best model weights. This study highlights the potential of knowledge enhancement techniques in medical imaging and encourages further exploration of multi-teacher knowledge distillation methods.

Future work could explore integrating additional datasets to enhance generalization further, applying the knowledge enhancement framework to other medical imaging tasks, and optimizing the model for real-time clinical applications.

CONFLICT OF INTEREST

The author declares no conflict of interest.

REFERENCES

Abràmoff, M. D., Garvin, M. K., & Sonka, M. (2010). Retinal imaging and image analysis. *IEEE Reviews in Biomedical Engineering*, *3*, 169-208. https://doi.org/10.1109/rbme.2010.2084567

Amritesh, Owais, M. M., Vemula, V., Amit, A., & Natarajan, S. (2023, May 3-5). *Localised Land-Use Classification Using U-Net and Satellite Imaging*. In: A. J. Kulkarni, & N. Cheikhrouhou (Eds.), Proceedings of the 2nd International Conference on Information Science and Applications (ICISA 2023), (pp. 235-248), Pune, India. https://doi.org/10.1007/978-981-99-6984-5_15

Anand, V., Gupta, S., Koundal, D., Nayak, S. R., Barsocchi, P., & Bhoi, A. K. (2022). Modified U-net architecture for segmentation of skin lesion. *Sensors*, *22*(3), 867. https://doi.org/10.3390/s22030867

Carballal, A., Novoa, F. J., Fernandez-Lozano, C., García-Guimaraes, M., Aldama-López, G., Calviño-Santos, R., Vazquez-Rodriguez, J. M., & Pazos, A. (2018). Automatic multiscale vascular image segmentation algorithm for coronary angiography. *Biomedical Signal Processing and Control*, *46*, 1-9. https://doi.org/10.1016/j.bspc.2018.06.007

Cervantes-Sanchez, F., Cruz-Aceves, I., Hernandez-Aguirre, A., Hernandez-Gonzalez, M. A., & Solorio-Meza, S. E. (2019). Automatic segmentation of coronary arteries in X-ray angiograms using multiscale analysis and artificial neural networks. *Applied Sciences*, *9*(24), 5507. https://doi.org/10.3390/app9245507

Chaudhuri, S., Chatterjee, S., Katz, N., Nelson, M., & Goldbaum, M. (1989). Detection of blood vessels in retinal images using two-dimensional matched filters. *IEEE Transactions on Medical Imaging*, *8*(3), 263-269. https://doi.org/10.1109/42.34715

Fraz, M. M., Remagnino, P., Hoppe, A., Uyyanonvara, B., Rudnicka, A. R., Owen, C. G., & Barman, S. A. (2012). Blood vessel segmentation methodologies in retinal images–a survey. *Computer Methods and Programs in Biomedicine*, *108*(1), 407-433. https://doi.org/10.1016/j.cmpb.2012.03.009

Fu, H., Xu, Y., Lin, S., Kee Wong, D. W., & Liu, J. (2016, October 17-21). *Deepvessel: Retinal vessel segmentation via deep learning and conditional random field*. In: S. Ourselin, L. Joskowicz, M. R. Sabuncu, G. Unal, & W. Wells (Eds.), Proceedings of the 19th International Conference on Medical Image Computing and Computer-Assisted Intervention (MICCAI 2016), (Part II, pp. 132-139). Athens, Greece. https://doi.org/10.1007/978-3-319-46723-8_16

Hinton, G., Vinyals, O., & Dean, J. (2015). Distilling the Knowledge in a Neural Network. https://doi.org/10.48550/arXiv.1503.02531

Isensee, F., Kickingereder, P., Wick, W., Bendszus, M., & Maier-Hein, K. H. (2018, September 16). *No New-Net*. In: A. Crimi, S. Bakas, H. Kuijf, F. Keyvan, M. Reyes, & T. van Walsum (Eds.), Proceedings of the 4th International Workshop on Brainlesion: Glioma, Multiple Sclerosis, Stroke and Traumatic Brain Injuries (BrainLes 2018), (Part II, pp. 234-244), Granada, Spain. https://doi.org/10.1007/978-3-030-11726-9_21

Jaeger, P. F., Kohl, S. A. A., Bickelhaupt, S., Isensee, F., Kuder, T. A., Schlemmer, H.-P., & Maier-Hein, K. H. (2019, December 13). *Retina U-Net: Embarrassingly simple exploitation of segmentation supervision for medical object detection*. In: Proceedings of the Machine Learning for Health Workshop (ML4H), (pp. 171-183), Vancouver, Canada.

Kamran, S. A., Hossain, K. F., Tavakkoli, A., Zuckerbrod, S. L., Sanders, K. M., & Baker, S. A. (2021, September 27 - October 1). *RV-GAN: Segmenting retinal vascular structure in fundus photographs using a novel multi-scale generative adversarial network*. In: M. de Bruijne, P. C. Cattin, S. Cotin, N. Padoy, S. Speidel, Y. Zheng, & C. Essert (Eds.), Proceedings of the 24th International Conference on Medical Image Computing and Computer-Assisted Intervention (MICCAI 2021), (Part VIII, pp. 34-44), Strasbourg, France. https://doi.org/10.1007/978-3-030-87237-3_4

Kuş, Z., & Kiraz, B. (2023). Evolutionary architecture optimization for retinal vessel segmentation. *IEEE Journal of Biomedical and Health Informatics*, *27*(2), 5895-5903 https://doi.org/10.1109/JBHI.2023.3314981

Li, J., Gao, G., Liu, Y., & Yang, L. (2023). MAGF-Net: A multiscale attention-guided fusion network for retinal vessel segmentation. *Measurement*, *206*, 112316. https://doi.org/10.1016/j.measurement.2022.112316

Liskowski, P., & Krawiec, K. (2016). Segmenting retinal blood vessels with deep neural networks. *IEEE Transactions on Medical Imaging*, *35*(11), 2369-2380. https://doi.org/10.1109/TMI.2016.2546227

Litjens, G., Kooi, T., Bejnordi, B. E., Setio, A. A. A., Ciompi, F., Ghafoorian, M., van der Laak, J. A. W. M., van Ginneken, B., & Sánchez, C. I. (2017). A survey on deep learning in medical image analysis. *Medical Image Analysis*, *42*, 60-88. https://doi.org/10.1016/j.media.2017.07.005

Liu, W., Yang, H., Tian, T., Cao, Z., Pan, X., Xu, W., Jin, Y., & Gao, F. (2022). Full-resolution network and dual-threshold iteration for retinal vessel and coronary angiograph segmentation. *IEEE Journal of Biomedical and Health Informatics*, *26*(9), 4623-4634. https://doi.org/10.1109/JBHI.2022.3188710

Mendonca, A. M., & Campilho, A. (2006). Segmentation of retinal blood vessels by combining the detection of centerlines and morphological reconstruction. *IEEE Transactions on Medical Imaging*, *25*(9), 1200-1213. https://doi.org/10.1109/TMI.2006.879955

Mou, L., Zhao, Y., Chen, L., Cheng, J., Gu, Z., Hao, H., Qi, H., Zheng, Y., Frangi, A., & Liu, J. (2019, October 13–17). *CS-Net: Channel and spatial attention network for curvilinear structure segmentation*. In: D. Shen, T. Liu, T. M. Peters, L. H. Staib, C. Essert, S. Zhou, P-T. Yap, & A. Khan (Eds.), Proceedings of the 22nd International Conference on Medical Image Computing and Computer-Assisted Intervention (MICCAI 2019), (Part I, pp. 721-730), Shenzhen, China. https://doi.org/10.1007/978-3-030-32239-7_80

Mu, Y., Li, K., Sun, Y., & Bao, Y. (2024). Semantic segmentation of corn leaf blotch disease images based on U-Net integrated with RFB structure and dual attention mechanism. *Agronomy (Basel, Switzerland)*, *14*(11), 2652. https://doi.org/10.3390/agronomy14112652

Niemeijer, M., Staal, J., van Ginneken, B., Loog, M., & Abramoff, M. D. (2004, February 14-19). *Comparative study of retinal vessel segmentation methods on a new publicly available database*. In: J. M. Fitzpatrick & M. Sonka (Eds.), Proceedings of the Medical Imaging 2004: Image Processing. SPIE Proceedings, (Vol. 5370, pp. 648-656), San Diego, California, United States. https://doi.org/10.1117/12.535349

Oktay, O., Schlemper, J., Folgoc, L. L., Lee, M., Heinrich, M., Misawa, K., Mori, K., McDonagh, S., Hammerla, N. Y., Kainz, B., Glocker, B., & Rueckert, D. (2018, July 4-6). Attention u-net: Learning where to look for the pancreas. In: Proceedings of the 1st Conference on Medical Imaging with Deep Learning (MIDL 2018), Amsterdam, The Netherlands. https://doi.org/10.48550/arXiv.1804.03999

Patton, N., Aslam, T. M., MacGillivray, T., Deary, I. J., Dhillon, B., Eikelboom, R. H., Yogesan, K., & Constable, I. J. (2006). Retinal image analysis: concepts, applications and potential. *Progress in Retinal and Eye Research*, *25*(1), 99-127. https://doi.org/10.1016/j.preteyeres.2005.07.001

Qin, D., Bu, J.-J., Liu, Z., Shen, X., Zhou, S., Gu, J.-J., Wang, Z.-H., Wu, L., & Dai, H.-F. (2021). Efficient medical image segmentation based on knowledge distillation. *IEEE Transactions on Medical Imaging*, *40*(12), 3820-3831. https://doi.org/10.1109/TMI.2021.3098703

Qu, Z., Zhuo, L., Cao, J., Li, X., Yin, H., & Wang, Z. (2023). TP-net: Two-path network for retinal vessel segmentation. *IEEE Journal of Biomedical and Health Informatics*, *27*(4), 1979-1990. https://doi.org/10.1109/JBHI.2023.3237704

Ronneberger, O., Fischer, P., & Brox, T. (2015, October 5-9). U-net: Convolutional networks for biomedical image segmentation. In: N. Navab, J. Hornegger, W. M. Wells, & A. F. Frangi (Eds.), Proceedings of the 18th International Conference on Medical Image Computing and Computer-Assisted Intervention (MICCAI 2015), (Part III, pp. 234-241), Munich, Germany. https://doi.org/10.1007/978-3-319-24574-4_28

Samuel, P. M., & Veeramalai, T. (2021). VSSC Net: vessel specific skip chain convolutional network for blood vessel segmentation. *Computer Methods and Programs in Biomedicine*, *198*, 105769. https://doi.org/10.1016/j.cmpb.2020.105769

Shen, L., Margolies, L. R., Rothstein, J. H., Fluder, E., McBride, R., & Sieh, W. (2019). Deep learning to improve breast cancer detection on screening mammography. *Scientific Reports*, *9*(1), 12495. https://doi.org/10.1038/s41598-019-48995-4

Staal, J., Abràmoff, M. D., Niemeijer, M., Viergever, M. A., & van Ginneken, B. (2004). Ridge-based vessel segmentation in color images of the retina. *IEEE Transactions on Medical Imaging*, *23*(4), 501-509. https://doi.org/10.1109/TMI.2004.825627

Sun, K., Xiao, B., Liu, D., & Wang, J. (2019, June 15-20). *Deep high-resolution representation learning for human pose estimation*. In: Proceedings of the 2019 IEEE/CVF Conference on Computer Vision and Pattern Recognition (CVPR) (pp. 5693-5703), Long Beach, CA, USA. https://doi.org/10.1109/CVPR.2019.00584

Wang, L., & Yoon, K.-J. (2021). Knowledge distillation and student-teacher learning for visual intelligence: A review and new outlooks. *IEEE Transactions on Pattern Analysis and Machine Intelligence*, *44*(6), 3048-3068. https://doi.ieeecomputersociety.org/10.1109/TPAMI.2021.3055564

Wang, W., Zhong, J., Wu, H., Wen, Z., & Qin, J. (2020, October 4–8). *RVSeg-net: An efficient feature pyramid cascade network for retinal vessel segmentation*. In: A. L. Martel, P. Abolmaesumi, D. Stoyanov, D. Mateus, M. A. Zuluaga, S. K. Zhou, D. Racoceanu, & L. Joskowicz (Eds.), Proceedings of the 23rd International Conference on Medical Image Computing and Computer-Assisted Intervention (MICCAI 2020), (Part V, pp. 796-805), Lima, Peru. https://doi.org/10.1007/978-3-030-59722-1_77

Wu, H., Wang, W., Zhong, J., Lei, B., Wen, Z., & Qin, J. (2021). SCS-net: A scale and context sensitive network for retinal vessel segmentation. *Medical Image Analysis*, *70*, 102025. https://doi.org/10.1016/j.media.2021.102025

Zana, F., & Klein, J.-C. (2001). Segmentation of vessel-like patterns using mathematical morphology and curvature evaluation. *IEEE Transactions on Image Processing*, *10*(7), 1010-1019. https://doi.org/10.1109/83.931095

Zhang, S., Fu, H., Yan, Y., Zhang, Y., Wu, Q., Yang, M., Tan, M., & Xu, Y. (2019, October 13-17). *Attention guided network for retinal image segmentation*. In: D. Shen, T. Liu, T. M. Peters, L. H. Staib, C. Essert, S. Zhou, P-T. Yap, & A. Khan (Eds.), Proceedings of the 22nd International Conference on Medical Image Computing and Computer-Assisted Intervention (MICCAI 2019), (Part I, pp. 797-805), Shenzhen, China. https://doi.org/10.1007/978-3-030-32239-7_88

Zhang, Z., & Lu, B. (2024). Efficient skin lesion segmentation with boundary distillation. *Medical & Biological Engineering & Computing*, *62*(9), 2703–2716. https://doi.org/10.1007/s11517-024-03095-y

Zhou, Y., Yu, H., & Shi, H. (2021, September 27–October 1). *Study Group Learning: Improving Retinal Vessel Segmentation Trained with Noisy Labels*. In: M. de Bruijne, P. C. Cattin, S. Cotin, N. Padoy, S. Speidel, Y. Zheng, & C. Essert (Eds.), Proceedings of the 24th International Conference on Medical Image Computing and Computer-Assisted Intervention (MICCAI 2021), (Part I, pp. 57-67), Strasbourg, France. https://doi.org/10.1007/978-3-030-87193-2_6

Zhou, Z., Rahman Siddiquee, M. M., Tajbakhsh, N., & Liang, J. (2018, September 20). *Unet++: A nested u-net architecture for medical image segmentation*. In: D. Stoyanov, Z. Taylor, G. Carneiro, T. Syeda-Mahmood, A. Martel, L. Maier-Hein, J. M. R. S. Tavares, A. Bradley, J. P. Papa, V. Belagiannis, J. C. Nascimento, Z. Lu, S. Conjeti, M. Moradi, H. Greenspan, & A. Madabhushi (Eds.), Proceedings of the 4th International Workshop and 8th International Workshop on Deep Learning in Medical Image Analysis and Multimodal Learning for Clinical Decision Support (DLMIA 2018, ML-CDS 2018), (pp. 3-11). Granada, Spain. https://doi.org/10.1007/978-3-030-00889-5_1

PbO Based MIS Nanostructure Device *C-V* and *I-V* Characteristics; Calculation Techniques, Comparisons

Ahmet Hakan SELÇUK[1*]

[1] *Balıkesir University, Department of Electrical and Electronics Engineering, Türkiye*

Keywords	Abstract
Barrier Hight Ideality Factor Lead Monoxide PbO Series Resistance Diode Parameter Extraction Schottky Diode	The electrical properties of an Al/PbO/p-Si nanostructure forming PbO based diode of MIS-type (metal-insulator semiconductor) diode have been investigated. This particular diode structure is relatively new and has limited documentation in the existing literature. The prepared heterostructure, whose capacitance and current-voltage (*C-V* and *I-V*) characteristics were measured at room temperature in dark conditions. Key parameters such as the ideality factor *n*, barrier height ϕ_b and series resistance R_s were calculated using multiple methods, including the Standard, Norde, Lien-So-Nicolet, and Cheung techniques. These parameters provided insight into the molecular dynamics influencing the electrical characteristics of the diode. The annealing process at 290°C for 20 minutes was found to have a significant impact on the electrical behaviour of the sample. This study highlights the potential of PbO-based diodes for use in high-performance nanostructure devices.

1. INTRODUCTION

Silicon-based (Si) devices exhibit high sensitivity to both infrared (IR) and visible light. However, their performance in the ultraviolet (UV) range is significantly limited due to their bandgap energy, which is approximately 2.8 eV (Venkataraj et al., 2002). To enhance UV detection capabilities, metal-oxide-semiconductor (MOS) devices offer a more promising approach due to their wide bandgap. Consequently, Si-based MOS devices have emerged as viable candidates for high-efficiency UV photodetectors (Makhlouf et al., 2017).

Lead monoxide (PbO) has gained attention for its unique properties, such as high carrier mobility and strong absorption of x-rays and gamma rays (Simon et al., 2005; Coşkun & Cetin, 2023). These characteristics make PbO a versatile material suitable for applications ranging from optoelectronics to radiation shielding (El-Sayed Abdo et al., 2003; Harish et al., 2010; Pıçakçı & Yalçın, 2023). PbO can exist in two primary crystalline forms, tetragonal α-PbO (red) and orthorhombic β-PbO (yellow), with a transition temperature around 763 K. These phases differ in their electronic properties, which significantly influence their performance in devices like UV detectors and radiation sensors (Patel et al., 2015; Lee et al., 2017).

In this research, a PbO-based MOS structure was fabricated, and its *C-V* and *I-V* characteristics were analysed. The equivalent circuit model of the diode is represented in Figure 1. It includes a series resistance (R_s) and a parallel conductance (G_p), which are crucial for accurately modelling the device characteristics. In most cases, G_p is negligible. The Shockley diode equation governs the *I-V* behaviour of the diode:
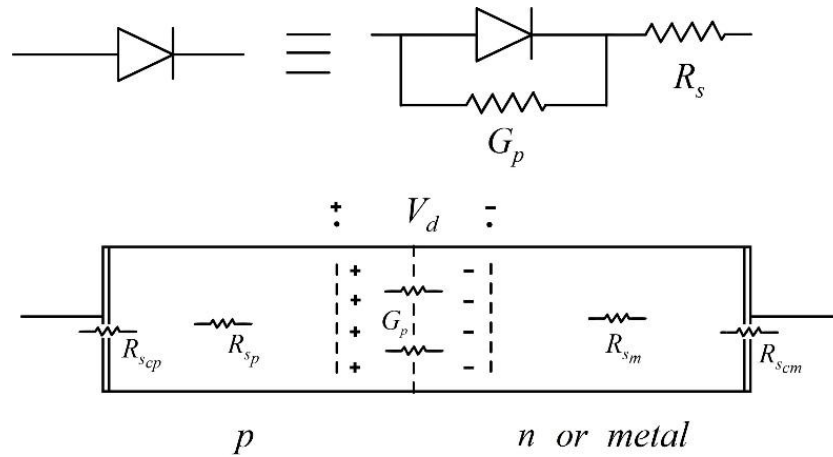
Figure 1. Equivalent circuit of a diode

$$I = I_s\left(e^{\frac{qV_d}{nkT}} - 1\right)$$ (1)

where I_s is the saturation current, q is the electronic charge, n is the ideality factor, k is the Boltzmann constant, and T is the absolute temperature. However, when considering the effect of the series resistance, the diode voltage (V_d) can be expressed as $V_d = V - IR_s$. Thus, the current equation is modified to include both series resistance and parallel conductance (Aubry & Meyer, 1994):

$$I = I_s\left(e^{\frac{q.(V-IR_s)}{nkT}} - 1\right) + G_p(V - IR_s)$$ (2)

This information is enough to access the Schottky diode in a circuit as an ohmic element. But it is convenient to calculate series resistor, barrier height and ideality factor, interface states in order to determine design parameters from both *C-V* and *I-V* measurements. For this purpose, several methods in the literature have been suggested. Those are Standard, Cheung, Norde, Lien-So-Nicolet Methods. Some other methods are also reported those are not employed in this study (Mahi et al., 2019; Li et al., 2020; Bashahu et al., 2022).

Fabrication and measurement of a new Schottky diode type is important for future material and sensor improvements as this work contributes. PbO based MIS structure diode investigation is very rare in the literature.

2. MATERIAL AND METHOD

PbO devices are printed on *p*-type Si (100) wafer. Its resistivity is maximum 10 Ω.cm (low resistivity with minimum value of 1, as mentioned by manufacturer) and has a thickness of 280 μm. RCA1 (Radio Corporation of America, cleaning technique 1: A laboratory invented chemical cleaning method) cleaning procedure is applied to the Si wafer (Selçuk et al., 2014; Aras et al., 2015; Kaymak et al., 2018).

The unpolished side of the wafer is coated with 99.999% Al by evaporation under a pressure of 3×10^{-6} Torr. The thickness of the coating is 124 nm. An evaporation coating system is filled with nitrogen and then vacuumed to 1×10^{-6} Torr. In this oxygen free environment, the sample is heated maximally up to 500°C, as the Al side up. This causes Al molecules penetrate Si structure. Then the surface is coated finally with Al of thickness 124 nm. A good ohmic contact is obtained.

The polished surface of the wafer is then coated with β-PbO by evaporation in a vacuum of 3×10^{-6} Torr. The thickness of the PbO coating, measured using an Edwards FTM6, is 15 nm. The sample is then annealed at 290°C during 20 minutes in the air.

Using a mask and evaporation, 128 nm deep Al disks of 1.3 mm diameter are printed above PbO coating. Figure 2 depicts the schematic of the heterostructure device. The measurements are performed at room temperature and in darkness, since the electrical behavior of the sample is easily affected by light. The *C-V* and *I-V* measurements are performed using an Agilent 4294A Impedance Analyzer and a Keithley 2400 Source Meter, respectively.
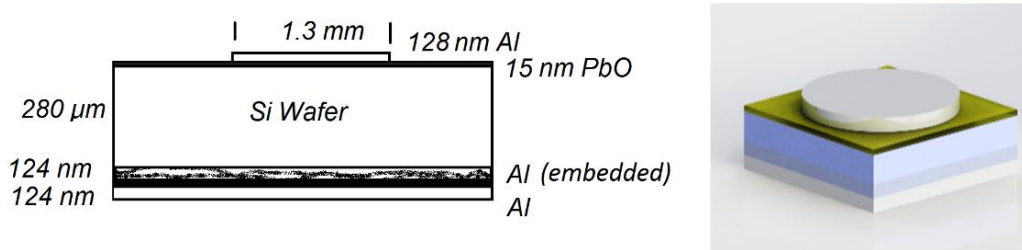
Figure 2. Heterostructure Al/PbO/p-Si diode structure representation

3. RESULTS AND DISCUSSION

3.1. *I-V* Measurement Analysis

The experimental results give the *I-V* and ln(*I*)-*V* curves as in Figure 3.
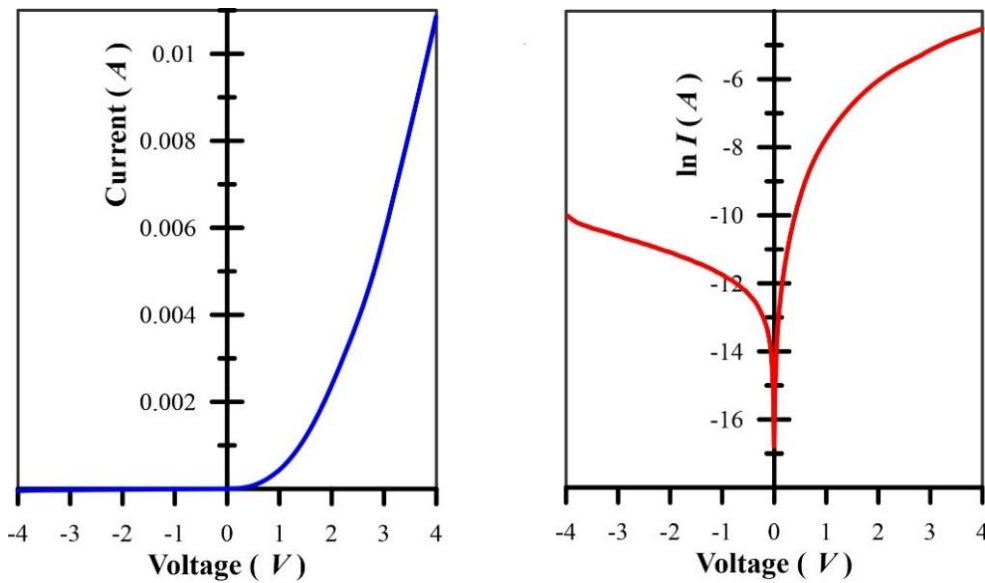
Figure 3. Experimental curves of I-V and ln(I)-V.

3.1.1. Standard Method

Assuming the parallel conductance G_p in the model given in Figure 1 is very low and neglecting the last term in Equation 2 results in

$$I = I_s \left(e^{\frac{q(V-IR_s)}{nkT}} - 1 \right) \quad (3)$$

A voltage range (V_1, V_2) is chosen from *I-V* graphics. This range is chosen so that the variation of ln *I-V* is linear (Figure 3). Note that the measured voltage *V* is different from the junction voltage V_d, that is $V_d = V - I R_s$. So, the lower limit of the range (that is V_1) must satisfy the condition $V_{d1} = V_1 - I_1 R_s >> nkT/q$. For the certain values of series resistance R_s a computer program is employed to correct the experimental curve ln *I* vs *V* to reach ln *I* vs V_d (=$V - R_s J$) considering a least square fit.

3.1.2. Cheung Method

To find the values n and R, team Cheung (1986) extracted the voltage from the equation and took its derivative with respect to $\ln I$. First, let's write the current I_s in terms of barrier height.

$$I_s = A_{eff}A^{**}T^2 e^{-\frac{q\phi_b}{kT}} \qquad (4)$$

where A_{eff} stands for the effective area of the junction, which is approximately $0.65^2\pi$ cm^2, and A^{**} is the Richardson constant, which is 32 /cm^2.K^2. Then an approximation is made. That is, when $V_d = V\text{-}IR_s > 3nkT/q$, the term -1 in Equation 3 can be neglected. After taking the voltage out

$$V = R_s I + n\phi_b + \frac{nkT}{q}\ln\left(\frac{I}{A_{eff}A^{**}T^2}\right) \qquad (5)$$

$$\frac{dV}{d\ln(I)} = IR_s + \frac{nkT}{q} \qquad (6)$$

So, if the graph $dV/d\ln(I)$ vs I is sketched, then it will be a line of slope R_s and an interception value on the y-axis of nkT/q. Thus, n and R_s can be calculated in this manner. After determining n and R_s, we then return to the Equation 5 to find ϕ_b. If the voltage and the term with natural logarithm of I are put together, the remaining terms define a line at the other side of the equation. Then, the slope of this line is proportional to R_s and the y axis intercept can be used to calculate the barrier height ϕ_b.

$$V - \frac{nkT}{q}\ln\left(\frac{I}{A_{eff}A^{**}T^2}\right) = R_s I + n\phi_b \qquad (7)$$

which is defined as $H(I)$. The graphics, obtained from Cheung method, are given in Figure 4. The correlation factor R^2 is also calculated as above 0.95.
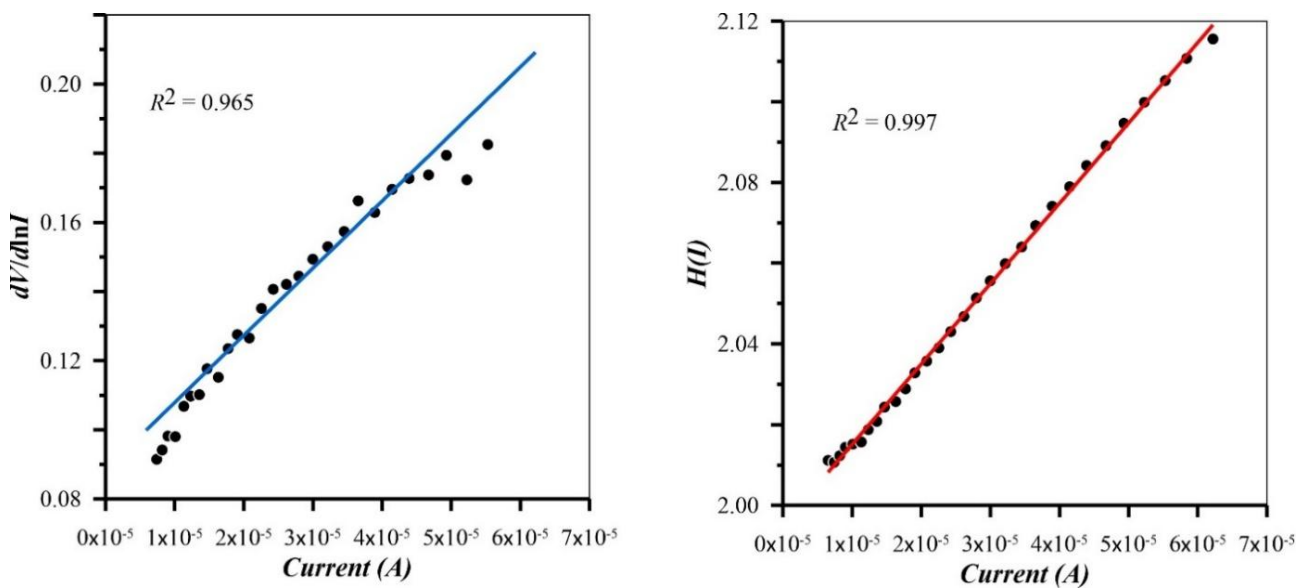
Figure 4. *dV/dln I and H(I) versus I curves of Cheung Method.*

3.1.3. Norde Method

Norde (1979) suggested a method for high series resistance values where the ideality factor *n* is 1. He rearranged Equation 3 such that the plot of a function $F(V)$ of voltage has some linear part when *V* is sufficiently high. Then the slope of this line gives the series resistance, where the interception on the *y* axis tells about the barrier height. $F(V)$ function graphics are shown in Figure 5.

$$F(V) = \frac{V}{2} - \frac{kT}{q} \ln\left(\frac{I}{AA^{**}T^2}\right) \tag{8}$$

Assuming $V_d \gg 3kT/q$ (since $e^3 > 20$, -1 can be neglected),

$$F(V) = \phi_b + IR_s - \frac{V}{2} \tag{9}$$
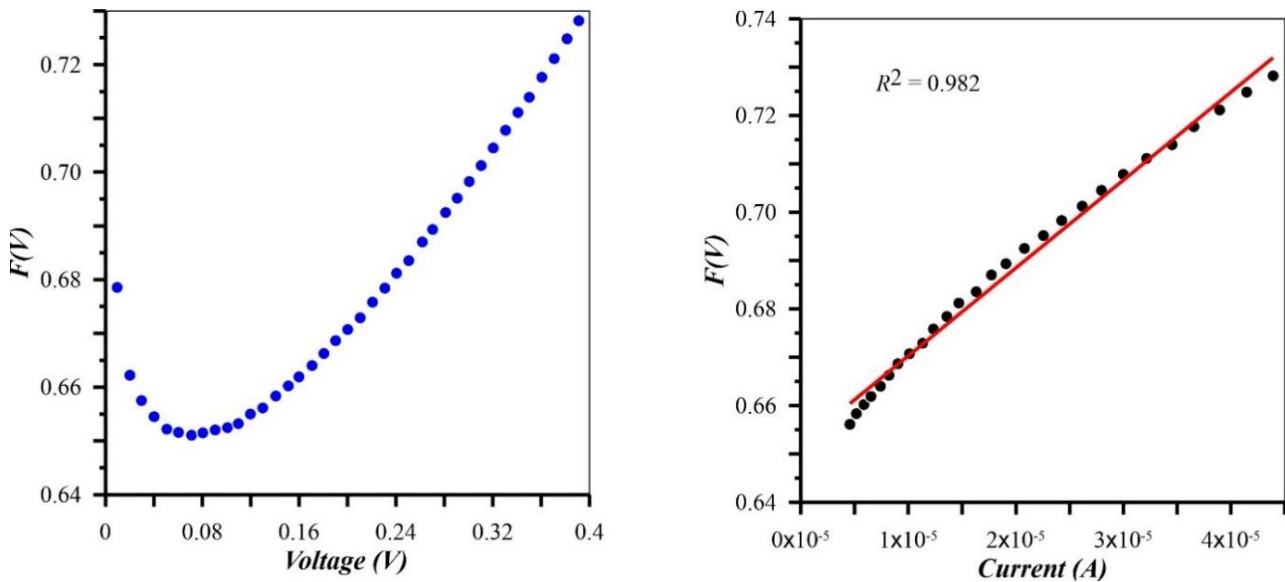
Figure 5. F(V) curves of Norde Method

3.1.4. Lien-So-Nicolet Method

Lien et al. (1984) suggested to consider more than one plot of the function below for different gamma values,

$$G_\gamma(V, I) = \frac{V}{\gamma} - \frac{kT}{q} \ln \frac{I}{A^{**}AT^2} \tag{10}$$

where γ is an arbitrary parameter which is greater than *n*. When $\gamma = 2$, then $G_2(V,I) = F(V,I)$, so it is the Norde plot. $G_\gamma(V,I)$ vs *I* graphics have a minimum at $I_{0\gamma} = (kT/qR_s)(\gamma-n)$. If the graphics of $I_{0\gamma}$ - γ is drawn, this will be a line with slope $m=kT/qR_s$ and its interception with the γ axis (γ_0) result in

$$R_s = \frac{kT}{qm} \, , \ \ n = \gamma_0 \tag{11}$$

Using more than one gamma value leads using more than one data value. This may result in more accurate results and allows to use linear regression (Figure 6).

The electrical parameters of the PbO-based diode were assessed using four distinct calculation methodologies. The outcomes are presented in Table 1.

Both graphics of methods and Table 1 show that the Standard and Cheung methods yield higher n values (2.92 and 3.18), indicating significant deviation from ideal behaviour. This may be due to interface states, high recombination rates, or defects at the PbO/semiconductor interface. The Lien-So-Nicolet method shows a slightly lower n value (2.64), but it still suggests non-ideal characteristics, too. The Norde method, with its assumption of $n=1$, may not accurately reflect the diode's actual behaviour. As a result, this assumption may lead to inconsistencies in barrier height and series resistance calculations compared to other methods, especially in PbO/semiconductor structures with high ideality factors.
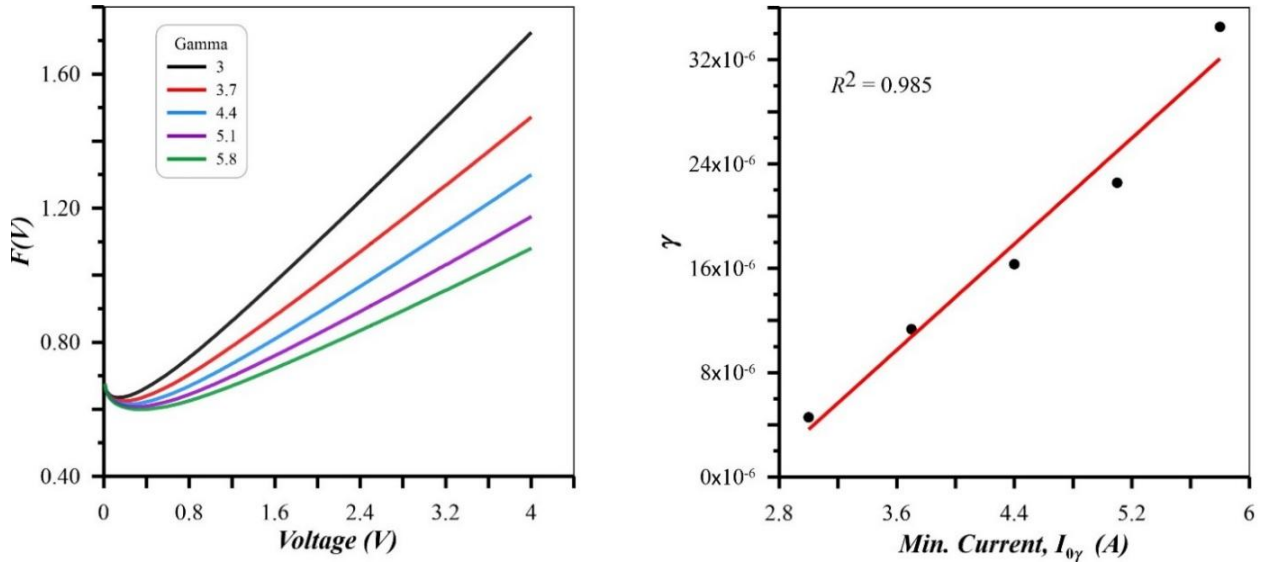
Figure 6. *F(V) and γ curves of Lien-So-Nicolet Method*

Table 1. *Calculation methods and results.*

Method	n	ϕ_b (eV)	R_s (Ohm)
Standard	2.92	0.64	-
Cheung	3.18	0.63	2097-1962
Norde	1 (assumed)	0.78	1580
Lien-So-Nicolet	2.64	-	2546

3.1.5. Interface States from *I-V* Characteristics

Card and Rhoderick (1971) predicted that MIS diodes with interface states D_{it}^{IV} would have an ideality factor n greater than unity that varies with applied potential.

$$n(V) = 1 + \frac{d_{ox}}{\varepsilon_i \varepsilon_0} \left(\frac{\varepsilon_s}{W_D} + q D_{it}^{IV}(V) \right) \tag{12}$$

By plotting the reciprocal of capacitance squared ($1/C^2$) against voltage, obtained from *C-V* measurements, the width of the depletion region can be determined. By analysing the forward-bias *I-V* characteristics of MIS diodes, it is possible to extract D_{it}^{IV}, which is in thermodynamic equilibrium with the semiconductor. Additionally, if the oxide layer thickness d_{ox} ($= \varepsilon_i \varepsilon_0 A / C_{ox}$) is unknown, it can be revealed from the accumulation region of the *C-V* plot (oxide capacitance C_{ox}). The effective barrier height ϕ_e is modulated by the applied bias owing to interfacial insulator layer and interface states at the semiconductor interface. This dependence of ϕ_e is incorporated into the ideality factor n.

$$\phi_e = \phi_b + \left(1 - \frac{1}{n(V)}\right)V \qquad (13)$$

The energy level of the interface states, denoted as E_{ss}, is referenced against the valence band maximum in p-type semiconductors, indicating their position within the band structure and is given by

$$E_{ss} - E_v = q(\phi_e - V) \qquad (14)$$

The extracted values from diode *I-V* are shown in Table 2. The values are chosen for calculation as the oxide thickness of 15 nm, dielectric constant of the oxide layer of 10.1, and the depletion layer thickness of 2196.2 Angstroms at 1 MHz.

As seen in Table 2 and Figure 7, the E_{ss}-E_v, D_{it}^{IV} values are in the range 0.607 to 0.697 eV and 5.648×10^{12} to 1.969×10^{13} /eV.cm^2, respectively. There is an increase in D_{it}^{IV} up to top of the valence band. High D_{it}^{IV} values typically indicate the presence of high density of defects at the interface, leading to a deviation from ideal behaviour. It shows that the trap levels are close to the conduction band which suggests that interface defects and traps significantly hinder the transition of charge carriers. The relatively stable range of E_{ss}-E_v values indicates that the increase in D_{it}^{IV} might correlate with an increased impact on the energy band, reflecting a more substantial effect on electronic properties. The high interface state density is likely a result of the growth of the thin orthorhombic oxide layer, as suggested by the observed trends in our measurements. The obtained results show that the investigated structure has high D_{it}^{IV} levels (order of 10^{13}/eV.cm^2), consistent with the findings in the literature.

Table 2. Interface states energy distribution of Al/PbO/p-Si from I-V characteristics

V (V)	$n(V)$	ϕ_e (eV)	E_{ss} - E_v (eV)	D_{it} (×10^{13}/eV.cm^2)
0.075	2.596	0.771	0.696	0.565
0.109	2.987	0.798	0.688	0.711
0.161	3.580	0.841	0.680	0.932
0.211	4.078	0.884	0.673	1.117
0.260	4.469	0.927	0.667	1.263
0.311	4.749	0.970	0.660	1.367
0.362	4.935	1.013	0.652	1.436
0.410	5.059	1.054	0.644	1.483
0.460	5.164	1.096	0.636	1.522
0.511	5.276	1.139	0.628	1.564
0.560	5.412	1.182	0.621	1.614
0.611	5.589	1.227	0.616	1.680
0.661	5.812	1.272	0.611	1.763
0.711	6.093	1.319	0.608	1.868
0.751	6.364	1.358	0.607	1.969
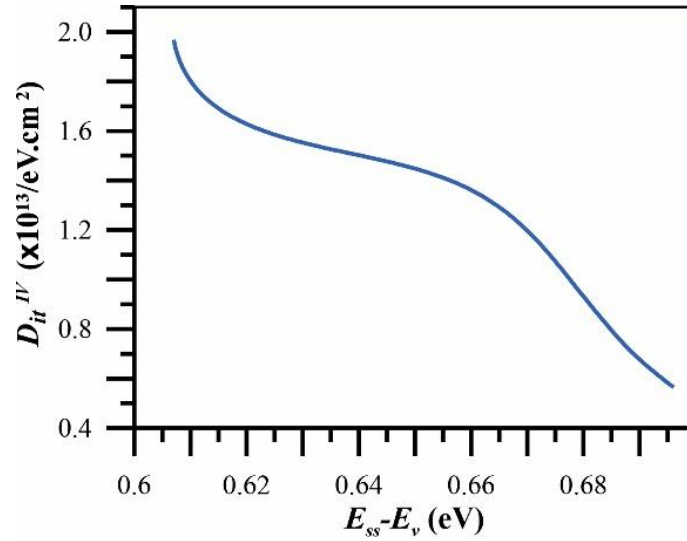
Figure 7. *Interface states versus E_{ss}-E_F plot of diode structure from I-V measurement*

3.2. *C-V* measurement Analysis

The capacitance and conductance (*C-V* and *G-V*) measurements have been performed, and the obtained $1/C^2$-*V* characteristics are illustrated in Figure 8 and 9. From *C–V* measurement, the value of barrier height ϕ_b (*C–V*) and other parameters, at frequency 1MHz, were calculated. Using $1/C^2$-*V* plot as seen in Figure 9, built-in voltage, (V_0) can be determined by finding intercept of axis of straight line with the *x*-axis where $C^{-2} = 0$. Additionally, the carrier doping density (N_A) can be revealed from slope of the line.

$$V_0 = V_D + \frac{kT}{q} \tag{15}$$

where V_D is the diffusion potential.

$$N_A = -\frac{2}{q\varepsilon_s A^2}\left(\frac{d(1/C^2)}{dV}\right)^{-1} \tag{16}$$

where *A* is the rectifying contact surface area and ε_s ($11.9\varepsilon_0$ (Sze & Ng, 2006) for Si) is the permittivity of the semiconductor. The ϕ_b (*C–V*) can be calculated from Equation 17.
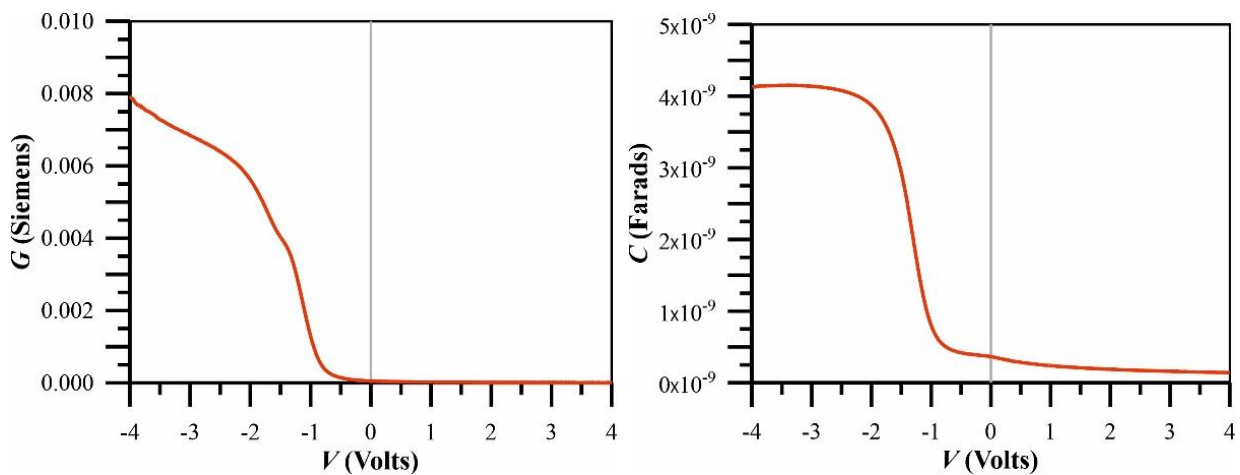
Figure 8. *C-V and G-V measurement of Al/PbO/p-Si MIS structure at 1MHz.*

$$\phi_b(C - V) = V_0 + E_F + \frac{kT}{q} - \Delta\phi_b \tag{17}$$

where $\Delta\phi_b = \sqrt{qE_m/(4\pi\varepsilon_s\varepsilon_0)}$ is called image force lowering and E_F is the Fermi energy level. Maximum electric field E_m at contact interface is given by

$$E_m = \sqrt{\frac{2qN_AV_D}{\varepsilon_s\varepsilon_0}} \tag{18}$$

E_F can be calculated by using relation

$$E_F = \frac{kT}{q}\ln\left(\frac{N_V}{N_A}\right) \tag{19}$$

where $N_V = 4.82 \times 10^{15}(T \times m_h^*/ m_0)^{3/2}$, in the valance band of semiconductor, is the effective density of states. Effective mass of hole m_h^*, in terms of the rest mass of the electron m_0, is $m_h^* = 0.16m_0$ (Sze & Ng, 2006). The expression provides an estimate of the spatial region where charge carriers are depleted, the depletion width, can be calculated using $W_D = \sqrt{2\varepsilon_s\varepsilon_0 V_D/(qN_A)}$ in the semiconductor. Based on the *C-V* measurement of structure, a barrier height (ϕ_b) was determined to be 0.835 eV (correlation factor of 0.999) with an image force lowering ($\Delta\phi_b$) of 0.027 eV, the depletion layer width (W_D) of 2196.2 Å, a carrier doping density (N_A) of 1.83×10^{16} cm^{-3} and a Fermi energy level (E_F) of 0.159 eV. The values of N_A and E_F suggest moderate carrier concentration and energy level alignment, while $\Delta\phi_b$ indicates the minor influence of image force lowering on the barrier height at the metal-semiconductor interface.
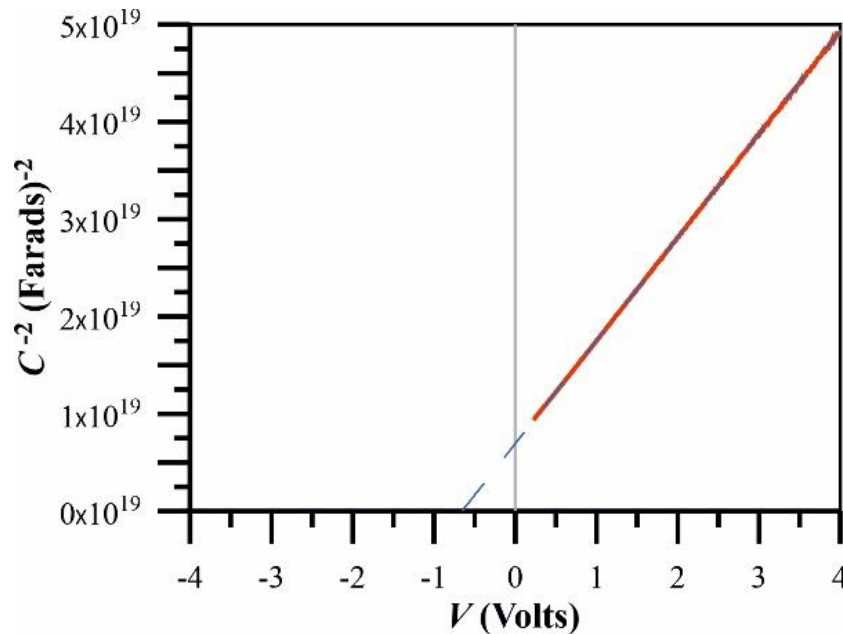
Figure 9. C $^{-2}$-V plot of Al/PbO/p-Si MIS structure

Additionally, series resistance (R_s) was extracted from the high-frequency *C* and *G* measurements using the Nicollian and Brews method (Nicollian & Brews, 1982). The series resistance can be calculated by considering the conductance and capacitance values at a given voltage in the accumulation region where it is strong, using the following formula.

$$R_s = \frac{G_{acc}}{G_{acc}^2 + \omega^2 C_{acc}^2} \tag{20}$$

where ω is the angular frequency. The change of the R_s of the Al/PbO/p-Si MIS structure is illustrated in Figure 10, with a peak resistance of 941.7 ohms.
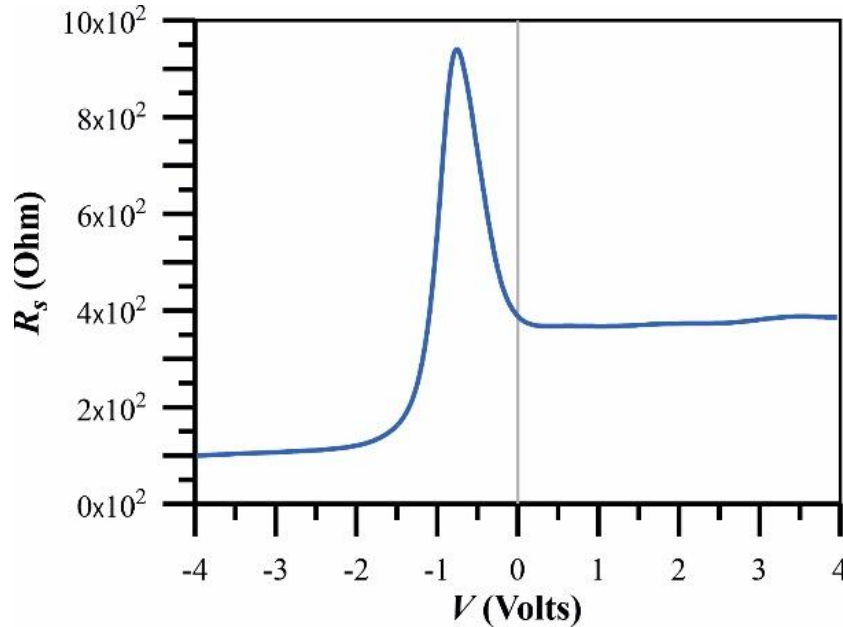
Figure 10. *Plot of series resistance of MIS structure at 1MHz.*

The interface states from capacitance measurement (D_{it}^{CV}) can evaluated by Hill-Coleman method (Hill & Coleman, 1980).

$$D_{it}^{CV} = \frac{2(G_{c,max}/\omega)}{qA\left[\left(G_{c,max}/\omega C_{ox}\right)^2 + (1 - C_c/C_{ox})^2\right]} \tag{21}$$

where C_c and $G_{c,max}$ are corrected capacitance and corrected maximum conductance, respectively. Corrected capacitance and conductance in terms of measured values can be derived from equation 22.

$$C_c = \frac{(G_m^2 + \omega^2 C_m^2)C_m}{G_m - (G_m^2 + \omega^2 C_m^2)R_s + \omega^2 C_m^2},$$

$$G_c = \frac{(G_m^2 + \omega^2 C_m^2)[G_m - (G_m^2 + \omega^2 C_m^2)R_s]}{G_m - (G_m^2 + \omega^2 C_m^2)R_s + \omega^2 C_m^2} \tag{22}$$

The calculated active and fast responding trap state density D_{it}^{CV} is 0.572×10^{13} /eV.cm^2 at 1MHz frequency. In PbO-based systems, high defect densities and oxygen vacancies tend to lead to D_{it}^{CV} values reaching the order of 10^{13}/eV.cm^2. According to theoretical analyses of MIS structures, this level indicates a high interface trap density, which can significantly affect device performance. This value implies increased recombination and reduced carrier mobility, resulting in noise and conductivity reduction, particularly in high-frequency applications.

Both *I-V* and *C-V* analyses revealed high interface state densities on the order of 10^{13} /eV.cm^2. They show consistent results, indicating a high defect density at the PbO/Si interface. This consistency between the two methods enhances the reliability of the analysis and underscores the need for improvements in the interface quality to reduce these defects. Optimizing the growth and annealing processes of the PbO layer may help reduce these defects and improve the electronic properties of the diode. Addressing these issues is essential for enhancing the performance of PbO-based MIS devices in high-frequency and sensor applications.

4. CONCLUSION

This study successfully demonstrated the fabrication and characterization of a PbO-based MIS diode on a p-type Si substrate, providing insights into its electrical properties through comprehensive different *I-V* and *C-V* analyses. The results indicate significant deviations from ideal diode behaviour, primarily attributed to high interface state densities and structural imperfections at the PbO/Si interface. The extracted parameters, including ideality factor, barrier height, and series resistance, revealed considerable variations among different evaluation methods, with barrier heights ranging from 0.63 to 0.78 eV and interface state densities on the order of 10^{13} /eV.cm^2.

The analysis also highlighted the influence of series resistance, which was found to vary depending on the evaluation method, ranging from 1580 to 2546 Ohm. High series resistance values can lead to increased power loss, voltage drops, and deviations in the *I-V* characteristics, particularly at higher forward bias conditions. By reducing the series resistance through process optimization could enhance the overall performance of the diode.

The consistency observed between the *I-V* and *C-V* analyses confirms the high defect density, emphasizing the critical role of interface states in influencing the electronic properties of the diode. These findings underscore the importance of optimizing the growth and annealing processes of the PbO layer to reduce defects and improve device performance, particularly in high-frequency and sensor applications. Future studies should focus on refining the fabrication techniques and exploring alternative passivation methods to achieve lower defect densities and enhanced material quality.

CONFLICT OF INTEREST

The author declares no conflict of interest.

REFERENCES

Aras, G., Orhan, E., Selçuk, A. B., Bilge Ocak, S., & Ertuğrul, M. (2015). Dielectric Properties of Al/Poly (methyl methacrylate) (PMMA)/p-Si Structures at Temperatures Below 300 K. *Procedia - Social and Behavioral Sciences*, *195*, 1740–1745. https://doi.org/10.1016/j.sbspro.2015.06.295

Aubry, V., & Meyer, F. (1994). Schottky diodes with high series resistance: Limitations of forward I-V methods. *Journal of Applied Physics*, *76*(12), 7973–7984. https://doi.org/10.1063/1.357909

Bashahu, M., Ngendabanyikwa, D., & Nyandwi, P. (2022). Non Ideal Schottky Barrier Diode's Parameters Extraction and Materials Identification from Dark I-V-T; Characteristics. *Journal of Modern Physics*, *13*(03), 285–300. https://doi.org/10.4236/jmp.2022.133020

Card, H. C., & Rhoderick, E. H. (1971). Studies of tunnel MOS diodes I. Interface effects in silicon Schottky diodes. *Journal of Physics D: Applied Physics*, *4*(10), 1589–1601. https://doi.org/10.1088/0022-3727/4/10/319

Coşkun, A., & Cetin, B. (2023). The effect of lead oxide on the change in gamma ray protection parameters of bismuth oxide. *European Journal of Science and Technology*, Special Issue 47, 18-21. https://doi.org/10.31590/ejosat.1234613

El-Sayed Abdo, A., Ali, M. A. M., & Ismail, M. R. (2003). Natural fibre high-density polyethylene and lead oxide composites for radiation shielding. *Radiation Physics and Chemistry*, *66*(3), 185–195. https://doi.org/10.1016/S0969-806X(02)00470-X

Harish, V., Nagaiah, N., Prabhu, T. N., & Varughese, K. T. (2010). Thermo-mechanical analysis of lead monoxide filled unsaturated polyester based polymer composite radiation shields. *Journal of Applied Polymer Science*, *117*(6), 3623–3629. https://doi.org/10.1002/app.32265

Hill, W. A., & Coleman, C. C. (1980). A single-frequency approximation for interface-state density determination. *Solid-State Electronics*, *23*(9), 987–993. https://doi.org/10.1016/0038-1101(80)90064-7

Kaymak, N., Oz Orhan, E., Ocak, S. B., & Selçuk, B. (2018). An investigation of the electrical properties of PbO based MOS-type different Schottky barrier diodes on a structure. *AIP Conference Proceedings*, *1935*(1), 160002. https://doi.org/10.1063/1.5026013

Lee, Y. K., Kim S. W., Kim, J. N., Kang, Y. N., Kim, J. Y., Lee, D. S., Kim, K. T., Han, M. J., Ahn, K. J, & Park, S. K. (2017). Feasibility study of a photoconductor-based dosimeter for quality assurance in radiotherapy. *Journal of Instrumentation*, *12*(09), P09035. https://doi.org/10.1088/1748-0221/12/09/P09035

Li, X., Xiao, F., Luo, Y., & Duan, Y. (2020). Parameter extraction method for a physics-based lumped-charge SiC MPS diode model. *IET Power Electronics*, *13*(14), 2992–3000. https://doi.org/10.1049/iet-pel.2020.0350

Mahi, K., Messani, B., & Aït-Kaci, H. (2019). Extraction of diode's electrical parameters under forward and room temperature conditions in an InAsSb based device. *Journal of Nano- and Electronic Physics*, *11*(4), 04030. https://doi.org/10.21272/jnep.11(4).04030

Makhlouf, M. M., EL-Nahass, M. M., & Zeyada, M. H. (2017). Fabrication, temperature dependent current-voltage characteristics and photoresponse properties of Au/α-PbO2/p-Si/Al heterojunction photodiode. *Materials Science in Semiconductor Processing*, *58*, 68–75. https://doi.org/10.1016/j.mssp.2016.11.015

Nicollian, E. H., & Brews, J. R. (1982). *MOS (Metal Oxide Semiconductor) Physics and Technology*. Wiley.

Patel, D. B., & Mukhopadhyay, I. (2015). Schottky junction solar cells based on nonstoichiometric PbOx films. *Journal of Physics D: Applied Physics*, *48*(2), 025102. http://doi.org/10.1088/0022-3727/48/2/025102

Pıçakçı, E., & Yalçın, Z. G., (2023). Effects of high level of lead (II) oxide (PbO) usage on accumulator and response surface method. *Black Sea Journal of Engineering and Science*, *6*(4), 375-386. https://doi.org/10.34248/bsengineering.1317900

Selçuk, A. B., Ocak, B. S., Kahraman, G., & Selçuk, A. H. (2014). Investigation of diode parameters using I-V and C-V characteristics of Al/maleic anhydride (MA)/p-Si structure. *Bulletin of Materials Science*, *37*(7), 1717-1724. https://doi.org/10.1007/s12034-014-0729-3

Simon, M., Ford, R. A., Franklin, A. R., Grabowski, S. P., Menser, B., Much, G., Nascetti, A., Overdick, M., Powell, M. J., & Wiechert, D. U. (2005). Analysis of lead oxide (PbO) layers for direct conversion X-ray detection. *IEEE Transactions on Nuclear Science*, *52*(5), 2035-2040. https://doi.org/10.1109/TNS.2005.856790

Sze, S. M., & Ng, K. K. (2006). *Physics of Semiconductor Devices*. Wiley.

Venkataraj, S., Kappertz, O., Drese, R., Liesch, C., Jayavel, R., & Wuttig, M. (2002). Thermal Stability of Lead Oxide Films Prepared by Reactive DC Magnetron Sputtering. *Physica Status Solidi (A)*, *194*(1), 192–205. https://doi.org/10.1002/1521-396X(200211)194:1<192::AID-PSSA192>3.0.CO;2-L

QGIS-based Analysis of Traffic Accident Regions in Muratpasa District in Antalya City

Mehmet Arikan YALCIN[1] Sevil KOFTECI[1*]

[1] *Akdeniz University, Faculty of Engineering, Antalya, Türkiye*

Keywords	Abstract
Highway Traffic Accident Hotspots QGIS SPSS	The objective of this study is to identify the specific locations where traffic accidents occur in the Muratpasa district of Antalya province. Muratpaşa district is the most crowded area especially in tourism season. For this reason, it is important to analyse traffic accidents in this district. To this end, data from the years 2017 to 2021, obtained from the General Directorate of Security of the Republic of Turkey, were employed. The Quantum Geographical Information Systems (QGIS) program was used to ascertain the regions exhibiting elevated accident risk, while the Kernel Density Estimation method was used to categorize the accidents. Furthermore, the ages of drivers involved in accidents, the relationship between age and accident occurrence, the causes of accidents, and the distribution of accidents by years and months were subjected to statistical analysis. The accidents were categorized in four categories according to causes. The study revealed that the risk of traffic accidents was elevated in three distinct regions within the Muratpasa district. It was observed that most of these accidents involved individuals between the ages of 20 and 30, with the primary cause identified as driver error of traffic.

1. INTRODUCTION

Traffic is a system that encompasses a multitude of fields, including transportation engineering, law, economics, urban and regional planning, sociology, and psychology. These fields collectively address the dynamic interaction of vehicles, pedestrians, and other road users. The contributions of these fields facilitate the provision of sustained and dependable transportation. A traffic accident can be defined as an event that disrupts the continuity of transportation as a result of unexpected and undesirable events on this road network, resulting in damage, injury or death to those involved in the accident.

The type and number of traffic accidents are influenced by a multitude of variables. The main factors include highway and environmental conditions, driver behavior, vehicle maintenance, and traffic density. The interaction, diversity, and complexity of these factors are investigated by using several methods. In recent years, data obtained with these methods have been widely analyzed with Geographic Information System (GIS) for accident analysis and prevention (Le et al., 2020; Sababhi et al., 2024; Sohaib et al., 2024). In addition to the use of GIS, statistical approaches such as Getis Ord Gi, Kernel Density Estimation, and Moran's are used in the analysis (Alam & Tabassum, 2023; Le et al., 2023).

Loo (2006) researched a spatial breakdown of accidents that occurred in Hong Kong between the years 1993 and 2004. To identify the regions in question, the researcher used three databases. These databases include accident regions, highway networks, and district councils. The author presented that the use of GIS enabled

the reduction in the number of personnel required to verify the accuracy of the identified locations. Additionally, this process revealed that approximately 65-80% of the police accident records about traffic accidents were found to be accurate. In 2004, it was determined that 12.7% of the police accident database contained erroneous highway names and 9.7% exhibited incorrect county names in this study (Loo, 2006). Clifton and Kreamer-Fults examined the pedestrian-car accidents around public schools in Baltimore City, Maryland, the injuries sustained in such accidents, and the relationship between these injuries and the physical and social characteristics of the area in which the schools are located (Clifton & Kreamer-Fults, 2007). A geographic information system (GIS)-based study was prepared by Zhang and Shi in the Beijing area to identify the locations with the highest concentration of traffic accidents. In addition, in this study, by using accident data, it is shown that the hotspot area is related to the volume of traffic, the driver's condition, the number of intersections on the highways, and the vehicle information system as a cause of accidents at the micro level by distracting the driver. The spatial differentiation pattern of traffic accidents was analyzed by K-means clustering method (Zhang & Shi, 2019). A GIS was used to identify areas at high risk of traffic accidents by spatial autocorrelation analysis using four years of accident data in the Oromia region and surrounding towns in Ethiopia by Tola et al. Getis Ord Gi* analysis was used to cluster accident severities (Tola et al., 2021). Mesquitela et al. (2022) used GIS to determine the regions where traffic accidents in Lisbon are concentrated. Kernel Density Estimation and Getis-Ord Gi* analyses were applied in this study. The presence of hotspots was determined spatially and evaluated environmentally (Mesquitela et al., 2022).

Antalya is one of the most prominent tourist destinations in the region. The city's population is growing at a rapid rate. Additionally, Muratpasa is among the most ancient settlements in Antalya.

The objective of this study is to ascertain the regions exhibiting elevated accident risk through the utilization of the 'kernel density estimation' method, employing data on traffic accidents that occurred between 2017 and 2021 within the borders of the central district of Muratpasa, Antalya, Turkey, in QGIS, a GIS-based program. A study specific to this region has not been identified in the literature review in recent years. Furthermore, variables such as the ages of the drivers involved in accidents, the causes of accidents, the distribution of injuries and fatalities after accidents, and the distribution of accidents by months were analyzed. Additionally, the locations where accidents occurred due to insufficient 'stopping visibility distance' were identified.

2. MATERIAL AND METHOD

2.1. Study Area

The selected working area in this study was the Muratpasa district of Antalya province. The location of the region is shown in Figure 1. Furthermore, as shown in Figure 1, the highest population density in Antalya is observed in the city center, which is identified as the Muratpasa district. According to Turkish Statistical Institute data, the population of the district has been increasing in the last 5 years except 2023. The data indicate that the district's population was 510368 in 2019, 513035 in 2020, 521183 in 2021, 526293 in 2022, and 512700 in 2023 (Turkish Statistical Institute, nd). At the same time, the province receives many tourists during the summer season, which leads to an increase in traffic. As there are some tourist spots in these areas, the traffic becomes even more intense. This high population and traffic density in Muratpasa district shows that a traffic accident on the motorway in the region has a significant direct or indirect impact on many civilians.

2.2. QGIS Software and Kernel Density Estimation

In this study, the QGIS program was used to make analysis as well as visualize maps. The software is open to continuous development with its user-friendly interface, accessibility and open-source nature (Khan & Mohiuddin, 2018; Moyroud & Portet, 2018). All these reasons were effective in the use of QGIS in the study. For the interaction of accidents, the radius was set as 0.01 and the pixel size as 0.001.

To determine hotspots by using Kernel Density Estimation Analysis, the coordinates of the traffic accident were entered into the GIS program. Kernel Density Estimation Analysis is one of the most widely used methods, as the results obtained can be mapped spatially, and densities can be readily determined. In this method, the data within the selected radius are subjected to analysis, resulting in the calculation of the density. Consequently, a smooth conical surface is generated (Yigit Katanalp et al., 2023). This method differs from

others in that it does not depend on assumptions about the density of the data set. Instead, it directly examines the distribution of the data set and the cluster itself (Zhang et al., 2021). Moreover, the bandwidth selected in this method is of significant importance (Harirforoush & Bellalite, 2019).

$$f(x,y) = \frac{1}{n*h^2} * \sum_{i=1}^{n} K * \left(\frac{d_i}{h}\right)$$
(1)

In Equation 1, f(x,y) represents the density assumption for point x, h denotes the width of the band, n signifies the number of observations, d_i (x, y) is the distance between the selected location and it's location, and K is the coefficient (Anderson, 2009).
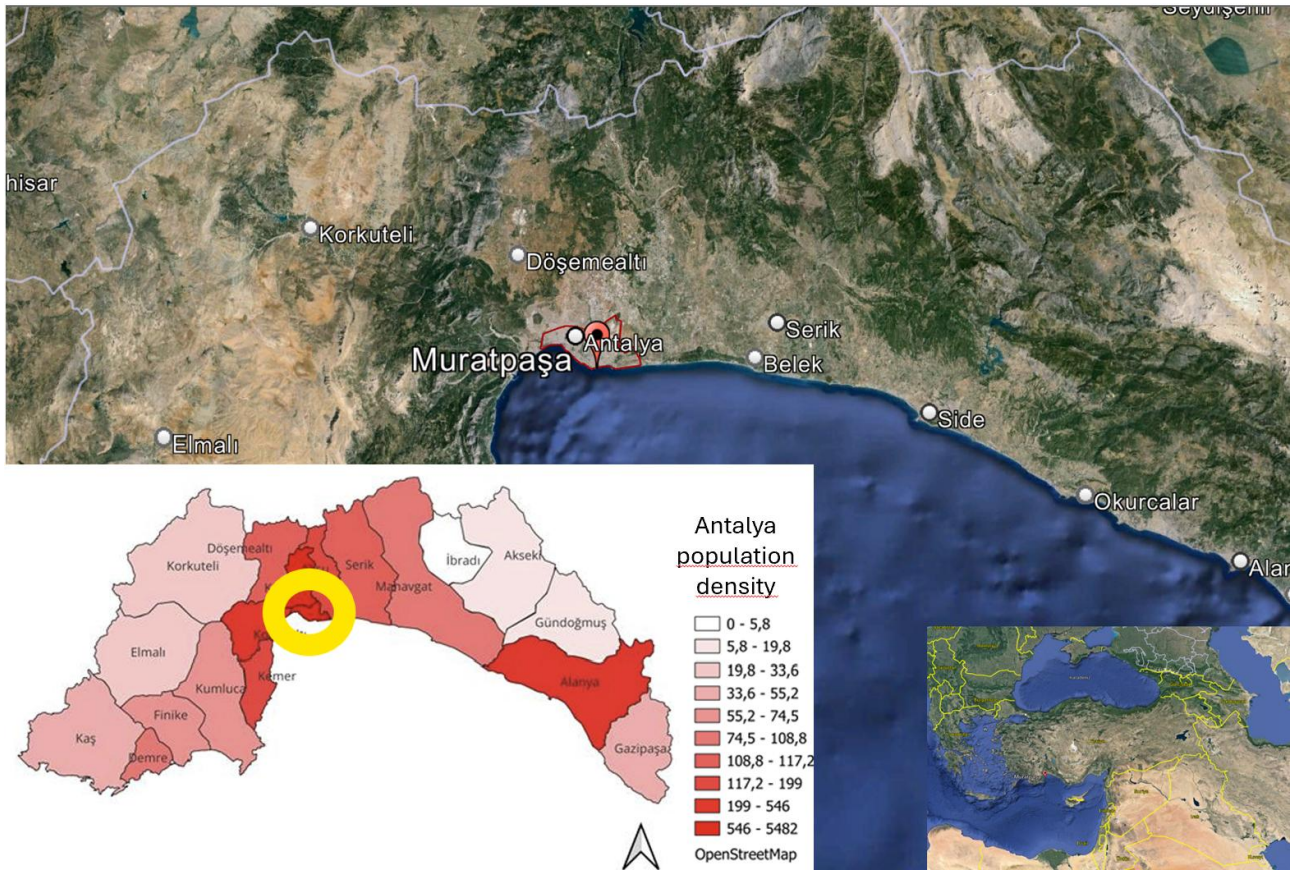
Figure 1. Location of Muratpasa district and population density Antalya province

2.3. Traffic Accidents Caused by Insufficient Sight Distance

It is of significant importance to consider the impact of sight distances on traffic safety when analyzing traffic accidents (Deng et al., 2008; Abdulhafedh, 2020). In traffic safety, several factors, such as the presence of trees and building corners, can impede drivers' visibility. This situation mostly results in traffic accidents. There are two primary categories of visibility deficiencies:

- Insufficient stopping sight distance,
- Insufficient overtaking sight distance.

Insufficient stopping sight distance

In this study, to analyze the Insufficient stopping sight distance effect on traffic accidents, the following accidents were selected based on data obtained from General Directorate of Security: those caused by rear-ending (accident number 1), failing to stop at a red light or stop sign (accident number 2), slowing down or

stopping in a way that disrupts traffic (accident number 3), and failing to slow down at pedestrian and school crossings or failing to give pedestrians the right of way (accident number 4).

In the QGIS program, the locations where accidents due to the reasons are concentrated were identified with heat maps. Equation 2 presents the stopping sight distances. The formula for the stopping sight distance is given in Equation 2, Equation 2 was employed in the creation of the table.

$$L_{fe} = 0,278 * V * t_r + 0,00394 * \frac{V^2}{f \pm s} \tag{2}$$

In Equation 2, V (km/h) represents the vehicle speed, t_r (sec) denotes the travel-reaction time, f is the coefficient of friction on the highway surface, and s is the slope of the highway. Due to the high rainfall in Antalya province in some seasons, the friction value on the platform decreases. In rainy weather, the f value drops to 0.35. The equation for the overtaking sight distance for no oncoming vehicles is given in Equation 3, and the formula for the overtaking sight distance for oncoming vehicles is given in Equation 4 (Yayla, 2004).

$$L_s = \frac{v_1 * (d_1 + d_2)}{v_1 - v_2} \tag{3}$$

In Equation 3, the variables v_1 and v_2 represent the speed of the vehicles, while the variables d_1 and d_2 represent the following distances.

$$L_s = \frac{v_1 * (d_1 + d_2)}{v_1 - v_2} + v_3 * \frac{(d_1 + d_2)}{v_1 - v_2} \tag{4}$$

In Equation 4, the symbols v_1 and v_2 represent the speed of vehicles traveling in the same direction, while the symbol v_3 represents the speed of the approaching from the opposite direction. The symbols d_1 and d_2 represent the following distances of vehicles traveling in the same direction.

2.4. Age of drivers involved in accidents and the relationship between age-accidents

In a study conducted using data on traffic accidents that occurred in Hosanna Town between 2015 and 2017, it was determined that the age range between 18 and 30 was the highest in traffic accidents (Hayidso et al., 2019).

In this study, an age analysis was conducted to examine the distribution of driver ages in traffic accidents in the region.

2.5. Causes of accidents

In a study conducted on the Lokoja-Abuja-Kaduna highway in Nigeria, it was observed that the most common cause of accidents was drivers violating the speed limit (Afolayan et al., 2022).

The causes of accidents were evaluated according to four main categories: speed-related accidents, accidents thought to be caused by lack of attention, accidents caused by non-compliance with the rules, and traffic accidents caused by other reasons.

2.6. Situation after the accident

In a study conducted in Karabük, the occurrence of black spots was identified through the analysis of data on traffic accidents that occurred between 2013 and 2017. In the same study, the health status of individuals involved in the accidents was examined, and it was determined that 0.38% of the accidents resulted in death, 61.52% in injury, and 35.11% in material damage (Doğru & Aydın, 2018).

In this study, the situation after the accident was examined under 5 main headings. These are:

1. Fatal accident,
2. Accident with injury,
3. Safe (no deaths or injuries) accident,
4. The driver is not in the vehicle, or the vehicle is parked.
5. Vehicle driver escapes from the accident area

3. RESULTS AND DISCUSSION

In this study, initially accident risk zone map was created by using QGIS. This map shown in Figure 2 was created using data on traffic accidents that occurred in the Muratpasa district. The coordinates of the regions with a high risk of accidents are shown in Figure 2 as the red region.
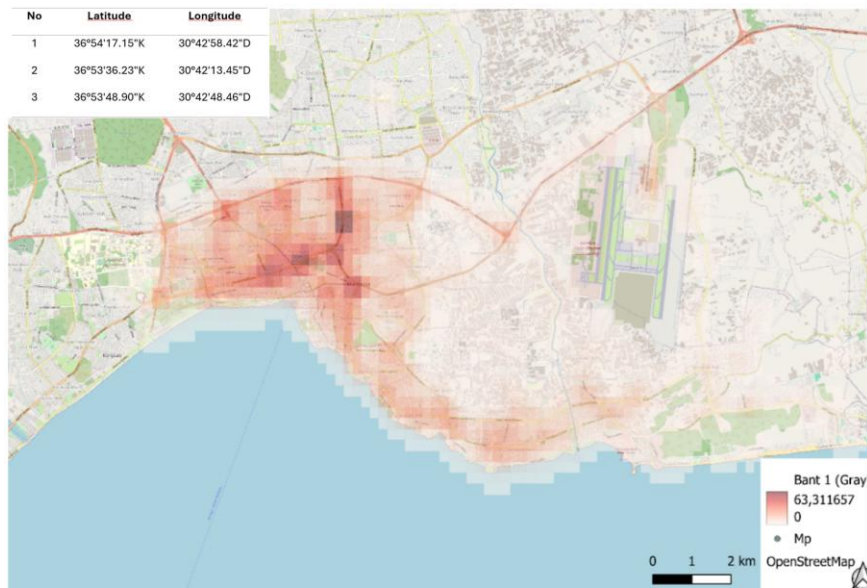
Figure 2. Accident risk zone map

To traffic accident analysis encompassed several parameters, not only including the place where the traffic accident occurred but also including the age of the drivers involved in the accident, the relationship between age and accident, the causes of the accident, the situation after the accident, and the distribution of accidents by month.

Age of drivers involved in accidents and the relationship between age-accidents

In this study, an age analysis was conducted to examine the distribution of driver ages in traffic accidents in the region. Furthermore, the potential correlation between the age of drivers involved in accidents in the region and the occurrence of such incidents was investigated through a correlation analysis conducted using the SPSS statistical software. Figure 3 shows the age distribution of drivers involved in traffic accidents in the Muratpasa district.
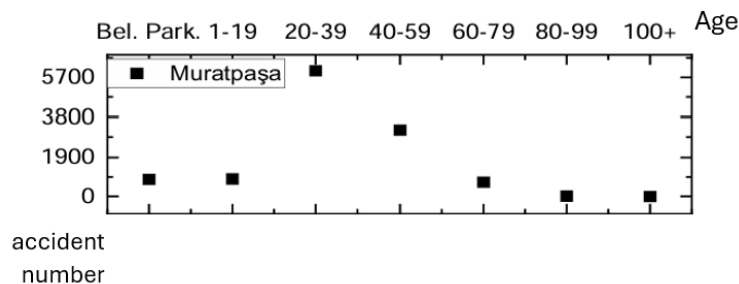
Figure 3. Age distribution of drivers involved in traffic accidents

In this study, drivers aged 20-39 years were found to be involved in the highest number of accidents, while drivers aged 40-59 years showed the second-degree highest level of involvement. In a study conducted using data on traffic accidents that occurred in Hosanna Town between 2015 and 2017, it was determined that the age range between 18 and 30 was the highest in traffic accidents (Hayidso et al., 2019). The results obtained are consistent with this study. This situation shows that more young drivers are involved in traffic accidents. This may have various reasons such as their novice driving and their tendency to drive fast. Figure 4 shows the graph of the health status of the individuals involved in the accident after the accident.
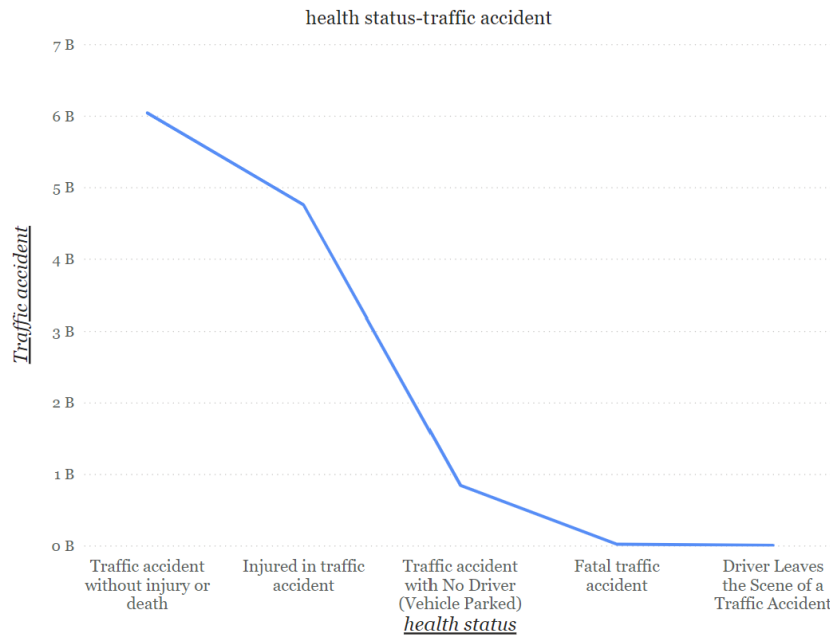
Figure 4. Health status of individuals involved in traffic accidents

A study conducted in Karabük identified that 0.38% of traffic accidents in that province resulted in fatalities, 35.11% in material damage, and 61.52% in injuries (Doğru & Aydın, 2018). In the study, the underlying causes of traffic accidents in the Muratpasa district of Antalya province were determined as drivers' failure to comply with the established rules, excessive speed, inattention and other contributing factors. It can be said that 95% of all traffic accidents do not result in death.

Causes of accidents due to lack of vision

In this study, firstly data related to the reason for accidents were grouped into two categories according to sight distance: The accidents caused by insufficient stopping sight distance and accidents caused by insufficient overtaking sight distance. Then, data related to causes of accidents based on stopping sight distance were numbered as below:

1. Reported as speed-related accidents (commonly caused by stop-and-go is the driver's failure to stop despite the light or officer's stop signal)
2. Accidents reported to be caused by lack of attention
3. Accidents reported as caused by non-compliance with the rules
4. Traffic accidents reported as caused by other reasons

Figure 5 shows the risk map of traffic accidents caused by insufficient stopping distance in the district. It has been determined that the most common cause of traffic accidents caused by stop-and-go is the driver's failure to stop despite the light or officer's stop signal. In a study conducted on the Lokoja-Abuja-Kaduna highway in Nigeria, it was determined that the most common cause of accidents was drivers violating the speed limit (Afolayan et al., 2022). In other words, accidents due to speed and accidents due to the vehicle's inability to stop because of speed occur frequently, as seen in this study. Also Figure 6 shows the accidents caused by insufficient overtaking sight distance

Figure 5. Accidents caused by insufficient stopping sight distance

Distribution of accidents by years and months

In this study, the distribution of traffic accidents by month was examined and the month in which the greatest number of accidents occurred was determined. The incidence of traffic accidents varies considerably between different regions and months. For example, a study revealed that the majority of traffic accidents occur during the winter season (Le et al., 2020). In a separate study, the occurrence of traffic accidents was determined to be particularly prevalent during the summer months. Because the intensity of traffic varies depending on the characteristics of the region. Antalya is the biggest tourism city in Turkey. Especially in summer, the population of Antalya increases by approximately doubled. As can be seen in Figure 6 the greatest number of traffic accidents in the district occurred in July. The lowest number of accidents was recorded in February. The data indicates that the highest number of traffic accidents in the district occurred in 2021.
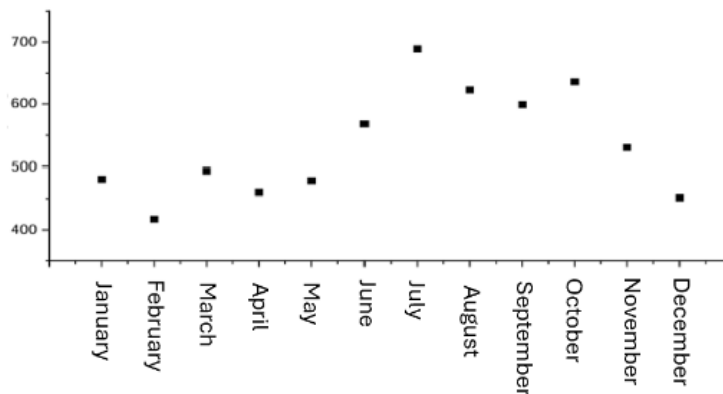
Figure 6. Distribution of accidents by months

4. CONCLUSION

The objective of this study is to identify the specific locations within the Muratpasa district of Antalya province that are most prone to traffic accidents. The Quantum Geographic Information System (QGIS) program was employed to facilitate the comprehension of the regions exhibiting a concentration of accidents. The regions where traffic accidents are concentrated are indicated by a dark red coloration. The results indicated that traffic accidents are concentrated in intersection areas.

The study revealed that the age group most frequently involved in traffic accidents in the Muratpasa district was that of individuals between the ages of 20 and 39. Given that Muratpasa district is an established settlement with a concentration of entertainment venues, it has been determined that the majority of traffic accidents occur

during periods of increased tourism. It has been determined that the majority of road traffic accidents are caused by driver errors. These include speeding, failure to comply with traffic regulations and driving under the influence of alcohol. The study also revealed that approximately 52 out of 100 individuals involved in accidents survived without injury, while seven accidents resulted in injury. Furthermore, the regions within the Muratpaşa district where accidents resulting from inadequate insufficient stopping sight distance were concentrated were identified. The analysis indicates that accidents caused by inadequate stopping visibility are concentrated in two regions.

As a result of all these findings, traffic control can be tightened in some accident-prone areas.

In addition, some factors may lead to incorrect data being entered at the scene. For example, latitude and longitude values in coordinate data may be confused. In such cases, the data should be checked and investigations carried out.

ACKNOWLEDGEMENT

AUTHOR CONTRIBUTIONS

Conceptualization, Sevil Köfteci and Mehmet Arikan Yalcin ; methodology, Sevil Köfteci and Mehmet Arikan Yalcin ; fieldwork, Sevil Köfteci and Mehmet Arikan Yalcin .; software, Mehmet Arıkan Yalçın and Sevil Köfteci; title, Sevil Köfteci and Mehmet Arikan Yalcin ; validation, Sevil Köfteci and Mehmet Arikan Yalcin ; laboratory work, Sevil Köfteci and Mehmet Arikan Yalcin .; formal analysis, Sevil Köfteci and Mehmet Arikan Yalcin ; research, Sevil Köfteci and Mehmet Arikan Yalcin ; sources, Sevil Köfteci and Mehmet Arikan Yalcin ; data curation, Sevil Köfteci and Mehmet Arikan Yalcin .; manuscript-original draft, Sevil Köfteci and Mehmet Arikan Yalcin ; manuscript-review and editing, Sevil Köfteci and Mehmet Arikan Yalcin ; visualization, Sevil Köfteci and Mehmet Arikan Yalcin .; supervision, Sevil Köfteci and Mehmet Arikan Yalcin ; project management, Sevil Köfteci and Mehmet Arikan Yalcin ; funding, Sevil Köfteci and Mehmet Arikan Yalcin . All authors have read and legally accepted the final version of the article published in the journal.

CONFLICT OF INTEREST

The authors declare no conflict of interest.

REFERENCES

Abdulhafedh, A. (2020). Highway stopping sight distance, decision sight distance, and passing sight distance based on AASHTO models. *Open Access Library Journal*, *7*(3), 1-24. http://doi.org/10.4236/oalib.1106095

Afolayan, A., Easa, S. M., Abiola, O. S., Alayaki, F. M., & Folorunso, O. (2022). GIS Based Spatial Analysis of Accident Hotspots: A Nigerian Case Study. *Infrastructures*, *7*(8), 103. http://doi.org/10.3390/infrastructures7080103

Alam, M. S., & Tabassum, N. J. (2023). Spatial pattern identification and crash severity analysis of road traffic crash hot spots in Ohio. *Heliyon*, *9*(5). http://doi.org/10.1016/j.heliyon.2023.e16303

Anderson, T. K. (2009). Kernel density estimation and K-means clustering to profile road accident hotspots. *Accident Analysis & Prevention*, *41*(3), 359-364. http://doi.org/10.1016/j.aap.2008.12.014

Clifton, K. J., & Kreamer-Fults, K. (2007). An examination of the environmental attributes associated with pedestrian–vehicular crashes near public schools. *Accident Analysis & Prevention*, *39*(4), 708-715. http://doi.org/10.1016/j.aap.2006.11.003

Deng, K., Zhang, H., & Huang, Y. (2008, October 20-22). *Safety analysis on road sight distance*. In: Proceedings of the 2008 International Conference on Intelligent Computation Technology and Automation (ICICTA) (Vol. 2, pp. 461-465). Changsha, China. https://doi.org/10.1109/icicta.2008.226

Doğru, E., & Aydın, F. (2018, October 3-6). *Coğrafi Bilgi Sistemleri Yardımıyla Trafik Kazalarının Analizi: Karabük Merkez İlçe Örneği.* In: Proceedings of the International Geography Symposium on the 30th Anniversary of TÜCAUM, (pp. 355-369), Ankara.

Harirforoush, H., & Bellalite, L. (2019). A new integrated GIS-based analysis to detect hotspots: A case study of the city of Sherbrooke. *Accident Analysis & Prevention*, *130*, 62-74. http://doi.org/10.1016/j.aap.2016.08.015

Hayidso, T. H., Gemeda, D. O., & Abraham, A. M. (2019). Identifying road traffic accidents hotspots areas using GIS in Ethiopia: a case study of Hosanna Town. *Transport and Telecommunication Journal*, *20*(2), 123-132. http://doi.org/10.2478/ttj-2019-0011

Khan, S., & Mohiuddin, K. (2018). Evaluating the parameters of ArcGIS and QGIS for GIS Applications. *International Journal of Advance Research in Science and Engineering*, *7*(3), 582-594. https://doi.org/10.1002/9781119457091.ch3

Le, K. G., Liu, P., & Lin, L.-T. (2020). Determining the road traffic accident hotspots using GIS-based temporal-spatial statistical analytic techniques in Hanoi, Vietnam. *Geo-spatial Information Science*, *23*(2), 153-164. http://doi.org/10.1080/10095020.2019.1683437

Le, K. G., Tran, Q. H., & Do, V. M. (2023). Urban Traffic Accident Features Investigation to Improve Urban Transportation Infrastructure Sustainability by Integrating GIS and Data Mining Techniques. *Sustainability*, *16*(1), 107. http://doi.org/10.3390/su16010107

Loo, B. P. Y. (2006). Validating crash locations for quantitative spatial analysis: a GIS-based approach. *Accident Analysis & Prevention*, *38*(5), 879-886. http://doi.org/10.1016/j.aap.2006.02.012

Mesquitela, J., Elvas, L. B., Ferreira, J. C., & Nunes, L. (2022). Data analytics process over road accidents data—a case study of Lisbon city. *ISPRS International Journal of Geo-Information*, *11*(2), 143. http://doi.org/10.3390/ijgi11020143

Moyroud, N., & Portet, F. (2018). Introduction to QGIS. In: N. Baghdadi, C. Mallet, & M. Zribi (Eds.), *QGIS and Generic Tools*, (pp. 1-17). Wiley. https://doi.org/10.1002/9781119457091.ch1

Sababhi, S., Aldala'in, S., Al Taani, A., Al Rawashdeh, S., Al Barari, T., Aladwan, Z., & Manan, T. S. B. A. (2024). Safety on Jordan's highways: A GIS-Based approach to identifying road accident hotspots. *GeoJournal*, *89*(3), 105. http://doi.org/10.1007/s10708-024-11115-5

Sohaib, M., Najeeb, A., Umair, M., Khan, M. A., Zubair, M. U., Jehan, Z., & Khattak, A. (2024). Improving urban road infrastructure analysis and design using an integrated BIM-GIS and traffic microsimulation framework. *Innovative Infrastructure Solutions*, *9*(7), 285. http://doi.org/10.1007/s41062-024-01609-z

Tola, A. M., Demissie, T. A., Saathoff, F., & Gebissa, A. (2021). Severity, spatial pattern and statistical analysis of road traffic crash hot spots in Ethiopia. *Applied Sciences*, *11*(19), 8828. http://doi.org/10.3390/app11198828

Turkish Statistical Institute (nd). https://www.tuik.gov.tr/

Yayla, N. (2004). *Karayolu Mühendisliği*, Birsen Yayınevi, İstanbul.

Yigit Katanalp, B., Eren, E., & Alver, Y. (2023). An integrated solution to identify pedestrian-vehicle accident prone locations: GIS-based multicriteria decision approach. *Journal of Transportation Safety & Security*, *15*(2), 137-176. http://doi.org/10.1080/19439962.2022.2048760

Zhang, J., & Shi, T. (2019). Spatial analysis of traffic accidents based on WaveCluster and vehicle communication system data. *EURASIP Journal on Wireless Communications and Networking*, *2019*(1), 124. http://doi.org/10.1186/s13638-019-1450-0

Zhang, Y., Sun, X., Chen, J., & Cheng, C. (2021). Spatial patterns and characteristics of global maritime accidents. *Reliability Engineering & System Safety*, *206*, 107310. http://doi.org/10.1016/j.ress.2020.107310

Photovoltaic Power Prediction with Teaching Learning Based Optimization Algorithm

Oğuz TAŞDEMİR[1]* iD

[1] Department of Electricity and Electronics, Vocational College of Kaman, Kırşehir Ahi Evran University, Kırşehir, Türkiye

Keywords	Abstract
Photovoltaic Power Current Developments Photovoltaic Power Estimation TLBO	The need for electrical energy has increased considerably due to technological developments. Reducing costs and losses, especially in the supply of electrical energy, is among the goals of energy companies. Photovoltaic energy has been an important alternative in reducing energy costs. However, there are significant power quality problems in transferring the generated photovoltaic energy to the grid. Therefore, the generated photovoltaic energy needs to be accurately estimated to be transferred to the grid smoothly. In the literature, many forecasting models have been used for photovoltaic power forecasting. Each of these forecasting models has estimated photovoltaic power using different input parameters, different estimation intervals, and different estimation algorithms. This paper was conducted using the Teaching-Learning Based Optimization (TLBO) algorithm as an alternative approach to photovoltaic power forecasting models. According to the forecasting results, the root mean square error (RMSE) for the test subset was obtained as 270.32 kW, and the mean absolute percentage error (MAPE) was found to be 3.87%. These results indicate that the TLBO algorithm demonstrates high accuracy for photovoltaic power forecasting and provides an effective alternative model in this field.

1. INTRODUCTION

With the escalation of the energy crisis, renewable energy sources like photovoltaic (PV) power, wind energy, and hydropower have garnered significant interest from numerous nations globally. Photovoltaic (PV) electricity is a significant contributor to the continuous, steady, and cost-effective functioning of power networks among the most prevalent renewable energy sources (Lin et al., 2022). In reaction to the growing need for renewable energy, photovoltaic power generation is consistently rising. The International Renewable Energy Agency (IRENA, 2024) projects that global renewable energy capacity will attain 3870 GW by the conclusion of 2023. Solar energy has the largest share in the global total with 1419 GW of capacity. Hydropower and wind power accounted for most of the rest, with total capacities of 1268 GW and 1017 GW, respectively (IRENA, 2024). Renewable energy capacity by source is shown in Figure 1.

Renewable energy capacity increased by 473 GW in 2023. Solar power continued to lead capacity growth with a large increase of 346 GW, followed by wind power with 116 GW. Solar and wind continued to dominate renewable capacity growth, together accounting for 97.6% of all net renewable capacity additions in 2023. The expansion of wind and solar energy has resulted in the highest annual increase in renewable generation capacity, as well as the highest percentage growth on record (IRENA, 2024). However, due to the randomness, uncertainty, and variability in photovoltaic power generation, there are significant challenges in connecting large-scale photovoltaic systems to the grid (Maghami et al., 2016). The fluctuation and intermittency of

photovoltaic power can cause unexpected losses in existing electricity systems (Liu et al., 2018). In addition, the unstable nature of photovoltaic power systems can lead to power outages, voltage fluctuations, and grid inefficiency. It is therefore evident that research into accurate prediction of photovoltaic power output and the facilitation of integration of photovoltaic power into the grid represents a significant and growing area of interest within the field of photovoltaic power generation (Saber et al., 2014). This is because the impact of power quality problems caused by photovoltaic systems can be reduced or completely eliminated by predicting the photovoltaic power to be generated. Figure 2 shows the increase in renewable energy capacity.
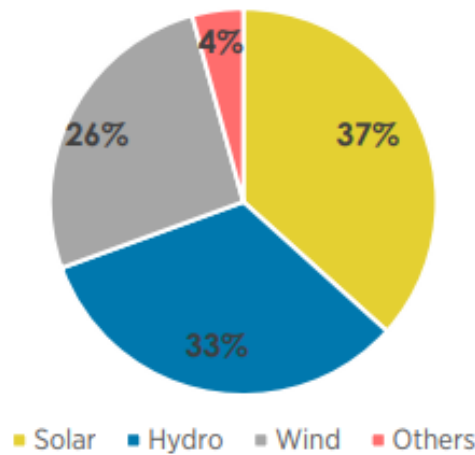
Figure 1. Renewable energy capacity by energy source (IRENA, 2024)
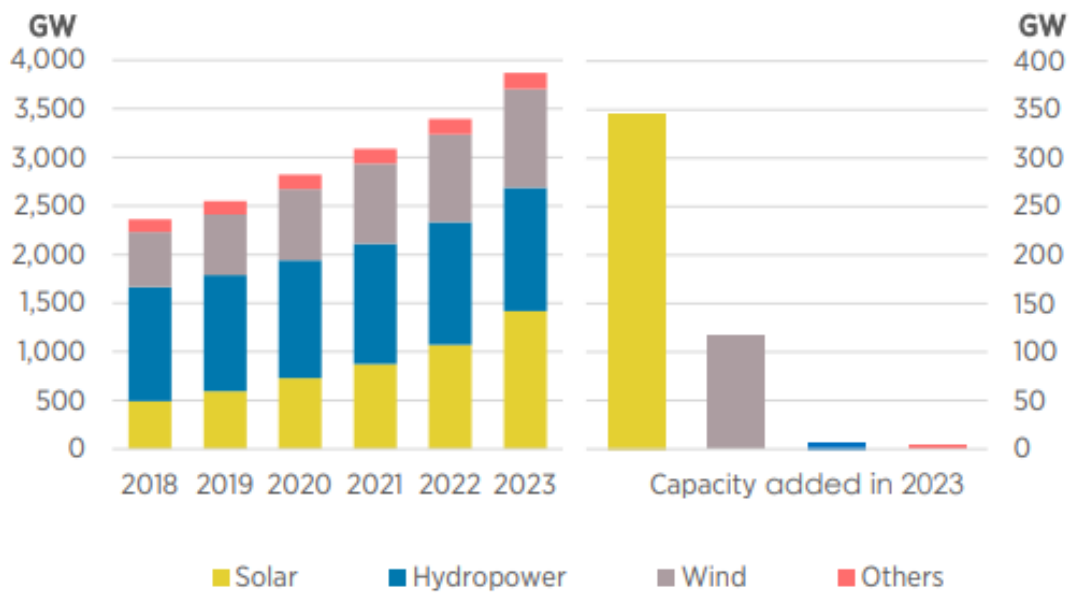
Figure 2. Renewable energy capacity growth (IRENA, 2024)

As a result of advances in artificial intelligence technology, photovoltaic power forecasting is performed in very short-term, short-term, medium-term, and long-term periods (Li et al., 2020). The four different time horizons used for photovoltaic power forecasting and their purposes can be explained as follows (Kleissl, 2013; Elsinga & Van Sark, 2017): The very short-term period covers forecasts of up to 15 minutes for load following, reserve capacity planning, and power quality. The short-term period includes forecasts between 15 minutes and 1 hour for market bidding, load following, and reserve capacity planning. The medium-term period covers forecasts from 1 hour to 1 day for baseload planning and market bidding. The long-term period includes forecasts beyond 1 day for energy management, power capacity dispatch, and market bidding. The different time horizons and purposes used in photovoltaic power forecasting are shown in Table 1.

Table 1. Applicability of photovoltaic power estimation at different times

Horizons	Period	Purposes
Ultra-short-term	One second to 15 minutes	Load following, reserve capacity planning, power quality
Short-term	15 minutes to one hour	Market bidding, load following, reserve capacity planning
Medium-term	One hour to one day	Base-load planning, market bidding
Long-term	Prediction after one day	Energy management, distribution of power capacity, market bidding

Photovoltaic power estimation can be categorized under three main headings: physical models, statistical methods, and machine learning models (Das et al., 2018). Physical models use the mathematical relationship between solar radiation and photovoltaic power output. These models are calculated based on numerical weather forecasts or satellite data. Statistical methods allow us to infer correlation and variation patterns based on statistical principles by analyzing historical data. However, since they focus on historical data, they usually neglect weather conditions (Tang et al., 2022). Machine learning methods, on the other hand, can learn the relationships between data by training large data sets. Therefore, they require less input than physical models (Dosdoğru & İpek, 2022). It is therefore possible to make direct predictions about future PV power by utilising historical data on PV power and meteorological variables.

The development of effective solar energy forecasting methods is of great significance in ensuring the optimal utilisation of renewable energy sources. In this context, the primary objective of the present study is to devise an alternative and efficacious model for solar energy forecasting. In this forecasting study, conducted using current data, particulate matter (PM10), one of the air pollution parameters, was included as an input variable alongside commonly used input data. This approach represents a pivotal contribution of the study.

2. PHOTOVOLTAIC POWER PREDICTION

A review of similar studies in the literature reveals the diversity of research on photovoltaic power forecasting and the difference in the methods used. Comparisons on the input data used for each forecasting model, forecasting models, forecasting period, forecasting accuracy, and the results obtained form the basis of the research in the literature. The studies in the literature generally cover very short, short, medium, and long-term periods. The literature review based on these periods is presented in detail in Table 2 to Table 5. While there is a range of estimates for photovoltaic power in the literature, the estimates in Table 1 are used as a reference for Table 2 through Table 5.

Table 2. Photovoltaic power predicted methods based on a very short-term period

Ref.	Input data	Prediction models	Prediction periods	Prediction accuracies	Prediction results
(Amarasinghe & Abeygunawardane, 2018)	Air temperature, global horizontal radiation, solar radiation, wind speed, global diffuse radiation	Artificial neural network (ANN)	1-min	RMSE=0,035 MAE=0,0117	ANN>SP
		Smart persistence (SP)		RMSE=0,1015 MAE=0,048	
(Han et al., 2019)	Wind speed, solar radiation, humidity, temperature	Kernel density estimation (KDE)	15-min	MAE(W)=1,88 RMSE(W)=4,19	KDE
(VanDeventer et al., 2019)	Photovoltaic power, ambient temperature, solar radiation	Genetic-algorithm-based support vector macihine (GASVM)	15-min	RMSE(W)=100,47 MAPE(%)=1,7	GASVM>SVM
		Suport vector machine (SVM)		RMSE(W)=680,85 MAPE(%)=11,22	

Table 3. *Photovoltaic power predicted methods based on short-term periods*

Ref.	Input data	Prediction models	Prediction periods	Prediction accuracies	Prediction results
(Das, 2021)	Photovoltaic power	Auto-regressive integrated moving average (ARIMA)	30-min	MAE=699,9 RMSE(W)=821,6	ARIMA>AM
		Analytical method (AM)		MAE=39117,2 RMSE(W)=39300,7	
(Korkmaz, 2021)	Solar radiation, temperature, photovoltaic power	Convolutional neural network (CNN)	1-h	R^2=0,9871 RMSE(kW)=0,309 MAE(kW)=0,175	CNN
(Cheng et al., 2019)	Surface solar radiation, solar radiation, relative humidity, surface temperature, average temperature, wind speed at 10m	Improved grey wolf optimizer algorithm (IMGWO)	1-h	RMSE=0,065	IMGWO>SPGP
		Sparse Gaussian process (SPGP)		RMSE=0,069	
(Theocharides et al., 2020)	Photovoltaic power, meteorological data, numerical weather forecast data	Artificial neural network (ANN)	1-h	nRMSE(%)=6,11 MAPE(%)=4,7	ANN

Table 4. *Photovoltaic power predicted methods based on medium-term period*

Ref.	Input data	Prediction models	Prediction periods	Prediction accuracies	Prediction results
(Ma & Zhang, 2022)	Solar radiation, temperature, relative humidity	Modified Firefly Algorithm (MFA) Elman artificial neural network (Elman)	1-day	MAE(kW)=1,12 MSE(kW)=1,69 RMSE(kW)=1,30	MFA-Elman> FA-Elman> Elman
		Firefly-based Elman neuronal network (FA-Elman)		MAE(kW)=1,56 MSE(kW)=2,98 RMSE(kW)=1,73	
		Elman neural network (Elman)		MAE(kW)=2,36 MSE(kW)=7,84 RMSE(kW)=2,80	
(Irmak et al., 2023)	Solar radiation, power output, temperature, relative humidity	Artificial neural network (ANN)	1-day	RMSE(kW)=2178,1 MAPE(%)=3,83	ANN
	Solar radiation, power output, PM10, temperature			RMSE(kW)=984,7 MAPE(%)=1,86	
(Irmak et al., 2024)	Temperature, power output, PM10, solar radiation	Artificial neural network based on the JAYA algorithm (JAYA-ANN)	1-day	RMSE(kW)=650,44 MAPE(%)=2,72	JAYA-ANN> ANN
		Artificial neural network (ANN)		RMSE(kW)=841,90 MAPE(%)=3,93	
(Qu et al., 2021)	Photovoltaic power	Single gated recurrent unit (SGRU)	1-day	NRMSE(%)=18,31 NMAE(%)=13,67	GRUP>MGRU> SGRU
		Gated recurrent unit pool (GRUP)		NRMSE(%)=6,83 NMAE(%)=4,12	
		Multiple gated recurrent unit (MGRU)		NRMSE(%)=14,5 NMAE(%)=11,18	

Table 5. *Photovoltaic power predicted methods based on long-term period*

Ref.	Input data	Prediction models	Prediction periods	Prediction accuracies	Prediction results
(Moreira et al., 2021)	Relative humidity, rainfall, ambient temperature, sunshine duration, cloudiness	Artificial neural network (ANN)	1-week	MAPE(%)=4,70	ANN
(Dandıl & Gürgen, 2019)	Current, voltage	Clonal selection algorithm (CSA)	1-month	MAPE(%)=1,629 RMSE=1,96	PSO>BP>CSA
		Back-propagation neural network (BP)		MAPE(%)=0,398 RMSE=0,520	
		Particle swarm optimization (PSO)		MAPE(%)=0,206 RMSE=0,270	
(Liang et al., 2023)	Air pressure, humidity, temperature, solar radiation, wind speed and direction	Fast outlier culling algorithm based decision trees-Improved whale bat optimisation algorithm-Least squares support vector regression (FCDT-IWBOA-LSSVR)	1-month	$R2=0,983$ MSE(kW)=1,913 RMSE(kW)=1,383 MAE(kW)=0,625	FCDT-IWBOA-LSSVR

As a result of the review of studies on photovoltaic power forecasting, the following useful conclusions can be drawn:

- Air temperature, solar radiation, and photovoltaic power parameters are the main parameters used for forecasting. Besides these primary parameters, secondary parameters such as relative humidity and wind speed are also important. However, some input parameters are less commonly used. For example, variables such as air pressure, rainfall, cloud cover, sunshine duration, and sky index are among these parameters.

- Artificial neural networks are one of the most widely used methods for the prediction of the power output of photovoltaic systems. After neural networks, other methods such as support vector machines, support vector regression, and autoregressive integrated moving averages come next and offer alternative approaches for photovoltaic power forecasting. However, collective learning aims to achieve more accurate results by combining different forecasting models. Exogenous variable-driven autoregressive modeling forecasts by taking into account the effects of exogenous variables (e.g. cloudiness, wind speed, etc.) on solar power generation. Radial basis functions allow the modeling of complex relationships by transforming input data. Recurrent neural networks and multilayer perceptrons are used to analyze time series data.

- Time intervals have an important role in the photovoltaic power forecasting process and are usually categorized according to specific periods. These time intervals affect the accuracy and precision of the forecasting methods. Studies generally cover very short-term, short-term, and mid-term forecasting periods. In particular, 15 minutes (very short term), 1 hour (short term), and 1 day (medium term) are the time intervals used for forecasting.

- Error measures are an essential component in the evaluation of photovoltaic power forecasts, as they provide insight into the discrepancies between predicted power values and actual observations. Commonly employed metrics for assessing the accuracy, precision, and reliability of prediction models include the mean absolute error, normalised root mean square error, mean absolute percentage error, and root mean square error.

- The breadth of the data input area in photovoltaic power forecasting can substantially influence the accuracy of the predictions. This indicates that an extensive data input area enables the forecasting model to utilize a broader array of information, hence enhancing prediction accuracy. Moreover, an extensive input data space enables the model to learn from a greater volume of data and to evaluate

the interrelationships among this data with enhanced precision. This enables the forecasting algorithm to generate more consistent and dependable forecasts.

- During seasons when weather variables change less, solar power systems exhibit a more constant performance. This makes it easier for forecasting models to more accurately predict future power generation based on historical data. Especially in summer, solar radiation and air temperature are generally more stable, which can contribute to more consistent results from forecasting models.

- In photovoltaic power forecasts, it is observed that forecast accuracy increases with decreasing forecast time. This suggests that forecasts with shorter time intervals may provide more reliable results. However, each forecast interval and method should be evaluated depending on specific conditions and requirements. For example, while short-term forecasts may be appropriate for maintaining the supply-demand balance on the power side, long-term forecasting is required to assess the economic situation. Therefore, a delicate balance must be maintained when determining the right forecasting strategies.

- In photovoltaic power forecasting, it was observed that the success rate of the forecasting model increased when the sampling time was reduced, i.e. in scenarios where data was collected more frequently and forecasts were updated more frequently. This suggests that more frequent data collection can improve forecast accuracy by enabling faster adaptation to current conditions. However, more frequent sampling and updating can increase data collection and processing costs. Furthermore, forecasts that are updated too frequently indicate that systems need to be constantly monitored and managed, which can increase operational burdens.

- The types of panels used in photovoltaic power estimation are an important factor that can affect the accuracy of the estimation. The different characteristics of these panels can cause differences in the perception and estimation of the factors affecting solar power generation.

- Hybrid models used in photovoltaic power forecasting, i.e. models that combine more than one forecasting method or model, have generally shown better performance. This success of hybrid models can be attributed to the fact that they combine the strengths of different forecasting methods to compensate for weaknesses and improve forecasting accuracy. However, building and optimizing hybrid models is often complex and requires a precise modeling and evaluation process.

- An important aspect is often overlooked in the literature, especially about the reliability and accuracy of forecasts: forecast intervals and forecast errors. In many studies, forecast intervals and forecast errors are not specified. This makes it difficult for researchers to assess the reliability of estimates and prevents monitoring changes over time. To increase the quality of studies and the credibility and transparency of the scientific knowledge production process, estimation intervals and errors should be specified.

- Photovoltaic power forecasts are critical to improve the efficiency of solar systems and optimize energy management. However, it would be useful to present commonly used error scales to assess the accuracy of these forecasts, as well as improvement percentages concerning the continuity reference model to enable appropriate benchmarking tests.

3. TEACHING LEARNING BASED OPTIMIZATION ALGORITHM

TLBO is a meta-heuristic algorithm that simulates the educational impact of an instructor on students in a classroom environment. This algorithm operates in two main stages: the teacher phase and the student phase. During the teacher phase, the instructor conveys knowledge to students, facilitating their progress. Conversely, the student phase models peer-to-peer learning, where students interact to share knowledge among themselves. Within the algorithm, the population represents the students and teacher, with the individual yielding the best solution taking the role of the class teacher. Initially, a random population is generated, and the individual with the highest objective function value is assigned as the teacher. In the teacher phase, this teacher attempts to raise the knowledge level of other individuals to match their own. In the student phase, the algorithm models student interactions, enabling mutual learning and improvement. This iterative process aims to enhance the solution quality generated by the algorithm (Rao et al., 2012; Rao & Patel, 2013).

• Teacher phase: In this phase, the teacher instructs the students and improves the current average result in the nth iteration. The difference in average results is calculated as shown in Equation 1.

$$\Delta MR_n = rand[(NM_n) - (TF_n \times MR_n)] \ where \ \ TF_n = \left(\frac{MR_n}{NM_n}\right) \tag{1}$$

Here, NM_n represents the new mean, MR_n denotes the mean results, and TF_n stands for the teaching factor. Based on the obtained difference in mean results, the current solution is updated according to Equation 2.

$$Xnew_n = Xold_n + \Delta MR_n \tag{2}$$

$Xnew_n$, given in Equation 2, is the updated value of $Xold_n$, and all $Xnew_n$ values are stored and passed as input to the student phase.

• Student phase: The knowledge of any student increases through interaction with other students, and the students' knowledge is updated according to Equations 3 and 4.

$$Xnew_n = Xold_n + rand(X_k - X_m), \ if \ f(X_k) < f(X_m) \tag{3}$$

$$Xnew_n = Xold_n + rand(X_m - X_k), \ if \ f(X_m) < f(X_k) \tag{4}$$

Here, X_k and X_m are randomly selected students, and the updated student value with the better fitness value is retained. The flow diagram of the TLBO method is given in Figure 3.

4. RESULTS OF THE PREDICTION OF THE PHOTOVOLTAIC POWER WITH THE TLBO ALGORITHM

In this study, solar radiation, particulate matter (PM10), ambient temperature, and historical power data were used for daily photovoltaic power forecasting. The dataset used in the study consists of daily recorded data over a three-month period. The TLBO algorithm was applied in the forecasting process, and the forecast results were analyzed separately for the training and test subsets. To evaluate the accuracy of the forecasting model, mean absolute percentage error (MAPE) and root mean square error (RMSE) metrics were employed. The MAPE value was calculated using Equation 5, while the RMSE value was calculated using Equation 6.

$$\text{MAPE} = \frac{1}{n}\sum_{i=1}^{n}\left(\frac{t_i - p_i}{t_i}\right) \times 100 \tag{5}$$

$$\text{RMSE} = \sqrt{\frac{1}{n}\sum_{i=1}^{n}(t_i - p_i)^2} \tag{6}$$

In the aforementioned equations, t_i signifies the actual measured value, p_i symbolizes the anticipated value, and n represents the total number of data points. The forecasting model was trained on a dataset consisting of 70% of the total data and evaluated on a test dataset comprising the remaining 30%.

Using the dataset, the MAPE values for the TLBO-based forecasting study were found to be 7.20% and 3.87% for the training and test subsets, respectively, while the RMSE values were 325.64 kW and 270.32 kW. The TLBO predictions and actual power production for the training and test subsets are shown in Figure 4.

For the forecast made using the entire dataset with the TLBO model, the MAPE value was found to be 6.18%, and the RMSE value was 241.02 kW. Figure 5 presents the actual power production and the TLBO model's forecast results for the complete dataset.
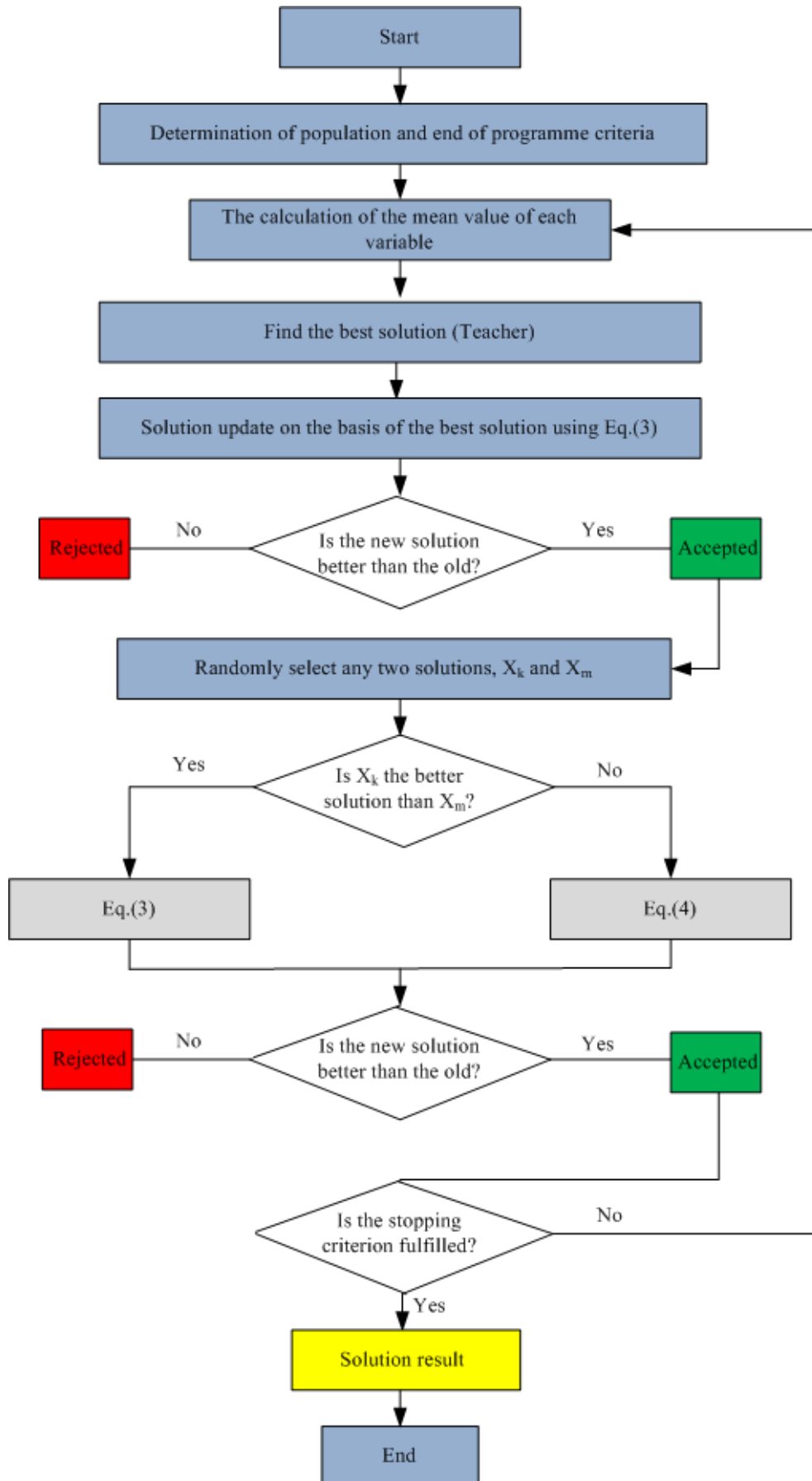
Figure 3. *TLBO flow diagram*
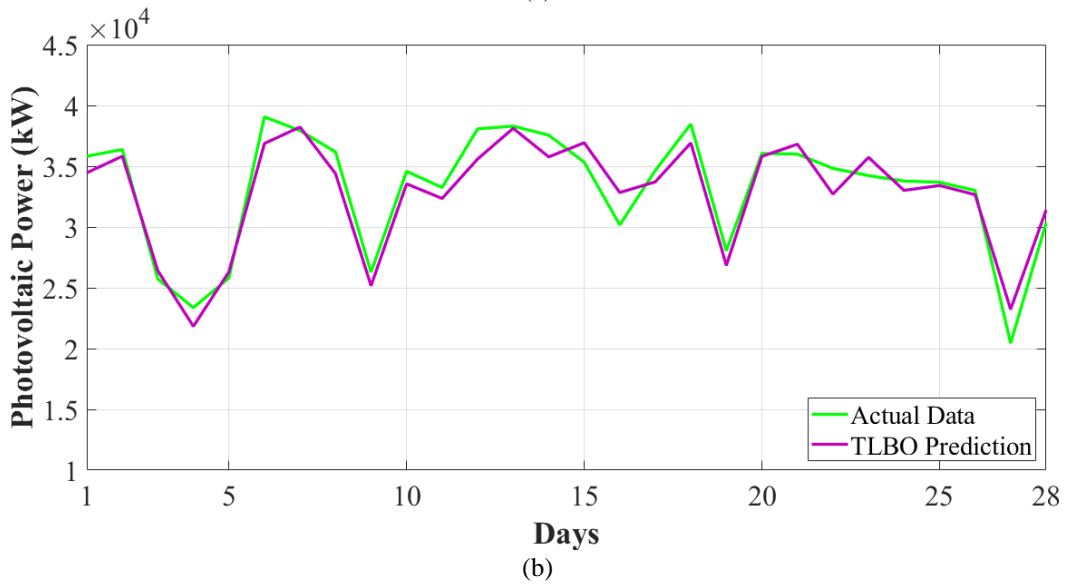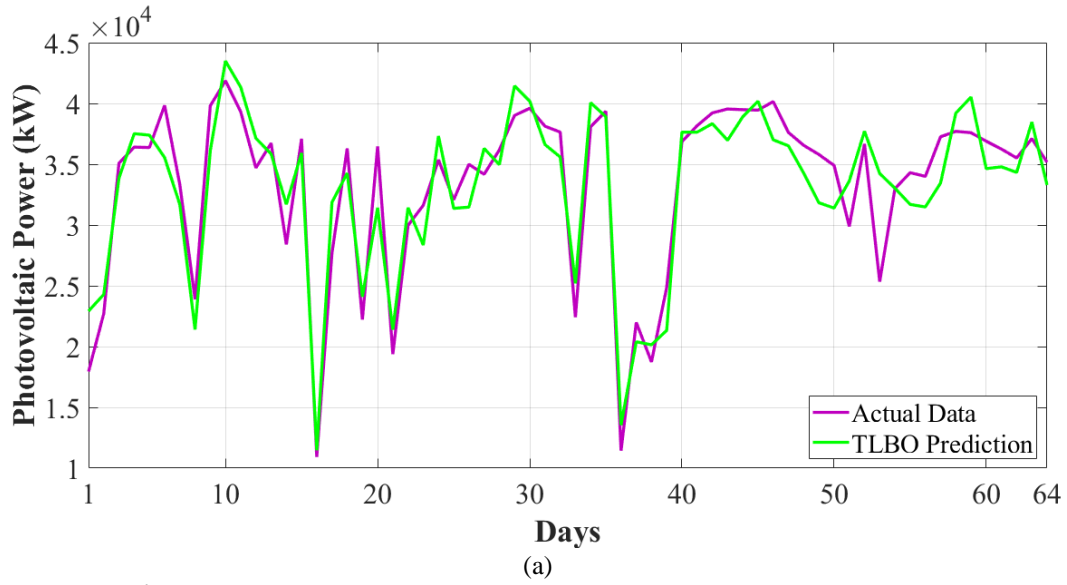
Figure 4. a) Training subset, b) Test subset
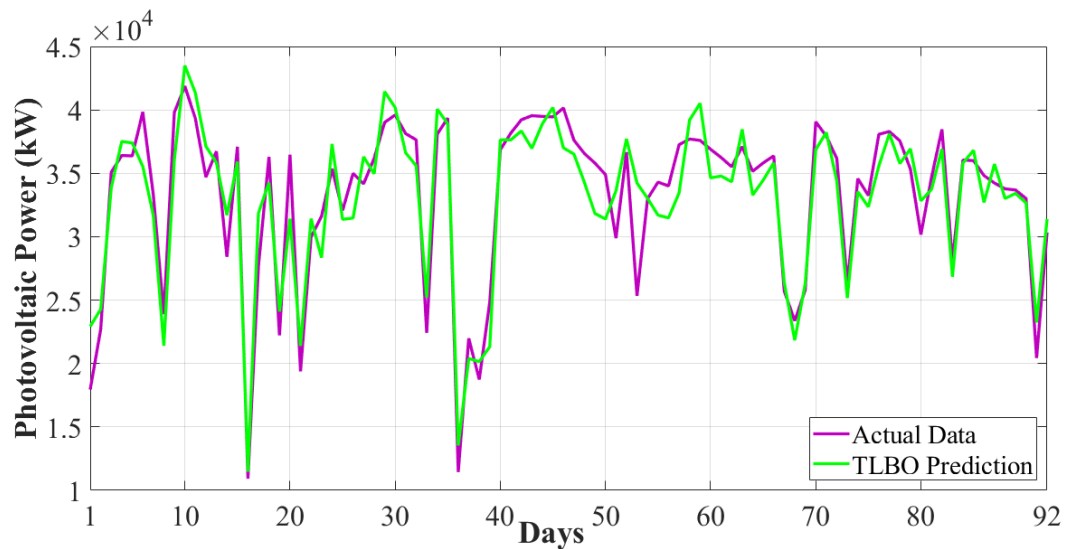
Figure 5. TLBO prediction and actual power generation

The proposed TLBO forecasting model has yielded highly successful results in photovoltaic power forecasting. The MAPE and RMSE values obtained from the forecast are presented in Table 6.

Table 6. MAPE and RMSE values

	MAPE (%)	**RMSE (kW)**
Data Set (training)	7.20	325.64
Data Set (test)	3.87	270.32
Data Set (all)	6.18	241.02

5. CONCLUSION

The objective of this study is to develop a TLBO model for the purpose of forecasting photovoltaic power generation. The developed TLBO model demonstrated highly successful performance in photovoltaic power forecasting, as evidenced by a MAPE of 3.87% and a RMSE of 270.32 kW obtained for the test subset. These performance results indicate that the TLBO algorithm makes a significant contribution, particularly in supporting day-ahead planning and ensuring the stability of power systems. By enabling the prediction of fluctuations in solar energy-based power generation, the model contributes to maintaining grid balance more effectively. In addition, the proposed TLBO model has enabled more accurate and stable results in photovoltaic power forecasting, establishing itself as an alternative method to other forecasting models in the literature. Future studies are encouraged to examine the performance of the TLBO model in more detail by considering different forecasting horizons, seasonal variations, and diverse input data. In this context, comparing the model under various climate conditions and with different data sources is deemed essential to assess its generalizability and potential for broader application.

CONFLICT OF INTEREST

The author declares no conflict of interest.

REFERENCES

Amarasinghe, G., & Abeygunawardane, S. (2018). An artificial neural network for solar power generation forecasting using weather parameters. In: Proceedings of the 112th Annual Sessions, Institution of Engineers Sri Lanka, (pp. 431-438), Colombo, Sri Lanka.

Cheng, Z., Liu, Q., & Xing, Y. (2019). A hybrid probabilistic estimation method for photovoltaic power generation forecasting. *Energy Procedia*, *158*, 173-178. http://www.doi.org/10.1016/j.egypro.2019.01.066

Dandıl, E., & Gürgen, E. (2019). Yapay Sinir Ağları Kullanılarak Fotovoltaik Panel Güç Çıkışlarının Tahmini ve Sezgisel Algoritmalar ile Karşılaştırılması. *Avrupa Bilim ve Teknoloji Dergisi*, *16*, 146-158. http://www.doi.org/10.31590/ejosat.540262

Das, S. (2021). Short term forecasting of solar radiation and power output of 89.6 kWp solar PV power plant. *Materials Today: Proceedings*, *39*, 1959-1969. http://www.doi.org/10.1016/j.matpr.2020.08.449

Das, U. K., Tey, K. S., Seyedmahmoudian, M., Mekhilef, S., Idris, M. Y. I., Deventer, W. V., Horan, B. & Stojcevski, A. (2018). Forecasting of photovoltaic power generation and model optimization: A review. *Renewable and Sustainable Energy Reviews*, *81*, 912-928. http://www.doi.org/10.1016/j.rser.2017.08.017

Dosdoğru, A. T., & İpek, A. B. (2022). Hybrid boosting algorithms and artificial neural network for wind speed prediction. *International Journal of Hydrogen Energy*, *47*(3), 1449-1460. http://www.doi.org/10.1016/j.ijhydene.2021.10.154

Elsinga, B., & Van Sark, W. G. J. H. M. (2017). Short-term peer-to-peer solar forecasting in a network of photovoltaic systems. *Applied Energy*, *206*, 1464-1483. http://www.doi.org/10.1016/j.apenergy.2017.09.115

Han, Y., Wang, N., Ma, M., Zhou, H., Dai, S., & Zhu, H. (2019). A PV power interval forecasting based on seasonal model and nonparametric estimation algorithm. *Solar Energy*, *184*, 515-526. http://www.doi.org/10.1016/j.solener.2019.04.025

IRENA, International Renewable Energy Agency. (2024). Renewable capacity highlights. (Accessed:04/09/2024) https://www.irena.org/-/media/Files/IRENA/Agency/Publication/2024/Mar/IRENA_RE_Capacity_Highlights_2024.pdf?rev=7692ae29458142dd8563618f496e0abb

Irmak, E., Yesilbudak, M., & Tasdemir, O. (2023, June 4-7). *Daily prediction of PV power output using particulate matter parameter with artificial neural networks*. In: Proceedings of the 11th International Conference on Smart Grid (icSmartGrid), (pp. 499-502). Paris, France. https://doi.org/10.1109/icSmartGrid58556.2023.10171103

Irmak, E., Yeşilbudak, M., & Taşdemir, O. (2024). Enhanced PV Power Prediction Considering PM10 Parameter by Hybrid JAYA-ANN Model. *Electric Power Components and Systems*, *52*(11), 1998-2007. http://www.doi.org/10.1080/15325008.2024.2322668

Korkmaz, D. (2021). SolarNet: A hybrid reliable model based on convolutional neural network and variational mode decomposition for hourly photovoltaic power forecasting. *Applied Energy*, *300*, 117410. http://www.doi.org/10.1016/j.apenergy.2021.117410

Kleissl, J. (2013). *Solar energy forecasting and resource assessment*. Academic Press.

Li, P., Zhou, K., Lu, X., & Yang, S. (2020). A hybrid deep learning model for short-term PV power forecasting. *Applied Energy*, *259*, 114216. http://www.doi.org/10.1016/j.apenergy.2019.114216

Liang, L., Su, T., Gao, Y., Qin, F., & Pan, M. (2023). FCDT-IWBOA-LSSVR: An innovative hybrid machine learning approach for efficient prediction of short-to-mid-term photovoltaic generation. *Journal of Cleaner Production*, *385*, 135716. http://www.doi.org/10.1016/j.jclepro.2022.135716

Lin, W., Zhang, B., Li, H., & Lu, R. (2022). Multi-step prediction of photovoltaic power based on two-stage decomposition and BILSTM. *Neurocomputing*, *504*, 56-67. http://www.doi.org/10.1016/j.neucom.2022.06.117

Liu, L., Zhao, Y., Chang, D., Xie, J., Ma, Z., Sun, Q., Yin, H., & Wennersten, R. (2018). Prediction of short-term PV power output and uncertainty analysis. *Applied Energy*, *228*, 700-711. http://www.doi.org/10.1016/j.apenergy.2018.06.112

Ma, X., & Zhang, X. (2022). A short-term prediction model to forecast power of photovoltaic based on MFA-Elman. *Energy Reports*, *8*, 495-507. http://www.doi.org/10.1016/j.egyr.2022.01.213

Maghami, M. R., Hizam, H., Gomes, C., Radzi, M. A., Rezadad, M. I., & Hajighorbani, S. (2016). Power loss due to soiling on solar panel: A review. *Renewable and Sustainable Energy Reviews*, *59*, 1307-1316. http://www.doi.org/10.1016/j.rser.2016.01.044

Moreira, M. O., Balestrassi, P. P., Paiva, A. P., Ribeiro, P. F., & Bonatto, B. D. (2021). Design of experiments using artificial neural network ensemble for photovoltaic generation forecasting. *Renewable and Sustainable Energy Reviews*, *135*, 110450. http://www.doi.org/10.1016/j.rser.2020.110450

Rao, R. V., & Patel, V. (2013). An improved teaching-learning-based optimization algorithm for solving unconstrained optimization problems. *Scientia Iranica*, *20*(3), 710-720. http://www.doi.org/10.1016/j.scient.2012.12.005

Rao, R. V., Savsani, V. J., & Balic, J. (2012). Teaching-learning-based optimization algorithm for unconstrained and constrained real-parameter optimization problems. *Engineering Optimization*, *44*(12), 1447-1462. http://www.doi.org/10.1080/0305215X.2011.652103

Qu, Y., Xu, J., Sun, Y., & Liu, D. (2021). A temporal distributed hybrid deep learning model for day-ahead distributed PV power forecasting. *Applied Energy*, *304*, 117704. http://www.doi.org/10.1016/j.apenergy.2021.117704

Saber, E. M., Lee, S. E., Manthapuri, S., Yi, W., & Deb, C. (2014). PV (photovoltaics) performance evaluation and simulation-based energy yield prediction for tropical buildings. *Energy*, *71*, 588-595. http://www.doi.org/10.1016/j.energy.2014.04.115

Tang, Y., Yang, K., Zhang, S., & Zhang, Z. (2022). Photovoltaic power forecasting: A hybrid deep learning model incorporating transfer learning strategy. *Renewable and Sustainable Energy Reviews*, *162*, 112473. http://www.doi.org/10.1016/j.rser.2022.112473

Theocharides, S., Makrides, G., Livera, A., Theristis, M., Kaimakis, P., & Georghiou, G. E. (2020). Day-ahead photovoltaic power production forecasting methodology based on machine learning and statistical post-processing. *Applied Energy*, *268*, 115023. http://www.doi.org/10.1016/j.apenergy.2020.115023

VanDeventer, W., Jamei, E., Thirunavukkarasu, G. S., Seyedmahmoudian, M., Soon, T. K., Horan, B., Mekhilef. S., & Stojcevski, A. (2019). Short-term PV power forecasting using hybrid GASVM technique. *Renewable Energy*, *140*, 367-379. http://www.doi.org/10.1016/j.renene.2019.02.087

Formulas and Finite Sums Covering Beta-type Rational Functions and Euler-Frobenius-type Polynomials

Damla GUN[1]* 🆔   Yilmaz SIMSEK[1] 🆔

[1] Department of Mathematics, Faculty of Science, Akdeniz University, Antalya, Türkiye

Keywords	Abstract
Special Numbers and Polynomials Stirling Type Numbers Generating Functions	The aim of this article is to derive some novel formulas and finite sums covering Stirling type numbers, the Frobenius Euler numbers and polynomials, the beta-type rational functions, and combinatorial numbers with the help of both generating functions and their functional equations, and also some special identities associated with special numbers and polynomials.

1. INTRODUCTION

Polynomial classes are one of the indispensable fields in both mathematics and all applied sciences, especially engineering. For this reason, thousands of important studies on polynomial classes have been encountered in recent years. The motivation and subject of this article focus on special classes of polynomials. In this study, we will examine special polynomials, especially those of the Euler-Frobenius type polynomials. This class has very intensive and important applications in spline theory. Consequently, the Frobenius-Euler polynomials are also known as the Euler-Frobenius polynomials. There are those who call these polynomials Eulerian polynomials. These polynomials are known as a generalization of the well-known Euler polynomials of the first kind. These polynomials belong to the class of the Appell polynomials, which is a subclass of the well-known Sheffer polynomials within the polynomial families. Polynomial classes of this type have valuable applications in many areas of mathematics, mathematical and applied physics, theoretical and applied chemistry, and even in engineering. Moreover, novel formulas, finite sums, and relations containing these polynomial classes are given.

Let ζ be a complex number: $\mathbb{C}$. The higher-order Frobenius-Euler numbers and polynomials are respectively described by,

$$\left(\frac{1-\mathrm{z}}{e^t - \mathrm{z}}\right)^\zeta = \sum_{n=0}^{\infty} \frac{H_n^{(\zeta)}(\mathrm{z})}{n!} t^n \tag{1}$$

and

$$\left(\frac{1-\mathrm{z}}{e^t - \mathrm{z}}\right)^\zeta = \sum_{n=0}^{\infty} \frac{H_n^{(\zeta)}(\chi; \mathrm{z})}{n!} t^n \tag{2}$$

*Corresponding Author, e-mail: damlagunn@gmail.com

(Carlitz & Sholander, 1963; Kucukoglu & Simsek, 2019).

Gun and Simsek (2023) defined the following monic polynomials, which are denoted by $u_{n}^{(\zeta)}(\chi; \mathfrak{z})$:

$$\left(\frac{1 + \mathfrak{z}}{\mathfrak{z}e^t + 1}\right)^{\zeta} = e^{-t\chi} \sum_{n=0}^{\infty} \frac{u_{n}^{(\zeta)}(\chi; \mathfrak{z})}{n!} t^{n}. \tag{3}$$

From (2) and (3), one has

$$u_{n}^{(\zeta)}(\chi; \mathfrak{z}) - H_{n}^{(\zeta)}\left(\chi; -\frac{1}{\mathfrak{z}}\right) = 0 \tag{4}$$

(Gun & Simsek, 2023).

For $\mathfrak{z} \in \mathbb{C}$ (or real number: $\mathbb{R}$), the second kind $\mathfrak{z}$ -Stirling numbers are described by

$$(\mathfrak{z}e^t - 1)^v = \sum_{n=0}^{\infty} \frac{v! \, S_2(n, v; \mathfrak{z})}{n!} t^{n}. \tag{5}$$

When $\mathfrak{z} = 1$ Eq. (5), yields the second kind Stirling numbers:

$$S_2(n, v; 1) - S_2(n, v) = 0 \tag{6}$$

(Simsek, 2013a; 2013b; 2018a; 2018b; 2023; Srivastava, 2011; Srivastava & Choi, 2001; 2012).

The Apostol Euler numbers of order ζ are described by

$$(\mathfrak{z}e^t + 1)^{-\zeta} = \sum_{n=0}^{\infty} \frac{2^{-\zeta}\mathcal{E}_{n}^{(\zeta)}(\mathfrak{z})}{n!} t^{n} \tag{7}$$

(Luo, 2006; Gun & Simsek, 2020; Simsek, 2013a; 2013b; 2018a; 2018b; 2023; Srivastava, 2011; Srivastava & Choi, 2001; 2012).
Replacing ζ by $-\zeta$, Eq. (7) reduces to the Apostol Euler numbers of negative order are described by

$$(\mathfrak{z}e^t + 1)^{\zeta} = \sum_{n=0}^{\infty} 2^{\zeta} \frac{\mathcal{E}_{n}^{(-\zeta)}(\mathfrak{z})}{n!} t^{n} \tag{8}$$

and also

$$\mathcal{E}_{n}^{(\zeta)}(\mathfrak{z}) = \sum_{z=1}^{n} (-1)^z S_2(n, z) \mathfrak{z}^z \frac{(\mathfrak{z} + 1)^{-z-\zeta}(\zeta)^{(z)}}{2^{-\zeta}}, \tag{9}$$

where $(\zeta)^{(n)}$ denotes

$$(\zeta)^{(n)} = \begin{cases} \zeta(\zeta + 1) \dots (\zeta + n - 1), & n \in \mathbb{N} \\ 1, & n = 0 \end{cases} \tag{10}$$

(Luo, 2006; Gun & Simsek, 2020; 2023; Srivastava, 2011; Srivastava & Choi, 2001; 2012).

The description of the beta-type rational functions $\mathfrak{M}_{j,n}(\mathfrak{z})$:

$$\left(\frac{\mathfrak{z}}{\mathfrak{z}+1}\right)^{\mathfrak{j}} = e^{t(-\mathfrak{z}-1)} \sum_{\mathfrak{n}=0}^{\infty} \mathfrak{M}_{\mathfrak{j},\mathfrak{n}}(\mathfrak{z}) \frac{1}{\mathfrak{n}!} t^{\mathfrak{n}}. \tag{11}$$

From Eq. (11), we have

$$\mathfrak{M}_{\mathfrak{j},\mathfrak{n}}(\mathfrak{z}) - \mathfrak{z}^{\mathfrak{j}}(1+\mathfrak{z})^{\mathfrak{n}-\mathfrak{j}} = 0, \tag{12}$$

where $\mathfrak{n}$ and $\mathfrak{z} \in \mathbb{R}$, (or $\mathbb{C}$) (Simsek, 2015; 2018c).

With the aid of (4), Gun and Simsek (2023) also defined the following polynomials $q_{\mathfrak{n}}(\mathfrak{z}; \zeta)$:

$$q_{\mathfrak{n}}(\mathfrak{z}; \zeta) - (1+\mathfrak{z})^{\mathfrak{n}} u_{\mathfrak{n}}^{(\zeta)}(\mathfrak{z}) = 0. \tag{13}$$

Gun and Simsek (2023) also gave the following formula:

$$q_{\mathfrak{n}}(\mathfrak{z}; \zeta) = \sum_{\mathfrak{j}=1}^{\mathfrak{n}} (-1)^{\mathfrak{j}} S_2(\mathfrak{n}, \mathfrak{j}) \mathfrak{M}_{\mathfrak{j},\mathfrak{n}}(\mathfrak{z})(\zeta)^{(\mathfrak{n})}. \tag{14}$$

Let $\mathbb{N}_0$ correspond to the set of nonnegative integers. For $v \in \mathbb{N}_0$ and $\mathfrak{z} \in \mathbb{C}$, Simsek (2018c) described the combinatorial numbers, $y_1(\mathfrak{n}, v; \mathfrak{z})$:

$$(\mathfrak{z}e^t + 1)^v = \sum_{\mathfrak{n}=0}^{\infty} \frac{v! \, y_1(\mathfrak{n}, v; \mathfrak{z})}{\mathfrak{n}!} t^{\mathfrak{n}} \tag{15}$$

and also

$$\mathfrak{k}^{\mathfrak{n}} \mathfrak{z}^{\mathfrak{k}} - \sum_{\mathfrak{j}=0}^{\mathfrak{k}} (-1)^{\mathfrak{k}-\mathfrak{j}} \binom{\mathfrak{k}}{\mathfrak{j}} y_1(\mathfrak{n}, \mathfrak{j}; \mathfrak{z}) \mathfrak{j}! = 0. \tag{16}$$

Combining Eq. (5) and Eq. (16), we have

$$S_2(\mathfrak{k}, v; \mathfrak{z}) + (-1)^{1+v} y_1(\mathfrak{k}, v; -\mathfrak{z}) = 0 \tag{17}$$

(Simsek, 2018c).

Therefore, this article is motivated to give novel formulas, finite sums, and relations containing special classes of polynomials. (Simsek, 2018a; 2018b; 2023).

2. FORMULAS AND FINITE SUMS COVERING BETA-TYPE RATIONAL FUNCTIONS AND COMBINATORIAL-TYPE NUMBERS AND POLYNOMIALS

We give some novel formulas and finite sums covering Stirling-type polynomials and numbers, the Frobenius Euler numbers and polynomials, the beta-type rational functions, and combinatorial numbers via not only generating functions, but also identities covering special numbers and polynomials.

Theorem 2.1. Let $\zeta \in \mathbb{C}$ and $\mathfrak{n} \in \mathbb{N}_0$.

$$\sum_{\mathfrak{k}=0}^{\infty} \binom{\zeta}{\mathfrak{k}} \mathfrak{z}^{\mathfrak{k}} \sum_{\mathfrak{m}=0}^{\mathfrak{n}} \binom{\mathfrak{n}}{\mathfrak{m}} u_{\mathfrak{m}}^{(\zeta)}(\chi; \mathfrak{z}) \, \mathfrak{k}^{\mathfrak{n}-\mathfrak{m}} - (1+\mathfrak{z})^{\zeta} \chi^{\mathfrak{n}} = 0.$$

Proof. Using the umbral calculus convention in Eq. (3) yields, we have

$$\left(\frac{1+\mathfrak{z}}{\mathfrak{z}e^t+1}\right)^\zeta = e^{u^{(\zeta)}(\chi;\mathfrak{z})t-t\chi}.$$

Assuming that $|\mathfrak{z}e^t| < 1$. Using binomial series yields, we have

$$\sum_{\mathfrak{n}=0}^\infty (1+\mathfrak{z})^\zeta \chi^\mathfrak{n} \frac{t^\mathfrak{n}}{\mathfrak{n}!} = \sum_{\mathfrak{k}=0}^\infty \binom{\zeta}{\mathfrak{k}} \mathfrak{z}^\mathfrak{k} \sum_{\mathfrak{n}=0}^\infty \sum_{\mathfrak{m}=0}^\mathfrak{n} \binom{\mathfrak{n}}{\mathfrak{m}} u_\mathfrak{m}^{(\zeta)}(\chi;\mathfrak{z}) \mathfrak{k}^{\mathfrak{n}-\mathfrak{m}} \frac{t^\mathfrak{n}}{\mathfrak{n}!}.$$

Aligning the coefficients $\frac{t^\mathfrak{n}}{\mathfrak{n}!}$ with each side completes the proof.

Substituting $\zeta = v$ into Theorem 2.1. and combining Eq. (12) with Theorem 2.1, after performing several calculations, we get the following corollary:

Corollary 2.2. Let $\zeta \in \mathbb{C}$ and $\mathfrak{n} \in \mathbb{N}_0$.

$$\chi^\mathfrak{n} - \sum_{\mathfrak{k}=0}^\infty \binom{v}{\mathfrak{k}} \mathfrak{M}_{\mathfrak{k},\mathfrak{k}-v}(\mathfrak{z}) \sum_{\mathfrak{m}=0}^\mathfrak{n} \binom{\mathfrak{n}}{\mathfrak{m}} u_\mathfrak{m}^{(v)}(\chi;\mathfrak{z}) \mathfrak{k}^{\mathfrak{n}-\mathfrak{m}} = 0.$$

Combining Theorem 2.1. with Eq. (4) yields, we get the following corollary:

Corollary 2.3. Let $\zeta \in \mathbb{C}$ and $\mathfrak{n} \in \mathbb{N}_0$.

$$(1+\mathfrak{z})^\zeta \chi^\mathfrak{n} - \sum_{\mathfrak{k}=0}^\infty \binom{\zeta}{\mathfrak{k}} \mathfrak{z}^\mathfrak{k} \sum_{\mathfrak{m}=0}^\mathfrak{n} \binom{\mathfrak{n}}{\mathfrak{m}} \mathfrak{k}^{\mathfrak{n}-\mathfrak{m}} H_\mathfrak{m}^{(\zeta)}\left(\chi; -\frac{1}{\mathfrak{z}}\right) = 0.$$

Joining Eq. (16) with Theorem 2.1. after performing several calculations, we get the following corollary:

Corollary 2.4. Let $\zeta \in \mathbb{C}$ and $\mathfrak{n} \in \mathbb{N}_0$.

$$(1+\mathfrak{z})^\zeta \chi^\mathfrak{n} + \sum_{\mathfrak{k}=0}^\infty \binom{\zeta}{\mathfrak{k}} \sum_{\mathfrak{m}=0}^\mathfrak{n} \binom{\mathfrak{n}}{\mathfrak{m}} u_\mathfrak{m}^{(\zeta)}(\chi;\mathfrak{z}) \frac{1}{\mathfrak{k}^\mathfrak{m}} \sum_{\mathfrak{j}=0}^\mathfrak{k} (-1)^{\mathfrak{k}+1-\mathfrak{j}} y_1(\mathfrak{n},\mathfrak{j};\mathfrak{z}) \binom{\mathfrak{k}}{\mathfrak{j}} \mathfrak{j}! = 0 \,.$$

Replacing $\mathfrak{z}$ by $-\mathfrak{z}$, Corollary 2.4. reduces to

Corollary 2.5. Let $\zeta, \mathfrak{z} \in \mathbb{C}$, $\mathfrak{n} \in \mathbb{N}_0$.

$$(1-\mathfrak{z})^\zeta \chi^\mathfrak{n} + \sum_{\mathfrak{k}=0}^\infty \binom{\zeta}{\mathfrak{k}} \sum_{\mathfrak{m}=0}^\mathfrak{n} \binom{\mathfrak{n}}{\mathfrak{m}} u_\mathfrak{m}^{(\zeta)}(\chi;-\mathfrak{z}) \frac{1}{\mathfrak{k}^\mathfrak{m}} \sum_{\mathfrak{j}=0}^\mathfrak{k} (-1)^{1+\mathfrak{k}} S_2(\mathfrak{n},\mathfrak{j};\mathfrak{z}) \binom{\mathfrak{k}}{\mathfrak{j}} \mathfrak{j}! = 0.$$

Theorem 2.6. Let $\zeta \in \mathbb{C}$ and $\mathfrak{n} \in \mathbb{N}_0$.

$$(1+\mathfrak{z})^\zeta \chi^\mathfrak{n} - \sum_{\mathfrak{k}=0}^\infty \mathfrak{z}^\mathfrak{k} \binom{\zeta}{\mathfrak{k}} \sum_{v=0}^\mathfrak{k} v! \binom{\mathfrak{k}}{v} \sum_{\mathfrak{m}=0}^\mathfrak{n} \binom{\mathfrak{n}}{\mathfrak{m}} S_2(\mathfrak{m},v) u_{\mathfrak{n}-\mathfrak{m}}^{(\zeta)}(\chi;\mathfrak{z}) = 0.$$

Proof. From Eq. (3) yields, we have

$$(1+\mathfrak{z})^\zeta \sum_{\mathfrak{n}=0}^\infty \chi^\mathfrak{n} \frac{t^\mathfrak{n}}{\mathfrak{n}!} = \sum_{\mathfrak{k}=0}^\infty \mathfrak{z}^\mathfrak{k} \binom{\zeta}{\mathfrak{k}} e^{t\mathfrak{k}} \sum_{\mathfrak{n}=0}^\infty u_\mathfrak{n}^{(\zeta)}(\chi;\mathfrak{z}) \frac{t^\mathfrak{n}}{\mathfrak{n}!}.$$

Thus

$$(1+\mathfrak{z})^\zeta \sum_{\mathfrak{n}=0}^\infty \chi^{\mathfrak{n}} \frac{t^{\mathfrak{n}}}{\mathfrak{n}!} = \sum_{\mathfrak{k}=0}^\infty \binom{\zeta}{\mathfrak{k}} \mathfrak{z}^{\mathfrak{k}} \sum_{v=0}^{\mathfrak{k}} \binom{\mathfrak{k}}{v} v! \frac{(e^t-1)^v}{v!} \sum_{\mathfrak{n}=0}^\infty u_{\mathfrak{n}}^{(\zeta)}(\chi;\mathfrak{z}) \frac{t^{\mathfrak{n}}}{\mathfrak{n}!}.$$

Combining Eq. (6) with above equation yields, we get

$$(1+\mathfrak{z})^\zeta \sum_{\mathfrak{n}=0}^\infty \chi^{\mathfrak{n}} \frac{t^{\mathfrak{n}}}{\mathfrak{n}!} = \sum_{\mathfrak{k}=0}^\infty \mathfrak{z}^{\mathfrak{k}} \binom{\zeta}{\mathfrak{k}} \sum_{v=0}^{\mathfrak{k}} \binom{\mathfrak{k}}{v} v! \sum_{\mathfrak{n}=0}^\infty S_2(\mathfrak{n},v) \frac{t^{\mathfrak{n}}}{\mathfrak{n}!} \sum_{\mathfrak{n}=0}^\infty u_{\mathfrak{n}}^{(\zeta)}(\chi;\mathfrak{z}) \frac{t^{\mathfrak{n}}}{\mathfrak{n}!}.$$

Hence

$$(1+\mathfrak{z})^\zeta \sum_{\mathfrak{n}=0}^\infty \chi^{\mathfrak{n}} \frac{t^{\mathfrak{n}}}{\mathfrak{n}!} = \sum_{\mathfrak{k}=0}^\infty \mathfrak{z}^{\mathfrak{k}} \binom{\zeta}{\mathfrak{k}} \sum_{v=0}^{\mathfrak{k}} v! \binom{\mathfrak{k}}{v} \sum_{\mathfrak{n}=0}^\infty \sum_{\mathfrak{m}=0}^{\mathfrak{n}} u_{\mathfrak{n}-\mathfrak{m}}^{(\zeta)} \binom{\mathfrak{n}}{\mathfrak{m}} S_2(\mathfrak{m},v)(\chi;\mathfrak{z}) \frac{t^{\mathfrak{n}}}{\mathfrak{n}!}.$$

Aligning the coefficients $\frac{t^{\mathfrak{n}}}{\mathfrak{n}!}$ with each side completes the proof.

Replacing $\mathfrak{z}$ by $-\frac{1}{\mathfrak{z}}$ respectively, Theorem 2.6., and also combining Eq. (4) yields, we get the following corollary:

Corollary 2.7. Let $\zeta,\mathfrak{z} \in \mathbb{C}$ with $\mathfrak{z} \neq 0$ and $\mathfrak{n} \in \mathbb{N}_0$.

$$\chi^{\mathfrak{n}}(\mathfrak{z}-1)^\zeta = \sum_{\mathfrak{k}=0}^\infty (-1)^{\mathfrak{k}} \binom{\zeta}{\mathfrak{k}} \mathfrak{z}^{\zeta-\mathfrak{k}} \sum_{v=0}^{\mathfrak{k}} v! \binom{\mathfrak{k}}{v} \sum_{\mathfrak{m}=0}^{\mathfrak{n}} S_2(\mathfrak{m},v) \binom{\mathfrak{n}}{\mathfrak{m}} H_{\mathfrak{n}-\mathfrak{m}}^{(\zeta)}(\chi;\mathfrak{z}).$$

Theorem 2.8. Let $\zeta,\mathfrak{z} \in \mathbb{C}$ and $\mathfrak{n} \in \mathbb{N}_0$.

$$(1+\mathfrak{z})^\zeta \chi^{\mathfrak{n}} - 2^\zeta \sum_{\mathfrak{k}=0}^{\mathfrak{n}} \binom{\mathfrak{n}}{\mathfrak{k}} \mathcal{E}_{\mathfrak{n}-\mathfrak{k}}^{(-\zeta)}(\mathfrak{z}) u_{\mathfrak{k}}^{(\zeta)}(\chi;\mathfrak{z}) = 0.$$

Proof. From Eq. (3) yields, we get

$$\sum_{\mathfrak{n}=0}^\infty (1+\mathfrak{z})^\zeta \chi^{\mathfrak{n}} \frac{t^{\mathfrak{n}}}{\mathfrak{n}!} = (\mathfrak{z}e^t+1)^\zeta \sum_{\mathfrak{n}=0}^\infty \frac{u_{\mathfrak{n}}^{(\zeta)}(\chi;\mathfrak{z})}{\mathfrak{n}!} t^{\mathfrak{n}}.$$

Thus

$$\sum_{\mathfrak{n}=0}^\infty (1+\mathfrak{z})^\zeta \chi^{\mathfrak{n}} \frac{t^{\mathfrak{n}}}{\mathfrak{n}!} = 2^\zeta \left(\frac{\mathfrak{z}e^t+1}{2} \right)^\zeta \sum_{\mathfrak{n}=0}^\infty \frac{u_{\mathfrak{n}}^{(\zeta)}(\chi;\mathfrak{z})}{\mathfrak{n}!} t^{\mathfrak{n}}.$$

Joining last equation with (8) yields, we have

$$\sum_{\mathfrak{n}=0}^\infty (1+\mathfrak{z})^\zeta \chi^{\mathfrak{n}} \frac{t^{\mathfrak{n}}}{\mathfrak{n}!} = 2^\zeta \sum_{\mathfrak{n}=0}^\infty \sum_{\mathfrak{k}=0}^{\mathfrak{n}} \binom{\mathfrak{n}}{\mathfrak{k}} u_{\mathfrak{k}}^{(\zeta)}(\chi;\mathfrak{z}) \mathcal{E}_{\mathfrak{n}-\mathfrak{k}}^{(-\zeta)}(\mathfrak{z}) \frac{t^{\mathfrak{n}}}{\mathfrak{n}!}.$$

Aligning the coefficients $\frac{t^{\mathfrak{n}}}{\mathfrak{n}!}$ with each side completes the proof.

Combining the Theorem 2.8. with Eq. (4) yields, we get the following corollary:

Corollary 2.9. Let $\zeta,\mathfrak{z} \in \mathbb{C}$ and $\mathfrak{n} \in \mathbb{N}_0$.

$$(1+\mathfrak{z})^\zeta \chi^{\mathfrak{n}} - 2^\zeta \sum_{\mathfrak{k}=0}^{\mathfrak{n}} \binom{\mathfrak{n}}{\mathfrak{k}} \mathcal{E}_{\mathfrak{n}-\mathfrak{k}}^{(-\zeta)}(\mathfrak{z}) H_{\mathfrak{k}}^{(\zeta)}\left(\chi; -\frac{1}{\mathfrak{z}}\right) = 0.$$

Substituting $\chi = 0$ into Theorem 2.8. and combining Eq. (13) yields, we get the following corollary:

Corollary 2.9. Let $\zeta, \mathfrak{z} \in \mathbb{C}$ and $n \in \mathbb{N}_0$.

$$0 = \sum_{k=0}^{n} \frac{\binom{n}{k} \mathcal{E}_{n-k}^{(-\zeta)}(\mathfrak{z}) q_k(\mathfrak{z}; \zeta)}{(1+\mathfrak{z})^k}.$$

Theorem 2.10. Le $\zeta, \mathfrak{z} \in \mathbb{C}$. Let $u_0(\chi; \mathfrak{z}) = 1$.

$$(1+\mathfrak{z})\chi^n - u_n(\chi; \mathfrak{z}) = \mathfrak{z} \sum_{k=0}^{n} u_k(\chi; \mathfrak{z}) \binom{n}{k}; \qquad (n > 0).$$

Proof. Substituting $\zeta = 1$ into Eq. (3) yields, we have

$$\left(\frac{1+\mathfrak{z}}{\mathfrak{z}e^t + 1}\right) e^{t\chi} = e^{u(\chi;\mathfrak{z})t}$$

and the umbral calculus convention and some calculation give:

$$(1+\mathfrak{z}) \sum_{n=0}^{\infty} \chi^n \frac{t^n}{n!} = \mathfrak{z} \sum_{n=0}^{\infty} (u(\chi; \mathfrak{z})+1)^n \frac{t^n}{n!} + \sum_{n=0}^{\infty} u_n(\chi; \mathfrak{z}) \frac{t^n}{n!}.$$

Aligning the coefficients $\frac{t^n}{n!}$ with each side completes the proof.

Substituting $\chi = 0$ into Theorem 2.10. and using Eq. (13) yields, we get the following corollary:

Corollary 2.11. Let $\zeta, \mathfrak{z} \in \mathbb{C}$ and $n \in \mathbb{N}_0$.

$$0 = \mathfrak{z} \sum_{k=0}^{n} \binom{n}{k} q_k(\mathfrak{z})(1+\mathfrak{z})^{-k} + q_n(\mathfrak{z})(1+\mathfrak{z})^{-n}.$$

Theorem 2.12. Let $\zeta, \mathfrak{z} \in \mathbb{C}$ with $\mathfrak{z} \neq 0$ and $n \in \mathbb{N}_0$.

$$\sum_{m=0}^{n} \binom{n}{m} H_m^{(\zeta)}\left(\chi; -\frac{1}{\mathfrak{z}}\right) H_{n-m}^{(\zeta)}\left(\chi; \frac{1}{\mathfrak{z}}\right) - 2^n u_n^{(\zeta)}(\chi; -\mathfrak{z}^2) = 0.$$

Proof. Replacing $\mathfrak{z}$ by $-\mathfrak{z}^2$ and t by $2t$ respectively, Eq. (3) reduces to

$$\left(\frac{\mathfrak{z}-1}{\mathfrak{z}e^t - 1}\right)^{\zeta} e^{t\chi} \left(\frac{1+\mathfrak{z}}{\mathfrak{z}e^t + 1}\right)^{\zeta} e^{t\chi} = \sum_{n=0}^{\infty} \frac{u_n^{(\zeta)}(\chi; -\mathfrak{z}^2)}{n!} 2^n t^n. \qquad (18)$$

Hence

$$\sum_{n=0}^{\infty} \sum_{m=0}^{n} H_m^{(\zeta)}\left(\chi; -\frac{1}{\mathfrak{z}}\right) \binom{n}{m} H_{n-m}^{(\zeta)}\left(\chi; \frac{1}{\mathfrak{z}}\right) \frac{t^n}{n!} = \sum_{n=0}^{\infty} u_n^{(\zeta)}(\chi; -\mathfrak{z}^2) 2^n \frac{t^n}{n!}.$$

Aligning the coefficients $\frac{t^n}{n!}$ with each side completes proof.

Theorem 2.13. Let $\zeta, \mathfrak{z} \in \mathbb{C}$ with $\mathfrak{z} \neq 1$ and $n \in \mathbb{N}_0$.

$$2^n u_n^{(-v)}(-\mathfrak{z}^2) = \frac{(v!)^2}{(\mathfrak{z}^2-1)^v} \sum_{m=0}^{n} \binom{n}{m} S_2(m, v; \mathfrak{z}) y_1(n-m, v; \mathfrak{z}).$$

Proof. Replacing ζ by $-v$ and χ by 0 respectively, Eq. (18) gives

$$\sum_{n=0}^{\infty} 2^n u_n^{(-v)}(-\mathfrak{z}^2) \frac{t^n}{n!} = (v!)^2 \frac{1}{(\mathfrak{z}^2-1)^v} \frac{(\mathfrak{z}e^t-1)^v}{v!} \frac{(\mathfrak{z}e^t+1)^v}{v!}.$$

Joining Eq. (5) with Eq. (15) yields, we have

$$\sum_{n=0}^{\infty} 2^n u_n^{(-v)}(-\mathfrak{z}^2) \frac{t^n}{n!} = \frac{(v!)^2}{(\mathfrak{z}^2-1)^v} \sum_{n=0}^{\infty} S_2(n,v;\mathfrak{z}) \frac{t^n}{n!} \sum_{n=0}^{\infty} y_1(n,v;\mathfrak{z}) \frac{t^n}{n!}.$$

Hence

$$\sum_{n=0}^{\infty} 2^n u_n^{(-v)}(-\mathfrak{z}^2) \frac{t^n}{n!} = \frac{(v!)^2}{(\mathfrak{z}^2-1)^v} \sum_{n=0}^{\infty} \sum_{m=0}^{n} S_2(m,v;\mathfrak{z}) \binom{n}{m} y_1(n-m,v;\mathfrak{z}) \frac{t^n}{n!}.$$

Aligning the coefficients $\frac{t^n}{n!}$ with each side completes proof.

Theorem 2.14. Let $\zeta, \mathfrak{z} \in \mathbb{C}$ with $\mathfrak{z} \neq 0$ and $n \in \mathbb{N}_0$.

$$\frac{(\mathfrak{z}^2-1)^\zeta}{2^\zeta} \sum_{m=0}^{n} \binom{n}{m} \mathcal{E}_{n-m}^{(\zeta)}(\mathfrak{z}) \chi^m = \zeta! \sum_{m=0}^{n} \binom{n}{m} u_m^{(\zeta)}(\chi;-\mathfrak{z}^2) S_2(n-m,\zeta;\mathfrak{z}).$$

Proof. By using Eq. (18) yields, we have

$$\frac{(\mathfrak{z}^2-1)^\zeta}{2^\zeta} \left(\frac{2}{\mathfrak{z}e^t+1}\right)^\zeta e^{2t\chi} = \sum_{n=0}^{\infty} u_n^{(\zeta)}(\chi;-\mathfrak{z}^2) 2^n \frac{(\mathfrak{z}e^t-1)^\zeta}{\zeta!} \zeta! \frac{t^n}{n!}.$$

Combining Eq. (5) with Eq. (8) yields

$$\frac{(\mathfrak{z}^2-1)^\zeta}{2^\zeta} \sum_{n=0}^{\infty} \mathcal{E}_n^{(\zeta)}(\mathfrak{z}) \frac{t^n}{n!} \sum_{n=0}^{\infty} \chi^n 2^n \frac{t^n}{n!} = \sum_{n=0}^{\infty} u_n^{(\zeta)}(\chi;-\mathfrak{z}^2) 2^n \frac{t^n}{n!} \sum_{n=0}^{\infty} S_2(n,\zeta;\mathfrak{z}) \zeta! \frac{t^n}{n!}.$$

Hence

$$\frac{(\mathfrak{z}^2-1)^\zeta}{2^\zeta} \sum_{n=0}^{\infty} \sum_{m=0}^{n} \binom{n}{m} \mathcal{E}_{n-m}^{(\zeta)}(\mathfrak{z}) 2^m \frac{\chi^m t^n}{n!} = \zeta! \sum_{n=0}^{\infty} \sum_{m=0}^{n} \binom{n}{m} u_m^{(\zeta)}(\chi;-\mathfrak{z}^2) 2^m S_2(n-m,\zeta;\mathfrak{z}) \frac{t^n}{n!}.$$

Aligning the coefficients $\frac{t^n}{n!}$ with each side completes the proof.

Substituting $\chi = 1$ into Theorem 2.14. and using Eq. (13) yields, after performing several calculations, we get the following corollary:

Corollary 2.15. Let $\zeta, \mathfrak{z} \in \mathbb{C}$ with $\mathfrak{z} \neq 1$ and $n \in \mathbb{N}_0$.

$$\sum_{m=0}^{n} \binom{n}{m} \mathcal{E}_{n-m}^{(\zeta)}(\mathfrak{z}) = 2^\zeta \zeta! \sum_{m=0}^{n} \binom{n}{m} \frac{(-1)^m q_m(-\mathfrak{z}^2;\zeta)}{(\mathfrak{z}^2-1)^{m+\zeta}} S_2(n-m,\zeta;\mathfrak{z}).$$

Theorem 2.16. Let $\zeta, \mathfrak{z} \in \mathbb{C}$ and $n \in \mathbb{N}_0$.

$$(\mathfrak{z}-1)^m \chi^n = m! \sum_{k=0}^{n} \binom{n}{k} u_{n-k}^{(m)}(\chi;-\mathfrak{z}) S_2(k,m;\mathfrak{z}).$$

Proof. Replacing ζ by $\mathfrak{m}$ and $\mathfrak{z}$ by $-\mathfrak{z}$ respectively, Eq. (3) yields, we have

$$(\mathfrak{z}-1)^{\mathfrak{m}} \sum_{\mathfrak{n}=0}^{\infty} \chi^{\mathfrak{n}} \frac{t^{\mathfrak{n}}}{\mathfrak{n}!} = \mathfrak{m}! \sum_{\mathfrak{n}=0}^{\infty} S_2(\mathfrak{n}, \mathfrak{m}; \mathfrak{z}) \frac{t^{\mathfrak{n}}}{\mathfrak{n}!} \sum_{\mathfrak{n}=0}^{\infty} u_{\mathfrak{n}}^{(\mathfrak{m})}(\chi; -\mathfrak{z}) \frac{t^{\mathfrak{n}}}{\mathfrak{n}!}.$$

Hence

$$(\mathfrak{z}-1)^{\mathfrak{m}} \sum_{\mathfrak{n}=0}^{\infty} \chi^{\mathfrak{n}} \frac{t^{\mathfrak{n}}}{\mathfrak{n}!} = \mathfrak{m}! \sum_{\mathfrak{n}=0}^{\infty} \sum_{\mathfrak{k}=0}^{\mathfrak{n}} S_2(\mathfrak{k}, \mathfrak{m}; \mathfrak{z}) \binom{\mathfrak{n}}{\mathfrak{k}} u_{\mathfrak{n}-\mathfrak{k}}^{(\mathfrak{m})}(\chi; -\mathfrak{z}) \frac{t^{\mathfrak{n}}}{\mathfrak{n}!}.$$

Aligning the coefficients $\frac{t^{\mathfrak{n}}}{\mathfrak{n}!}$ with each side completes the proof.

Combining the above Theorem 2.16. and Eq. (17) yields, we get the following corollary:

Corollary 2.17. Let $\zeta, \mathfrak{z} \in \mathbb{C}$ and $\mathfrak{n} \in \mathbb{N}_0$.

$$(1+\mathfrak{z})^{\mathfrak{m}} \chi^{\mathfrak{n}} = \mathfrak{m}! \sum_{\mathfrak{k}=0}^{\mathfrak{n}} \binom{\mathfrak{n}}{\mathfrak{k}} u_{\mathfrak{n}-\mathfrak{k}}^{(\mathfrak{m})}(\chi; \mathfrak{z}) y_1(\mathfrak{k}, \mathfrak{m}; \mathfrak{z}).$$

Theorem 2.18. Let $\zeta, \mathfrak{z} \in \mathbb{C}$ and $\mathfrak{n} \in \mathbb{N}_0$.

$$\sum_{\mathfrak{j}=1}^{\mathfrak{k}} (-1)^{\mathfrak{j}} S_2(\mathfrak{n}, \mathfrak{j}) \mathfrak{z}^{\mathfrak{j}} (\zeta)^{(\mathfrak{j})} \mathfrak{M}_{\mathfrak{j},2\mathfrak{j}}(\mathfrak{z}) \sum_{\mathfrak{k}=0}^{\mathfrak{j}-1} \frac{1}{\zeta+\mathfrak{k}} = \frac{d}{d\zeta} \left\{ u_{\mathfrak{n}}^{(\zeta)}(\mathfrak{z}) \right\}.$$

Proof. Substituting $\chi = 1$ into Eq. (3) yields, we have

$$\left(\frac{1+\mathfrak{z}}{2}\right)^{\zeta} \sum_{\mathfrak{n}=0}^{\infty} \frac{\mathcal{E}_{\mathfrak{n}}^{(\zeta)}(\mathfrak{z})}{\mathfrak{n}!} t^{\mathfrak{n}} = \sum_{\mathfrak{n}=0}^{\infty} \frac{u_{\mathfrak{n}}^{(\zeta)}(\mathfrak{z})}{\mathfrak{n}!} t^{\mathfrak{n}}.$$

Combining the Eq. (9) and taking derivative wrt ζ yields, we have

$$\frac{d}{d\zeta} \left\{ (1+\mathfrak{z})^{\zeta} \sum_{\mathfrak{n}=0}^{\infty} \sum_{\mathfrak{j}=1}^{\mathfrak{n}} (-1)^{\mathfrak{j}} S_2(\mathfrak{n}, \mathfrak{j}) \mathfrak{z}^{\mathfrak{j}} \frac{(\zeta)^{(\mathfrak{j})}}{(\mathfrak{z}+1)^{\mathfrak{j}+\zeta}} \frac{t^{\mathfrak{n}}}{\mathfrak{n}!} \right\} = \sum_{\mathfrak{n}=0}^{\infty} \frac{d}{d\zeta} \left\{ u_{\mathfrak{n}}^{(\zeta)}(\mathfrak{z}) \right\} \frac{t^{\mathfrak{n}}}{\mathfrak{n}!}.$$

Aligning the coefficients $\frac{t^{\mathfrak{n}}}{\mathfrak{n}!}$ with each side completes the proof.

3. RESULTS AND DISCUSSION

The results in this paper are obtained by blending formulas, finite sums via generating functions and their functional equations methods. These results have the value of being a resource for researchers in applied sciences.

4. CONCLUSION

Generating functions for special numbers and polynomials covering Stirling type numbers, the Frobenius Euler numbers and polynomials, the beta-type rational functions, and also combinatorial numbers have been given. Using these functions, some novel formulas and finite sums, containing combinatorial numbers, Stirling-type numbers, the Frobenius Euler numbers and polynomials, and beta-type rational functions, have been derived.

Since these numbers and polynomials are related to spline curves, our future project is to blend the results of this paper with many different kinds of spline curves and their applications.

AUTHOR CONTRIBUTIONS

The authors jointly prepared this article and made equal contributions.

CONFLICT OF INTEREST

The authors declare no potential conflict of interests.

REFERENCES

Carlitz, L., & Sholander, M. (1963). The product of two Eulerian polynomials. *Mathematics Magazine*, *36*(1), 37–41. https://doi.org/10.2307/2688134

Gun, D., & Simsek, Y. (2020). Some new identities and inequalities for Bernoulli polynomials and numbers of higher order related to the Stirling and Catalan numbers. *Revista de la Real Academia de Ciencias Exactas, Fsicas y Naturales. Serie A. Matematicas*, *114*(4), 167. https://doi.org/10.1007/s13398-020-00899-z

Gun, D., & Simsek, Y. (2023). Modification exponential Euler type splines derived from Apostol-Euler numbers and polynomials of complex order. *Applicable Analysis and Discrete Mathematics*, *17*(1), 197–215. https://doi.org/10.2298/AADM220712011G

Kucukoglu, I., & Simsek, Y. (2019). Identities and relations on the q-Apostol type Frobenius-Euler numbers and polynomials. *Journal of the Korean Mathematical Society*, *56*(1), 265–284. https://doi.org/10.4134/JKMS.j180185

Luo, Q.-M. (2006). Apostol-Euler polynomials of higher order and Gaussian hypergeometric functions. *Taiwanese Journal of Mathematics, 10*(4), 917–925. https://doi.org/10.11650/twjm/1500403883

Simsek, Y. (2013a). Identities associated with generalized Stirling type numbers and Eulerian type polynomials. *Mathematical and Computational Applications*, *18*(3), 251-263. https://doi.org/10.3390/mca18030251

Simsek, Y. (2013b). Generating functions for generalized Stirling type numbers, array type polynomials, Eulerian type polynomials and their applications. *Fixed Point Theory and Algorithms for Sciences and Engineering*, *87*. https://doi.org/10.1186/1687-1812-2013-87

Simsek, Y. (2015). Beta-type polynomials and their generating functions. *Applied Mathematics and Computation*, *254*, 172–182. https://doi.org/10.1016/j.amc.2014.12.118

Simsek, Y. (2018a). Construction of some new families of Apostol-type numbers and polynomials via Dirichlet character and *p*-adic *q*-integrals. *Turkish Journal of Mathematics*, *42*(2), 557–577. https://doi.org/10.3906/mat-1703-114

Simsek, Y. (2018b). Combinatorial sums and binomial identities associated with the Beta-type polynomials. *Hacettepe Journal of Mathematics and Statistics*, *47*(5), 1144-1155. https://doi.org/10.15672/HJMS.2017.505

Simsek, Y. (2018c). New families of special numbers for computing negative order Euler numbers and related numbers and polynomials. *Applicable Analysis and Discrete Mathematics*, *12*(1), 1-35. https://www.jstor.org/stable/90020602

Simsek, Y. (2023). Generating functions for series involving higher powers of inverse binomial coefficients and their applications. *Mathematical Methods in the Applied Sciences*, *46*(12), 12591-12617. https://doi.org/10.1002/mma.9199

Srivastava, H. M. (2011). Some generalizations and basic (or q -) extensions of the Bernoulli, Euler and Genocchi polynomials. *Applied Mathematics & Information Sciences*. *5*(3), 390–444.

Srivastava, H. M., & Choi, J. (2001). *Series associated with the zeta and related functions*. Dordrecht: Kluwer Academic Publishers.

Srivastava, H. M., & Choi, J. (2012). *Zeta and q-zeta functions and associated series and integrals*. Amsterdam: Elsevier Science Publishers.

Experimental Study on Gasification of Banknote Waste: Effects of Torrefaction Pre-Treatment and Co-Gasification on Producer Gas Composition

Hakan KAVUŞTU[1]   Emir Hüseyin ŞIMŞEK[1*]

[1] Ankara University, Department of Chemical Engineering, Ankara, Türkiye

Keywords	Abstract
End-of-Life Banknote Banknote Waste Gasification Co-Gasification Torrefaction Fluidized Bed	There is approximately 500,000 tonnes of potential end-of-life banknote waste worldwide, which is increasing by 2-3% per year. This waste consists of cotton and polymer-based banknotes printed on substrates whose raw materials are cotton and polypropylene, respectively. The vast majority of banknotes in circulation are cotton-based banknotes. End-of-life cotton banknotes, which are lignocellulosic biomass, are generally disposed of by landfill and incineration. Studies to reduce the environmental impact of these wastes to find more effective ways of using them is becoming increasingly important. Syngas, which can be used for the production of electricity, energy and chemicals is obtained by gasification of end-of-life cotton banknotes. In this study, DSC and FTIR analysis were performed as part of the characterization tests of the cotton-based banknote sample. As a result of the analysis, the sample was found to have characteristics similar to those of cotton. Within the scope of the investigation of thermal decomposition kinetics, activation energies were calculated as 134-171 kJ/mol by the Flynn-Wall-Ozawa (FWO) and Kissinger-Akahira-Sunose (KAS) methods. Experiments were performed in a fluidized-bed reactor at 800°C with an inlet H_2O/O_2 ratio of 25. The content of the producer gas formed during gasification was examined according to the maximum mole fraction achieved. In order to facilitate handling, storage and transportation and to improve fuel quality, the effect of torrefaction pre-treatment on the producer gas content was studied by conducting torrefaction to the cotton-based banknote sample at 250°C for 10 min. To overcome the disadvantages of plastic gasification in terms of operational sustainability, the cotton and polymer-based banknote samples were co-gasified. With the torrefaction pre-treatment, the mole fractions of H_2, CO and CH_4 increased, while the mole fraction of CO_2 decreased. This finding revealed the effects of Boudouard, hydrogasification, water-gas and steam reformation reactions. With the co-gasification of cotton and polymer-based banknote samples, H_2, CO and CO_2 mole fractions decreased while CH_4 mole fraction increased. This result showed that as the proportion of polymer-based banknote samples in the feedstock increased, the conversion efficiency decreased and the hydrogasification reaction became dominant.

1. INTRODUCTION

Energy production is one of the most important economic factors that provides development and increases efficiency. In the context of energy sustainability, the importance of renewable energy sources is increasing due to (i) rapidly growing demand for energy, (ii) the fact that most of this demand is met by fossil fuels, and (iii) increasing concerns about global warming and environmental pollution caused by the use of fossil fuels (Jahromi et al., 2021; Zhang et al., 2024). The total energy supply increased by 15% between 2000 and 2021, and oil (29.5%), coal (27.2%), natural gas (23.6%), biofuels and waste (9.5%) were the sources with the largest share in the total energy supply in 2021 (IEA, 2021). Modern bioenergy sources, which provide more than half of the renewable energy supply, can exist in solid, liquid and gaseous forms. According to the

International Energy Agency (IEA) Energy Policy Scenario, the modern solid bioenergy supply will reach 57 Exajoules (EJ) in 2050 (IEA, 2023).

Biomass, which is a carbon-neutral and renewable energy source, has an important role in sustainable energy policies (George et al., 2019). Biomass can be classified according to the different raw material types such as agricultural, forest, municipal, industrial wastes and wood (Hussain et al., 2023). Biomass differs in terms of their properties such as molecular morphology and thermal stability, and the type and structure of biomass directly affect the product quality and yield to be obtained as a result of thermochemical conversion. Lignocellulosic biomass is basically composed of cellulose, hemicellulose and lignin (Chan et al., 2019).

In principle, banknotes are printed on cotton and polymer (polypropylene) based materials (Luján-Ornelas et al., 2018). The vast majority of banknotes produced worldwide are cotton-based banknotes with a high cotton content (DLR, 2022). Cotton-based banknote production generally includes (i) the production of banknote paper containing cotton, security thread, foil and (ii) the printing on banknote paper with inks. The Euro banknote consists of an average 0.815 g of cotton, 0.082 g of ink, 0.010 g of security thread, and 0.049 g of foil (Hanegraaf et al., 2019).

Banknotes in circulation are routinely sorted by central banks. At the end of banknote processing, worn or damaged banknotes which are not fit for circulation in terms of quality standards are considered as end-of-life banknotes (BoI, 2023). End-of-life cotton banknotes can be classified as lignocellulosic biomass due to their high cotton content (Yousef et al., 2020; Kavuştu & Şimşek, 2023). Banknote demand is basically determined by (i) the increase in the amount of banknotes in circulation, (ii) the issuance of new series of banknotes, and (iii) the renewal of end-of-life banknotes (DLR, 2023). It is estimated that there are approximately 500 billion banknotes in circulation worldwide and more than 150 billion banknotes are produced each year (G+D, 2024). The amount of banknote production worldwide tends to increase by 2-3% per year (K&B, 2022). These production data mean that (i) the potential amount of end-of-life banknote waste is approximately 500,000 tonnes assuming an average banknote weight of 1 g, (ii) nearly 150,000 tonnes of potential waste will be generated annually, and (iii) this amount will continue to increase by 2-3% each year. End-of-life banknotes are mostly disposed of by landfill and incineration (RDK, 2022). The European Central Bank (ECB) has increased the use of incineration and recycling with the ban of the disposal of the waste banknotes by landfill and combustion in order to reduce their environmental impact (ECB, 2023)

In gasification, biomass is converted into a gas mixture (synthesis gas/syngas/producer gas), which can be used for the production of liquid fuels, chemicals and energy, with the gasification agent at the gasifier temperature of 600-1400°C (Ng et al., 2013). Air, oxygen, steam and CO_2 are generally used as gasification agents. The high nitrogen content in the gasification agent reduces the calorific value of the syngas, while the use of pure oxygen is costly. In addition to providing a higher gasification rate compared to the use of CO_2 with gasification by feeding steam, a product with high calorific value and low tar content can be obtained (Xie et al., 2021). The gasification process basically consists of the following stages: (i) drying, where the moisture in the biomass is removed, (ii) pyrolysis, where volatile components are vaporized, (iii) oxidation (combustion) of combustible materials with oxygen (O_2), and (iv) reduction (char gasification) occurring as a result of the contact of coal formed by pyrolysis with carbon dioxide (CO_2) and water (H_2O) (Baruah & Baruah, 2014).

In gasification, syngas is produced, which contains combustible gases such as hydrogen (H_2), carbon monoxide (CO), methane (CH_4) and non-combustible gases such as nitrogen (N_2) and carbon dioxide (CO_2). Operating conditions, the types of feedstock and gasifier affect the composition of the syngas (Das et al., 2020). Transition metal catalysts contribute to the reduction of tar formation and the increase of the quality of the syngas (Meng et al., 2023). Banknotes can contain many of the elements that can be used as catalysts, such as zeolites that can be synthesized at different Si/Al ratios (Yousef et al., 2020; Kavuştu & Şimşek, 2023). Bubbling fluidized-bed gasifier has advantages such as (i) ease of operation, (ii) good mixing and high-quality gas-solid contact, (iii) increased mass, heat transfer and chemical conversion efficiency, and (iv) ability to operate under different operating conditions (Parrillo et al., 2021). Kinetic studies for the devolatilisation of lignocellulosic biomass contribute to understanding biomass decomposition behaviour.

Non-isothermal methods such as Flynn-Wall-Ozawa (FWO) and Kissinger-Akahira-Sunose (KAS) are widely used in estimating kinetic parameters and extent of conversion (Mohammed et al., 2022).

With the torrefaction pre-treatment, which is pyrolysis that occurs at relatively low temperatures, the fuel quality of biomass and the syngas yield can be increased in addition to facilitating handling, storage and transportation of biomass (Cabuk et al., 2020). In the study of Sadaka (2013), as a result of torrefaction of cotton gin waste, the moisture and volatile solid content decreased, while the bulk density and calorific value increased, and generally more carbon conversion and gasification efficiency were obtained compared to raw waste by gasification. With co-gasification, where two or more feedstocks are mixed and gasified, the mass transfer, gasification rate, reactivity and efficiency can be increased and the amount of pollutant gases can be reduced (Hanchate et al., 2021).

Polymer banknotes are printed on substrates made of biaxially-oriented polypropylene film (BOPP) (BoC, 2011). Using only plastic as feedstock in gasification has some disadvantages such as (i) having a very high calorific value, making gasifier temperature control difficult, (ii) its sticky structure making operation difficult, and (iii) increasing tar formation. In order to overcome these disadvantages, the product quality and yield can be increased by co-gasification of plastic and biomass in a bubbling fluidized-bed gasifier (Parrillo et al., 2023). One of the most suitable plastic types for co-gasification with biomass is polypropylene (PP) (Block et al., 2018). Co-gasification of biomass and plastic has advantages such as accelerating plastic degradation with the catalytic effect of the biomass char, and reducing char formation due to the increase in syngas yield (Ajorloo et al., 2024).

There are studies examining the end-of-life cotton-rich banknotes by (i) biochemical processes such as methane production by "anaerobic digestion" (Mancilla-Leytón et al., 2024), glucose production by "fermentation" (Sheikh et al., 2013; Yousef et al., 2021) and (ii) thermochemical processes such as bio-oil, bio-gas and char formation by "pyrolysis" (Yousef et al., 2020), producer gas production by "gasification" (Kavuştu & Şimşek, 2023).

In the present study, Differential Scanning Calorimetry (DSC) and Fourier Transform Infrared Spectroscopy (FTIR) analysis were performed within the scope of characterization tests of the end-of-life cotton-rich samples. Thermal decomposition kinetics were examined by Flynn-Wall-Ozawa (FWO) and Kissinger-Akahira-Sunose (KAS) methods. The effects of (i) torrefaction of cotton-based banknote sample and (ii) co-gasification of cotton and polymer-based banknote samples on the producer gas content as maximum mole fractions were investigated within the scope of experiments on gasification in a fluidized-bed reactor. The main novelty of this study is to investigate the effects of torrefaction pre-treatment and co-gasification on producer gas composition with gasification of end-of-life banknotes.

2. MATERIAL AND METHOD

2.1. Materials

In this study, the following samples were used: (i) 5 Turkish Lira (TL) banknote samples, which were put into circulation in 2009 and were printed on a substrate made of cotton fibers and (ii) 1 Romanian Leu (RON) banknote samples, which entered into circulation in 2005 and were printed on a substrate made of polypropylene resin. The physical properties of banknote samples are given in Table 1.

Table 1. Physical properties of 5 TL and 1 RON samples

Sample	Physical Properties		
	Thickness (μm)	Grammage (g/m^2)	Particle Density (g/cm^3)
5 TL (Kavuştu & Şimşek, 2023)	116	98.5	0.85
1 RON	96	90.8	0.95

2.2. Preparation of Samples

The samples were sieved from a mesh after turning into small particles. 5 TL and 1 RON samples with a mean particle size of 890 µm were prepared. Additionally, the 5 TL sample with a mean size of 890 µm was torrefied with inert gas (N$_2$: 99.9%) at 250°C for 10 min in the gasifier. The prepared samples are demonstrated in Figure 1.

Figure 1. Prepared banknote samples: a) raw and b) torrefied cotton-based; c) polymer-based

2.3. Characterization Techniques

Cotton-based raw sample shown in Figure 1a was used in characterization tests. Differential Scanning Calorimetry (DSC) analysis was performed using a TA Instruments SDT 650 Simultaneous DSC/TGA, at six different heating rates between 5-30°C/min and a temperature range of 25-1000°C in nitrogen. Fourier Transformed Infrared Spectroscopy (FTIR) analysis was performed using a Perkin Elmer Pyris STA 6000 Simultaneous TGA/FTIR at six different heating rates between 5-30°C/min and a temperature range of 30-950°C in nitrogen.

2.4. Activation Energy Determination

The thermal analysis data used to investigate the thermal decomposition kinetics were obtained from our previous study (Kavuştu & Şimşek, 2023) in which thermogravimetric analysis was performed on 5TL banknote sample at six different heating rates in the range of 5-30°C/min. The formula used to calculate the activation energy with FWO and KAS methods is given in Table 2 (Yousef et al., 2020).

Table 2. FWO and KAS methods

Method	Formula	x	y	Slope
Flynn-Wall-Ozawa (FWO)	$\ln\beta = \left(\dfrac{\ln AEa}{Rf(y)}\right) - 5.335 - \dfrac{1.051Ea}{RT}$	1/T	$\ln(\beta)$	-1.0516 Ea/R
Kissinger-Akahira-Sunose (KAS)	$\ln\left(\dfrac{\beta}{T^2}\right) = \ln\left(\dfrac{AR}{Eaf(y)}\right) - \dfrac{-Ea}{RT}$	1/T	$\ln(\beta/T^2)$	-Ea/R

2.5. Gasification Experiments

An experimental setup consisting of a gas preparation unit, a fluidized-bed reactor and a gas analyzer was used (Figure 2). In the gas preparation unit consisting of PID controlled flow meters (MKS), the mixture of steam and air was prepared at the desired rates by adjusting the bubble column temperature. The mixture of steam-air was fed to the fluidized-bed reactor at the minimum fluidization velocity in order to prevent the elutriation of sample particles in the reactor. 3 g of sample was fed to the furnace-reactor combined system consisting of a gas distributor, a ceramic furnace and an atmospheric pressure cylindrical fluidized-bed reactor. Experiments were performed for 600 s of operation time. After the undesired components such as sulfur oxides (SO$_x$) and nitrogen oxides (NO$_x$) in the gas formed in the reactor were trapped in the conditioning unit, the CO, CO$_2$, CH$_4$, H$_2$ and O$_2$ mole fraction (% y_i) values were determined with the gas analyzer (GASBOARD-3100P).
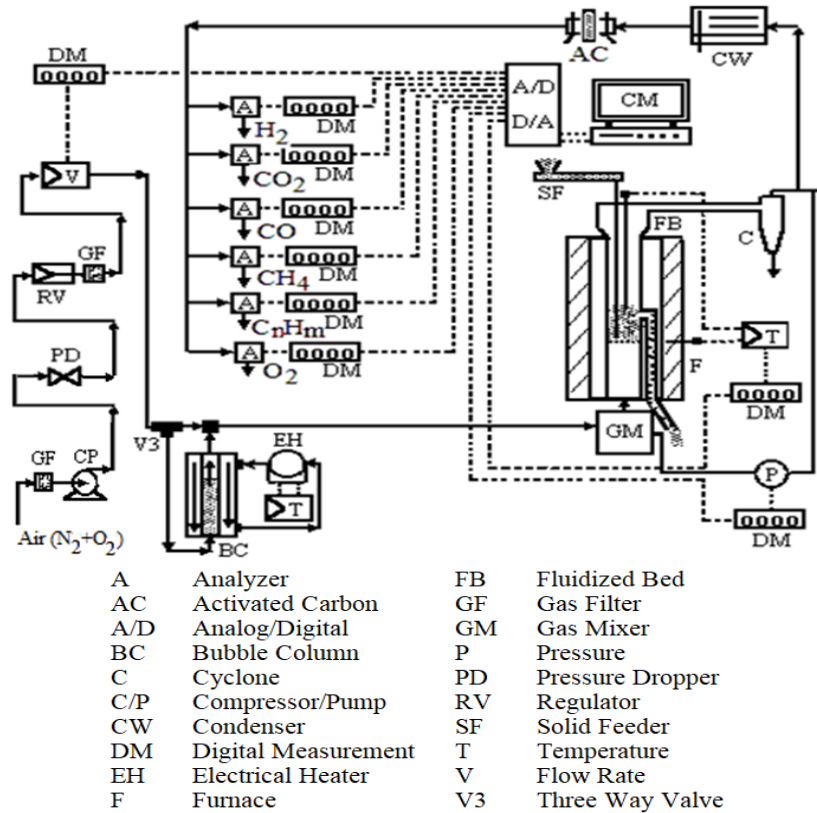
A	Analyzer	FB	Fluidized Bed
AC	Activated Carbon	GF	Gas Filter
A/D	Analog/Digital	GM	Gas Mixer
BC	Bubble Column	P	Pressure
C	Cyclone	PD	Pressure Dropper
C/P	Compressor/Pump	RV	Regulator
CW	Condenser	SF	Solid Feeder
DM	Digital Measurement	T	Temperature
EH	Electrical Heater	V	Flow Rate
F	Furnace	V3	Three Way Valve

Figure 2. The experimental set-up

2.6. Gasification Reactions

Gasification reactions that may affect the producer gas content obtained from gasification experiments were investigated. Water-gas, water-gas shift, steam reforming and hydrogasification reactions occur in the presence of steam (Kumar et al., 2009). With the Boudouard reaction, which includes the reaction of C with CO_2, the syngas with a high CO content can be produced. The need for a gas purification process is reduced by converting of CO_2, which has a greenhouse effect, into CO (Huang et al., 2021). Main gasification reactions are shown in Table 3 (Block et al., 2018).

Table 3. Main gasification reactions

Gasification Reactions		ΔH^0_{298K} (kJ/mol)
Complete Oxidation	$C + 0,5O_2 \Leftrightarrow CO$	-111
Partial Oxidation	$C + 0,5O_2 \Leftrightarrow CO_2$	-283
Water-gas Reaction	$C + H_2O \Leftrightarrow CO + H_2$	+131
Water-gas Shift Reaction	$CO + H_2O \Leftrightarrow CO_2 + H_2$	-42
Steam Reforming Reaction	$CH_4 + H_2O \Leftrightarrow CO + 3H_2$	+206
Hydrogasification Reaction	$C + 2H_2 \Leftrightarrow CH_4$	-75
Boudouard Reaction	$C + CO_2 \Leftrightarrow 2CO$	+173

3. RESULTS AND DISCUSSION

The cotton-based banknote sample has a similar structure to cotton gin waste and cotton fibers in terms of characterization test results (Table 4).

Table 4. Comparison of characterization analysis of cotton and cotton-based banknote sample

Sample	Proximate Analysis (wt.%)		Calorific Value (MJ/kg)	Elemental Analysis (wt.%)					Lignocellulosic Analysis (wt.%)		
	Volatile Solid Matter	Ash	Higher Calorific Value	C	H	N	S	O	Cellulose	Hemicellulose	Lignin
Cotton-based Banknote (5 TL) (Kavuştu & Şimşek, 2023)	81.12	4.83	17.42	38.95	6.70	0.65	-	53.70	71.82	2.83	17.64
Cotton Gin Waste (Raveendran et al., 1995)	88.00	5.40	17.48	42.70	6.00	0.10	-	49.50	77.80	16.00	-
Cotton Fiber (Corradini et al., 2009)									88.3±0.3	8.0±0.3	4.8±0.5

The higher calorific value of the cotton-based banknote sample is higher than that of oil palm empty fruit bunch (17.02 MJ/kg), beef cattle manure (15.93 MJ/kg), rice straw (16.28 MJ/kg) and rice hulls (16.14 MJ/kg) (Widjaya et al., 2018). The effect of lignin content of biomass on energy content is greater than cellulose and hemicellulose (Elbersen et al., 2017). The lignin content in the cotton-based banknote sample is higher than that in the wheat straw (17 %), rice straw (12 %) and poultry litter (11 %) (Ren et al., 2019).

3.1. DSC Analysis Results

The DSC curves obtained at six different heating rates in the range of 5-30°C/min are shown in Figure 3. Endothermic peaks observed in the range of 93.51-179.91°C at different heating rates indicated physical changes and the removal of moisture from the fibers. Exothermic peaks observed in the range of 357.04-398.11°C represented radical and char formation reactions of small molecules such as CO, CO_2 and acetaldehyde, which were converted into intermediate products with the increase in temperature (Smith et al., 2024). Afterwards, the endothermic values obtained indicated the ongoing decomposition, which was more prominent at the heating rate of 10°C/min. In the study of Smith et al. (2024), where DSC analysis was performed on cotton, an endothermic peak was observed in the range of 120-150°C and an exothermic peak at 372°C, similar to the cotton-based banknote sample.
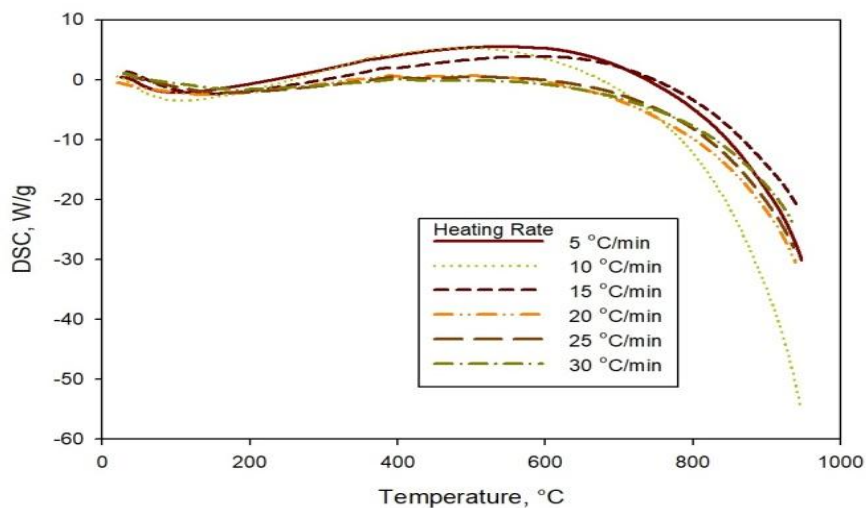
Figure 3. DSC curves of cotton-based banknote sample

3.2. FTIR Analysis Results

The FTIR spectrum obtained at six different heating rates in the range of 5-30°C/min are shown in Figure 4. The bands from 3500-3700 cm^{-1} represented the O–H or N–H stretching of carbohydrates, proteins and adsorbed water. The peaks in the 2800-3200 cm^{-1} presented the C-H stretching in cellulose, hemicellulose and hydrocarbons. The peaks in the 1300-1800 cm^{-1} indicated the C=O stretching modes of carbonyl groups originating from esters, carboxylic acids, ketones and aldehydes. The C-O stretching in the bands of 1000-1200 cm^{-1} indicated the presence of ethers, alcohols and phenols (Portella et al., 2016; He et al., 2022; Pang et al., 2024). With FTIR analysis of cotton-based banknote sample, similar peaks were obtained with the cotton organs and tissues in the study of He et al. (2022) and cotton fibers in the study of Portella et al. (2016).
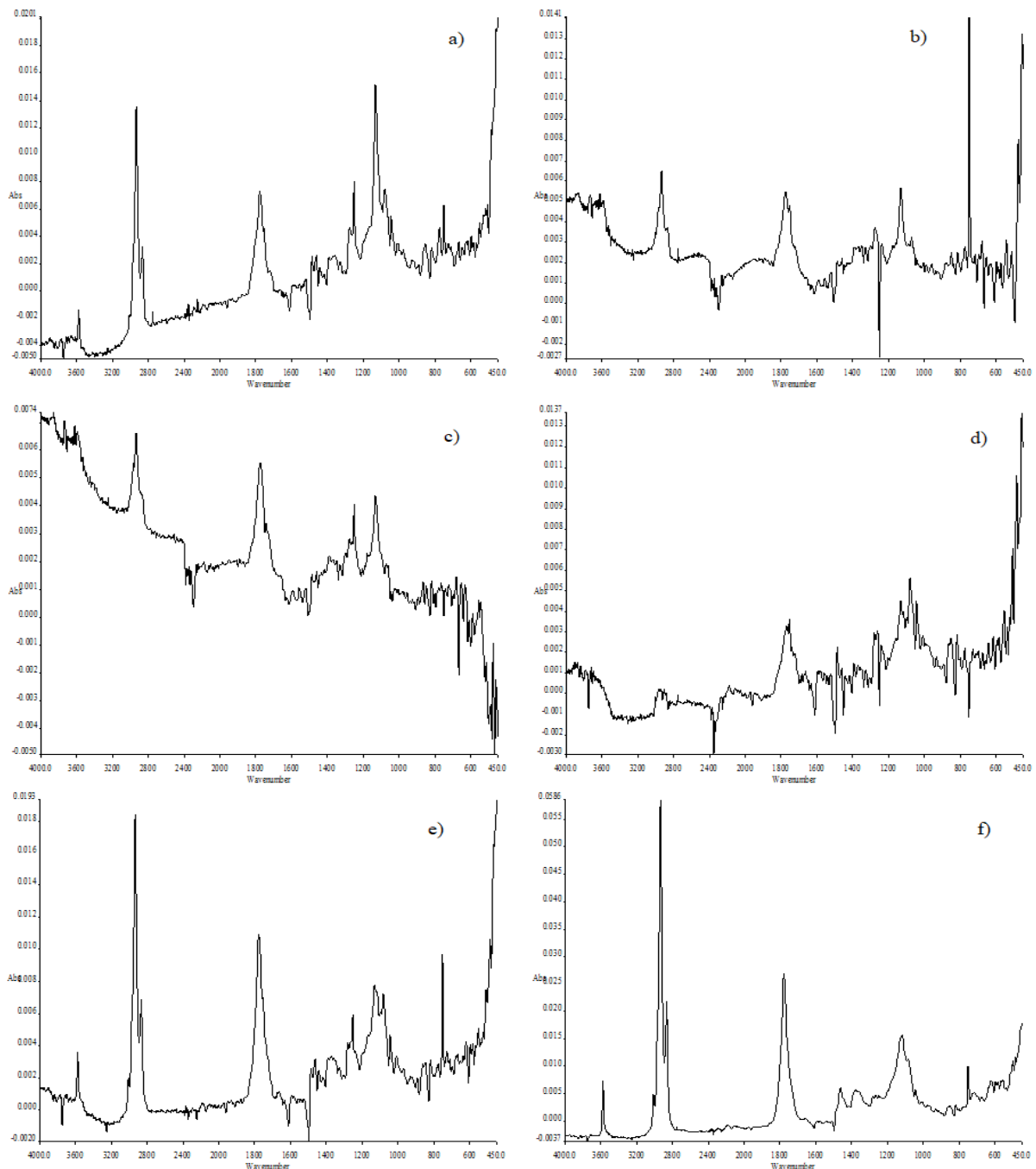
Figure 4. *FTIR spectrum of cotton-based banknote sample at heating rates (°C/min) of*
***a)** 5, **b)** 10, **c)** 15, **d)** 20, **e)** 25, and **f)** 30*

3.3. Activation Energy Results

The plots obtained for different extent of conversions using the KAS and FWO methods are shown in Figure 5, and the calculated activation energies are given in Table 5. The regression lines and calculated activation energies obtained from the KAS and FWO methods were compatible with each other. The activation energies of the cotton-based banknote sample were calculated in the range of 134-171 kJ/mol, and these values continued to increase until the x=0.6 conversion and then started to decrease. In the study of Yousef et al. (2020), the activation energies of the end-of-life Egyptian Pound (EGP) cotton-rich banknote were calculated in the range of 157-276 kJ/mol by FWO and KAS methods, and these values continued to increase until the x=0.7 conversion and then started to decrease. Multi-step reactions occurred due to the ink, hemicellulose, lignin and other materials contained in the sample, making it difficult to examine thermal degradation (Yousef et al., 2020). The difference in activation energies of TL and EGP banknotes is due to the difference in their chemical composition and structure. In the study of Corradini et al. (2009), the average activation energy for cotton fibers was calculated as 150.4±3.6 kJ/mol by FWO method. This value was nearly the same as the value calculated with FWO as 154.25 kJ/mol for the cotton-based banknote sample.
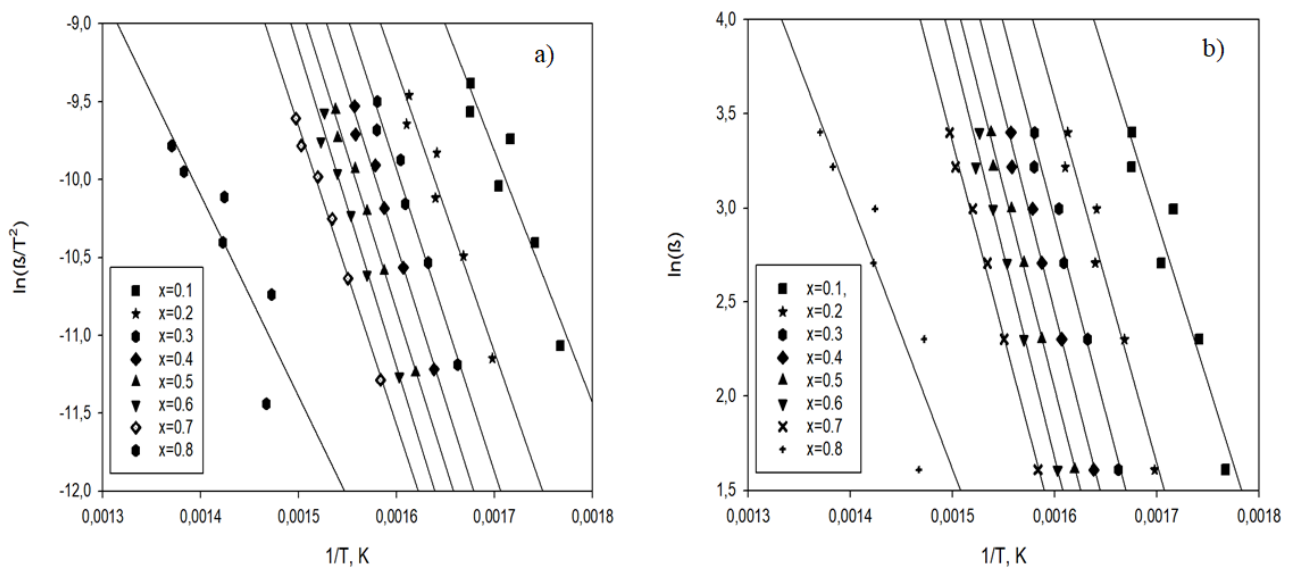
Figure 5. a) KAS and b) FWO plots of cotton-based banknote sample

Table 5. Activation energies for cotton-based banknote sample

Ea (kJ/mol)	Extent of Conversion (x)								
	0.1	0.2	0.3	0.4	0.5	0.6	0.7	0.8	Mean
Flynn-Wall-Ozawa (FWO)	136.638	152.946	162.841	167.563	167.689	171.419	161.734	113.168	154.250
Kissinger-Akahira-Sunose (KAS)	134.011	150.767	160.970	165.793	165.800	169.612	159.269	107.308	151.691

3.4. Effect of Torrefaction Pre-Treatment on Experimental Mole Fractions

Raw and torrefied (250°C for 10 min) cotton-based banknote samples were used as feedstocks. Gasification experiments were carried out at 800°C with an inlet H_2O/O_2 ratio of 25. Mole fraction-time curves obtained with gasification are given in Figure 6a and 6b. Considering the maximum mole fractions achieved, with torrefaction pre-treatment, H_2 mole fraction increased from 4.44% to 4.64%; CO mole fraction increased from 9.32% to 10.71% and CH_4 mole fraction increased from 3.47% to 3.65%, while CO_2 mole fraction decreased from 6.28% to 5.48%. The decrease in CO_2 mole fraction showed the effects of Boudouard reaction, the increase in CH_4 mole fraction showed the effects of hydrogasification reaction, and the increase in mole fractions of H_2 and CO showed the effects of water-gas and steam reforming reactions. The increase

in CO mole fraction and the decrease in CO_2 mole fraction also showed that the effect of water-gas shift reaction was limited. The experimental results were consistent with the studies of Singh and Yadav (2021) and Sarker et al. (2022) in which the syngas yield increased as a result of gasification with torrefied biomass.

3.5. Effect of Co-Gasification Pre-Treatment on Experimental Mole Fractions

Samples prepared by mixing cotton and polymer-based banknote samples with the ratios of 50:50 and 75:25 (wt.%) were used as feedstocks. Gasification experiments were carried out at 800°C with an inlet H_2O/O_2 ratio of 25. Mole fraction-time curves obtained with gasification are given in Figure 6c and 6d. Considering the maximum mole fractions achieved, with the co-gasification of cotton and polymer-based samples at 75:25 ratio, H_2 mole fraction decreased from 4.44% to 3.71%; CO mole fraction decreased from 9.32% to 8.02% and CO_2 mole fraction decreased from 6.28% to 4.77%, while CH_4 mole fraction increased from 3.47% to 4.69%, compared to the raw cotton-based sample. With the co-gasification of cotton and polymer-based samples at 50:50 ratio compared to 75:25 ratio, H_2 mole fraction decreased from 3.71% to 3.68%; CO mole fraction decreased from 8.02% to 6.68% and CO_2 mole fraction from decreased 4.77% to 4.74%, while CH_4 mole fraction increased from 4.69% to 5.65%. Producer gas production was generally achieved efficiently and the decreasing maximum mole fractions indicated that the conversion efficiency of the gasification reactions and therefore the energy content of the gas decreased with the increasing ratio of the polymer-based sample in the feedstock. The increase in only the CH_4 mole fraction indicated that the hydrogasification reaction was effective and the effect of the steam reforming reaction was reduced. The conversion of feedstock primarily to tar with low char yield with the gasification of cellulose-rich biomass with plastic may have limited gas efficiency (Ajorloo et al., 2024). On the other hand, the difference in materials and inks contained in cotton and polymer-based samples may have also caused this result.
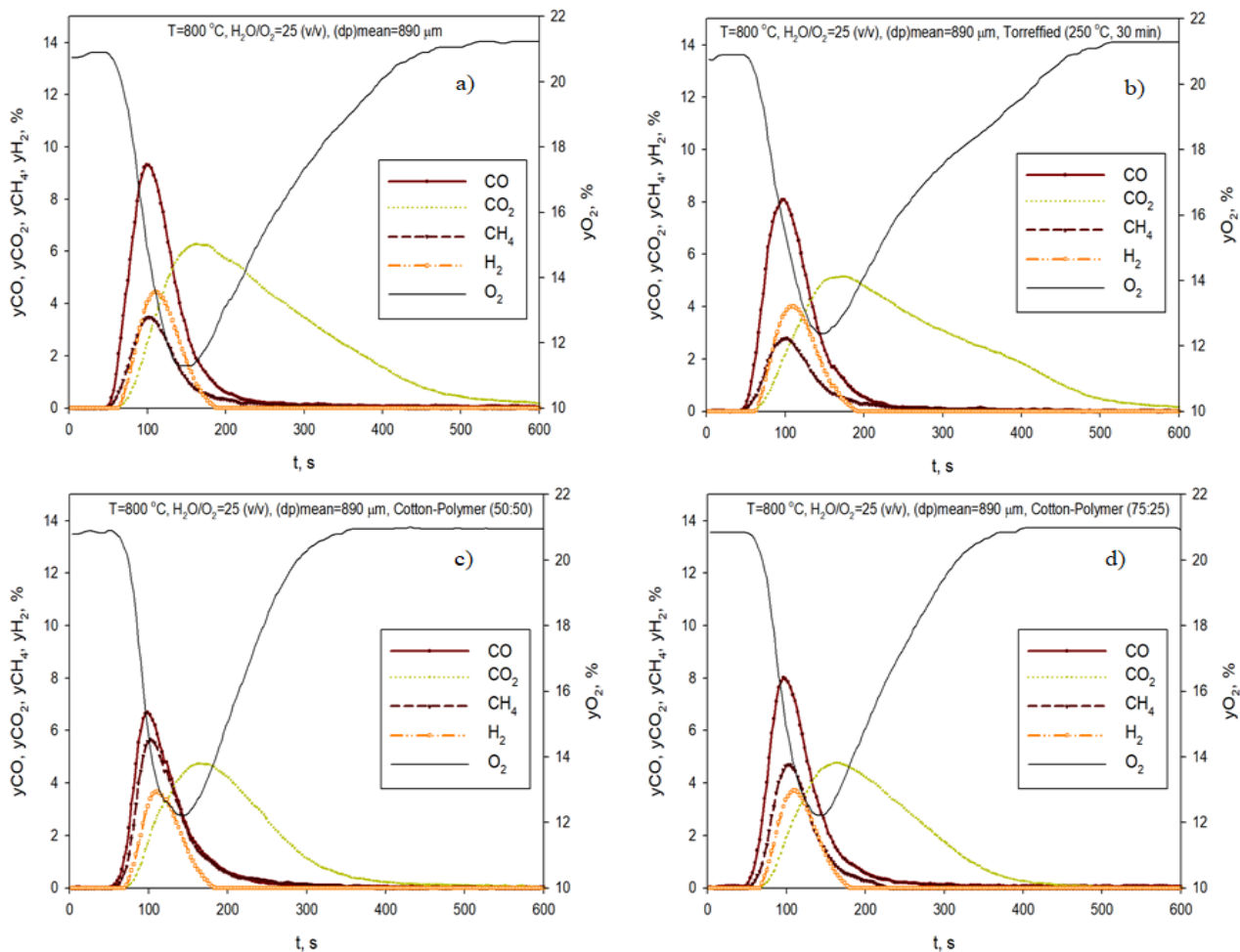
Figure 6. *Mole fraction-time curves for **a)** raw, **b)** torrefied cotton-based banknote samples; **c)** 50:50, **d)** 75:25 cotton:polymer-based banknote samples*

4. CONCLUSION

The results of DSC and FTIR analysis performed on the cotton-rich banknote sample and the calculated mean activation energy by FWO method showed that the cotton-based banknote sample had characteristic structures similar to those of cotton and thus end-of-life cotton banknotes could be used as a biomass source. With the non-isothermal kinetic methods of Flynn-Wall-Ozawa (FWO) and Kissinger-Akahira-Sunose (KAS), the activation energies were calculated as 134-171 kJ/mol at different conversions and the activation energy started to decrease after the x=0.6 conversion. This situation showed that the multi-step reactions occurring due to the complex structure of the sample had made it difficult to study the thermal decomposition.

In the gasification experiments performed at 800°C with an inlet H_2O/O_2 ratio of 25, the effects of torrefaction pre-treatment and co-gasification on the producer gas content were investigated with mole fraction- time curves. With the gasification torrefied (250°C for 10 min) cotton-based banknote sample, the H_2, CO, CH_4 mole fractions and product yield increased, while the CO_2 mole fraction decreased. With the increase in the polymer-based sample ratio in the feedstock, the gas product yield and H_2, CO, CO_2 mole fractions decreased, while the CH_4 mole fraction increased. In the gasification of torrefied cotton-based banknote sample, the water-gas, water-gas shift, steam reforming and hydrogasification reactions, which took place in the steam environment, were effective; while in the co-gasification of the cotton and polymer-based banknote samples, the hydrogasification reaction was effective.

In conclusion, the results of the study showed that (i) end-of-life cotton banknotes can be effectively used as a biomass source in thermochemical processes, (ii) torrefaction can facilitate the storage and transportation of dispersed waste banknotes, and thus improved fuel properties can increase producer gas efficiency, (iii) producer gas can be efficiently obtained by co-gasification of end-of-life cotton and polymer-based banknotes considering the diversity of these wastes.

AUTHOR CONTRIBUTIONS

Methodology, H.K. and E.H.Ş.; laboratory work, H.K.; manuscript-original draft, H.K.; manuscript-review and editing, H.K. and E.H.Ş. All authors have read and legally accepted the final version of the article published in the journal.

ACKNOWLEDGEMENT

CONFLICT OF INTEREST

The authors declare no conflict of interest.

REFERENCES

Ajorloo, M., Ghodrat, M., Scott, J., & Strezov, V. (2024). Experimental analysis of the effects of feedstock composition on the plastic and biomass co-gasification process. *Renewable Energy*, *231*, 120960. https://doi.org/10.1016/j.renene.2024.120960

Baruah, D., & Baruah, D. C. (2014). Modeling of biomass gasification: A review. *Renewable and Sustainable Energy Reviews*, *39*, 806-815. https://doi.org/10.1016/j.rser.2014.07.129

Block, C., Ephraim, A., Weiss-Hortala, E., Minh, D. P., Nzihou, A., & Vandecasteele, C. (2018). Co-pyrogasification of plastics and biomass, a Review. *Waste and Biomass Valorization*, *10*(3), 483-509. https://doi.org/10.1007/s12649-018-0219-8

BoC. (2011). *Life cycle assessment of Canada's polymer bank notes and cotton-paper bank notes final report*. Bank of Canada.

BoI. (2023). *Environment Report 2023*. Bank of Italy.

Cabuk, B., Duman, G., Yanik, J., & Olgun, H. (2020). Effect of fuel blend composition on hydrogen yield in co-gasification of coal and non-woody biomass. *International Journal of Hydrogen Energy*, *45*(5), 3435-3443. https://doi.org/10.1016/j.ijhydene.2019.02.130

Chan, Y. H., Cheah, K. W., How, B. S., Loy, A. C. M., Shahbaz, M., Singh, H. K. G., Yusuf, N. R., Shuhaili, A. F. A., Yusup, S., Ghani, W. A. W. A. K. G., Rambli, J., Kansha, Y., Lam, H. L., Hong, B. H., & Ngan, S. L. (2019). An overview of biomass thermochemical conversion technologies in Malaysia. *The Science of the Total Environment*, *680*, 105-123. https://doi.org/10.1016/j.scitotenv.2019.04.211

Corradini, E., Teixeira, E. M., Paladin, P. D., Agnelli, J. A., Silva, O. R. R. F., & Mattoso, L. H. C. (2009). Thermal stability and degradation kinetic study of white and colored cotton fibers by thermogravimetric analysis. *Journal of Thermal Analysis and Calorimetry*, *97*(2), 415-419. https://doi.org/10.1007/s10973-008-9693-8

Das, B., Bhattacharya, A., & Datta, A. (2020). Kinetic modeling of biomass gasification and tar formation in a fluidized bed gasifier using equivalent reactor network (ERN). *Fuel*, *280*, 118582. https://doi.org/10.1016/j.fuel.2020.118582

DLR. (2022). *Annual Report 2022*. De La Rue plc.

DLR. (2023). *Annual Report 2023*. De La Rue plc.

ECB. (2023). *Product Environmental Footprint study of euro banknotes as a payment instrument*. European Central Bank.

Elbersen, W., Lammens, T. M., Alakangas, E. A., Annevelink, B., Harmsen, P., & Elbersen, B. (2017). Lignocellulosic Biomass Quality: Matching Characteristics With Biomass Conversion Requirements. In: C. Panoutsou (Eds.), *Modeling and Optimization of Biomass Supply Chains*, (pp. 55-78). https://doi.org/10.1016/b978-0-12-812303-4.00003-3

George, J., Arun, P., & Muraleedharan, C. (2019). Experimental investigation on co-gasification of coffee husk and sawdust in a bubbling fluidised bed gasifier. *Journal of the Energy Institute*, *92*(6), 1977-1986. https://doi.org/10.1016/j.joei.2018.10.014

G+D (2024). Number of Banknotes in circulation worldwide (Accessed:01/09/2024) https://www.gi-de.com/en/currency-technology/banknote-solutions/banknote-production/banknote-printing

Hanchate, N., Ramani, S., Mathpati, C., & Dalvi, V. H. (2021). Biomass gasification using dual fluidized bed gasification systems: A review. *Journal of Cleaner Production*, *280*, 123148. https://doi.org/10.1016/j.jclepro.2020.123148

Hanegraaf, R., Larçin, A., Jonker, N., Mandley, S., & Miedema, J. (2019). Life cycle assessment of cash payments in the Netherlands. *The International Journal of Life Cycle Assessment*, *25*(1), 120-140. https://doi.org/10.1007/s11367-019-01637-3

He, Z., Liu, Y., Kim, H. J., Tewolde, H., & Zhang, H. (2022). Fourier transform infrared spectral features of plant biomass components during cotton organ development and their biological implications. *Journal of Cotton Research*, *5*(1). https://doi.org/10.1186/s42397-022-00117-8

Huang, J., Zhang, H., Tan, Q., Li, L., Xu, R., Xu, Z., & Li, X. (2021). Enhanced conversion of CO_2 into O_2-free fuel gas via the Boudouard reaction with biochar in an atmospheric plasmatron. *Journal of CO_2 Utilization*, *45*, 101429. https://doi.org/10.1016/j.jcou.2020.101429

Hussain, M., Ali, O., Raza, N., Zabiri, H., Ahmed, A., & Ali, I. (2023). Recent advances in dynamic modeling and control studies of biomass gasification for production of hydrogen rich syngas. *RSC Advances*, *13*(34), 23796-23811. https://doi.org/10.1039/d3ra01219k

IEA. (2021). Energy supply (Accessed:01/09/2024) https://www.iea.org/world/energy-mix

IEA. (2023). *World Energy Outlook 2023*. International Energy Agency.

Jahromi, R., Rezaei, M., Samadi, S. H., & Jahromi, H. (2021). Biomass gasification in a downdraft fixed-bed gasifier: Optimization of operating conditions. *Chemical Engineering Science*, *231*, 116249. https://doi.org/10.1016/j.ces.2020.116249

K&B (2022). Annual increase trend in banknote production (Accessed:01/09/2024) https://www.koenig-bauer.com/en/news/details/article/90-of-the-worlds-banknotes-are-swiss-1

Kavuştu, H., & Şimşek, E. H. (2023). Characterization and gasification of end-of-life banknotes rich in cotton content. *Waste Management*, *171*, 473-481. https://doi.org/10.1016/j.wasman.2023.09.034

Kavuştu, H. (2024). *Gasification of end-of-life banknotes rich in cotton content in a fluidized bed reactor and modelling (in Turkish)*. PhD Thesis, Ankara University.

Kumar, A., Jones, D., & Hanna, M. (2009). Thermochemical Biomass Gasification: A Review of the Current Status of the Technology. *Energies*, *2*(3), 556-581. https://doi.org/10.3390/en20300556

Luján-Ornelas, C., del C Sternenfels, U. M., & Güereca, L. P. (2018). Life cycle assessment of Mexican polymer and high-durability cotton paper banknotes. *The Science of the Total Environment*, *630*, 409-421. https://doi.org/10.1016/j.scitotenv.2018.02.177

Mancilla-Leytón, J., Fernández-Rodríguez, M., De La Lama-Calvente, D., & Borja, R. (2024). Evaluation of batch mesophilic anaerobic digestion of waste Euro banknotes for methane Production: Preliminary studies and kinetic approach. *Waste Management*, *173*, 22-28. https://doi.org/10.1016/j.wasman.2023.11.003

Meng, S., Li, W., Li, Z., & Song, H. (2023). Recent progress of the transition metal-based catalysts in the catalytic biomass gasification: A mini-review. *Fuel*, *353*, 129169. https://doi.org/10.1016/j.fuel.2023.129169

Mohammed, H. I., Garba, K., Ahmed, S. I., & Abubakar, L. G. (2022). Thermodynamics and kinetics of Doum (Hyphaene thebaica) shell using thermogravimetric analysis: A study on pyrolysis pathway to produce bioenergy. *Renewable Energy*, *200*, 1275-1285. https://doi.org/10.1016/j.renene.2022.10.042

Ng, R. T., Tay, D. H., Ghani, W. a. W. a. K., & Ng, D. K. (2013). Modelling and optimisation of biomass fluidised bed gasifier. *Applied Thermal Engineering*, *61*(1), 98-105. https://doi.org/10.1016/j.applthermaleng.2013.03.048

Pang, Y., Zhu, X., Li, N., & Wang, Z. (2024). Study on CO_2 co-gasification of cellulose and high-density polyethylene via TG-FTIR and ReaxFF MD. *Process Safety and Environmental Protection*. https://doi.org/10.1016/j.psep.2024.04.119

Parrillo, F., Ardolino, F., Calì, G., Marotto, D., Pettinau, A., & Arena, U. (2021). Fluidized bed gasification of eucalyptus chips: Axial profiles of syngas composition in a pilot scale reactor. *Energy*, *219*, 119604. https://doi.org/10.1016/j.energy.2020.119604

Parrillo, F., Ardolino, F., Boccia, C., Calì, G., Marotto, D., Pettinau, A., & Arena, U. (2023). Co-gasification of plastics waste and biomass in a pilot scale fluidized bed reactor. *Energy*, *273*, 127220. https://doi.org/10.1016/j.energy.2023.127220

Portella, E. H., Romanzini, D., Angrizani, C. C., Amico, S. C., & Zattera, A. J. (2016). Influence of Stacking Sequence on the mechanical and dynamic mechanical properties of cotton/glass fiber reinforced polyester composites. *Materials Research*, *19*(3), 542-547. https://doi.org/10.1590/1980-5373-mr-2016-0058

Raveendran, K., Ganesh, A., & Khilar, K. C. (1995). Influence of mineral matter on biomass pyrolysis characteristics. *Fuel*, *74*(12), 1812-1822. https://doi.org/10.1016/0016-2361(95)80013-8

Ren, J., Cao, J., Zhao, X., Yang, F., & Wei, X. (2019). Recent advances in syngas production from biomass catalytic gasification: A critical review on reactors, catalysts, catalytic mechanisms and mathematical models. *Renewable and Sustainable Energy Reviews*, *116*, 109426. https://doi.org/10.1016/j.rser.2019.109426

RDK. (2022). Summary banknote recycling study November 2022 (Accessed:01/09/2024) https://www.royaldutchkusters.com/blog/summary-banknote-recycling-study-2022

Sadaka, S. S. (2013). Gasification of raw and torrefied cotton gin wastes in an auger system. *Applied Engineering in Agriculture*, 405-414. https://doi.org/10.13031/aea.29.9919

Sarker, T. R., Nanda, S., Meda, V., & Dalai, A. K. (2022). Process optimization and investigating the effects of torrefaction and pelletization on steam gasification of canola residue. *Fuel*, *323*, 124239. https://doi.org/10.1016/j.fuel.2022.124239

Sheikh, M. M. I., Kim, C. H., Park, H. J., Kim, S. H., Kim, G. C., Lee, J. Y., Sim, S., & Kim, J. W. (2013). Alkaline pretreatment ımproves saccharification and ethanol yield from waste money bills. *Bioscience Biotechnology and Biochemistry*, *77*(7), 1397-1402. https://doi.org/10.1271/bbb.130002

Singh, D., & Yadav, S. (2021). Steam gasification with torrefaction as pretreatment to enhance syngas production from mixed food waste. *Journal of Environmental Chemical Engineering*, *9*(1), 104722. https://doi.org/10.1016/j.jece.2020.104722

Smith, D. L., Montemayor, M. D., Carosio, F., & Grunlan, J. C. (2024). Universal intumescent polyelectrolyte complex treatment for cotton, polyester, and blends thereof. *Polymer Degradation and Stability*, *228*, 110936. https://doi.org/10.1016/j.polymdegradstab.2024.110936

Widjaya, E. R., Chen, G., Bowtell, L., & Hills, C. (2018). Gasification of non-woody biomass: A literature review. *Renewable and Sustainable Energy Reviews*, 89, 184-193. https://doi.org/10.1016/j.rser.2018.03.023

Xie, J., Zhong, W., Shao, Y., & Zhou, G. (2021). Simulation of co-gasification of coal and wood in a dual fluidized bed system. *Advanced Powder Technology*, *32*(1), 52-71. https://doi.org/10.1016/j.apt.2020.11.017

Yousef, S., Eimontas, J., Striūgas, N., Trofimov, E., Hamdy, M., & Abdelnaby, M. A. (2020). Conversion of end-of-life cotton banknotes into liquid fuel using mini-pyrolysis plant. *Journal of Cleaner Production*, *267*, 121612. https://doi.org/10.1016/j.jclepro.2020.121612

Yousef, S., Kuliešienė, N., Sakalauskaitė, S., Nenartavičius, T., & Daugelavičius, R. (2021). Sustainable green strategy for recovery of glucose from end-of-life euro banknotes. *Waste Management*, *123*, 23-32. https://doi.org/10.1016/j.wasman.2021.01.007

Zhang, X., Xu, W., Rauf, A., & Ozturk, I. (2024). Transitioning from conventional energy to clean renewable energy in G7 countries: A signed network approach. *Energy*, *307*, 132655. https://doi.org/10.1016/j.energy.2024.132655

Investigation of the Effect of Mechanical Alloying on the Wear Behavior of AA7020/Fe₃O₄/GNP Hybrid Composite Materials

Ufuk TAŞCI[1*] iD

[1] Department of Graduate School of Natural and Applied Sciences, Gazi University, Ankara, Türkiye

Keywords	Abstract
Mechanical Alloy Hybrid Composite Graphene Fe₃O₄ Tribology Behavior	In this study, the mechanical properties of composite/hybrid composites were investigated by reinforcing 10% Fe3O4 and 0.25% nanographene by weight into the AA7020 alloy, which is widely preferred, especially in the defense and aviation industries. The prepared mixture powders were subjected to a mechanical alloying process for 1 and 8 hours in a ball mill with a 1/16 powder-ball ratio to distribute them homogeneously. The mixed hybrid/composite powders were produced in a metal mold using a powder metallurgy hot pressing method at 250 MPa load and 575°C temperature for 60 minutes. The microstructural properties of the test samples were investigatedIn addition, density, microhardness and wear test results were examined in terms of mechanical properties. The hybrid sample with 8h mechanical alloying obtained the highest hardness value (118.5 HV) and the lowest friction coefficient (0.1965 μm).

1. INTRODUCTION

Aluminum and its alloys are widely preferred in defense, aerospace, and aviation fields due to their advantageous properties, including low density, high specific strength, hardness, excellent electrical conductivity, and corrosion resistance (Kumar et al., 2023). In addition, due to their low density, aluminum alloys are used in studies to reduce fuel consumption and CO_2 emissions for automotive applications. 7XXX alloys have low density, excellent specific strength and bending rigidity. For this reason, the 7020 alloy belongs to the Al-Zn-Mg-(Cu) group within the 7XXX series and is preferred in the latest technological aviation, space, automotive and rail system applications (Kumar et al., 2014; Kaya et al., 2022). Despite their high mechanical properties, aluminum alloys exhibit low tribological performance under certain conditions (Sharma et al., 2021; Kumar et al., 2022). In particular, metal matrix composites (MMCs) have been developed and continue to be improved to enhance the weak aspects of these materials for modern technologies (Karakoç et al., 2019).

Current aluminum composite materials are favored due to their low density, durability, and enhanced thermal conductivity. However, despite the advanced properties of MMCs, there remains a need to improve their strength and tribological properties (Jiang et al., 2018; Reddy et al., 2018; Özkan et al., 2022). As highlighted in recent studies, hybrid-reinforced composite materials are being utilized. Oxides and ceramics are commonly used in the production of particle-reinforced composite materials. Typically, ceramic reinforcement particles in micron and nano sizes, such as B_4C, Al_2O_3, Graphene, WS_2, HBN, TiC, Fe_3O_4, and SiC, are employed (Karakoç et al., 2019; Sardar et al., 2020; Zheng et al., 2020; Taşçı et al., 2024).

Production of metal matrix composite materials typically involves manufacturing methods such as conventional casting, stir casting, infiltration, mechanical alloying, and powder metallurgy (PM). However, hybrid/composite materials produced using casting and infiltration methods face a significant challenge in achieving a homogeneous distribution of reinforcement particles within the matrix. To address this, the initial powders are prepared in ball mixers and produced using the powder metallurgy method (Lakshmikanthan et al., 2022; Taşcı & Bostan, 2022; Srivyas et al., 2023; Michael & John, 2024).

The study aims to investigate the effect of 1-hour and 8-hour milling durations, particularly on the mechanical and wear behavior, to ensure the homogeneous distribution of 10 wt.% Fe_3O_4 and 0.25 wt.% GNP hybrid reinforcements within the AA7020 matrix, produced via the powder metallurgy (PM) method.

2. MATERIAL AND METHOD

2.1. Materials and Methods

This study used AA7020 matrix powders (avg. 75 μm), Fe_3O_4 powders (avg. 40 μm), and high-purity nanographene powders with an average size of 5 nm. Mechanical alloying (MA) was carried out by adding 10 wt% Fe_3O_4 powders and 0.25 wt% nanographene powders to AA7020 alloy using an atmosphere-controlled high-energy ball mixer for 1 and 8 h. The mixer was operated at 300 rpm with a powder-to-ball ratio of 1/16. The schematic drawing of the milling process during the MA process is given in Figure 1.
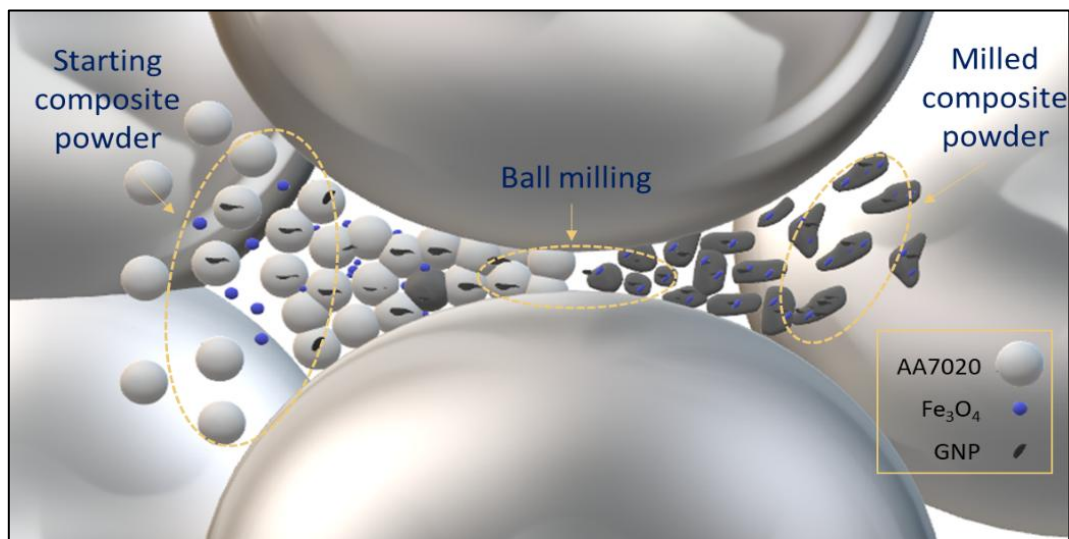
Figure 1. Preparation of composite powders in ball mill (Taşcı et al., 2024)

The mixed powders were pressed into 10x10x10 mm^3 cylindrical samples in a powder metal die using the hot pressing method at 575°C and 250 MPa pressure. Table 1 presents the chemical composition of the AA7020 alloy powder material used as the matrix in producing the hybrid composite material.

Table 1. Chemical composition of AA7020 alloy

Element	Zn	Mg	Ti	Zr	Fe	Si	Cu	Cr	Mn	Al
Content (%)	4.5	1.40	0.25	0.070	0.4	0.35	0.2	0.10	0.040	Remainder

2.2. Microstructure and Mechanical Analysis

The hybrid composite materials of AA7020+Fe_3O_4+GNP, produced by hot pressing, were sanded in an automatic grinding and polishing machine in a water-based environment using sandpapers of 600, 800, 1000, and 1200 grit, respectively. In sequence, the sanded samples were then polished using diamond suspensions on diamond pads of 9, 6, and 3 microns. Following the polishing process, a final polishing was performed with a 0.001-micron colloidal solution to remove scratches on the sample surface altogether. Lastly, the samples

were etched for 15 seconds using Keller's reagent (1 ml HF + 200 ml H_2O) and examined under an optical microscope. The microstructure images of the samples were captured using a Leica DM4000 M optical microscope.

A scanning electron microscope (SEM) was employed to analyze the morphology of the powders, microstructure images, wear surfaces after wear testing. SEM images, EDS analysis, and mapping of the composites were conducted using a TESCAN MAIA[3] XMU model SEM. Phase analysis was performed using X-ray diffraction (XRD) with a Bruker D_8 Advance X-ray diffractometer.

The hybrid composite materials hardness HV0.5 (ASTM E10-08) and wear (ASTM G99-05) tests (20N load and 1500m wear distance) were conducted in accordance with the relevant standards. Figure 2 presents a schematic diagram of the wear test.
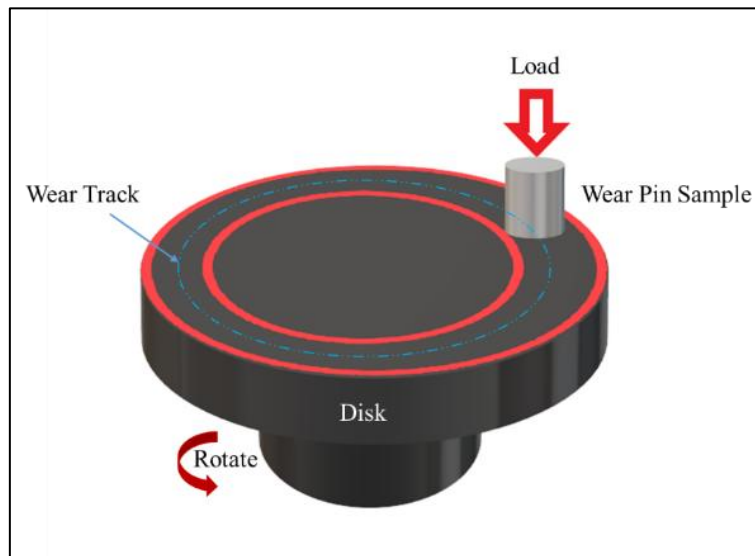
Figure 2. Wear test setup on composite materials produced in the study (Taşcı et al., 2024)

3. RESULTS AND DISCUSSION

3.1. Properties of Starting Powder Materials

The SEM images of the AA7020 alloy powder used as the matrix, along with the Fe_3O_4 and GNP reinforcement powders, are presented in Figure 3. The morphology of the AA7020 alloy powder appears spherical, the Fe_3O_4 powder particles exhibit a complex shape, and the GNP shows a two-dimensional lamellar structure.
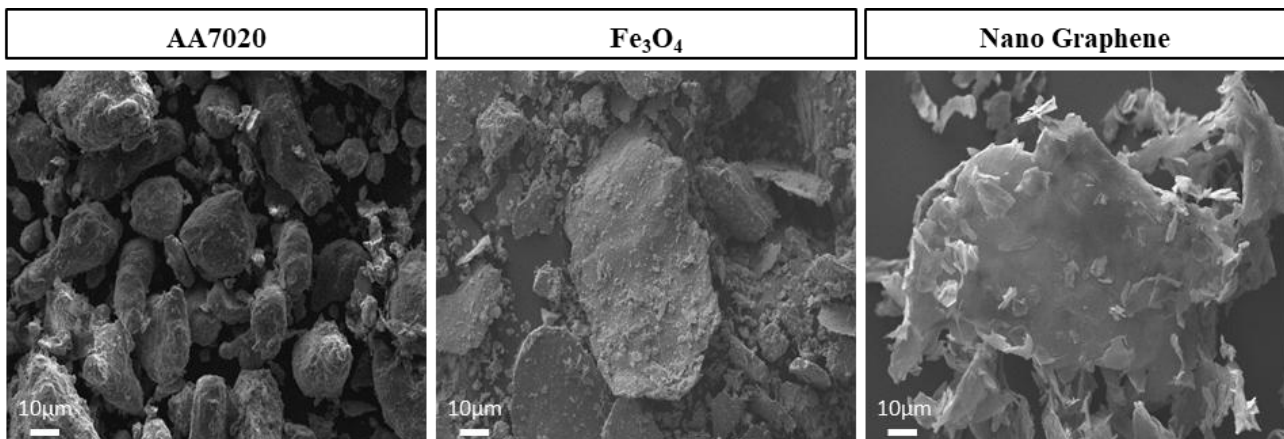
Figure 3. Images of starting powder materials

The composite powders' morphology changed significantly from their initial shapes after milling for different durations (1 and 8 hours). SEM analyses, presented in Figure 4, illustrate the effect of the mixing method on the distribution of Fe_3O_4 and GNP reinforcements within the powders. The composite powder, dry-milled with balls, becomes more flattened and adopts a lamellar form compared to the spherical, unreinforced AA7020 powder.
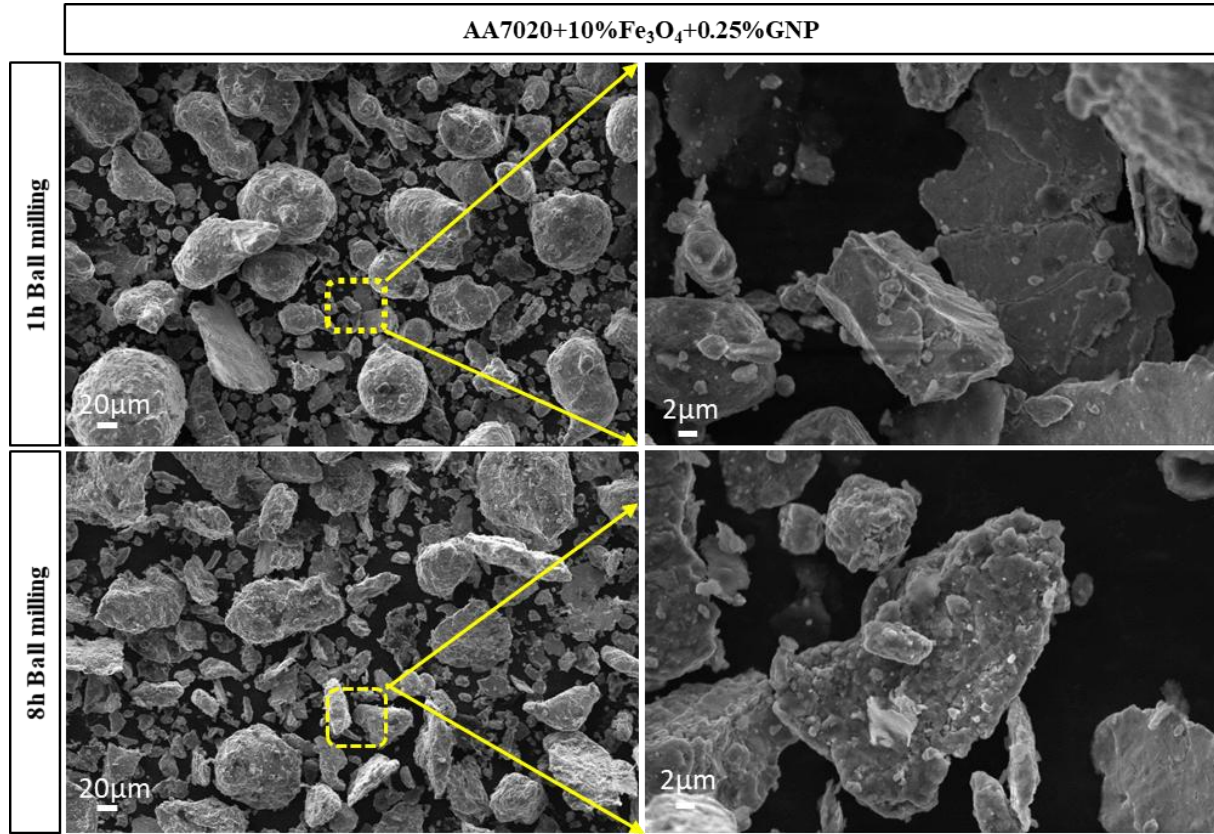
Figure 4. SEM analysis image of hybrid powders produced by mechanical alloying

3.2. Microstructural Analysis

The XRD analysis results of the AA7020+10%Fe_3O_4+0.25%GNP hybrid composite material are shown in Figure 5. When the analysis result was examined, it was determined that it contained α-Al matrix phase, Fe_3O_4, GNP, and $AlMg_4Zn_{11}$ intermetallic phase.

In Figure 6, ground hybrid powders were produced by hot pressing at 575°C at 250 MPa pressure in a protective atmosphere. Optical microscope images of the starting matrix AA7020 and hybrid composite AA7020+Fe_3O_4+GNP materials are given.

The homogeneous distribution of reinforcement particles in hybrid composite materials is critical regarding mechanical properties. Figure 6 shows that the agglomeration level in hybrid materials is at low rates due to the mechanical alloying process. Thanks to the ball alloying, AA7020 matrix powders are flattened, and the reinforcement particles are located at the grain boundaries of the matrix powders. Despite being a hybrid reinforcement, the porosity rate is formed at very low levels thanks to mechanical alloying.

Figure 7 shows the microstructure SEM analysis image of the materials. When the images are examined, it is determined that the GNP reinforcement AA7020 matrix powders are significantly flattened due to the 8h grinding process compared to the 1h grinding process. It is thought that with the increase of mechanical alloying time, GNPs flatten the morphology of AA7020 powder without creating cracks with their lubricating properties within the structure. In addition, it was observed that 10% Fe_3O_4 powders by weight were distributed homogeneously in the matrix with increasing alloying time.
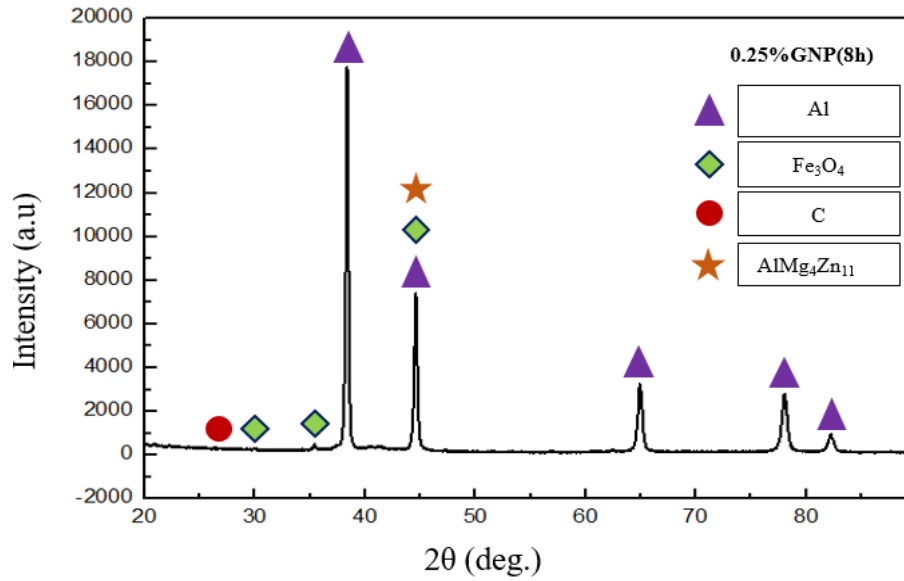
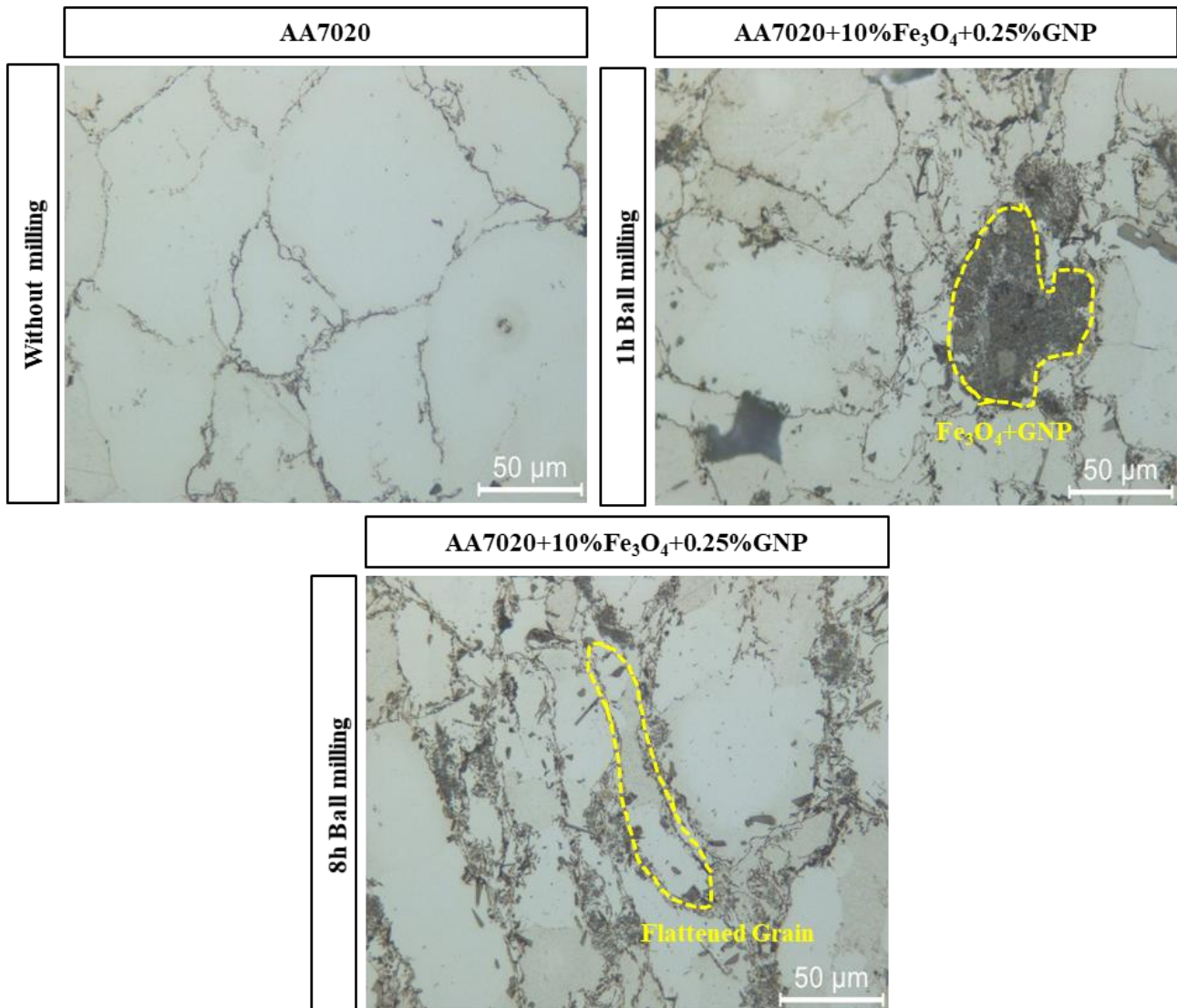*Figure 5. XRD analysis of AA7020+Fe₃O₄+GNP hybrid composites*

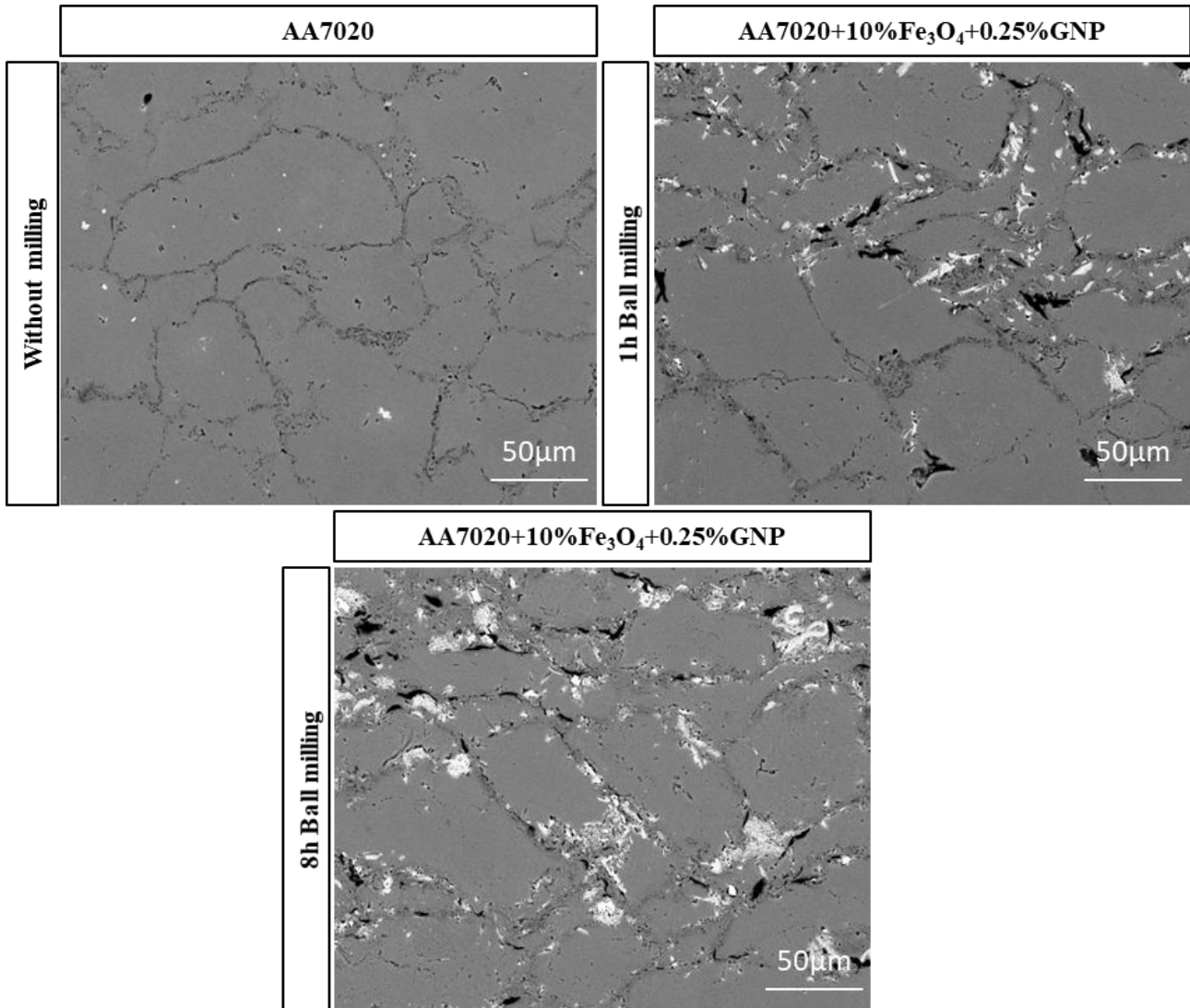*Figure 6. Optical image of AA7020 alloy and hybrid composite materials*

Figure 7. SEM image of AA7020+10%Fe₃O₄+0.25%GNP hybrid composite material

3.3. Mechanical Properties

The density and hardness results of the test samples are given in Figure 8. When the graph was examined, the highest density value was 99.3% in the 4h milled hybrid reinforced sample. The lowest density value was determined as 98.8% in the AA7020 sample. When the hardness values are examined, the highest was measured as 118.5 HV in the 8h milled $10\%Fe_3O_4+0.25\%GNP$ reinforced sample. The lowest hardness value was determined in the AA7020 alloy without reinforcement and milling process.

3.4. Tribological Behavior

Figure 9 shows the test samples weight loss and specific wear rate (SWR) results. The highest weight loss value was 0.0185 in the AA7020 sample without reinforcement and alloying. The lowest value among the SWR ratios was $4.33 * 10^{-7}$ mm³/Nm in the hybrid reinforced sample with an 8h grinding process. A similar behavior to the hardness values was observed in the SWR results with increasing grinding hours. This decreases weight loss and SWR values due to increasing hardness values (Kanthavel et al., 2016; Taşcı et al., 2024).
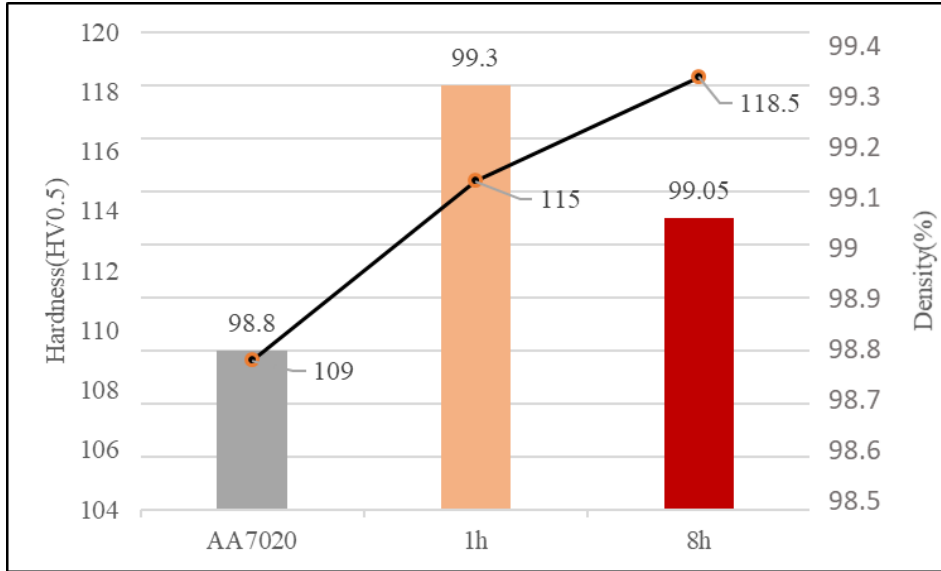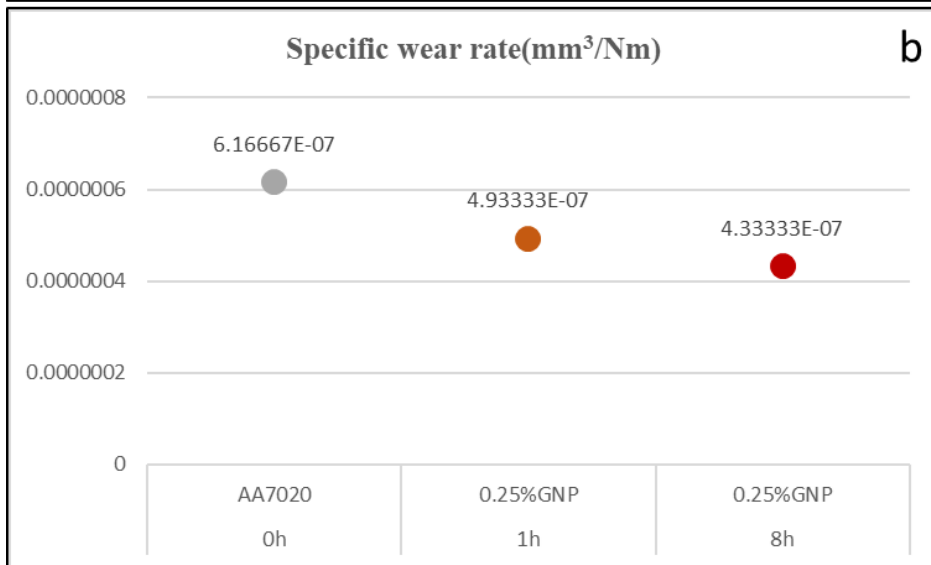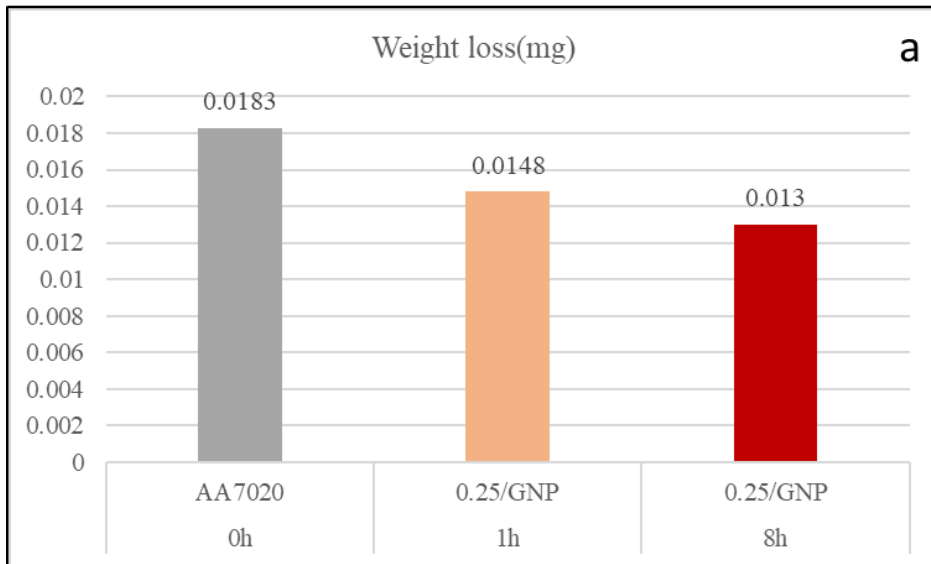
Figure 8. *Density and hardness*

Figure 9. *Weight loss and Specific wear rate*

In wear tests, the resistance to movement between the sample and the abrasive surfaces is known as friction. This resistance is typically defined by the dimensionless coefficient of friction (COF). It is thought that the GNP particles act as lubricants and cause a decrease in the coefficient of friction values depending on the grinding times during the wear test. It is also known that increasing hardness values support this situation. In Figure 10, the highest COF value was determined in the AA7020 sample, while the lowest value was determined as 0.1965 μm in the 8h ground AA7020+10%Fe_3O_4+0.25%GNP sample.

Figure 11 shows the SEM analyses after applying the wear test to the test samples under a 20N load. When the images are examined, deep grooves, debris, plastic deformation, and delamination are detected in the AA7020 alloy without reinforcement and milling. Micro ploughings and plastic deformations increase with the increase in milling time. It is thought that the fact that hybrid reinforcement materials are more complex than the matrix causes the formation of layered regions and deeper grooves. It was observed that the GNP tribe layer was formed, especially in the worn image of the 8h milled sample. This situation was also detected in the SEM/EDS analysis given in Figure 12. The wear behavior of hybrid reinforced composite materials is similar to abrasive wear. The wear behavior of hybrid reinforced materials showed very little difference when applied at different times in the ball milling process.
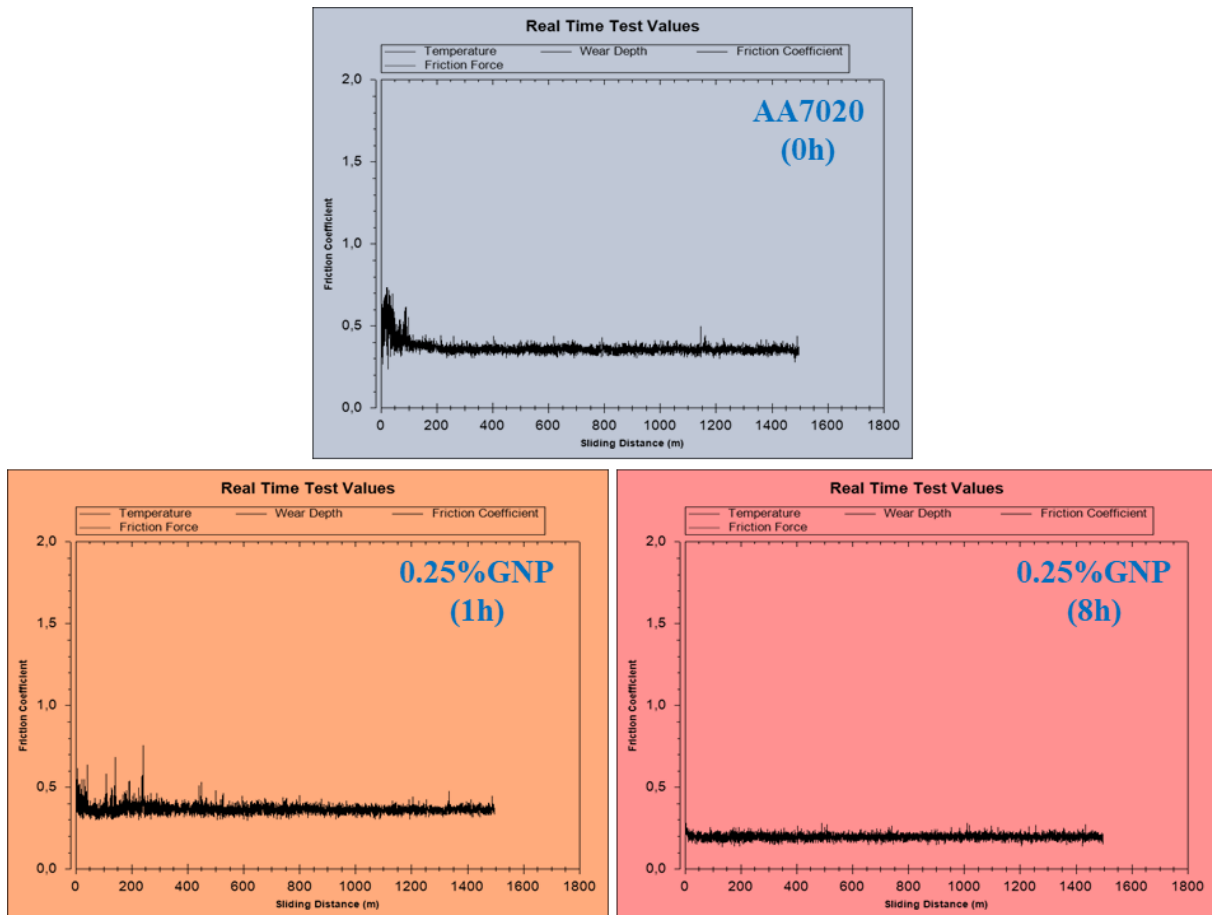

Figure 10. Coefficient of friction

In Figure 13, 3D optical profilometer analysis was applied to the test samples after the wear test. When the 3D optical profilometer analyses were examined, it was seen that the AA7020 sample without reinforcement and grinding process was suitable for the wear surface SEM images. It was determined that delamination and regional part breaks occurred mainly. The analysis of hybrid reinforced composite samples determined that the decrease in deep grooves and the increase in plastic deformations with the increase in grinding time affected the surface roughness values. The hardness, COF, and SWR values determined Ra values. While the highest value was determined in the AA7020 alloy without reinforcement (1.077 μm), the lowest value was determined as 0.8886 μm in the 8h milled hybrid reinforced composite sample.
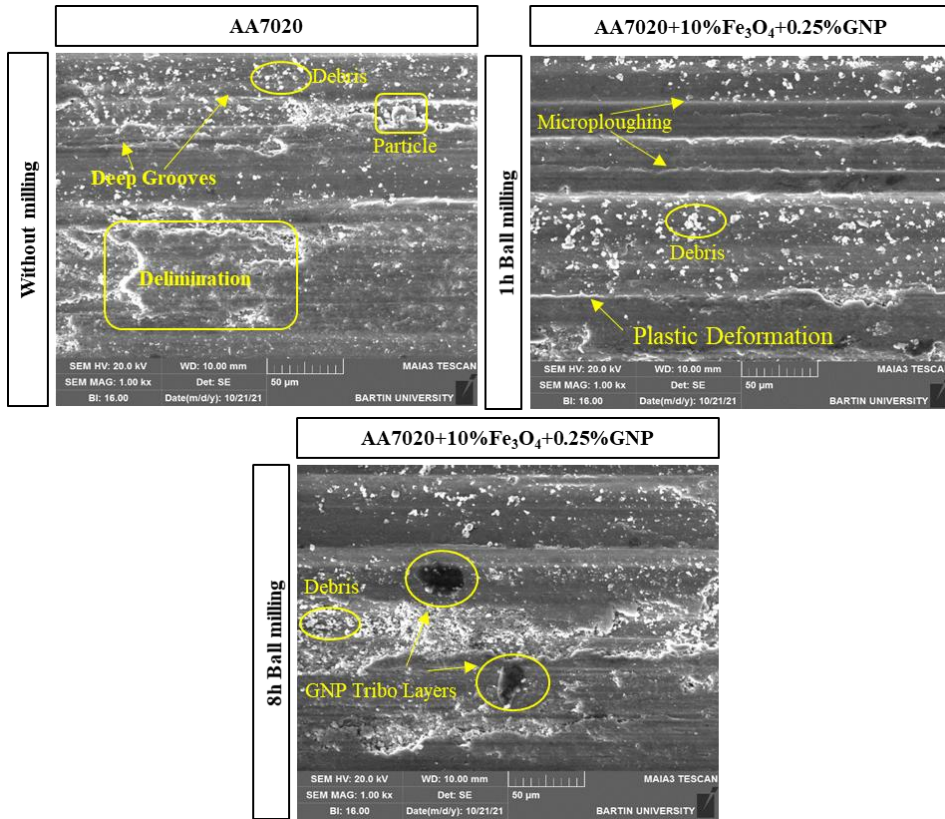
Figure 11. *SEM pictures of the worn surfaces*

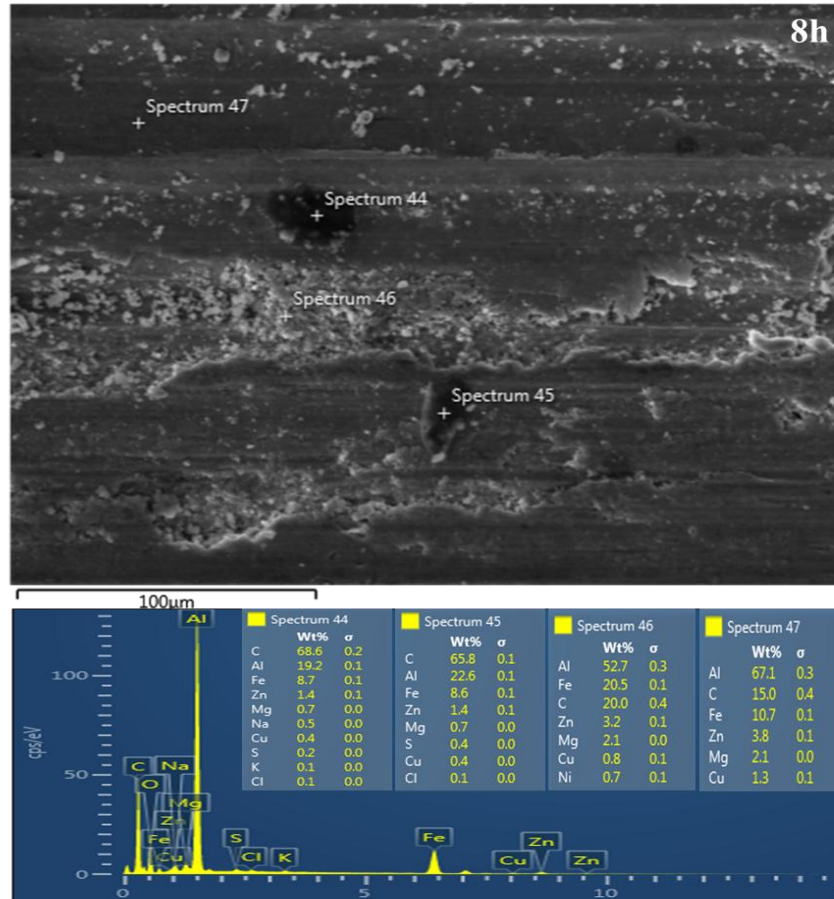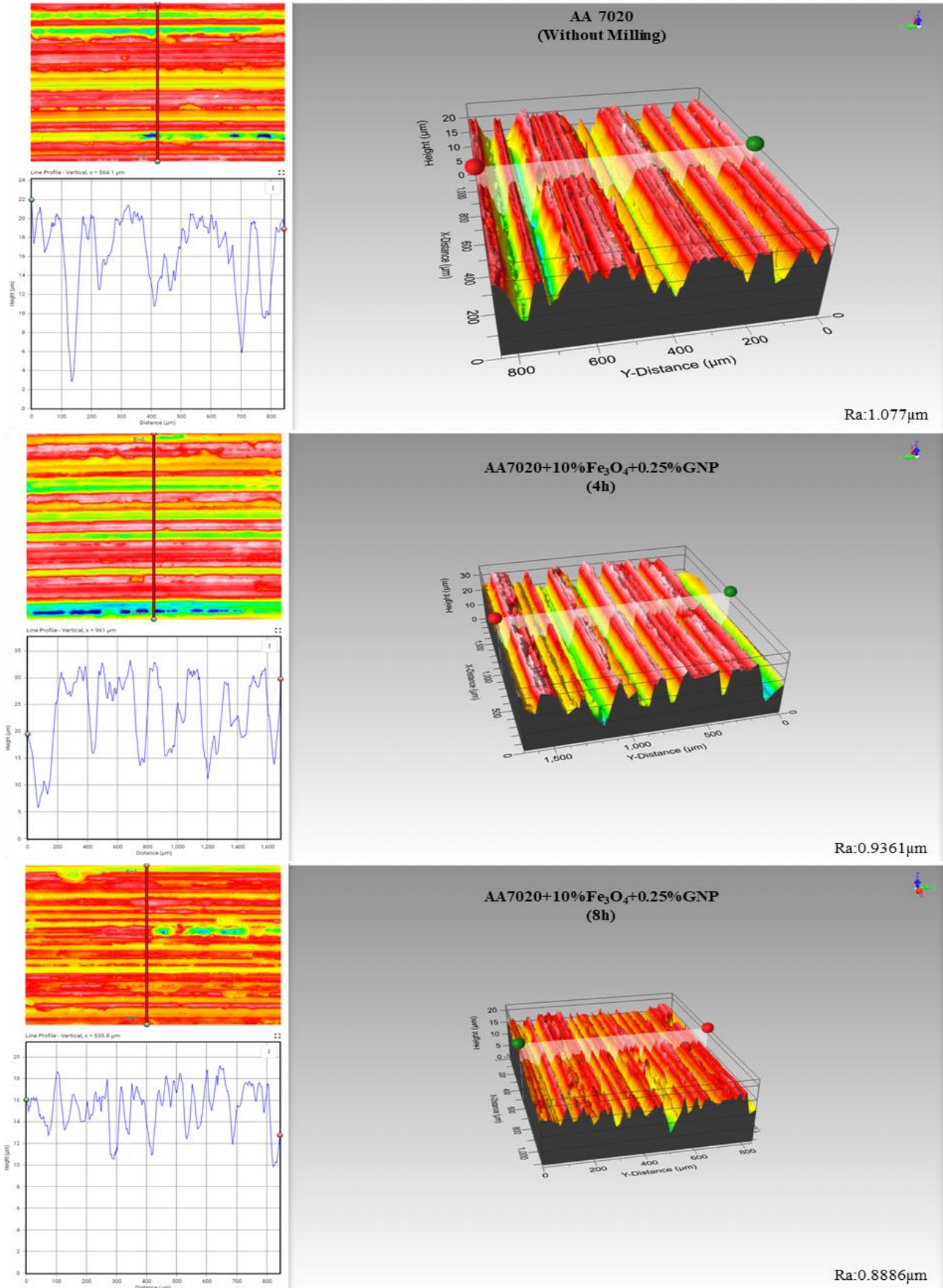**Figure 12.** *EDS analysis result images of the worn surface of hybrid composites (8h) material*

Figure 13. *3D optical profilometer images of the worn surfaces*

4. CONCLUSION

In this study, AA7020 alloy and AA7020+10%Fe_3O_4+0.25%GNP hybrid reinforced composite materials were produced by powder metallurgy hot pressing method. Hybrid-reinforced composite materials were prepared in a ball mixer for 1 and 8 hours. The density, microstructure, hardness, and wear properties of the produced materials were examined. Experimental results are given below.

1. The experimental results revealed a promising trend in the properties of the hybrid-reinforced composite materials. The highest density value, 99.30%, was observed in the 1h milled hybrid reinforced composite material, indicating a significant improvement over the unmilled and non-reinforced AA7020 alloy composite material, which had a density value of 98.8%.

2. The lowest hardness was 109 HV0.5 in unreinforced AA7020 alloy, while the highest hardness value was 118.5 in AA7020+10%Fe_3O_4+0.25%GNP(8h) hybrid reinforced composite material.

3. It was observed that the friction coefficient decreased with increasing grinding time. The highest friction coefficient was determined in the AA7020 alloy material without reinforcement (0.3862 μm). The highest friction coefficient value was determined as 0.1965 μm in the AA7020+10%Fe_3O_4+0.25%GNP(8h) material, decreasing by approximately 50%.

4. It improved the wear resistance and minimized volume losses with increasing grinding time. The lowest specific wear rate was in the AA7020+10%Fe_3O_4+0.25%GNP(8h) hybrid composite ($6.16* 10^{-7}$ mm^3/Nm) material, while the highest specific wear rate was in the AA7020 alloy ($4.33* 10^{-6}$ mm^3/Nm)..

ACKNOWLEDGEMENT

CONFLICT OF INTEREST

The author declares no conflict of interest.

REFERENCES

Jiang, J., Xiao, G., Che, C., & Wang, Y. (2018). Microstructure, mechanical properties and wear behavior of the rheoformed 2024 aluminum matrix composite component reinforced by Al_2O_3 nanoparticles. *Metals*, *8*(6), 460. https://doi.org/10.3390/met8060460

Kanthavel, K., Sumesh, K. R., & Saravanakumar, P. (2016). Study of tribological properties on Al/Al_2O_3/MoS_2 hybrid composite processed by powder metallurgy. *Alexandria Engineering Journal*, *55*(1), 13-17. https://doi.org/10.1016/j.aej.2016.01.024

Karakoç, H., Ovalı, İ., Dündar, S., & Çıtak, R. (2019). Wear and mechanical properties of Al6061/SiC/B_4C hybrid composites produced with powder metallurgy. *Journal of Materials Research and Technology*, *8*(6), 5348-5361. https://doi.org/10.1016/j.jmrt.2019.09.002

Kaya, H., Büyük, U., Çadırlı, E., Şahin, M., & Gündüz, M. (2022). The Effect of Growth Rate on the Microstructure and Mechanical Properties of 7020 Alloys. *Journal of Materials Engineering and Performance*, *31*(2), 1622-1630. https://doi.org/10.1007/s11665-021-06298-8

Kumar, M., Sotirov, N., & Chimani, C. M. (2014). Investigations on warm forming of AW-7020-T6 alloy sheet. *Journal of Materials Processing Technology*, *214*(8), 1769-1776. https://doi.org/10.1016/j.jmatprotec.2014.03.024

Kumar, D., Angra, S., & Singh, S. (2022). Mechanical properties and wear behaviour of stir cast aluminum metal matrix composite: a review. International *Journal of Engineering*, *35*(4), 794-801. https://doi.org/10.5829/ije.2022.35.04A.19

Kumar, D., Angra, S., & Singh, S. (2023). High-temperature dry sliding wear behavior of hybrid aluminum composite reinforced with ceria and graphene nanoparticles. *Engineering Failure Analysis*, *151*, 107426. https://doi.org/10.1016/j.engfailanal.2023.107426

Lakshmikanthan, A., Angadi, S., Malik, V., Saxena, K. K., Prakash, C., Dixit, S., & Mohammed, K. A. (2022). Mechanical and tribological properties of aluminum-based metal-matrix composites. *Materials*, *15*(17), 6111. https://doi.org/10.3390/ma15176111

Michael, A., & John, E. R. (2024). Thermo-Mechanical, Tribological and Microstructural Properties of Aluminium AA8011/B$_4$C/Graphene Based Hybrid Composites. *Transactions of the Indian Institute of Metals*, *77*(4), 1217-1228. https://doi.org/10.1007/s12666-023-03238-z

Özkan, Z., Gökmeşe, H., & Gökmen, U. (2022). Investigation of the microstructure-hardness and wear performances of hybrid/composite materials Al$_2$O$_3$/SiC particle reinforced in AA 7075 matrix. *Science of Sintering*, *54*(2), 177-187. https://doi.org/10.2298/SOS2202177O

Reddy, P. S., Kesavan, R., & Vijaya Ramnath, B. (2018). Investigation of mechanical properties of aluminium 6061-silicon carbide, boron carbide metal matrix composite. *Silicon*, *10*, 495-502. https://doi.org/10.1007/s12633-016-9479-8

Sardar, S., Karmakar, S. K., & Das, D. (2020). Experimental investigation on two-body abrasion of cast aluminum–alumina composites: influence of abrasive size and reinforcement content. *Journal of Tribology*, *142*(3), 031702. https://doi.org/10.1115/1.4045378

Sharma, D. K., Badheka, V., Patel, V., & Upadhyay, G. (2021). Recent developments in hybrid surface metal matrix composites produced by friction stir processing: a review. *Journal of Tribology*, *143*(5), 050801. https://doi.org/10.1115/1.4049590

Srivyas, P. D., Gupta, A., Medhi, T., Arumugam, S., Kumar, D., & Mohan, S. (2023). Corrosion and Tribo-Investigations on Alumina–Graphene-Doped Hybrid Aluminium Composites. *Transactions of the Indian Institute of Metals*, *76*(12), 3281-3291. https://doi.org/10.1007/s12666-023-02999-x

Taşcı, U., & Bostan, B. (2022). Investigation of microstructure and tribological behavior of WE43/nano B$_4$C composites produced by spark Plasma sintering. *Gazi University Journal of Science Part A: Engineering and Innovation*, *9*(4), 562-569. https://doi.org/10.54287/gujsa.1214668

Taşcı, U., Yılmaz, T. A., Karakoç, H., & Karabulut, Ş. (2024). Enhancing Wear Resistance and Mechanical Behaviors of AA7020 Alloys Using Hybrid Fe$_3$O$_4$-GNP Reinforcement. *Lubricants*, *12*(6), 215. https://doi.org/10.3390/lubricants12060215

Zheng, K., Du, X., Qi, H., Zhao, T., Liu, F., & Sun, B. (2020). Sliding-Wear Behavior of Aluminum-Matrix Composites Reinforced with Graphene and SiC Nanoparticles. *Materials and Technology*, *54*(1). https://doi.org/10.17222/mit.2019.104

JOURNAL OF SCIENCE

PART A: ENGINEERING AND INNOVATION